

ELECTRONIC POPULATION MANIPULATION IN AN RFQ ION TRAP FOR THE  
STUDY OF RARE TRANSITION METAL ISOTOPES

By

Jeremy D. Lantis

A DISSERTATION

Submitted to  
Michigan State University  
in partial fulfillment of the requirements  
for the degree of

Chemistry - Doctor of Philosophy

2020

## ABSTRACT

# ELECTRONIC POPULATION MANIPULATION IN AN RFQ ION TRAP FOR THE STUDY OF RARE TRANSITION METAL ISOTOPES

By

**Jeremy D. Lantis**

Laser spectroscopy techniques have been extensively used to determine fundamental properties of the atomic nuclei across broad swaths of the chart of the nuclides, including both stable and unstable (radioactive) nuclei. However, the transition metal region has proven difficult to study with laser spectroscopy due to the electronic structure of the transition metals and short half-lives of radioactive nuclei. Experimental access to the transition metal region for laser spectroscopy studies would contribute to the understanding of nuclear structure and provide important data for nuclear stockpile stewardship. In order to gain experimental access to the transition metal region, an optical pumping technique can be performed to manipulate the electronic populations of ions. Ions in low-energy electronic states are excited to a state that preferentially decays to one accessible for precision laser spectroscopy measurements. This work presents the results of commissioning experiments of an optical pumping system at the BEam COoling and LAser (BECOLA) spectroscopy facility, located at the National Superconducting Cyclotron Laboratory. An optical pumping simulation was developed to predict the gain in sensitivity for the first- and second-row transition metals from optical pumping and guide the commissioning experiments. The results of the simulation show that most transition metal elements can benefit from the optical pumping technique. New instrumentation, including a pulsed laser system and a free-space light transport system, were installed at BECOLA to perform the optical pumping technique on ions in a Radio-Frequency

Quadrupole(RFQ) cooler/buncher ion trap. The commissioning experiments were performed with a beam of stable  $Zr^+$ , produced by an offline plasma discharge sputter ion source and delivered to the BECOLA RFQ ion trap. Two optical pumping schemes were investigated, exciting ions from the  $4d^25s\ ^4F_{3/2}$  and  $4d^25s\ ^4F_{5/2}$  states. The manipulation of the electronic populations was probed through changes in the fluorescence signal in subsequent collinear laser spectroscopy measurements through the excitation of ions in the  $4d^25s\ ^4F_{3/2}$  state. The electronic populations of ions in the RFQ ion trap were successfully manipulated while the ions are quickly rethermalized to a room temperature distribution by collisions with a He buffer gas. The experimental results were in good agreement with the optical pumping simulation and based on that validation, BECOLA is well situated to study rare isotopes of essentially all transition metal elements at the Facility for Rare Isotope Beams(FRIB).

## ACKNOWLEDGMENTS

I could not have finished this project or dissertation without the help of countless individuals.

I first want to thank Kei Minamisono, for your mentorship and guidance through my time in graduate school. You pushed me to do my best and helped me develop as a scientist. I also want to thank Paul Mantica, for your advice and support through my time in graduate school, and for introducing me to the world of nuclear chemistry. In addition, I would like to thank Greg Severin and Oscar Naviliat-Cuncic for serving on my guidance committee.

I also need to acknowledge other members of the BECOLA group, past and present. First, I would like to recognize David Garand, who started the pulsed laser project at BECOLA and contributed substantially to the optical pumping simulation. I also want to thank Kristian König, Andrew Miller, Robert Powel, and Skyy Pineda for their help with the commissioning experiments and their friendship. It is always easier to come to the lab knowing friendly faces are waiting.

Finally, I want to thank my wife and family. Mom and Dad, thank you for your encouragement through every level of school. You always supported me, and I wouldn't be here without you or your sacrifices. Every year I appreciate more and more the opportunities that you gave me. Lydia, you are my best friend and I need to thank you for everything that you have done to support me through my time in graduate school. I could not have finished this dissertation without you.

# TABLE OF CONTENTS

<b>LIST OF TABLES</b> . . . . .	<b>viii</b>
<b>LIST OF FIGURES</b> . . . . .	<b>xi</b>
<b>KEY TO ABBREVIATIONS</b> . . . . .	<b>xxii</b>
<b>Chapter 1 Introduction</b> . . . . .	<b>1</b>
1.1 Laser Spectroscopy of Transition Metal Isotopes . . . . .	1
1.1.1 First-Row Transition Metals . . . . .	2
1.1.2 Second Row Transition Metals . . . . .	4
1.2 Stockpile Stewardship . . . . .	6
1.2.1 Neutron Capture Cross Section . . . . .	7
1.2.2 Separation of Nuclear Waste . . . . .	9
1.3 Laser Spectroscopy of Radioactive Nuclei . . . . .	10
1.3.1 Issues Facing Laser Spectroscopy of Transition Metals . . . . .	11
1.3.1.1 Production of Rare Transition Metal Isotopes . . . . .	12
1.3.1.2 Inaccessibility of Ground State Electronic Transitions . . . . .	12
1.3.1.3 Charge Exchange Reactions for Laser Spectroscopy . . . . .	13
1.4 Electronic Population Manipulation . . . . .	15
1.4.1 Mechanism of Laser Excitation . . . . .	15
1.4.2 Optical Pumping for Electronic Population Manipulation . . . . .	19
1.5 Organization of Dissertation . . . . .	20
<b>Chapter 2 Hyperfine Interactions</b> . . . . .	<b>22</b>
2.1 Atomic Structure and Nuclear Properties . . . . .	22
2.1.1 Isotope Shift and Charge Radius . . . . .	22
2.1.1.1 Mass Shift . . . . .	23
2.1.1.2 Field Shift . . . . .	24
2.1.2 Hyperfine Splitting and Nuclear Moments . . . . .	25
2.2 King Plot Analysis . . . . .	27
2.2.1 King Plot Analysis of $Zr^+$ . . . . .	28
<b>Chapter 3 Optical Pumping Simulation</b> . . . . .	<b>31</b>
3.1 Design Principle . . . . .	31
3.1.1 3 Level Solution of Rate Equations . . . . .	33
3.1.2 Simulation Data . . . . .	38
3.2 Assumptions . . . . .	39
3.2.1 Conditions Inside the Ion Trap . . . . .	39
3.2.2 Laser Conditions . . . . .	44
3.3 Operation of the Optical Pumping Simulation . . . . .	45

3.3.1	Choice of CLS Step and Output . . . . .	45
3.4	Results for Transition Metals . . . . .	46
3.4.1	First-Row Transition Metals . . . . .	46
3.4.2	Second-Row Transition Metals . . . . .	48
<b>Chapter 4</b>	<b>Experiment . . . . .</b>	<b>50</b>
4.1	Experimental Techniques . . . . .	50
4.1.1	Collinear Spectroscopy . . . . .	50
4.1.1.1	Doppler Shift Effect . . . . .	51
4.1.1.2	Beam Bunching . . . . .	57
4.2	BECOLA Facility . . . . .	58
4.2.1	Production of Ion Beams . . . . .	59
4.2.2	Radiofrequency Ion Trap . . . . .	62
4.2.3	CLS Beamline . . . . .	67
4.2.4	Continuous Wave Laser System . . . . .	69
4.3	New Developments to BECOLA Facility . . . . .	72
4.3.1	Pulsed Laser System . . . . .	72
4.3.2	Free-Space Light Transport System . . . . .	80
4.3.2.1	Pulsed Laser Fiber Optic Cable System . . . . .	81
4.3.2.2	Free-Space Light Transport . . . . .	83
4.3.2.3	Optical Layout . . . . .	85
4.3.2.4	Stability . . . . .	89
4.3.2.5	Safety System . . . . .	91
4.4	Experimental Method . . . . .	92
4.4.1	Choice of Zr Ion . . . . .	92
4.4.2	Transition Schemes . . . . .	94
4.4.2.1	Depopulation of the Ground State . . . . .	96
4.4.2.2	Augmentation of the Ground State . . . . .	98
4.4.3	Measurement Method . . . . .	98
4.4.3.1	Timing Sequence . . . . .	98
4.4.3.2	Determination of Optical Pumping Effect . . . . .	100
<b>Chapter 5</b>	<b>Results . . . . .</b>	<b>102</b>
5.1	Properties of Optical Pumping in the RFQ Ion Trap . . . . .	102
5.1.1	Laser Beam Size . . . . .	102
5.1.2	Laser Power . . . . .	106
5.1.3	Linewidth . . . . .	108
5.2	Depopulation of the Zr <sup>+</sup> Ground State . . . . .	110
5.3	Augmentation of the Zr <sup>+</sup> Ground State . . . . .	113
5.4	Quenching of Optical Pumping . . . . .	114
5.4.1	Extrapolation of the Optical Pumping Effect . . . . .	121
<b>Chapter 6</b>	<b>Discussion . . . . .</b>	<b>125</b>
6.1	Improvements to the BECOLA Facility . . . . .	125
6.1.1	Free-Space Light Transport System . . . . .	125

6.1.2	Characteristics of the Pulsed Laser System . . . . .	129
6.2	Optical Pumping in the RFQ Ion Trap . . . . .	131
6.2.1	Ion Bunch Size . . . . .	131
6.2.2	Laser Power . . . . .	132
6.2.3	Linewidth . . . . .	133
6.3	Manipulation of Electronic Populations . . . . .	135
6.3.1	Quenching of Optically Pumped Populations . . . . .	136
6.4	Outlook . . . . .	139
6.4.1	Optical Pumping Simulation Accuracy . . . . .	140
6.4.2	FRIB Reach . . . . .	140
6.4.3	Future Laser Systems . . . . .	142
<b>Chapter 7</b>	<b>Conclusion . . . . .</b>	<b>145</b>
<b>APPENDICES</b>	<b>. . . . .</b>	<b>147</b>
	<b>APPENDIX A</b> Optical Pumping Schemes of First and Second-Row Transition Metals . . . . .	<b>148</b>
	<b>APPENDIX B</b> Logic of Shutter Control System . . . . .	<b>164</b>
<b>REFERENCES</b>	<b>. . . . .</b>	<b>166</b>

## LIST OF TABLES

Table 1.1:	Radioactive isotopes of the first-row transition metal elements that have had the charge radii determined experimentally. Few studies have been performed far from stability. . . . .	3
Table 1.2:	Radioactive isotopes of the second-row transition metal elements for which the charge radii have been determined. . . . .	6
Table 1.3:	The 7 Long-Lived Fission Products of $^{235}\text{U}$ and their respective yields and half-lives. Methods to separate these isotopes from nuclear waste are desired to reduce the threat of environmental contamination and ensure proper disposal. . . . .	9
Table 2.1:	Isotope shifts and charge radii of the stable isotopes of Zr . . . . .	29
Table 3.1:	Typical operating parameters of the BECOLA RFQ ion trap, used to calculate the effective ion temperature. . . . .	42
Table 3.2:	Percentage of total electronic population available for CLS measurements of the first-row transition metals, with and without optical pumping. Elements that require charge exchange reactions are indicated. . . . .	47
Table 3.3:	Percentage of total electronic population available for CLS measurements of the second-row transition metals, with and without optical pumping. Elements that require charge exchange reactions are indicated. . . . .	49
Table 4.1:	Pulsed laser wavelengths and powers tested during installation of the Cobra-Stretch laser system at BECOLA. . . . .	77
Table 4.2:	Standard deviation of the relative laser light position at four locations. The data was collected at four locations, on the laser table, at the entrance of the steel pipe connecting the BECOLA laser and experimental areas, at the exit of the steel pipe, and in the lower laser safety box before injection into the beamline. . . . .	91
Table 4.3:	Natural abundances of the stable isotopes of Zr. . . . .	92

Table 4.4:	Decay branches and transition probabilities from the $4d^25p\ ^4G_{5/2}$ state of $Zr^+$ , comparing theoretical calculations from the Kurucz database [75] with experimental results from [103]. The theoretical predictions included decays to three states that were not observed experimentally, and are marked as '-'. . . . .	95
Table 5.1:	Effective absorption linewidth of the $^4F_{3/2}$ to $^4G_{5/2}$ transition in $Zr^+$ at different pulsed laser powers. . . . .	110
Table 5.2:	Results of the depopulation of the ground state of $Zr^+$ using the $^4F_{3/2}$ to $^4G_{5/2}$ . Results reported as the optical pumping effect. . . . .	113
Table 5.3:	Time constant of the quenching of the optically pumped electronic populations by collisional decay with the He buffer gas, across a range of pressures. The time constants of both the depopulating optical pumping scheme and populating optical pumping scheme are shown. If the time constant was not measured at a specific pressure, '-' is shown. . . . .	117
Table 6.1:	Einstein coefficient $A$ limits based on saturation of the transition using similar conditions as the commissioning experiments, namely a laser beam size of $0.27\text{ cm}^2$ . The wavelength ranges are those that were tested during installation of the pulsed laser system. . . . .	133
Table 6.2:	Experimental reach of the first- and second-row transition metals at BECOLA during the FRIB era. BECOLA will be in a unique position to study wide chains of virtually every element in the region. . . . .	142
Table A.1:	Low-energy populated states of $Sc^+$ . . . . .	149
Table A.2:	Optical Pumping Schemes of $Sc^+$ . . . . .	150
Table A.3:	Low-energy populated states of $Ti^+$ . . . . .	151
Table A.4:	Optical Pumping Schemes of $Ti^+$ . . . . .	152
Table A.5:	Low-energy populated states of $V^+$ . . . . .	153
Table A.6:	Optical Pumping Schemes of $V^+$ . . . . .	153
Table A.7:	Optical Pumping Schemes of $Cr^+$ . . . . .	154
Table A.8:	Optical Pumping Schemes of $Mn^+$ . . . . .	155

Table A.9:	Low-energy populated states of Fe <sup>+</sup> . . . . .	155
Table A.10:	Optical Pumping Schemes of Fe <sup>+</sup> . . . . .	156
Table A.11:	Low-energy populated states of Co <sup>+</sup> . . . . .	156
Table A.12:	Optical Pumping Schemes of Co <sup>+</sup> . . . . .	157
Table A.13:	Low-energy populated states of Y <sup>+</sup> . . . . .	157
Table A.14:	Optical Pumping Schemes of Y <sup>+</sup> . . . . .	158
Table A.15:	Low-energy populated states of Zr <sup>+</sup> . . . . .	159
Table A.16:	Optical Pumping Schemes of Zr <sup>+</sup> . . . . .	159
Table A.17:	Low-energy populated states of Nb <sup>+</sup> . . . . .	160
Table A.18:	Optical Pumping Schemes of Nb <sup>+</sup> . . . . .	161
Table A.19:	Optical Pumping Schemes of Mo <sup>+</sup> . . . . .	161
Table A.20:	Optical Pumping Schemes of Ru <sup>+</sup> . . . . .	162

## LIST OF FIGURES

Figure 1.1:	Charge radii of the first-row transition metals as a function of neutron number. No experimental results have been published to date for radioactive isotopes of V, Cr, Co. References for each chain can be found in Table 1.1. . . . .	2
Figure 1.2:	Charge radii of the Ca region, modified from [9]. The Ca region features the absence of a kink signature of the $N = 20$ shell closure, as is seen at $N = 28$ . Measurements of Sc and Ti beyond the shell closure will help illuminate the evolution of the nuclear structure in the region and how the additional proton in the $f_{7/2}$ shell impacts the $N = 20$ shell closure. . . . .	4
Figure 1.3:	$B(E2)$ values of Cr, Fe, Ge, Se, and Kr isotopes as a function of neutron number, data taken from [24]. A sharp increase in collectivity is observed surrounding the $N = 40$ subshell closure, indicating an onset of deformation. . . . .	5
Figure 1.4:	Charge radii of the second-row transition metals as a function of neutron number. No experimental results have been published to date for radioactive isotopes of Y, Zr, Nb, Mo, and Cd. References for each chain can be found in Table 1.2. . . . .	5
Figure 1.5:	Neutron capture network of Zr, from [39]. During events with high neutron flux, a sample rapidly undergoes neutron capture and beta decay to create many different species. Accurate modeling of the neutron flux requires the neutron capture cross sections of all species to be well known, but for many radioactive nuclei no measurements have been performed. For the Zr network, arrows in purple indicate cross sections that have been experimentally determined. . . . .	8
Figure 1.6:	Laser spectroscopy across the chart of the nuclides, modified from [4]. Nuclides marked in black are stable isotopes and isotopes in red are radioactive isotopes that have been studied using laser spectroscopy. The nuclides marked in green have been studied at the BECOLA facility. . . . .	11

Figure 1.7:	Simulated electronic populations after charge exchange neutralization of a 30 keV $\text{Ni}^+$ beam with Na vapor, data taken from [58]. The vertical dashed line indicates the entry energy of the electron. The levels surrounding the entry energy are initially populated and marked in red, but quickly decay to low-energy metastable states. The final population after decay is shown in blue. . . . .	14
Figure 1.8:	Mechanisms for the exchange of electrons between levels. Through interaction with light, stimulated excitation can excite an electron from a ground state to a higher-lying state or cause stimulated decay to the ground state, producing an additional photon. Additionally, electrons in the excited state can spontaneously decay and emit a photon. . . . .	16
Figure 1.9:	Population manipulation of electronic populations to improve the sensitivity of CLS measurements at BECOLA. Pulsed laser light is used to optically pump electrons from a populated low-lying state to an excited state that preferentially decays to a state accessible to the BECOLA CW laser systems for CLS measurements. . . . .	19
Figure 2.1:	Hyperfine splitting of the levels associated with the $^4\text{F}_{3/2}$ to $^4\text{G}_{5/2}$ transition of $^{91}\text{Zr}$ . $^{91}\text{Zr}$ has a nuclear spin of $I = 5/2$ and results in 9 peaks in the hyperfine spectra. The magnetic dipole and electric quadrupole moments can be extracted from the widths of the splittings. . . . .	26
Figure 2.2:	Hyperfine spectra of the stable isotopes of Zr as a function of the isotope shift relative to $^{90}\text{Zr}$ . The spectrum of $^{91}\text{Zr}$ features hyperfine splitting due to the non-zero spin of the nucleus. . . . .	28
Figure 2.3:	King Plot of the stable isotopes of Zr. The measured modified isotope shift is plotted as a function of the modified charge radius. The x-axis is shifted by $1080 \text{ u fm}^2$ to reduce the error correlation between the slope and the y-intercept of the fit. The charge radii of the stable Zr isotopes are known, and the charge radii of newly measured radioactive isotopes can be determined through the linear regression line, shown as a red line. . . . .	30
Figure 3.1:	Simplification of the electronic states involved in the optical pumping process. As ions from the ground state are optically pumped to low-lying metastable states, the ions will no longer interact with the laser light. Spontaneous decay from the low-lying metastable states is negligible over the time scales involved in the optical pumping process, and the states can be pooled together to simplify calculation. . . . .	32

Figure 3.2:	Proportion of ion population in the ground, metastable, and excited states as a function of time. The pulsed laser temporal width is 6 ns, marked by the vertical blue bar. While the ions are irradiated by the laser, the ground state population is optically pumped to the low-lying metastable states. After the laser pulse, the ions remaining in the excited state exponentially decay to the ground and metastable states. . . . .	38
Figure 3.3:	Proportion of electronic population in the low-lying states of $Zr^+$ as a function of temperature. At low temperatures, almost all ions exist in the ground state, with other low-lying states becoming populated as the temperature rises. . . . .	40
Figure 3.4:	Simulated radial distribution of ions in the BECOLA RFQ ion trap, calculated using the 3DCylPIC software. The green circle describes the 95% inclusion radius of the radial distribution, approximately 1.4 mm in radius. The orange circle describes the extent of the trapping region defined by the RFQ rods. . . . .	43
Figure 3.5:	Results of the optical pumping simulation for the first-row transition metals compared to traditional CLS measurements. Most elements will experience a substantial gain in sensitivity through optical pumping, although some elements require very deep UV light that cannot be produced at BECOLA and therefore have no viable optical pumping schemes. . . . .	47
Figure 3.6:	Results of the optical pumping simulation for the second-row transition metals compared to traditional CLS measurements. Most elements will experience a significant gain in sensitivity through optical pumping. . . . .	48
Figure 4.1:	Magnitude of the mean velocity as a function of time in the ion trap and He buffer gas pressure. The lines are to guide the eyes. The He buffer gas serves to cool the beam and limits the velocity of the ions as they move through the RF field. Doppler broadening of the absorption linewidth is reduced as the ions slow. . . . .	53

Figure 4.2:	Doppler broadened absorption linewidth from RF motion as a function of He buffer gas pressure, calculated from the 3DCyIPIC software [80]. The optical pumping process was performed in an RFQ ion trap and the motion of the ions from the RF field was used to determine the absorption linewidth. As the He buffer gas pressure increases, the neutral He atoms serve to limit the velocity of the trapped ions and the absorption linewidth reaches a plateau. The orange line indicates the expected Doppler broadened linewidth in air at 300 K. The BECOLA RFQ ion trap is operated at 80 mTorr of He buffer gas pressure and the Doppler broadened absorption linewidth from the RF motion is comparable to the expected linewidth in air. . . .	54
Figure 4.3:	The relationship between kinetic energy and velocity. Three sets of ions with the same energy spread will have velocity spreads that become progressively narrower as the ion energy increases. CLS measurements take advantage of the kinetic compression of the linewidth to remove broadening effects and perform precise measurements of the transition frequency. . . . .	56
Figure 4.4:	Hyperfine spectra of $^{90}\text{Zr}$ measured using CLS. The width of the hyperfine spectra is approximately 60 MHz. . . . .	57
Figure 4.5:	Diagram of BECOLA Beamline . . . . .	59
Figure 4.6:	Cross section of the BECOLA PIG ion source. The PIG ion source can generate ion beams of many metallic elements via plasma sputtering, at rates up to 10s of nA. . . . .	60
Figure 4.7:	Photograph of the BECOLA PIG ion source. The PIG is attached to the BECOLA beamline with a 6 inch flange. . . . .	61
Figure 4.8:	Cathode and Anticathode composed of Zr. The Zr cathodes quickly eroded over the course of the commissioning experiments. As the erosion progressed, the hole in the anticathode expanded and the cathode developed a large hole as well, which prevented operation of the PIG ion source. . . . .	62
Figure 4.9:	Schematic of the BECOLA RFQ ion trap, taken from [78]. The RFQ ion trap features three sections separated by differential pumping barriers. Ions are cooled through collisions with a He buffer gas in the cooling section, and are trapped in preparation for bunched beam CLS measurements in the trapping region. . . . .	63

Figure 4.10:	Diagram of the crosscut geometry of the BECOLA RFQ rods, taken from [78]. The view of the rods is longitudinal, with the beam direction coming out of the page. The crosscut design produces a linear drag field across the length of the RFQ ion trap with only two power supplies. . . . .	64
Figure 4.11:	Diagram of the segmented electrodes of the BECOLA RFQ trapping region, taken from [78]. The diagram is a crosscut of the RFQ ion trap, with the beam traveling to the right. Voltages are applied to the segmented electrodes to produce a potential well to trap the ions and allow them to be released in bunches for laser spectroscopy measurements. . . . .	65
Figure 4.12:	Measured time spectra of $^{90}\text{Zr}$ with different numbers of ions trapped. The time spectrum on the right of the figure featured the fewest number of ions per bunch and had a FWHM of approximately $1.5 \mu\text{s}$ . The time spectrum on the right contained approximately 10 times more ions per bunch, resulting in a significantly broader FWHM in time. . . . .	67
Figure 4.13:	Diagram of the photon detection region in the BECOLA CLS beamline, taken from [89]. The photon detection region is located immediately after the charge exchange cell. The new design of the photon collection system is placed directly after the old design. The photon detection region serves to collect and focus fluorescence to photomultiplier tubes for CLS measurements. . . . .	69
Figure 4.14:	The BECOLA laser room is located approximately 15 m away from the BECOLA experimental area. The CW laser light is transported to the CLS beamline with the use of fiber optic cable. The output of the fiber optic cable is located in a laser safety box, where the laser light can be prepared for injection into the CLS beamline. . . . .	71
Figure 4.15:	Laser path through the Cobra-Stretch dye laser system from [97]. Laser light from the INDI pump laser excites the lasing medium in the 20 mm oscillator cell and the 40 mm amplifier cell. The output wavelength is selected by the grating position, which is amplified in the amplifier cell, before entering the internal SHG unit where the frequency of light is doubled. . . . .	73
Figure 4.16:	Amplifier dye cell of the Cobra-Stretch pulsed laser system. The dye acts as a lasing medium and is circulated through the cell to prevent laser-induced breakdown of the dye molecules and extend its lifetime. The amplifier cell is 20 mm in length. . . . .	74

Figure 4.17:	Conversion efficiency as a function of wavelength for different dyes across the range of 540-910 nm. Dyes in the range of 540-910 nm are pumped by second harmonic light at 532 nm produced by the INDI pulsed laser. Figure taken from Sirah Cobra-Stretch User's Manual [97]. . . . .	75
Figure 4.18:	Conversion efficiency as a function of wavelength for different dyes across the range of 370-580 nm. Dyes in the range of 370-580 nm are pumped by third harmonic light at 355 nm produced by the INDI pulsed laser. Figure taken from Sirah Cobra-Stretch User's Manual [97]. . . . .	76
Figure 4.19:	The width of the temporal pulse produced by the Cobra-Stretch laser system. The laser light was attenuated using a neutral density filter before being captured on a photodiode. . . . .	78
Figure 4.20:	Laser beam profiles of the INDI pump laser(Top) and Cobra-Stretch dye laser(Bottom) as seen on burn paper. The laser profile of the INDI system is circular and the power is evenly distributed, while the laser beam profile of the Cobra-Stretch is elliptical and the power is not evenly distributed. . . . .	79
Figure 4.21:	Power distribution of pulsed laser light produced by the Cobra-Strech system. Multiple modes of light are produced by the laser, resulting in a profile with three local maxima. . . . .	80
Figure 4.22:	The BECOLA laser room is located approximately 15 meters away from the BECOLA experimental area. The free-space light transport system uses mirrors to deliver light to the experimental area with minimal loss of power. . . . .	81
Figure 4.23:	New laser safety boxes constructed in the BECOLA experimental area. Laser light from the BECOLA laser room is sent through a 10-m long steel pipe to the laser boxes. The upper box contains two breadboards to direct the light through steel pipes to the lower boxes for preparation before injection into the CLS beamline and RFQ ion trap. . . . .	84
Figure 4.24:	Optical layout on the pulsed laser table. The yellow light shows the path of the pulsed laser light. The light is translated from the output of the Cobra-Stretch system to a mirror using a pair of periscope mirrors. The light passes through two lenses, which are used as a telescoping system to slowly focus the light through the light transport system. The light is then reflected upward to an inverted breadboard.	86

Figure 4.25:	Optical layout of the inverted breadboard in the BECOLA laser area. The light is translated to the breadboard by a pair of mirrors used as a periscope. The light is reflected by two mirrors which can be used for alignment through a 10 m long pipe to the BECOLA experimental area. . . . .	87
Figure 4.26:	Optical layout of the pulsed laser safety box used to prepare the pulsed laser light for injection into the RFQ ion trap. The light is translated down to the safety box from the 10 m long pipe using a pair of mirrors used as a periscope. The light is reflected by two mirrors which can be used to align the laser light through the RFQ ion trap. The diagram below shows the laser light path in yellow and the reflected light path in green, mirrors are blue ovals, the backstop is black, and the wedged window is a red oval. The red lines indicate where the optical elements are located in the photograph. . . . .	88
Figure 4.27:	Center of laser beam tracked across 25 minutes at four different locations. Each set of data is relative to the average position of the laser light. The data was collected at four locations, on the laser table, at the entrance of the steel pipe connecting the BECOLA laser and experimental areas, at the exit of the steel pipe, and in the lower laser safety box before injection into the beamline. Although movement of the beam is small in the BECOLA laser room, the laser light moves on the order of millimeters by the end of the free-space light transport system. . . . .	90
Figure 4.28:	Partial electronic states of $Zr^+$ [76]. The hyperfine levels of each electronic state are not shown, as the level density of $Zr^+$ is very high.	93
Figure 4.29:	Optical pumping scheme for the depopulation of the ground state of $Zr^+$ . Ions from the ground state are excited to the $4d^25p\ ^4G_{5/2}$ state. Approximately 32% of ions decay to metastable states that are dark to subsequent CLS measurements, reducing the sensitivity. . . . .	96
Figure 4.30:	Optical pumping scheme for the augmentation of the ground state of $Zr^+$ . Ions from the first excited state are excited to the $4d^25p\ ^4G_{5/2}$ state. Approximately 66% of ions decay to the ground state, increasing the sensitivity of subsequent CLS measurements. . . . .	97
Figure 4.31:	Optical pumping scheme for the augmentation of the ground state of $Zr^+$ . Ions from the first excited state are excited to the $4d^25p\ ^4G_{5/2}$ state. Approximately 66% of ions decay to the ground state, increasing the sensitivity of subsequent CLS measurements. . . . .	99

Figure 4.32:	Example of optical pumping data, pumping ions from the ground state with the ${}^4F_{3/2}$ to ${}^4G_{5/2}$ transition of $Zr^+$ . As the ion bunch passes the PMTs at approximately $30 \mu s$ , the fluorescent photons are captured. The photon counts were measured as a function of time and shutter status. A time gate was applied to remove background. The time gate is shown as vertical lines around the peak. . . . .	100
Figure 5.1:	Optical pumping effect as a function of pulsed laser beam position. The pulsed laser light was moved off of the trapped ions and scanned in one direction across the trapped ions to approximate its size. . . .	104
Figure 5.2:	Spectra of fluorescent photon counts as a function of time, with and without optical pumping. The measurement was performed with a tightly focused laser beam and high laser power and the optical pumping effect is much larger than expected. . . . .	105
Figure 5.3:	Optical pumping effect as a function of the laser power for the ${}^4F_{3/2}$ to ${}^4G_{5/2}$ transition in $Zr^+$ . The transition quickly saturates, but experiences a second sharp increase in the optical pumping effect above 40 mW. . . . .	107
Figure 5.4:	Optical pumping effect as a function of the laser power for the ${}^4F_{3/2}$ to ${}^4G_{5/2}$ transition in $Zr^+$ . A fast transition, the optical pumping effect quickly saturates. . . . .	108
Figure 5.5:	Effective absorption linewidth of the ${}^4F_{3/2}$ to ${}^4G_{5/2}$ transition in $Zr^+$ at different laser powers. As the laser power increases, the transition remains saturated even as the laser moves off resonance, resulting in a flat-top spectrum. . . . .	109
Figure 5.6:	Depopulation of the ground state of $Zr^+$ via optical pumping. The fluorescent photons are measured using CLS as a function of time. The ion beam is kept in resonance with the probe laser and alternating measurements were made with and without the pump laser. . . . .	111
Figure 5.7:	Depopulation of the ground state of $Zr^+$ via optical pumping and probing the increased electronic population of the first excited state. . . . .	112
Figure 5.8:	Augmented population of the ground state of $Zr^+$ via optical pumping. The fluorescent photons are measured using CLS as a function of time. The ion beam is kept in resonance with the probe laser and alternating measurements were made with and without the pump laser. . . . .	114

Figure 5.9:	Optical pumping effect of $Zr^+$ as a function of number of laser pulses used to irradiate the trapped ions. The blue bars show the expected optical pumping effect based on the optical pumping simulation, with the orange bars showing the experimental results. The experimental results show no enhancement of the optical pumping effect, providing evidence that collisions with the He buffer gas re-thermalize the trapped ions to a room temperature distribution. . . . .	115
Figure 5.10:	Quenching of the optically pumped electronic populations in $Zr^+$ . The ions held in the RFQ ion trap were excited with a pulsed laser and held for increasing lengths of time. Interactions with the He buffer gas used in the RFQ ion trap leads to cooling of the trapped ions back to a room temperature Boltzmann distribution. . . . .	116
Figure 5.11:	Quenching of the optically pumped electronic populations in the depopulating pumping scheme of $Zr^+$ . . . . .	116
Figure 5.12:	Optical pumping effect as a function of the release time of the trapped ions after irradiation by the pulsed laser light across a range of pressures. The quenching of the optically pumped electronic populations takes a longer time at lower pressures. . . . .	118
Figure 5.13:	Optical pumping effect as a function of the release time of the trapped ions after irradiation by the pulsed laser light across a range of pressures. The quenching of the optically pumped electronic populations takes a longer time at lower pressures. The curves of 50 mTorr, 80 mTorr, and 120 mTorr feature a zoom in of the data. . . . .	119
Figure 5.14:	Optical pumping effect as a function of release delay of the ions after they are irradiated by pulsed laser light, comparing corrected and uncorrected data points for additional ions that enter the trap after the laser pulse. The overall correction is small. . . . .	120
Figure 5.15:	Collisional decay rate between He and the optically pumped electronic populations of $Zr^+$ . The decay rate follows a linear relationship with the pressure of the He buffer gas. . . . .	121
Figure 5.16:	Comparison of the extrapolated optical pumping effect with the experimentally observed optical pumping effect. The results of the depopulating optical pumping are shown on top and the results of the populating optical pumping scheme are shown on bottom. The extrapolated data is based on the time constant of the quenching of the optically pumped electronic populations. . . . .	122

Figure 5.17:	Extrapolated optical pumping effect of the trapped ions immediately after irradiation by the pulsed laser, as a function of pressure. The simulated values are shown as orange and blue bands respectively. The experimental data agrees with the simulated value of the optical pumping effect using experimental branching ratios from Ljung <i>et al.</i> [103] . . . . .	123
Figure 5.18:	Extrapolated optical pumping effect of the trapped ions immediately after irradiation by the pulsed laser, as a function of pressure. The simulated optical pumping effect using the Kurucz and Ljung branching ratios are shown as green and orange bands respectively. The experimental results agree well with the simulated value based on the Ljung simulation value. . . . .	124
Figure 6.1:	Frequency doubled CW laser light produced by a Sirah WaveTrain system. The frequency doubled light was measured approximately 2 m from the WaveTrain system. No lenses were used to focus or collimate the light. The doubled laser light features higher order modes of light seen as halo structures. The higher order light can propagate through the free-space light transport system and induce high stray light background. . . . .	127
Figure 6.2:	Simulated optical pumping effect as a function of the temporal width of the laser pulse. Assuming that the transition remains saturated, the ground state of $Zr^+$ can be almost completely depopulated with a laser pulse of approximately 100 ns in width. . . . .	130
Figure 6.3:	Power broadening of spectral lines. As the laser power increases, the wings of the spectral profile raise and can excite transitions far from the center of the center frequency. . . . .	134
Figure 6.4:	Comparison of the experimental optical pumping effect as a function of pressure with the simulated optical pumping effect with collisional rethermalization added. The simulation shows good agreement with the experimental results and demonstrates that the rethermalization process can be accounted for in simulation. . . . .	139
Figure 6.5:	Chart of the nuclides zoomed in on the first- and second-row transition metals. Isotopes in black are stable, isotopes in blue are radioactive and have previously been studied using laser spectroscopy, isotopes in green will be accessible for studies at BECOLA, and isotopes in pink have previously been studied at BECOLA. . . . .	141

Figure 6.6: Simulated optical pumping effect of the depopulating optical pumping scheme in  $Zr^+$ . The 10 kHz laser system is able to deliver more laser pulses to the ion bunch, but more laser pulses are required to depopulate the ground state due to the lower energy density of the laser light. . . . . 143

Figure B.1: Schematic diagram of the connectivity of the electronic modules used to control the physical shutter for measurement of the optical pumping effect. . . . . 165

## KEY TO ABBREVIATIONS

- AVLIS - Atomic Vapor Laser Ionization Separation
- BECOLA - Beam Cooling and Laser Spectroscopy
- CLS - Collinear Laser Spectroscopy
- CTBT - Comprehensive Test Ban Treaty
- CW - Continuous Wave
- DMSO - Dimethyl Sulfoxide
- FIFO - Fan-in/Fan-out
- FRIB - Facility for Rare Isotope Beams
- FSR - Free Spectral Range
- ISOL - Isotope Separator On-Line
- LLFP - Long-Lived Fission Products
- NIST - National Institute for Standards and Technology
- NSM - Normal Mass Shift
- NSCL - National Superconducting Cyclotron Laboratory
- PIG - Penning Ionization Gauge
- PMT - Photomultiplier Tube
- RFQ - RadioFrequency Quadrupole
- RILIS - Resonant Ionization Laser Ion Source
- SDM - Scale Down Module
- SMS - Specific Mass Shift
- SNR - Signal-to-Noise

# Chapter 1

## Introduction

The BEam COoling and LAser (BECOLA) spectroscopy facility [1, 2] at the National Superconducting Cyclotron Laboratory(NSCL) at Michigan State University uses precision laser spectroscopy techniques to study the nuclear structure of rare isotopes. Rare isotopes are those that do not naturally occur, and are instead produced at particle accelerator facilities. Although laser spectroscopy is a powerful tool [3, 4], the study of transition metal isotopes with this technique has remained difficult, as will be discussed in Section 1.3. The goal of the experiments described here was to develop an optical pumping system to manipulate the electronic populations of transition metal ions in a Radio-Frequency Quadrupole(RFQ) ion trap, enabling the study of transition metal elements that were previously inaccessible to laser spectroscopy measurements. In the following chapter, the motivation to study rare transition metal isotopes for nuclear structure and stockpile stewardship studies is introduced, as well as the issues that make laser spectroscopy of these elements difficult.

### 1.1 Laser Spectroscopy of Transition Metal Isotopes

One of the fundamental properties of the atomic nucleus is its size. Laser spectroscopy measurements can provide information about the charge radius of the nucleus, or the extent of the proton distribution [5, 6]. Measurements of the charge radius can provide critical information about the nuclear strong force and serve as a benchmark for nuclear theory

[3, 7, 4]. The focus of this work is on the first- and second-row transition metals, and the following sections will discuss interesting cases for laser spectroscopy studies from the region.

### 1.1.1 First-Row Transition Metals

Laser spectroscopy measurements have been extended to most elements of the first-row transition metals, with the exception of V, Cr, and Co, and few measurements have been performed on radioactive isotopes of the transition metals, especially far from stability [8]. The charge radii trends of the first-row transition metals can be seen in Figure 1.1. The

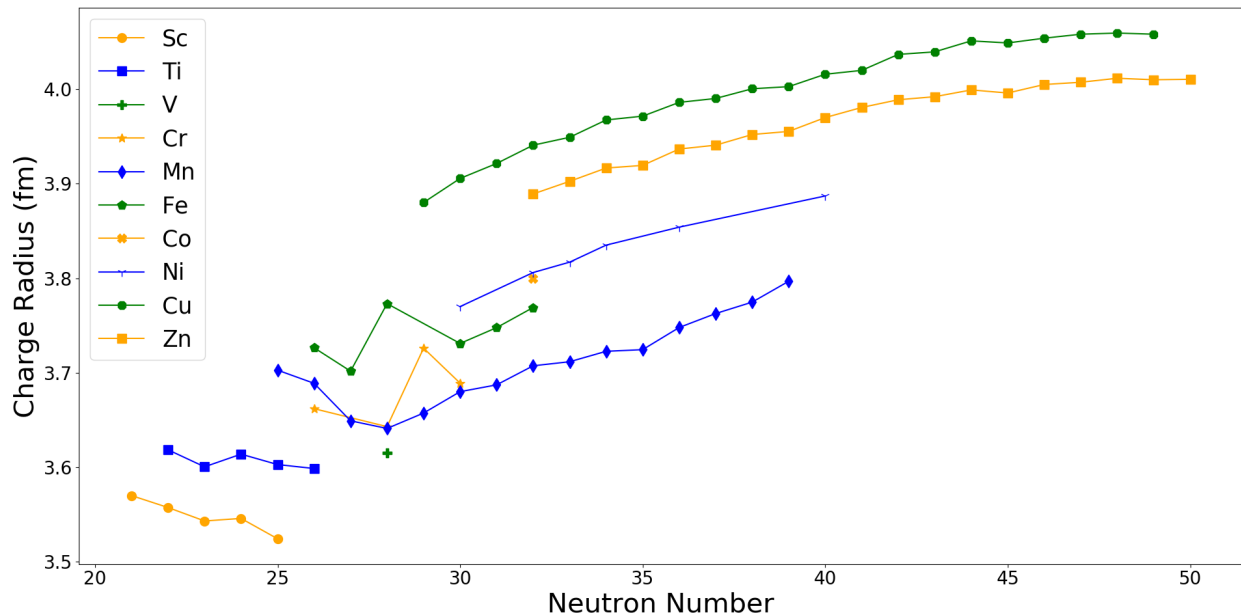


Figure 1.1: Charge radii of the first-row transition metals as a function of neutron number. No experimental results have been published to date for radioactive isotopes of V, Cr, Co. References for each chain can be found in Table 1.1.

charge radii chains in Figure 1.1 include the stable isotopes of each element. The radioactive isotopes that have been studied for each element are shown in Table 1.1.

From a nuclear structure perspective, the first-row transition metals contain many interesting cases for future study at BECOLA, with two examples to follow. The lightest

Table 1.1: Radioactive isotopes of the first-row transition metal elements that have had the charge radii determined experimentally. Few studies have been performed far from stability.

Element	Mass Number	Reference
Sc	42-44,46	[9]
Ti	44	[10]
Mn	50-54, 56-64	[11]
Fe	52,53	[12]
Ni	68	[13]
Cu	58-62,64,66-75	[14]
	76-78	[15]
Zn	62,63,65,69,71-80	[16]

transition metals, Sc and Ti, are of interest towards the  $N = 20$  shell closure. The charge radii of the region around  $N = 20$  has been extensively measured, as can be seen in Figure 1.2. Typically a kink in the charge radius is observed across a shell closure, as seen at the  $N = 28$  shell closure, but such a kink is absent or weak for lighter elements such as Ca [17], K [18, 19], and Ar [20] across the  $N = 20$  shell closure. The absence of the shell closure signature has been attributed to a balance of a monopole proton-core polarization below  $N = 20$  and an onset of deformation above  $N = 20$  [18].  $^{40}\text{Ca}$  is a doubly-magic nucleus, and experimental properties should exhibit trends that indicate the enhanced stability that it brings. Determination of the charge radii of Sc and Ti across the  $N = 20$  shell closure will illustrate if the absence of the  $N = 20$  shell closure persists beyond Ca.

Another important example from the first row of transition metals is the case of the Fe region around the subshell closure at  $N = 40$  [21]. Studies of neutron-rich Fe isotopes have shown an increase in collectivity surrounding  $N = 40$  manifested by a sharp increase in the  $B(E2)$  [22, 23], shown in Figure 1.3. Typically the  $B(E2)$  value reaches a local minimum at a shell closure, but a local maximum is observed across the potential  $N = 40$  subshell closure, suggesting that the subshell closure is weak or absent. As the  $B(E2)$

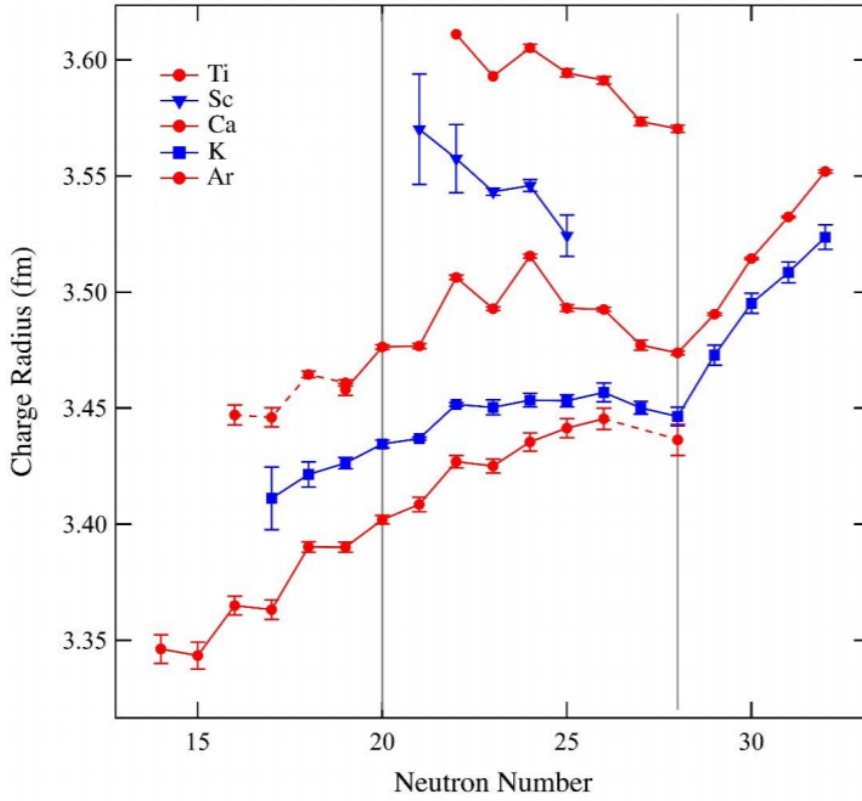


Figure 1.2: Charge radii of the Ca region, modified from [9]. The Ca region features the absence of a kink signature of the  $N = 20$  shell closure, as is seen at  $N = 28$ . Measurements of Sc and Ti beyond the shell closure will help illuminate the evolution of the nuclear structure in the region and how the additional proton in the  $f_{7/2}$  shell impacts the  $N = 20$  shell closure.

is directly related to deformation of the nucleus, charge radii measurements will provide complementary information about the static and dynamic deformation of the nucleus and evolution of the shell structure of this region.

### 1.1.2 Second Row Transition Metals

In common with the first-row transition metals, few laser spectroscopy studies of radioactive isotopes of the second row have been performed [8]. The charge radii trends of the second-row transition metals are shown in Figure 1.4. Although no experimental results have been

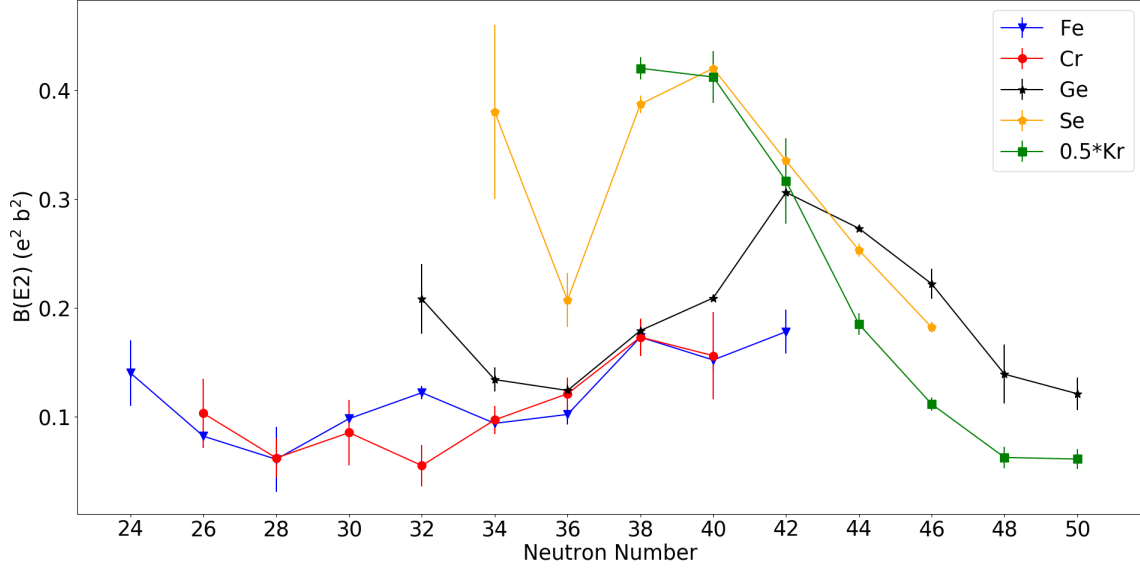


Figure 1.3:  $B(E2)$  values of Cr, Fe, Ge, Se, and Kr isotopes as a function of neutron number, data taken from [24]. A sharp increase in collectivity is observed surrounding the  $N = 40$  subshell closure, indicating an onset of deformation.

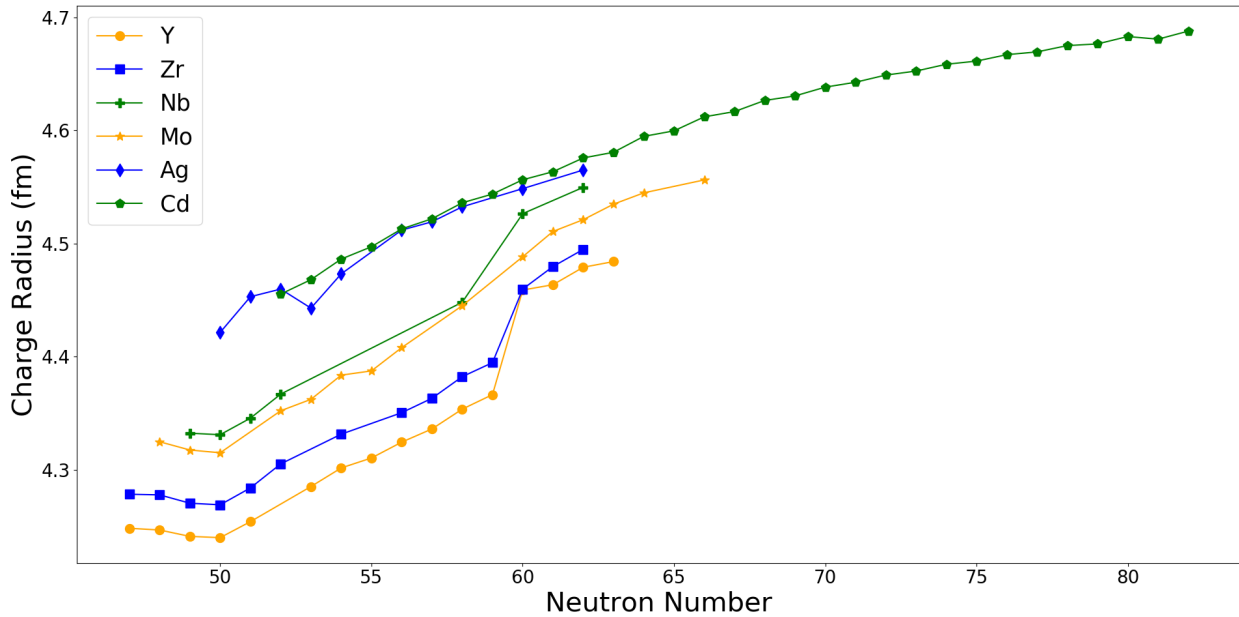


Figure 1.4: Charge radii of the second-row transition metals as a function of neutron number. No experimental results have been published to date for radioactive isotopes of Y, Zr, Nb, Mo, and Cd. References for each chain can be found in Table 1.2.

published for Tc, Ru, Rh, or Pd, other elements in the second row have been extensively studied, complete with measurements far from stability. The radioactive isotopes of the

Table 1.2: Radioactive isotopes of the second-row transition metal elements for which the charge radii have been determined.

Element	Mass Number	Reference
Y	86-88,90-102	[25]
Zr	87-89	[26]
	97-102	[27]
Nb	90-02,99,101,103	[28]
Mo	90,91,102-108	[29]
Ag	97-101	[30]
	103-105	[31]
Cd	100-105,107,109,115,117-130	[32]

second-row transition metals for which the charge radius has been determined are listed in Table 1.2 with references.

There has been interest in possible shape coexistence in nuclei around  $^{80}\text{Zr}$ .  $^{80}\text{Zr}$  is an important isotope for the astrophysical rapid proton ( $rp$ ) process, as the reaction flow is controlled by its beta-plus decay [33]. Nuclear structure calculations have predicted the coexistence of spherical, prolate, and oblate shapes in Zr as well as in surrounding nuclei and isotopes [34], with calculations predicting different deformations [35]. As  $^{80}\text{Zr}$  is near the proton dripline, experimental data are sparse. Laser spectroscopy measurements of the region will be possible in the FRIB era, and will provide critical information for the theoretical description of the region.

## 1.2 Stockpile Stewardship

The transition metal region is of vital importance for nuclear stockpile stewardship [36, 37, 38, 39]. Since the development of a nuclear weapons program in the 1940's, the United States government has been tasked with maintaining a safe and effective nuclear weapon stockpile. In 1996, the United States became party to the Comprehensive Nuclear Test-Ban

Treaty (CTBT), banning all nuclear explosions in all environments. The age of the nuclear stockpile grows each year, and many weapons have exceeded their designed lifetimes [40]. To remain in compliance with the CTBT, verification of the readiness of the nuclear stockpile is left to complex modeling and simulation [40]. The parameters of these codes rely heavily on properties of the nucleus, especially for nuclei that are far from stability. For accurate predictions of the conditions within the weapons and in explosions, the properties of nuclei far from stability need to be known with high precision or predicted with high accuracy.

Laser spectroscopy studies of the transition metal region will benefit the stewardship program through reinforcement of nuclear theory as well as more direct methods such as separation of nuclear waste and will be discussed in the following sections.

### 1.2.1 Neutron Capture Cross Section

One important parameter for the modeling of nuclear explosions is the neutron flux. One method for measuring the neutron flux is through the use of tracer elements, typically transition metal isotopes such as  $^{90}\text{Zr}$  [38]. During detonation, the nucleus of a tracer element may undergo a series of multiple neutron captures and decays, allowing for the production of many different species. The relationship between the possible species that are produced can be described using what is known as a neutron capture network, as shown in Figure 1.5 from [39]. Accurate calculations of the neutron flux are reliant on knowledge of the neutron capture cross section for each isotope that can be produced. Unfortunately, the neutron capture cross section is not known for many radioactive species. It is not possible to produce targets of short-lived species, preventing direct measurement of the neutron capture cross section.

There are ongoing efforts to calculate the cross section indirectly, using methods such

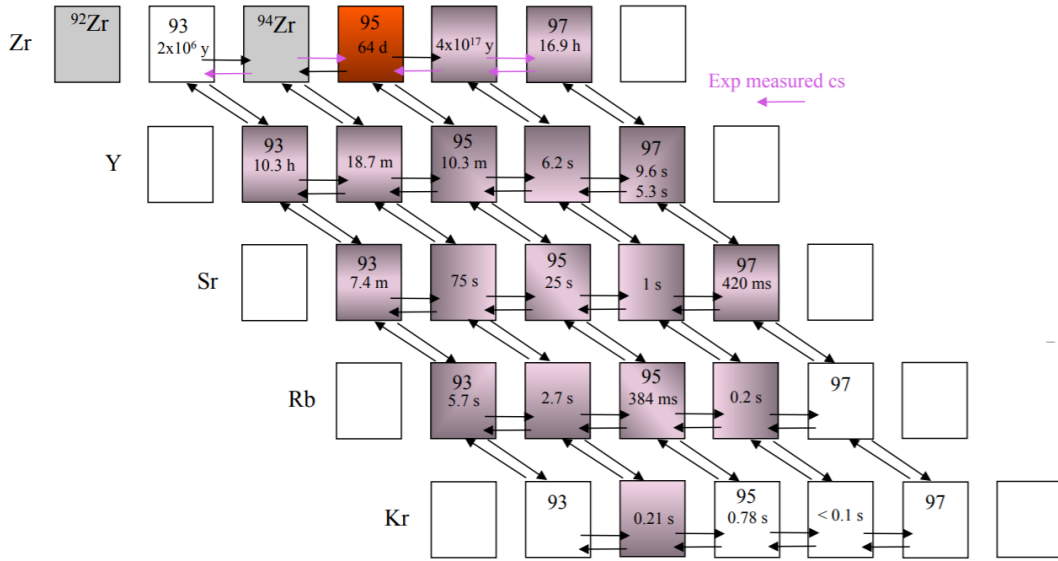


Figure 1.5: Neutron capture network of Zr, from [39]. During events with high neutron flux, a sample rapidly undergoes neutron capture and beta decay to create many different species. Accurate modeling of the neutron flux requires the neutron capture cross sections of all species to be well known, but for many radioactive nuclei no measurements have been performed. For the Zr network, arrows in purple indicate cross sections that have been experimentally determined.

as surrogate nuclear reactions [41] and measurements of the nuclear level density and  $\gamma$ -ray strength function [42]. Without these methods, the current stockpile stewardship codes rely on theoretical calculations as inputs for their simulations. However, the uncertainty in the accuracy of the theoretical results for the less-studied, short-lived isotopes in the neutron capture network leads to large uncertainties in the neutron flux determination. Through laser spectroscopy measurements, the nuclear size and shape can be deduced with high precision, providing important data for constraining the neutron capture cross section and strengthening the framework behind their calculations.

Table 1.3: The 7 Long-Lived Fission Products of  $^{235}\text{U}$  and their respective yields and half-lives. Methods to separate these isotopes from nuclear waste are desired to reduce the threat of environmental contamination and ensure proper disposal.

Isotope	Fission Yield (%)	$t_{1/2}$ (My)
$^{99}\text{Tc}$	6.13	0.21
$^{126}\text{Sn}$	0.11%	0.23
$^{79}\text{Se}$	0.04%	0.32
$^{93}\text{Zr}$	5.45%	1.53
$^{135}\text{Cs}$	6.9%	2.3
$^{107}\text{Pd}$	1.25	6.5
$^{129}\text{I}$	0.84 %	15.7

## 1.2.2 Separation of Nuclear Waste

Another crucial field for the US nuclear stockpile stewardship program is the development of methods for isotope-selective separation. The Atomic Vapor Laser Ionization Separation (AVLIS) technique [43] has been successfully utilized to efficiently separate isotopes. The material of interest is first heated to a high temperature ( $>2000$  K) and vaporized to a neutral beam. Laser light tuned to an optical transition of the desired species is employed to resonantly ionize the neutral beam and the produced cations can be separated and collected using an electric field. The AVLIS technique has a high degree of selectivity provided that the isotope shift between the target and other isotopes is larger than the bandwidth of the ionization laser. The AVLIS technique has been used to both enrich  $^{235}\text{U}$  for nuclear fuel as well as to separate the long-lived fission product  $^{107}\text{Pd}$  [44]. There is particular interest in separation of the 7 long-lived fission products (LLFP) from  $^{235}\text{U}$ , detailed in Table 1.3. The LLFPs make up a significant proportion of nuclear waste and as their long half-lives make them a threat to environmental contamination, there is interest in ways to safely separate [45, 44], or transmute them [46, 47]. Of the LLFPs, three transition metal isotopes are represented,  $^{99}\text{Tc}$ ,  $^{93}\text{Zr}$ , and  $^{107}\text{Pd}$ .

Due to a lack of knowledge of the hyperfine spectrum of  $^{93}\text{Zr}$  and the small isotope shift between the stable  $^{90}\text{Zr}$  and  $^{91}\text{Zr}$  isotopes, other laser methods are being developed for separation [45]. At BECOLA, precision measurements of the hyperfine spectra of  $^{93}\text{Zr}$  can be performed and assist in these efforts.

### 1.3 Laser Spectroscopy of Radioactive Nuclei

Until the development of the laser in 1960 [48], studies of the isotope shift were restricted to emission spectra. As laser technology developed, it became possible to perform laser spectroscopy to measure the isotope shift of atomic beams with high precision [49] using Collinear Laser Spectroscopy (CLS), which will be given a more in-depth description in Chapter 3. Since the development of CLS, fundamental properties of the ground and isomeric states of the nucleus, such as the spin, differential mean-square charge radii, and nuclear moments, have been deduced for radioactive nuclei across broad swaths of the chart of the nuclides [4], as seen in Figure 1.6. As particle accelerators for low-energy nuclear physics have grown more powerful, the reach of laser spectroscopy experiments has also been extended to isotopes far from stability. At next generation facilities such as the Facility for Rare Isotope Beams (FRIB), laser spectroscopy studies will even be able to produce isotopes at the nucleon driplines at sufficient rates for laser spectroscopy studies. The CLS technique measures the fluorescence of the ion or atom, which occurs on timescales faster than the decay of the nucleus.

Although FRIB will bring higher beam rates of rare isotopes, there are still technical challenges to study certain regions of the chart of the nuclides, such as the transition metals. Key nuclei far from stability in the chart of the nuclides, such as  $^{78}\text{Ni}$  with a rate of 7

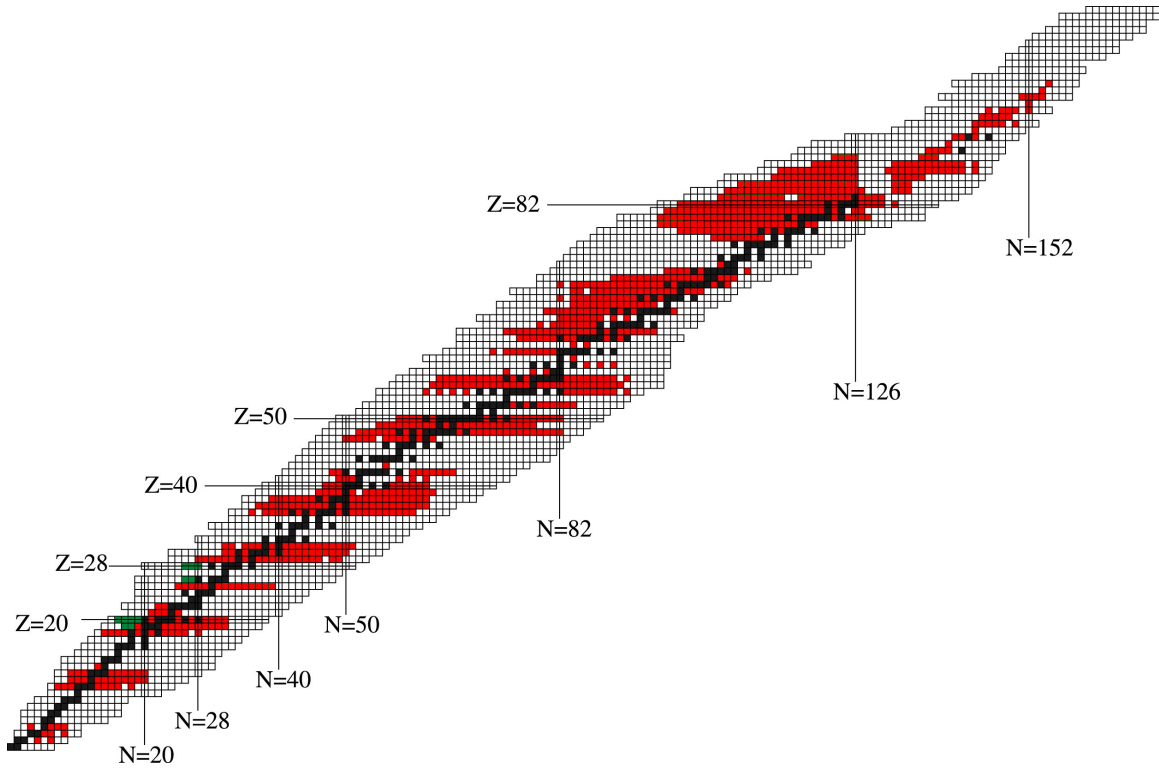


Figure 1.6: Laser spectroscopy across the chart of the nuclides, modified from [4]. Nuclides marked in black are stable isotopes and isotopes in red are radioactive isotopes that have been studied using laser spectroscopy. The nuclides marked in green have been studied at the BECOLA facility.

per second [50] at the ultimate performance (200 MeV, 400 kW) of FRIB, will still be challenging to measure, making sensitivity of the laser spectroscopic measurement of the utmost importance.

### 1.3.1 Issues Facing Laser Spectroscopy of Transition Metals

As previously discussed, there have been relatively few laser spectroscopy measurements of transition metals far from stability. Both the electronic structure of the transition metals and the nuclear properties make them difficult to study, and highly sensitive techniques are necessary.

### 1.3.1.1 Production of Rare Transition Metal Isotopes

One of the significant impediments to the study of rare transition metal isotopes is their production. A majority of past laser spectroscopy experiments on radioactive nuclei were performed at Isotope Separation On-Line (ISOL) facilities [51, 52], where a high-energy beam of protons impinges on a thick production target. The production target is heated to a very high temperature ( $>2000$  K), producing a vapor of the different species in the target. The resulting vapor is ionized and mass separated for experimental measurements.

The ISOL production method faces difficulty producing beams of transition metal isotopes with short half-lives [53]. Many transition metals are refractory elements with high melting points, which in combination with chemistry within the target, leads to long release times. When the release time from the target approaches the nuclear lifetime, it is difficult to realize production rates sufficient for laser spectroscopy measurements.

In comparison to the ISOL production method, the NSCL and FRIB use an in-flight production method. The ion beam produced by the accelerator is impinged on a thin target and the nuclei that result from the projectile-fragmentation reactions are separated in flight through the A1900 separator [54]. The in-flight production method has a distinct advantage for refractory elements because the separation process is not dependent on any chemical properties, and subsequently allows for higher beam rates delivered to experimental systems for the transition metals. However, in general the production yields are smaller using the in-flight production method.

### 1.3.1.2 Inaccessibility of Ground State Electronic Transitions

An additional constraint on the study of transition metal isotopes with laser spectroscopy comes from their electronic configurations. Electronic transitions can only be probed from

populated states, often the ground state. Ground state laser transitions for transition metal elements typically require deep UV laser light in the range of 100-300 nm. The production of 3<sup>rd</sup> and 4<sup>th</sup> harmonic light is necessary to reach the deep UV regime. Harmonic light generation is an inefficient, nonlinear optical process and scales with the square of the power of the fundamental light [55]. Typically, laser spectroscopy studies for the determination of the charge radius use narrow linewidth, continuous wave(CW) laser systems with relatively low output power. 2<sup>nd</sup> harmonic light generation is a well established technique with CW laser systems, but systems capable of producing 4<sup>th</sup> harmonic light suitable for isotope shift measurements have only recently been developed [32].

### 1.3.1.3 Charge Exchange Reactions for Laser Spectroscopy

If there is no suitable ground-state transition in the ionic state, a beam of neutral atoms can instead be produced through charge exchange reactions [56, 57]. One method for atomic charge exchange passes the ion beam of interest through a chamber containing a cloud of alkali vapor, where the ions are neutralized.

Many transition metal elements have accessible transitions in the neutral state and charge exchange reactions have allowed the study of radioactive transition metal isotopes with Fe [12], Ni [13], and Cu [14] to name just a few examples.

Although charge exchange reactions have allowed the study of transition metal isotopes that would otherwise remain out of the reach of current systems, the atomic beams that are produced suffer from reduced sensitivity due to fractionation of the electronic population. The fractionation process has been described in detail before [58], but a short explanation follows. During the neutralization process, the incoming electrons populate the electronic levels surrounding the entry energy. The high-energy states quickly decay to low-energy

metastable states. In elements with high level densities, such as the d-block transition metals, there are typically many different metastable states that can be populated. The high level density is important to populate many highly-excited electronic states that will decay to low-energy states, but can also lead to fractionation of the electronic population. After taking into account the losses due to neutralization efficiency and the fractionation, only a few percentage of the total ion beam can be probed.

To illustrate, Figure 1.7 (taken from [58]) shows the simulated electronic populations of Ni after charge exchange with a Na atom. After the charge exchange process, the ground state of Ni is only populated at 15% of the total atomic population. Typically, the neutralization efficiency of the charge exchange cell is approximately 50%, limiting the overall efficiency of converting the ionic beam to an atomic beam to 7.5%.

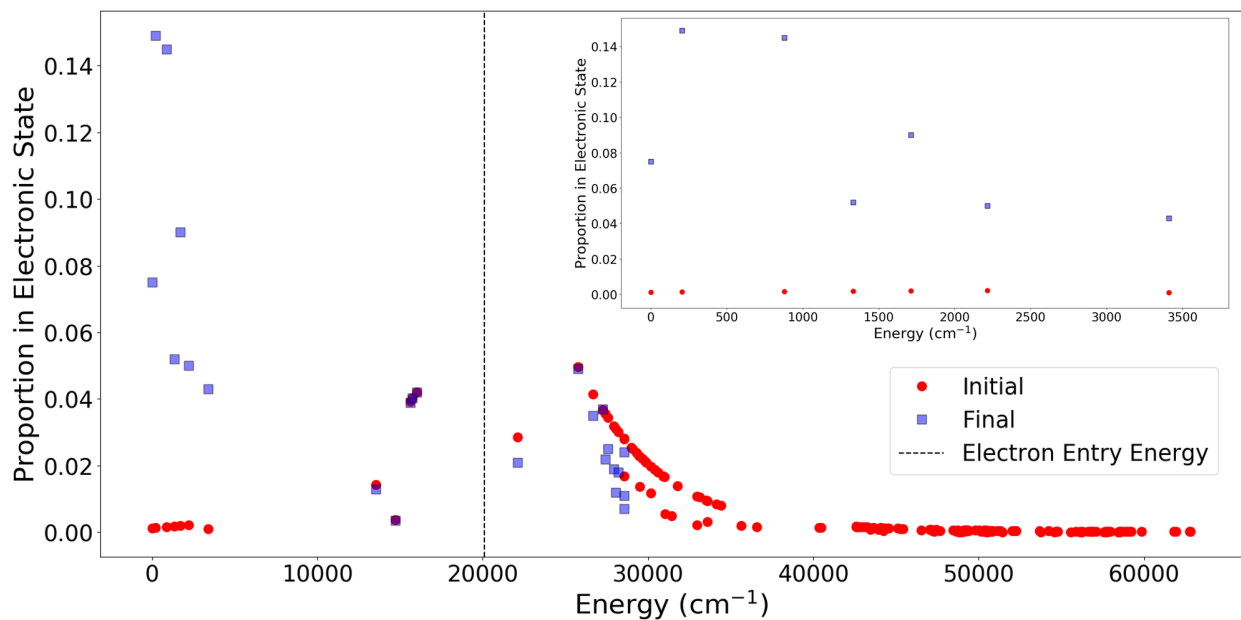


Figure 1.7: Simulated electronic populations after charge exchange neutralization of a 30 keV  $\text{Ni}^+$  beam with Na vapor, data taken from [58]. The vertical dashed line indicates the entry energy of the electron. The levels surrounding the entry energy are initially populated and marked in red, but quickly decay to low-energy metastable states. The final population after decay is shown in blue.

## 1.4 Electronic Population Manipulation

One method to overcome the issues caused by the unfavorable electronic structure of the transition metals is by redistributing the electronic populations to states favorable for laser spectroscopy. The electronic population manipulation can be achieved using a technique known as optical pumping. Although a simple concept, the discovery of optical pumping resulted in the Nobel Prize for Alfred Kastler in 1966 and has been instrumental for important scientific developments, such as the laser. Optical pumping has been used to produce polarized beams of rare nuclei for measurements of nuclear electromagnetic moments using  $\beta$ -NMR [59] and the angular correlation parameters in  $\beta^+$  decay of  $^{37}\text{K}$  [60] with the included references providing examples of experiments that have been performed with polarized beams. A more detailed description of the optical pumping process will be given in Chapter 3, but a short description follows.

### 1.4.1 Mechanism of Laser Excitation

It is useful to begin with an ideal two level system to introduce how electrons are excited, introducing rate equations and saturation of the excited state population.

There are three processes responsible for the movement of electrons between energy levels during the laser excitation and can be used to determine the rate of change of population for each state involved. These processes are stimulated excitation, stimulated decay, and spontaneous decay, and are illustrated in Figure 1.8.

Through stimulated excitation, an electron is excited from a ground state,  $g$ , to a higher energy state,  $e$  by absorbing a photon. The time dependent change in the electronic population of state  $g$ , represented by  $N_g$ , due to absorption of a photon with energy  $h\nu$  is given

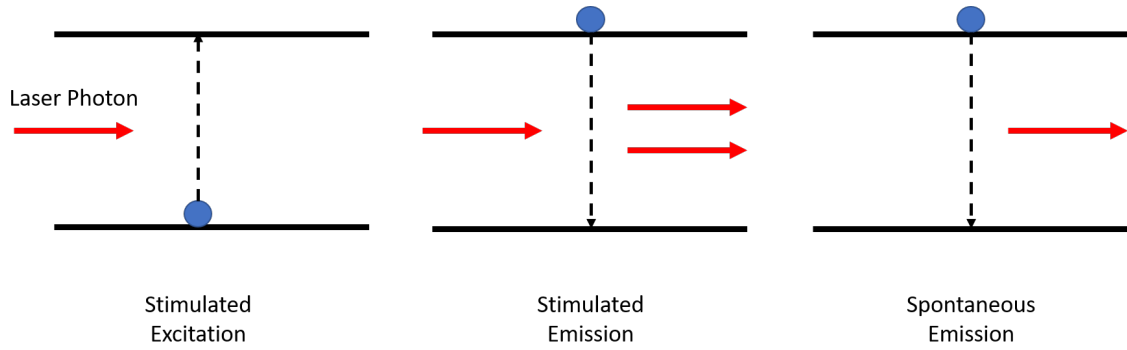


Figure 1.8: Mechanisms for the exchange of electrons between levels. Through interaction with light, stimulated excitation can excite an electron from a ground state to a higher-lying state or cause stimulated decay to the ground state, producing an additional photon. Additionally, electrons in the excited state can spontaneously decay and emit a photon.

as

$$\frac{d}{dt}N_g = -B_{ge}\rho(\nu)N_g \quad (1.1)$$

where  $B_{ge}$  is the probability of stimulated excitation and called the Einstein coefficient of stimulated excitation, and  $\rho(\nu)$  is the energy density of the light at frequency  $\nu$ . In addition to stimulating the excitation of electrons, the applied radiation field can perturb the upper state  $e$ , and cause a stimulated emission from state  $e$  to the ground state  $g$ , resulting in a second photon of frequency  $\nu$ . The rate of change of the population of state  $e$  due to stimulated emission is given as

$$\frac{d}{dt}N_e = -B_{eg}\rho(\nu)N_e \quad (1.2)$$

where  $B_{eg}$  is the probability of the stimulated emission and called the Einstein coefficient of stimulated emission. The upper and lower  $B$  coefficients are related to each other by

$$B_{eg} = \frac{g_g}{g_e}B_{ge} \quad (1.3)$$

where  $g_g$  and  $g_e$  are the degeneracies of the two levels. The upper  $B$  coefficient can be related to the  $A$  Einstein coefficient, which is the Einstein coefficient of spontaneous emission, by

$$B_{eg} = \frac{\pi c^3}{\hbar \lambda^3} A_{eg} \quad (1.4)$$

Finally, an electron in state  $e$  can spontaneously decay to state  $g$  in the absence of any applied radiation. The rate of change of the excited state  $e$  due to spontaneous decay is given as

$$\frac{d}{dt} N_e = -A_{eg} N_e \quad (1.5)$$

where  $A_{eg}$  is the Einstein coefficient of spontaneous emission.  $A_{eg}$  is directly related to the lifetime of the excited state,  $\tau_e$ , by

$$\tau_e = \frac{1}{A_{eg}} \quad (1.6)$$

By adding the absorption and emission processes given in the above equations, the total rate of population change in states  $g$  and  $e$  can be given by

$$\frac{d}{dt} N_g = B_{eg} \rho(\nu) N_e + A_e N_e - B_{ge} \rho(\nu) N_g \quad (1.7)$$

and

$$\frac{d}{dt} N_e = -B_{eg} \rho(\nu) N_e - A_e N_e + B_{ge} \rho(\nu) N_g \quad (1.8)$$

While the external radiation field from the light is applied to the electronic system, the populations of states  $g$  and  $e$  will change until the competing transitions reach equilibrium

and the rate of change reaches 0.

$$\frac{d}{dt}N_g = \frac{d}{dt}N_e = 0 \quad (1.9)$$

Substituting the rate equations from Equations 1.2 and 1.5, the ratio of the populations of the two states at equilibrium can be determined as follows.

$$B_{ge}\rho(\nu)N_g = B_{eg}\rho(\nu)N_e + A_eN_e \quad (1.10)$$

Rearranging Equation 1.10 gives,

$$\frac{N_e}{N_g} = \frac{B_{ge}\rho}{B_{eg}\rho + A_{eg}} \quad (1.11)$$

At laser power densities where  $B_{eg}\rho \gg A_{eg}$ , Equation 1.11 can be simplified to

$$\frac{N_e}{N_g} = \frac{B_{ge}}{B_{eg}} = \frac{g_e}{g_g} \quad (1.12)$$

And the populations at equilibrium will be a ratio of the degeneracies of the state.

In an ideal two state system, the population of the ground state cannot exceed 50% of the total electronic population due to stimulated emission. Optical pumping occurs when electrons in the excited state can decay to more than one low-energy electronic state. Electrons that decay to other electronic states become "dark", as they are no longer resonant with the laser light. Electrons in dark states will not experience stimulated emission and can accumulate until the entire population exists in "dark" states.

## 1.4.2 Optical Pumping for Electronic Population Manipulation

The goal of this project was to develop an optical pumping system to improve the sensitivity of laser fluorescence measurements for transition metal isotopes. Taking advantage of the optical pumping phenomenon, electronic populations can be pumped from inaccessible ground states to low-energy metastable states that are accessible to narrow-linewidth CW lasers for precision measurements. For some elements that do have accessible ground state transitions, electronic populations from other low-energy states can be pumped to the ground state to improve the sensitivity. An example of an optical pumping scheme is shown in Figure 1.9

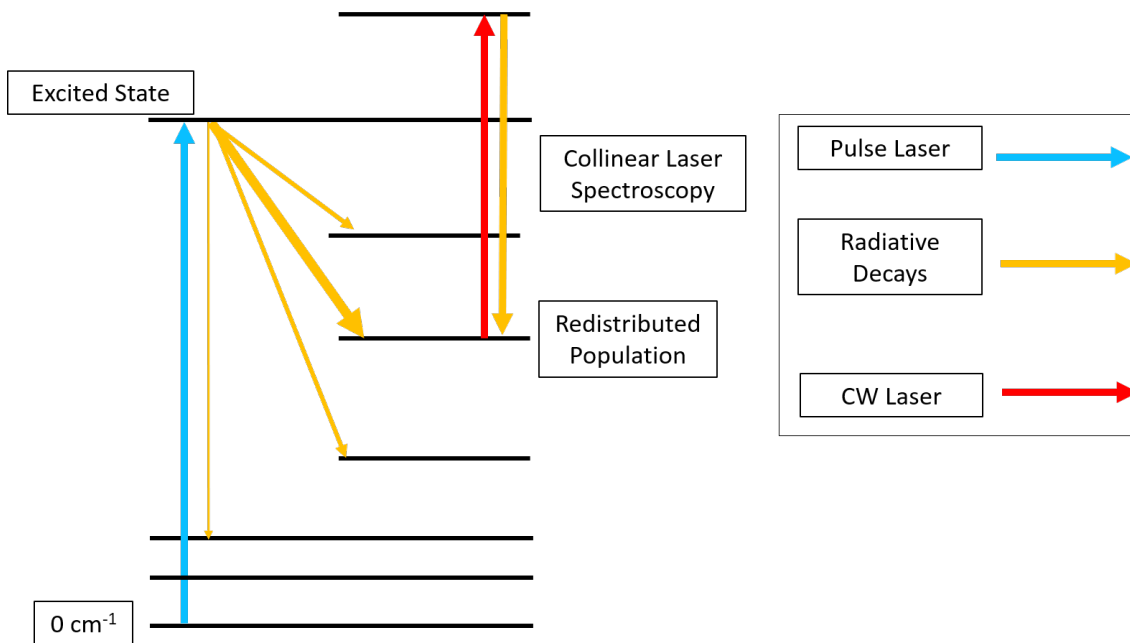


Figure 1.9: Population manipulation of electronic populations to improve the sensitivity of CLS measurements at BECOLA. Pulsed laser light is used to optically pump electrons from a populated low-lying state to an excited state that preferentially decays to a state accessible to the BECOLA CW laser systems for CLS measurements.

Optical pumping of transition metal isotopes has been performed at other laser spectroscopy facilities, for Nb [28], Y [61], and Mn [62] isotopes. The optical pumping technique is performed in an RFQ cooler/buncher ion trap, where the ions can be held for extended

periods of time, allowing for long interaction times between the laser light and the ions, up to ms. After the manipulation of the electronic populations, the ions can be released and probed using CLS.

The pumping step is performed using high-powered pulsed laser light, as  $3^{rd}$  and  $4^{th}$  harmonic light is more readily available due to higher energy density, allowing access to ground state transitions.

Combining the increase in sensitivity that results from optical pumping with the increase in beam rates available at FRIB, the BECOLA facility will have the ability to study transition metal isotopes far from stability.

## 1.5 Organization of Dissertation

In this dissertation, the development of an optical pumping system to manipulate the electronic populations of transition metal isotopes at BECOLA is described. The optical pumping technique increases the sensitivity of laser spectroscopy measurements at BECOLA and will allow for the charge radii and nuclear moments of rare transition metal isotopes to be determined through the hyperfine spectra. The interactions between the nucleus and electron that allow laser spectroscopy measurements to determine fundamental properties of the nucleus are described in Chapter 2. Results of a new King Plot Analysis of  $Zr^+$  are described. An optical pumping simulation was developed to guide experimental efforts and is described in detail in Chapter 3, as well as results of the simulation and potential for transition metal isotope experiments. The experimental method of the commissioning experiments of the optical pumping system are described in Chapter 4. The experimental techniques used to perform fluorescent laser spectroscopy at BECOLA as well as the techniques used to per-

form the electronic population manipulation are described. An introduction to Collinear Laser Spectroscopy (CLS) is given as well as a description of the optical pumping technique. Features of the BECOLA facility are discussed as well as two new upgrades, a pulsed laser system and free-space light transport system. The results of the commissioning experiments are featured in Chapter 5. Chapter 6 is a discussion of the experimental results. Finally, Chapter 7 is a summary of the thesis as well as discussion of the outlook for future radioactive beam experiments using the optical pumping system and beyond.

# Chapter 2

## Hyperfine Interactions

In this chapter, the interactions between the nucleus and electron are described, as well as how these interactions can be used to determine fundamental properties of the nucleus.

### 2.1 Atomic Structure and Nuclear Properties

Various techniques have been established to determine the charge radius of the nucleus, such as electron scattering [63], charge changing cross-section measurements [64], as well as the isotope shift of K X-rays [65] and muonic atoms [66]. An additional technique, utilized at the BECOLA facility, is the measurement of the isotope shift in optical transitions.

The isotope shift in optical transitions arises from the hyperfine interaction between the nucleus and the valence electrons. From the center-of-gravity isotope shift between two isotopes of the same element, the differential mean-square charge radius can be determined, and from the splitting of the hyperfine spectra, the nuclear spin, nuclear magnetic dipole moment, and electric quadrupole moment can be determined. Measurement of the hyperfine spectra can reveal a trove of information about the nuclear structure.

#### 2.1.1 Isotope Shift and Charge Radius

Soon after the discovery of the nucleus, experimental observations showed that changes in the nuclear mass led to shifts in lines of molecular spectra. In the 1930s, the isotope shift

phenomenon was finally observed in atomic spectra [67] and although initially believed to be a result of the change in mass between isotopes, in 1935 experimental evidence showed that the charge distribution in the nucleus contributed to the shift as well [68]. The isotope shift,  $\delta\nu^{A,A'}$ , is the frequency of light necessary to excite an electronic transition between two isotopes of masses  $A$  and  $A'$ .

$$\delta\nu^{A,A'} = \nu^{A'} - \nu^A \quad (2.1)$$

There are two contributions to the isotope shift, a mass shift due to the change in the mass of the nucleus  $\delta\nu_m^{A',A}$ , and a shift due to a change in the nuclear volume known as the field shift  $\delta\nu_f^{A',A}$

$$\delta\nu^{A',A} = \delta\nu_m^{A',A} + \delta\nu_f^{A',A} \quad (2.2)$$

### 2.1.1.1 Mass Shift

The mass shift also has two components, the specific mass shift (SMS) and the normal mass shift (NMS) which can be represented by constants  $K_{SMS}$  and  $K_{NMS}$ .

$$\delta\nu_m^{A',A} = (K_{SMS} + K_{NMS}) \frac{m_{A'} - m_A}{m_{A'} m_A} \quad (2.3)$$

where  $m_A$  is the mass of an isotope with mass number  $A$  and  $m_{A'}$  is the mass of an isotope with mass number  $A'$ .

The two contributions to the mass shift are due to different changes in the nuclear motion as the reduced mass of the electron-nucleus system changes. In systems with more than one electron, the movements of the electrons are correlated which gives rise to the specific mass shift. The constant  $K_{SMS}$  has no analytical solution and is very difficult to calculate.

Currently, ab initio methods have only been able to calculate  $K_{SMS}$  for systems up to 5 electrons [69]. In contrast, the NMS contribution is much easier to calculate. When an electron is excited to a higher state, its kinetic energy and momentum changes and the nuclear motion must adapt. The change due to the NMS is proportional to the reduced mass of the system and  $K_{NMS}$  is simplified to  $m_e\nu^A$ , where  $m_e$  is the mass of the electron and  $\nu^A$  is the transition frequency. With both contributions to the mass shift, the constants  $K_{NMS}$  and  $K_{SMS}$  can be combined to one constant,  $K$ .

### 2.1.1.2 Field Shift

The second contribution to the isotope shift is the Field shift, also known as the volume shift. The finite size of the nucleus has an effect on the binding energy of electrons, which have wavefunctions that have a non-zero probability density within the nuclear volume. The shift in the energy of an electronic state due to the influence from the nuclear volume,  $E_{FNS}$ , can be described as,

$$E_{FNS} = \frac{Ze^2}{6\epsilon_0} \langle r_c^2 \rangle |\psi(0)|^2 \quad (2.4)$$

which is proportional to the electron density at the nucleus,  $|\psi(0)|^2$ , and the nuclear mean-square charge radius  $\langle r_c^2 \rangle$ . The change in the nuclear volume causes a shift in the energy of the electronic state due to the change in the electron probability density in the nuclear volume, producing a shift in transition frequency. A s-electron with angular momentum  $L = 0$  has a large effect due to its finite probability at the nucleus.

$$\delta\nu_F^{A',A} = \frac{Ze^2}{6h\epsilon_0} \langle r_c^2 \rangle (\Delta|\psi(0)|^2)_{i \rightarrow f} \quad (2.5)$$

Equation 2.5 can be simplified to show that the relationship between two isotopes with mean square charge radii  $\langle r_c^2 \rangle^A$  and  $\langle r_c^2 \rangle^{A'}$  is

$$\delta\nu_F^{A',A} = \frac{Ze^2}{6h\epsilon_0} (\Delta|\psi(0)|^2) (\langle r_c^2 \rangle^{A'} - \langle r_c^2 \rangle^A) = F\delta\langle r_c^2 \rangle^{A',A} \quad (2.6)$$

where the terms outside of the differential mean-square charge radius has been reduced to the field shift constant  $F$ . With solutions for the field and mass shifts, the total isotope shift can be expressed as

$$\delta\nu^{A',A} = KM + F\delta\langle r_c^2 \rangle \quad (2.7)$$

where  $M$  is the reduced mass of the two isotopes with masses  $A$  and  $A'$ ,

$$M = \frac{m_A m_{A'}}{m_A + m_{A'}} \quad (2.8)$$

### 2.1.2 Hyperfine Splitting and Nuclear Moments

The hyperfine interaction between nuclei with non-zero spin and the electron gives rise to a shift in the energy of an electronic state relative to the fine level given by

$$\Delta E = \frac{X}{2} A^{hf} + \frac{3X(X+1) - 4I(I+1)J(J+1)}{8I(2I-1)J(2J-1)} B^{hf} \quad (2.9)$$

$$X = F(F+1) - I(I+1) - J(J+1)$$

where  $I$  is the nuclear spin,  $J$  is the atomic spin, and  $F$  is the quantum number defined by the sum of the atomic and nuclear spins. In Figure 2.1 it is shown the hyperfine splitting of the levels associated with the  ${}^4F_{3/2}$  to  ${}^4G_{5/2}$  transition of  ${}^{91}\text{Zr}$ .

Measurement of the hyperfine spectrum allows the deduction of the  $A^{hf}$  and  $B^{hf}$  hyper-

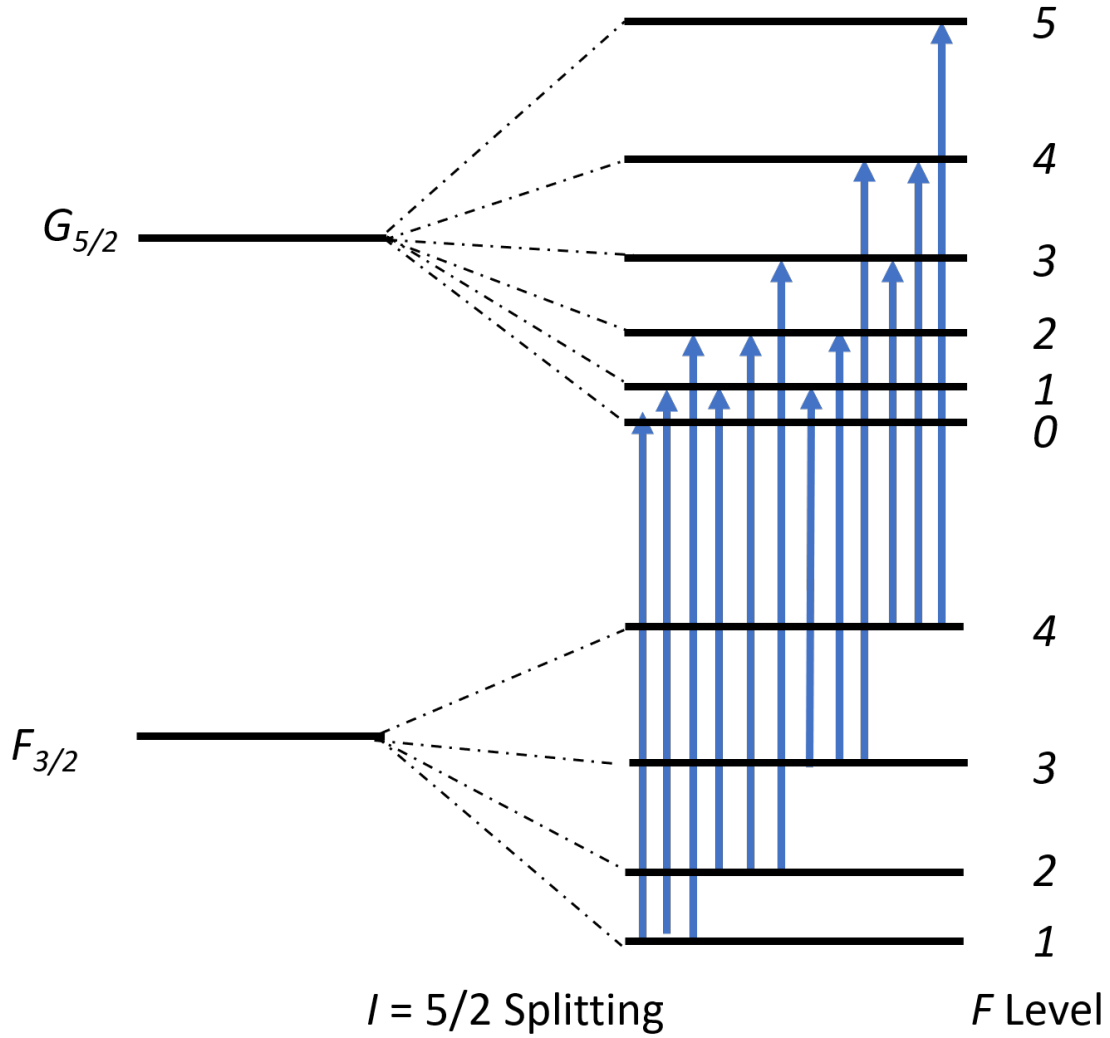


Figure 2.1: Hyperfine splitting of the levels associated with the  ${}^4F_{3/2}$  to  ${}^4G_{5/2}$  transition of  ${}^{91}\text{Zr}$ .  ${}^{91}\text{Zr}$  has a nuclear spin of  $I = 5/2$  and results in 9 peaks in the hyperfine spectra. The magnetic dipole and electric quadrupole moments can be extracted from the widths of the splittings.

fine coupling constants of the electronic state, which contain information about the magnetic-dipole and electric-quadrupole moments,  $\mu$  and  $Q$ , of the nucleus as given by

$$\begin{aligned}
 A^{hf} &= \mu \frac{B_0}{IJ} \\
 B^{hf} &= eQV_{zz}
 \end{aligned}
 \tag{2.10}$$

Here  $B_0$  and  $V_{zz}$  are the magnetic field and electric field gradients that are produced at the nucleus by the electrons.

## 2.2 King Plot Analysis

As previously shown, the isotope shift has two contributions from the mass shift and the field shift, which contain constants  $K$  and  $F$ , which are element and transition dependent and must be known to extract the differential mean-square charge radius. The  $K$  and  $F$  factors can be determined through what is known as a King plot analysis [70] provided that the charge radii of at least three isotopes are known.

The King plot analysis starts by modifying the isotope shifts by dividing each side of the equation by  $M$  from Equation 2.8.

$$\delta v_{modif}^{AA'} = M^{-1} \delta v^{AA'} = FM^{-1} \delta \langle r_c^2 \rangle^{AA'} + K \quad (2.11)$$

The modified differential provides a linear relationship between the differential mean-square charge radius and the modified isotope shift. The data points should lie on a straight line and through a linear regression the  $F$  factor can be determined as the slope of the line and the  $K$  factor through the y-intercept. After deducing the atomic factors, the differential mean-square charge radius can be extracted from the isotope shift for any isotope of the particular element, and is indispensable for the study of radioactive isotopes.

## 2.2.1 King Plot Analysis of $\text{Zr}^+$

The commissioning experiments of the optical pumping system were performed using a beam of  $\text{Zr}^+$ . Although previous experiments have been performed to determine the isotope shift and differential mean-square charge radii of radioactive Zr isotopes [26, 27], these particular experiments utilized the ground state transitions of  $d^2s^4F_{3/2}$  to  $d^2p^4F_{5/2}$  [27] and  $d^2s^4F_{3/2}$  to  $d^2p^4D_{3/2}$  [26], whereas the commissioning experiments used the  $^4F_{3/2}$  to  $^4G_{5/2}$  transition. The  $^4F_{3/2}$  to  $^4G_{5/2}$  transition had not been previously used for isotope shift measurements, and the atomic factors  $F$  and  $K_0$  have not been determined. The hyperfine spectra of the stable Zr isotopes were measured using CLS to determine the atomic factors. The hyperfine spectra of the stable isotopes of Zr are shown in Figure 2.2. The isotope shift is given relative

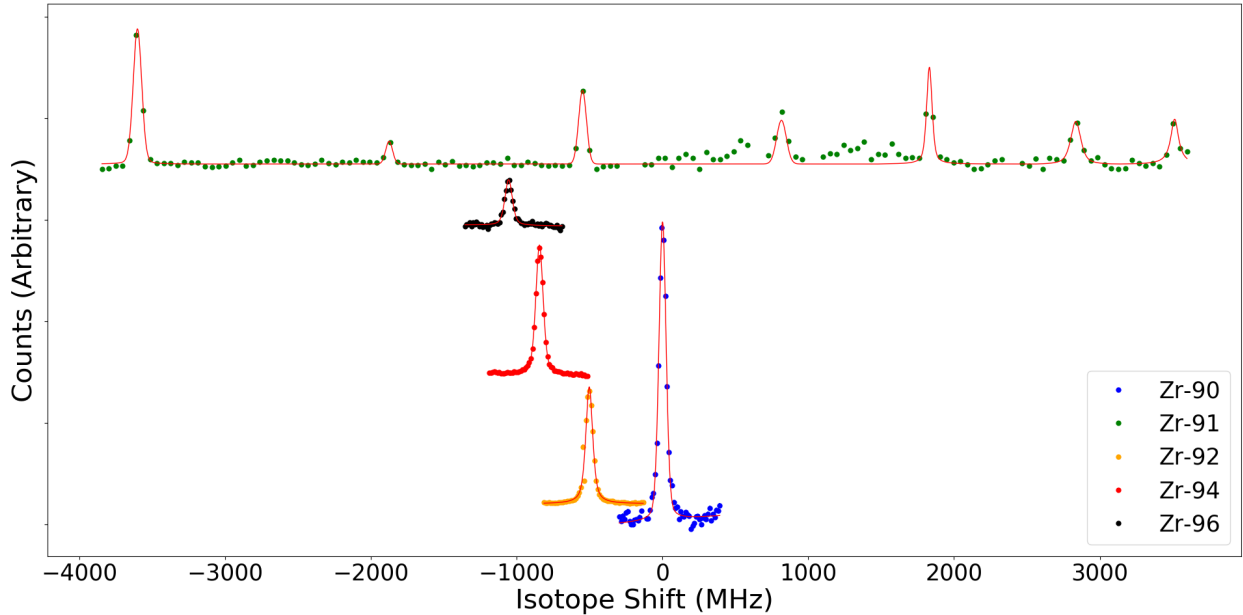


Figure 2.2: Hyperfine spectra of the stable isotopes of Zr as a function of the isotope shift relative to  $^{90}\text{Zr}$ . The spectrum of  $^{91}\text{Zr}$  features hyperfine splitting due to the non-zero spin of the nucleus.

to  $^{90}\text{Zr}$ , the most abundant stable isotope. The isotope shifts relative to  $^{90}\text{Zr}$  were extracted from the hyperfine spectra, and are summarized in Table 2.1. The charge radii of the stable

Table 2.1: Isotope shifts and charge radii of the stable isotopes of Zr

<b>A</b>	$\delta\nu/\text{MHz}$	$\delta\langle r_c^2 \rangle^{90,A}/\text{fm}^2$ [71]	$\langle r^2 \rangle^{1/2}/\text{fm}$
90	0	0	4.269
91	-199(1)	0.128	4.284
92	-509.63	0.309	4.305
94	-849.19	0.534	4.331
96	-1061.61	0.708	4.351

isotopes of Zr have already been determined and values from Fricke *et al.* [71] were used.

A linear regression fit was used to extract the atomic factors and resulted in the values seen in Equations 2.12 and 2.13.

$$F = -2.24(14) \text{ MHz/fm}^2 \quad (2.12)$$

$$K = 749(80) \text{ GHzu} \quad (2.13)$$

The newly determined atomic factors can be used in future experiments involving radioactive Zr beams at BECOLA, but as measurements reach further from stability the impact of the systematic error of the Atomic Factors will grow progressively larger. The correlation between the slope,  $F$ , and  $K$  can be reduced by shifting the isotope shifts by an adjustment factor  $\alpha$ , and results in a significant reduction in the error correlation between the slope and y-intercept that leads to a smaller uncertainty in the deduced differential mean-squared charge radius. The procedure to reduce the correlation was described by York *et al.* [72], and utilized in King Plot analyses of Cd [32] and Ni [73] isotopes. The adjusted King Plot is shown in Figure 2.3. An adjustment factor of  $\alpha = 1080 \text{ ufm}^2$  was used and reduced the correlation between the slope and y-intercept to -0.002. The slope of the regression line remains unchanged by the correlation reduction procedure, but the  $K_\alpha$  is modified to the

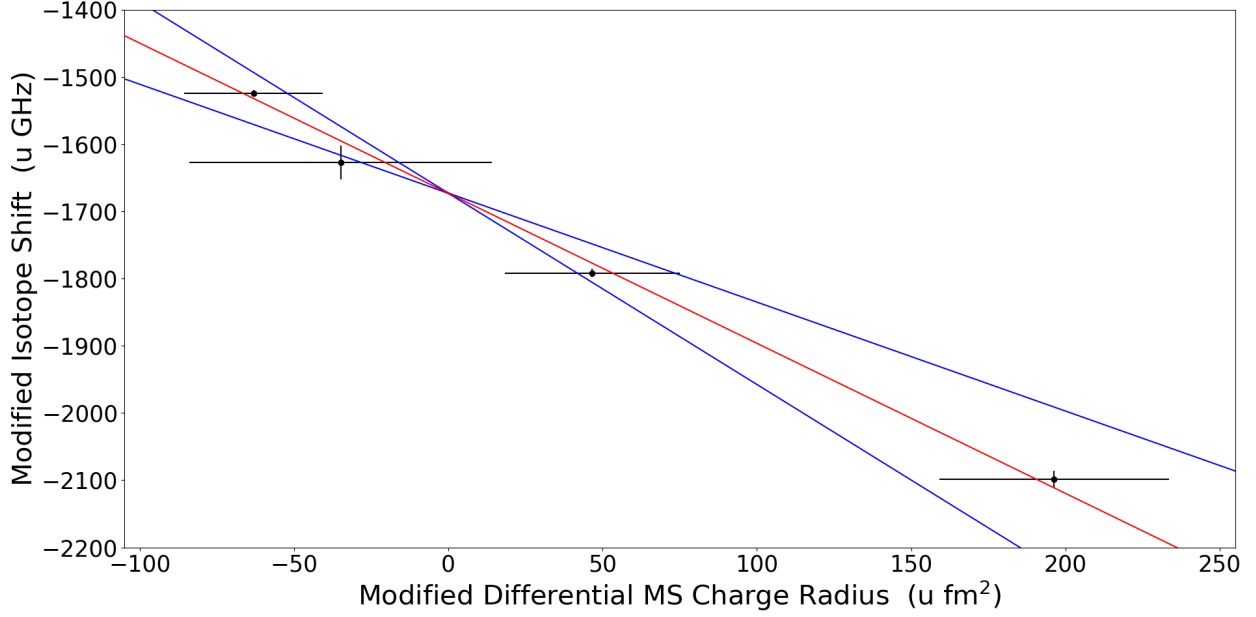


Figure 2.3: King Plot of the stable isotopes of Zr. The measured modified isotope shift is plotted as a function of the modified charge radius. The x-axis is shifted by  $1080 \text{ u fm}^2$  to reduce the error correlation between the slope and the y-intercept of the fit. The charge radii of the stable Zr isotopes are known, and the charge radii of newly measured radioactive isotopes can be determined through the linear regression line, shown as a red line.

value seen in Equation 2.14.

$$K_\alpha = -1671(4) \text{ GHz u} \quad (2.14)$$

With the adjustment factor, the error in the new y-intercept is reduced by an order of magnitude by removing the correlation between the errors. The mass shift term loses its physical meaning, but allows for the extraction of the charge radii of newly-measured isotopes with reduced error.

# Chapter 3

## Optical Pumping Simulation

In this chapter, the development of an optical pumping simulation is discussed. The optical pumping simulation was used to guide the commissioning experiments and will be used to determine potential optical pumping schemes for future experiments at BECOLA. The design principle of the simulation, the source of the electronic level and transition data used to generate the pumping schemes, assumptions, and results of the simulation are discussed here, as well as implications for future experiments in the FRIB era.

### 3.1 Design Principle

The core of the optical pumping simulation is a solution of the electronic transition rate equations that can be used to model the resulting electronic populations as a radiation field is applied to a system of ions or atoms. As discussed in Chapter 1, the solution of a two-level system is straightforward, but becomes more complex with increasing numbers of electronic states. As transition metals are d-block elements, they typically have high level densities and the decay of an excited state may branch to many low-energy metastable states. The optical pumping simulation uses a three-level solution from Zizek *et al* [74].

The three-level solution is used to model the optical pumping process due to the long lifetimes of the metastable states involved, on the order of seconds. As only the ground and excited states of the electronic system will interact directly with the radiation field, the

metastable states are "dark" and they will not experience stimulated excitation or emission. The pulsed laser light has a pulse duration of approximately 6 ns, much shorter than the lifetimes of the low-energy metastable states. As the electronic populations will only accumulate in the metastable states over the time scale of the simulation, all of the low-energy metastable states can be pooled together, simplifying the electronic states that need to be considered, as illustrated in Figure 3.1. The branching ratios of the spontaneous emis-

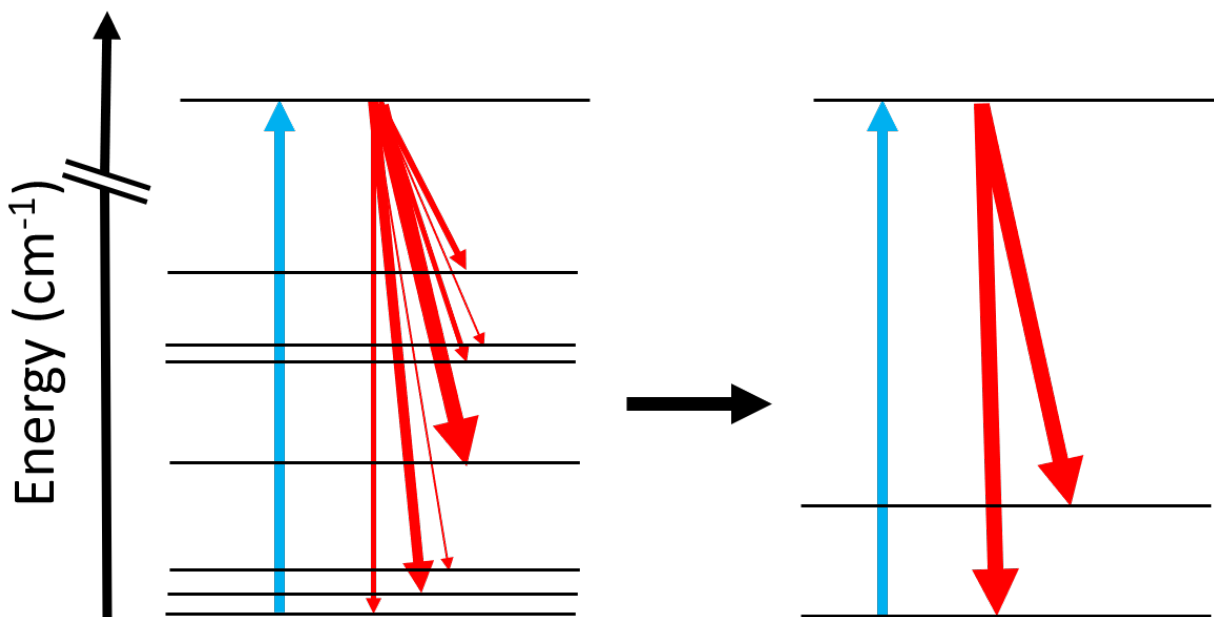


Figure 3.1: Simplification of the electronic states involved in the optical pumping process. As ions from the ground state are optically pumped to low-lying metastable states, the ions will no longer interact with the laser light. Spontaneous decay from the low-lying metastable states is negligible over the time scales involved in the optical pumping process, and the states can be pooled together to simplify calculation.

sion to each metastable state are known, allowing the population of the pooled state to be disentangled, and the final population distribution to be calculated.

### 3.1.1 3 Level Solution of Rate Equations

The optical pumping simulation is based on a solution to the electronic transition rate equations of a three-level system, with ground state  $g$ , excited state  $e$ , and metastable state  $m$  [74]. To begin, the rate equations of the populations of the three states can be written as

$$\begin{aligned}
 \frac{\delta N_g^*}{\delta t} &= N_e^* R_{eg} + N_m^* R_{mg} - N_g^* (R_{gm} + R_{ge}) \\
 \frac{\delta N_m^*}{\delta t} &= N_e^* R_{em} + N_g^* R_{gm} - N_m^* (R_{mg} + R_{me}) \\
 \frac{\delta N_e^*}{\delta t} &= N_g^* R_{ge} + N_m^* R_{me} - N_e^* (R_{em} + R_{eg})
 \end{aligned} \tag{3.1}$$

where  $R_{ij}$  is the rate from state  $i$  to state  $j$ , and  $N_i^*$  is the population density in state  $i$ . The values of the rates of change are calculated based on the Einstein coefficients  $A$  and  $B$  for the transition, the laser power, and collisional effects. As an example, the rate of change from state  $i$  to state  $j$  is

$$R_{ij} = B_{ij} \frac{E}{c} + k_{ij} \tag{3.2}$$

where  $E$  is the energy of the laser and  $k$  is the collisional excitation rate.

The rate equations can be simplified by converting the population density with respect to the total number density,  $N_T$ .

$$\begin{aligned}
 N_m &= N_m^*/N_T \\
 N_e &= N_e^*/N_T
 \end{aligned} \tag{3.3}$$

The simplified rate equations are then

$$\begin{aligned}\frac{\delta N_m}{\delta t} &= R_{gm} - N_m(R_{mg} + R_{me} + R_{gm}) + N_e(R_{em} - R_{gm}) \\ \frac{\delta N_e}{\delta t} &= R_{ge} + N_m(R_{me} - R_{ge}) - N_e(R_{eg} + R_{em} + R_{ge})\end{aligned}\quad (3.4)$$

The result is a system of linear equations that can be solved using determinants, where  $D$  is the differential operator.

$$\begin{aligned}[(D + R_m)(D + R_e) - R_{me}^* R_{em}^*]N_m &= \begin{bmatrix} R_{gm} & -R_{em}^* \\ R_{ge} & D + R_e \end{bmatrix} \\ [(D + R_m)(D + R_e) - R_{me}^* R_{em}^*]N_e &= \begin{bmatrix} D + R_m & R_{gm} \\ -R_{me}^* & R_{ge} \end{bmatrix}\end{aligned}\quad (3.5)$$

It is assumed that the laser power as a function of time is a step function. The rates depend on the populations of the electronic states, the Einstein coefficients, which are constants, and the laser power, which is an independent parameter. If the laser power is a step function, it is then constant as the transition is excited, and all coefficients become constants that can be solved as

$$[D^2 + (R_m + R_e)D + (R_m R_e - R_{me}^* R_{em}^*)]N_m = R_{gm}R_e + R_{em}^*R_{ge} \quad (3.6)$$

$$[D^2 + (R_m + R_e)D + (R_m R_e - R_{me}^* R_{em}^*)]N_e = R_{ge}R_m + R_{me}^*R_{gm} \quad (3.7)$$

To make things more clear later on, a series of substitutions are performed.

$$\begin{aligned}
L &= R_m + R_e & Q_m &= R_{gm}R_e + R_{em}^*R_{ge} \\
P &= R_mR_e - R_{me}^*R_{em}^* & Q_e &= R_{ge}R_m + R_{gm}R_{me}^*
\end{aligned} \tag{3.8}$$

which reduce equations 3.6 and 3.7 to,

$$\begin{aligned}
(D^2 + LD + P)N_m &= Q_m \\
(D^2 + LD + P)N_e &= Q_e
\end{aligned} \tag{3.9}$$

The antiderivative of the equations are

$$\begin{aligned}
N_m(t) &= C_1e^{-\xi_1t} + C_2e^{-\xi_2t} \\
N_e(t) &= C_3e^{-\xi_1t} + C_4e^{-\xi_2t}
\end{aligned} \tag{3.10}$$

where the terms in the exponents are

$$\begin{aligned}
\xi_1 &= \frac{L}{2} - \sqrt{\frac{L^2}{4} - P} \\
\xi_2 &= \frac{L}{2} + \sqrt{\frac{L^2}{4} - P}
\end{aligned} \tag{3.11}$$

In these equations, the  $C_x$  terms are arbitrary constants that are related and will be derived later. The integrals for Equations 3.6 and 3.7 are

$$C_m = Q_m/(\xi_1\xi_2) \tag{3.12}$$

$$C_e = Q_e/(\xi_1\xi_2) \tag{3.13}$$

which allow for complete solutions for the populations of states  $m$  and  $e$  as a function of time,

$$N_m(t) = C_1 e^{-\xi_1 t} + C_2 e^{-\xi_2 t} + \frac{Q_m}{\xi_1 \xi_2} \quad (3.14)$$

$$N_e(t) = C_3 e^{-\xi_1 t} + C_4 e^{-\xi_2 t} + \frac{Q_e}{\xi_1 \xi_2} \quad (3.15)$$

The derivation of the  $C_x$  constants can be performed from the complete solution. By solving  $N_m(t)$  and  $N_e(t)$  using the derivatives found in Equation 3.4, we have

$$C_3 = C_1 \frac{R_m - \xi_1}{R_{em}^*} \quad (3.16)$$

$$C_4 = C_2 \frac{R_m - \xi_2}{R_{em}^*} \quad (3.17)$$

With the above simplification, only two constants occur in the system of equations and they can be found with the boundary conditions of the initial populations in states  $m$  and  $e$ . From Equations 3.4 and 3.8, the initial populations are

$$N_{mi} = Q_m/P \quad N_{ei} = Q_e/P \quad (3.18)$$

By solving the solution with the initial conditions, the constants are found to be

$$C_1 = \frac{Q_m/B - N_{mi}}{\xi_2 - \xi_1} (R_m - \xi_1) \frac{R_m - \xi_2}{R_{em}^*} - \frac{Q_e/B - N_{ei}}{\xi_2 - \xi_1} (R_m - \xi_2)/R \quad (3.19)$$

$$C_2 = -\frac{Q_m/P - N_{mi}}{\xi_2 - \xi_1}(R_m - \xi_1) + \frac{Q_e/P - N_{ei}}{\xi_2 - \xi_1}(R_m - \xi_2)/R \quad (3.20)$$

By providing the following substitutions for ease of reading,

$$\begin{aligned} K_1 &= \frac{Q_m/P - N_{mi}}{\xi_2 - \xi_1}(R_m - \xi_1) \\ K_2 &= \frac{Q_e/P - N_{ei}}{\xi_2 - \xi_1}(R_m - \xi_2) \\ RR &= \frac{R_m - \xi_2}{R_{em}^*} \end{aligned} \quad (3.21)$$

The final solutions for the electronic populations can be given as

$$N_m(t) = (K_1 RR - K_2/R)e^{-\xi_1 t} + (-K_1 + K_2/R)e^{-\xi_2 t} + Q_m/B \quad (3.22)$$

$$N_e(t) = (K_1 RR - K_2/R)\frac{R_m - \xi_1}{R_{em}^*}e^{-\xi_1 t} + (-K_1 + K_2/R)\frac{R_m - \xi_2}{R_{em}^*}e^{-\xi_2 t} + Q_m/B \quad (3.23)$$

As  $N_m$  and  $N_e$  are relative to the total population, the population of the ground state can be described as

$$N_g(t) = N_T - N_m(t) - N_e(t) \quad (3.24)$$

With the function describing the population of each level over time, the simulation is able to determine the change in population between electronic states during the optical pumping process. As an example, in Figure 3.2 is shown the proportion of ions in the ground, pooled metastable, and excited states as a function of time for the  $^4F_{3/2}$  to  $^4G_{5/2}$  transition in  $Zr^+$ , with the assumptions that no collisional decay or excitation occurs and that the temporal

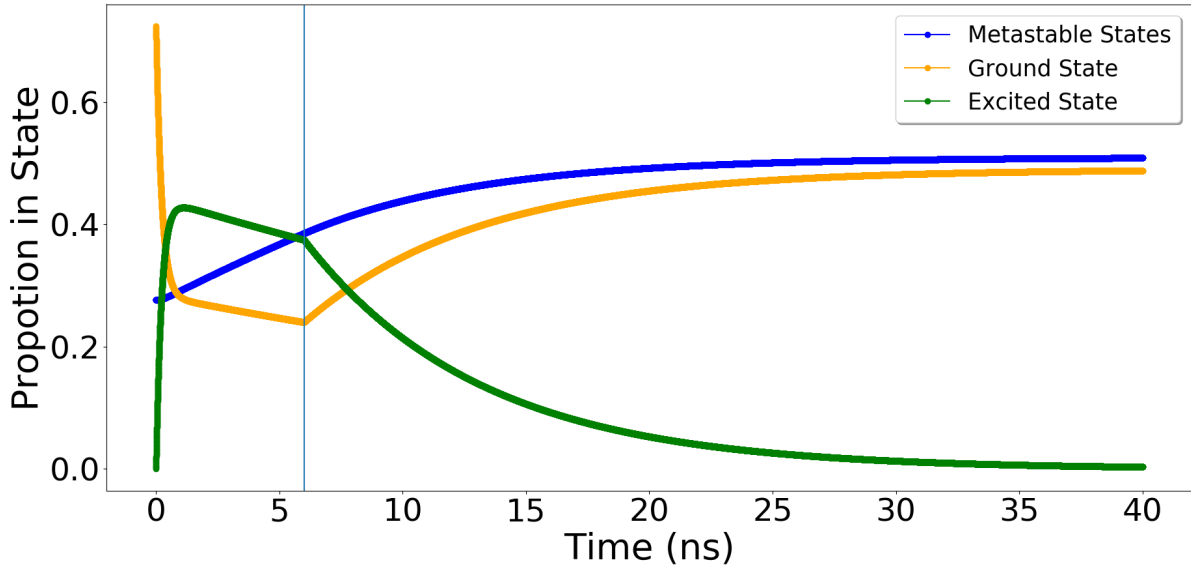


Figure 3.2: Proportion of ion population in the ground, metastable, and excited states as a function of time. The pulsed laser temporal width is 6 ns, marked by the vertical blue bar. While the ions are irradiated by the laser, the ground state population is optically pumped to the low-lying metastable states. After the laser pulse, the ions remaining in the excited state exponentially decay to the ground and metastable states.

shape of the laser pulse is a square well. The excited state has a lifetime of 7.1 ns and the initial ground state population is 72.3%, following a Boltzmann distribution. The laser light has a temporal width of 6 ns, indicated by the thin blue vertical line. As the ions are irradiated by the laser light, the transition is quickly saturated. Ions are optically pumped to the metastable states, and after the laser pulse the remaining ions in the excited state quickly decay to the ground and metastable states.

### 3.1.2 Simulation Data

Accurate information on the electronic structure of the transition metals is vital for the optical pumping simulation. The optical pumping simulation relies on information about the electronic levels and transitions from the Kurucz [75] and National Institutes of Standards

and Technology (NIST) [76] spectral databases. The NIST Spectral Database provided experimentally measured atomic energy levels, while the Kurucz Database provided theoretical values for electronic transitions and transition probabilities.

## 3.2 Assumptions

Several assumptions were made in performing the optical pumping simulations, involving both the optical pumping process and conditions inside the ion trap.

### 3.2.1 Conditions Inside the Ion Trap

Two key assumptions were made in the optical pumping simulation about the conditions of the ion trap. The first assumption is that the trapped ions are effectively cooled to room temperature by collisions with the He buffer gas, which is at room temperature. The temperature of the ion beam is important as the populations of the low-energy electronic states are dependent on the temperature.

For a given temperature, the electronic populations of a species is described by the Boltzmann distribution. Based on the energy of the electronic state and the temperature of the cloud of ions, the relative populations of each level can be determined. The probability distribution for state  $i$  is given by

$$p_i = \frac{g_i}{Q} e^{-E_i/kT} \quad (3.25)$$

where  $g_i$  is the degeneracy of the state,  $E_i$  is the energy of the electronic state,  $k$  is the

Boltzmann constant, and  $Q$  is the partition function,

$$Q = \sum_{i=1}^n g_i e^{-E_i/kT} \quad (3.26)$$

Division by the partition function is necessary to make sure that all probabilities sum to 1. At low temperatures, the ground state is predominantly populated for most species. As an example, the electronic state populations of  $\text{Zr}^+$  are presented as a function of temperature in Figure 3.3. At room temperature, the ground state contains approximately 72% of the total population, the first excited state at  $314 \text{ cm}^{-1}$  contains 23% of the total population, and the second excited state at  $763 \text{ cm}^{-1}$  contains approximately 3% of the total population. As the temperature rises, even higher-energy states are populated.

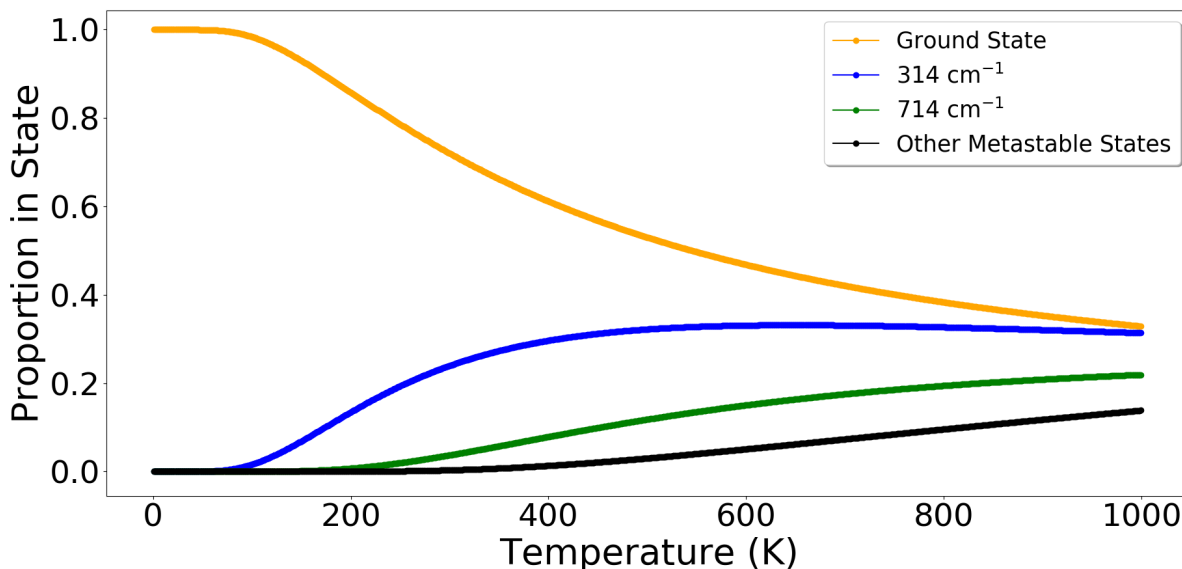


Figure 3.3: Proportion of electronic population in the low-lying states of  $\text{Zr}^+$  as a function of temperature. At low temperatures, almost all ions exist in the ground state, with other low-lying states becoming populated as the temperature rises.

In laser spectroscopy measurements, the signal is directly proportional to the population of the state being probed. Species with low level densities, such as  $\text{Ca}^+$ , which has a first

excited state at  $13650 \text{ cm}^{-1}$ , will have almost all ions in the ground state, but a species such as  $V^+$ , which has 5 states below  $350 \text{ cm}^{-1}$ , only 33% of the total population will be in the ground state, limiting the sensitivity of laser spectroscopy measurements.

As the ion beam passes through the cooling section of the RFQ ion trap, collisions with the He buffer gas cool the beam to the temperature of the gas itself. The BECOLA RFQ ion trap [77, 78] was operated at room temperature during the experiments described in this thesis.

The temperature of the trapped ions in the trap can be calculated using the effective ion temperature treatment, as developed by Tolmachev *et al.* [79]. Through the effective ion temperature treatment, it is assumed that ions accelerated through the RF field will move coherently and will eventually acquire the same internal activation energy as ions outside of any electric field. Instead, the temperature will be dictated by the temperature of the buffer gas.

The effective temperature of the trapped ions,  $T_{eff}$ , is

$$T_{eff} = \frac{m_r}{m_g} T_B + \frac{2m_r \langle K_i \rangle}{3km_i} \quad (3.27)$$

where  $m_r$  is the reduced mass of the ion-buffer gas system,  $m_g$  is the mass of the buffer gas,  $m_i$  is the mass of the ion,  $T_B$  is the temperature of the buffer gas,  $k$  is the Boltzmann constant and  $\langle K_i \rangle$  is the kinetic energy of the ions in the laboratory frame. The kinetic energy of the ions can be determined through,

$$\langle K_i \rangle = \frac{m_g \omega^2 r_0^2 V_{DC}^2}{16000 V_{RF}^2} \quad (3.28)$$

Table 3.1: Typical operating parameters of the BECOLA RFQ ion trap, used to calculate the effective ion temperature.

<b>Parameter</b>	
$\omega$	7.5 MHz
$r_0$	3.5 mm
$V_{DC}$	-4 V
$V_{RF}$	72 V

where  $\omega$  is the angular frequency of the applied RF field,  $r_0$  is the radius of the radius of the trapping region defined by the RFQ rods,  $V_{DC}$  is the applied DC voltage field applied to create the trapping potential, and  $V_{RF}$  is the peak of the applied RF voltage field. A more detailed discussion RFQ ion trap will follow in Chapter 4, and a schematic of the trapping region is shown in Figure 4.11. The effective temperature of the trapped ions was consistent with room temperature using the operating parameters of the present  $Zr^+$  measurements shown in Table 3.1.

The second assumption of the trap conditions considered in the optical pumping simulation is that the trapped ions occupy a small volume within the ion trap and that the laser light completely irradiates the trapped ions. The trapping region of the BECOLA RFQ ion trap in the transverse direction relative to the ion beam is 7 mm in diameter, but due to confinement through the RF field and DC potential, the trapped ions are contained within a smaller volume. The assumption is supported by simulation results performed with the 3DCyIPIC software [80], developed at the NSCL by R. Ringle to characterize space charge and buffer gas effects of ions in different kinds of ion traps. The 3DCyIPIC simulation solves Poisson's equation in cylindrical coordinates across a grid to calculate both the spatial and velocity distribution of ions in a trap.

The 3DCyIPIC simulation was used to estimate the distribution of ions across the RFQ

ion trap, with the results shown in Figure 3.4.

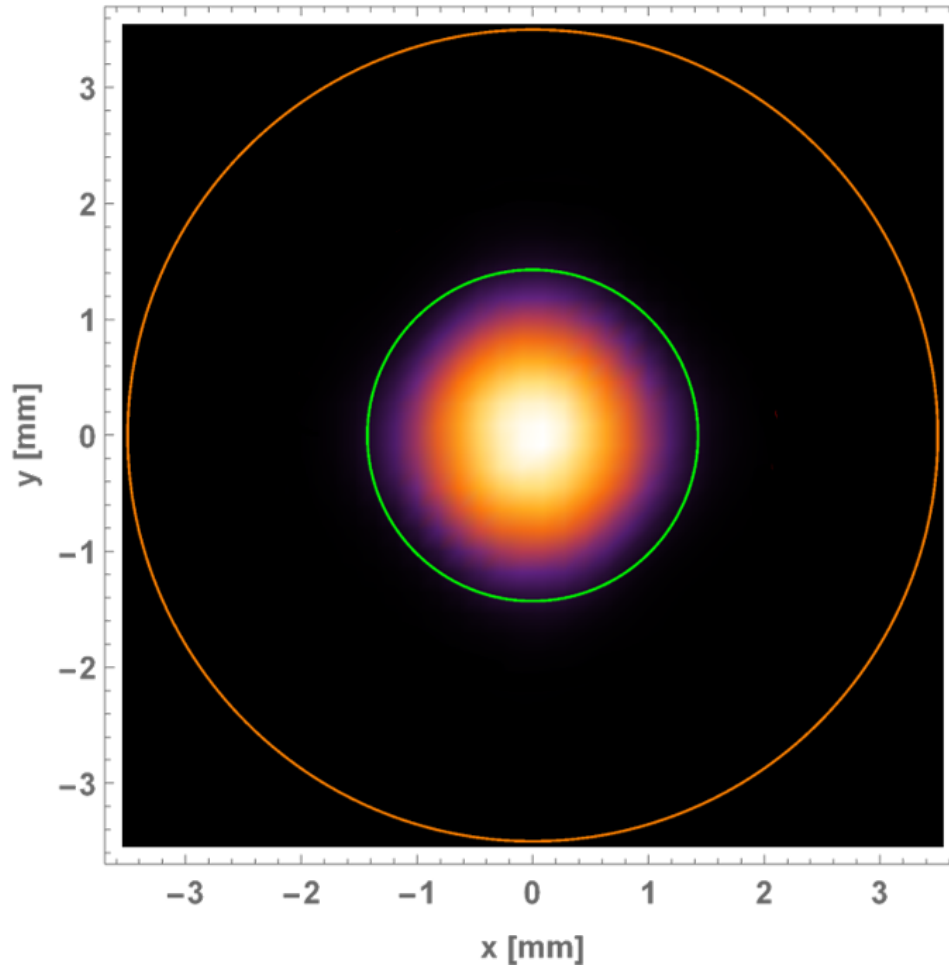


Figure 3.4: Simulated radial distribution of ions in the BECOLA RFQ ion trap, calculated using the 3DCyIPIC software. The green circle describes the 95% inclusion radius of the radial distribution, approximately 1.4 mm in radius. The orange circle describes the extent of the trapping region defined by the RFQ rods.

The simulation results suggest that 95% of ions in the trapping region are contained transversely within a 1.4 mm radius of the center of the trapping region.

The simulation was repeated with the He buffer gas temperature parameter set to 200 K. The trapped ion distribution in the simulation was not sensitive to the temperature of the He buffer gas, indicating that space charge effects are primarily responsible for the size of the distribution.

The optical pumping process will not be sensitive to the distribution of the ions in the axial direction.

### 3.2.2 Laser Conditions

Other assumptions within the optical pumping simulation are made about the qualities of the laser light used to irradiate the trapped ions and perform the optical pumping. First, it is assumed that the pulsed laser light fully saturates the electronic transition. The intensity of light that is required to saturate a transition can be determined from the rate equations and the Einstein coefficient  $A$  of the transition. For the simulations, it is assumed that the energy density of the laser light is well above the saturation energy density, which can be determined from the frequency of the transition and the lifetime of the excited state [81].

$$E_{sat} = \frac{\pi h c}{3 \lambda^3 \tau} \quad (3.29)$$

where  $h$  is the Planck constant,  $c$  is the speed of light,  $\lambda$  is the wavelength of the transition, and  $\tau$  is the lifetime of the excited state. For a transition at 360 nm and an excited state with a lifetime of 5 ns, the saturation energy density corresponds to 11.4 mW/cm<sup>2</sup>. Pulsed laser systems typically feature pulse widths on the scale of nanoseconds, meaning that the peak laser intensity is measured in MW/cm<sup>2</sup> and saturation should be easily achieved.

The second assumption is that all of the trapped ions are irradiated by the laser beam. If the laser beam is misaligned, a portion of the ions in the trapping region will not interact with the light and optical pumping will not occur. A telescope optics system and optical elements equipped with piezo motors with high positional resolution will allow for control of the laser beam size and position, and will be discussed later.

### 3.3 Operation of the Optical Pumping Simulation

The following section presents the practical aspects of using the optical pumping simulation. The simulation begins with the user providing a series of constraints for the electronic transition search process. The element of interest, charge state, minimum and maximum wavelengths, as well as the minimum transition speed are specified as inputs. Based on the element and charge state, a text file, which contains information about the electronic states and their degeneracies from the Kurucz and NIST databases, is read.

The first step of the simulation is the determination of possible first steps for the pumping scheme. As optical pumping must be performed on an electronic state that has some population, the population distribution among low-energy states below  $1000\text{ cm}^{-1}$  is calculated. Another text file containing the possible transitions for the specific element and charge state is read and used to identify transitions involving low-lying electronic states that are populated at room temperature. Based on the constraints used as input, the transitions are filtered to avoid any that do not fulfill the desired characteristics. After selection of the possible pumping transitions, the rate equations are solved for each transition and tracks the electronic population to the low-energy metastable states.

#### 3.3.1 Choice of CLS Step and Output

After tracking the decays from the excited state, the potential transitions from the populated metastable states are chosen. Any unpopulated metastable state is not considered as a viable initial state for CLS measurements. Based on constraints to the wavelength and transition speed, the possible CLS transitions are filtered again.

After selection of possible CLS transitions, the simulation is complete. The possible

optical pumping schemes are collected and sorted in order of highest population in the starting state for CLS measurements. The list of schemes is saved to a text file in a chart form. The chart first lists the pumping step of the scheme, with the ground and excited states, the speed of the transition, the wavelength of light required, and the branching ratios to the ground state and to the metastable state for the CLS step. Next the same information is listed for the CLS step of the scheme as well as the population of the ground state after optical pumping.

## 3.4 Results for Transition Metals

The simulation was used to determine the benefit of optical pumping for the first and second-row transition metals.

### 3.4.1 First-Row Transition Metals

The first-row transition metals have many interesting isotopes for nuclear structure studies, as detailed in Chapter 1. Studies of all elements in the first row except for Sc and Ti require atomic charge exchange reactions, which severely limits the sensitivity of measurements due to fractionation of the electronic population (See Section 1.3.1.3). The results of the simulation for these elements are seen in Figure 3.5, with more detail of the results shown in Table 3.2. A significant gain in sensitivity is predicted for most isotopes in the first row, especially for Fe and Co isotopes which feature a 11-14 fold improvement. More detailed optical pumping schemes are provided in Appendix A.

Although optical pumping will benefit most elements, there are no available optical pumping schemes for ions of Ni, Cu, and Zn. Ground state electronic transitions of these elements

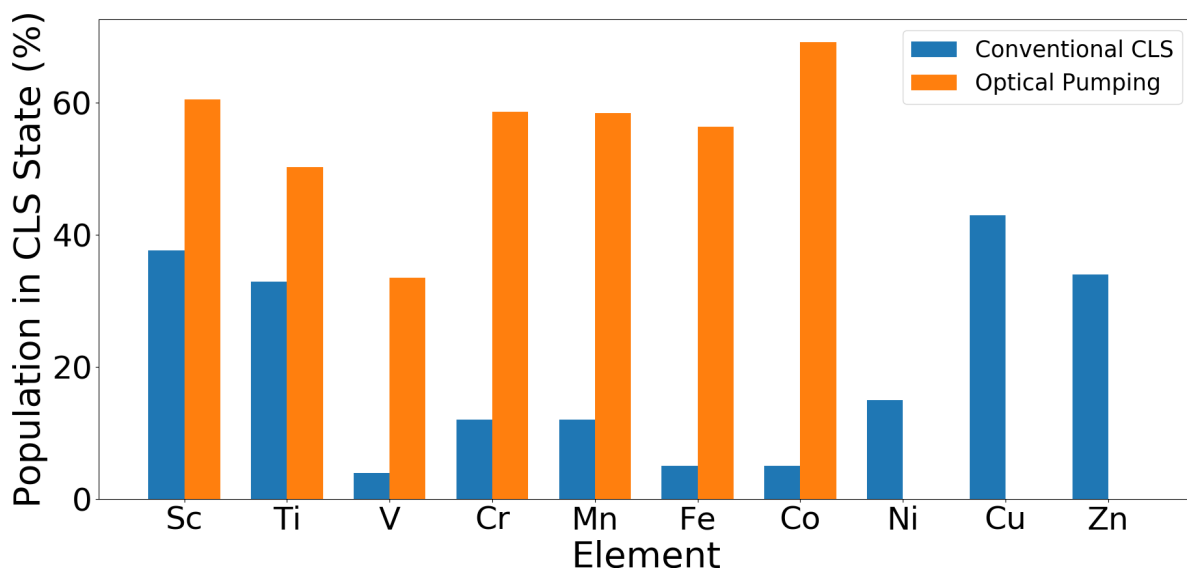


Figure 3.5: Results of the optical pumping simulation for the first-row transition metals compared to traditional CLS measurements. Most elements will experience a substantial gain in sensitivity through optical pumping, although some elements require very deep UV light that cannot be produced at BECOLA and therefore have no viable optical pumping schemes.

Table 3.2: Percentage of total electronic population available for CLS measurements of the first-row transition metals, with and without optical pumping. Elements that require charge exchange reactions are indicated.

Element	Population Without Optical Pumping	Charge Exchange	Population With Optical Pumping
Sc	37.6	No	60.5
Ti	32.9	No	50.3
V	4	Yes	33.5
Cr	12	Yes	58.6
Mn	12	Yes	58.4
Fe	5	Yes	56.4
Co	5	Yes	69.2
Ni	15	Yes	N/A
Cu	43	Yes	N/A
Zn	34	Yes	N/A

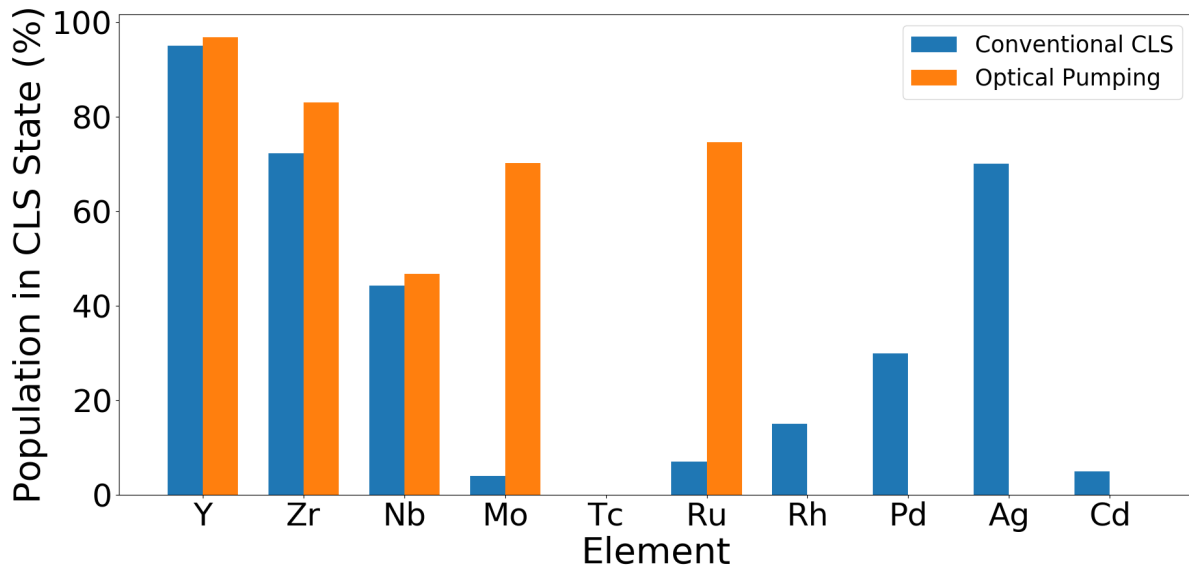


Figure 3.6: Results of the optical pumping simulation for the second-row transition metals compared to traditional CLS measurements. Most elements will experience a significant gain in sensitivity through optical pumping.

require light far into the vacuum UV regime ( $<200$  nm). Production of vacuum UV light is not possible with the BECOLA pulsed laser system, and would require transportation through vacuum to avoid absorption by molecules in air.

### 3.4.2 Second-Row Transition Metals

Simulations of the second-row transition metals also show promising results for future studies. Most elements in the second row require charge exchange, which contributes to the fact that there have been no published results for radioactive beam studies of isotopes between Mo and Ag, although a limited number of such experiments have been performed. The simulation results are shown in Figure 3.6, with more detail in Table 3.3

The results of the simulation show that the second-row transition metals will not benefit as greatly as elements of the first row, but many species will see an increase in sensitivity.

Table 3.3: Percentage of total electronic population available for CLS measurements of the second-row transition metals, with and without optical pumping. Elements that require charge exchange reactions are indicated.

Element	Population Without Optical Pumping	Charge Exchange	Population With Optical Pumping
Y	94.9	No	96.8
Zr	72.3	No	83.0
Nb	44.3	No	46.7
Mo	4	Yes	70.2
Tc	N/A	N/A	N/A
Ru	7	Yes	74.6
Rh	15	Yes	N/A
Pd	30	Yes	N/A
Ag	70	Yes	N/A
Cd	34	Yes	N/A

The largest increase in sensitivity is seen in Mo and Ru, featuring a 17- and 10-fold increase, respectively.

The case of Tc must also be discussed. The benefit of optical pumping is unknown for Tc due to a lack of information about its electronic structure, as there are no stable isotopes of Tc. To date, few studies have been performed on Tc isotopes, mostly limited to resonance ionization spectroscopy studies [82, 83]. Future measurements of rare Tc isotopes would require preparation work in collaboration with other groups capable of performing level search measurements to identify the location of electronic states and potential transitions. Also, as no stable isotopes exist, future studies will rely on atomic theory calculations for the atomic factors used to extract the charge radius from the isotope shift. Tc was not considered a potential candidate for future experiments in this work.

# Chapter 4

## Experiment

The experimental techniques used to perform the optical pumping commissioning experiments are described, as well as the features of the BECOLA facility, improvements to the infrastructure of BECOLA, and how optical pumping was performed are described in this chapter.

### 4.1 Experimental Techniques

#### 4.1.1 Collinear Spectroscopy

BECOLA utilizes collinear laser spectroscopy (CLS) [84] to precisely measure the hyperfine spectra of radioactive nuclei and extract the mean-square charge radii and nuclear moments. In a CLS system, a beam of ions propagates collinearly with a laser beam, which excites an electronic transition of the ions, and the fluorescence is detected using photomultiplier tubes (PMT). Typically, the laser light used to probe the electronic transition is held at a steady frequency and a small scanning voltage is applied to the photon detection region to Doppler shift the frequency of light seen by the ion beam. It is possible to scan the frequency of the laser light, but such a scan requires re-adjustment of the laser optics and precise measurement of the change in laser frequency. The stability of the laser also becomes an issue at frequencies close to the edge of the wavelength range of the laser system. It is

easier in comparison to apply a scanning voltage to Doppler shift the absorption frequency.

#### 4.1.1.1 Doppler Shift Effect

The CLS technique is capable of performing high precision measurements by taking advantage of the Doppler effect. The absorption linewidth of a transition is dominated by Doppler broadening effects, caused by movement of ions relative to the laser light.

The FWHM of the natural absorption linewidth of an electronic transition is related to its lifetime, such that

$$\Delta\nu = \frac{1}{2\pi\tau} \quad (4.1)$$

where  $\tau$  is the lifetime of the excited state of the transition. The excited state of the transitions studied in this experiment has a lifetime of approximately 7 ns, which corresponds to a natural absorption linewidth of 22 MHz.

The impact of Doppler broadening can be calculated from the temperature of the ion cloud and the Doppler shift. The Doppler shift at non-relativistic velocities is,

$$f = f_0\left(1 + \frac{v}{c}\right) \quad (4.2)$$

As the resonant frequency shifts due to the velocity of the ions moving towards or away from the laser, the distribution of absorption frequencies of the laser light will be,

$$P(f)df = P(v)\frac{dv}{df}df \quad (4.3)$$

where  $P(v)$  is the distribution of ion velocities, which can be described by the Boltzmann

distribution.

$$P(v)dv = \sqrt{\frac{m}{2\pi kT}} e^{-\frac{mv^2}{2kT}} dv \quad (4.4)$$

By solving Equation 4.2 for the velocity of the ion and substituting it into Equation 4.3, we find

$$P(f)df = \frac{c}{f_0} P_v\left(c\left(\frac{f}{f_0} - 1\right)\right)df \quad (4.5)$$

Through substitution of Equation 3.7 and simplification, the distribution of frequencies can be expressed as a Gaussian distribution,

$$P(f)df = \sqrt{\frac{mc^2}{2\pi kT}} f_0^2 e^{-\frac{mc^2(f-f_0)^2}{2kTf_0^2}} df \quad (4.6)$$

As it is a Gaussian distribution, the full width half max (FWHM) of the distribution i.e. the Doppler broadened linewidth, is given by

$$FWHM = \sqrt{\frac{8kT\ln(2)}{mc^2}} f_0 \quad (4.7)$$

The in-air Doppler broadening of the transition used in this experiment increases the absorption linewidth to 1.1 GHz, much larger than the natural linewidth, but the 3DCyLPIC software [80] used to determine the size of the trapped ion distribution in Chapter 3 can also be used to estimate the effect of the RF field on the velocity of the ions, and in turn the Doppler broadening of the absorption linewidth from the RF motion.

The 3DCyLPIC software provides a means to solve for the velocity distribution of the trapped ions, which can be directly related to the Doppler broadening. A series of simulations were performed to calculate the velocity distribution of the ions as a function of the He buffer

gas pressure. The magnitude of the mean velocity as a function of time in the ion trap and He buffer gas pressure is shown in Figure 4.1. The results show that at lower He buffer gas

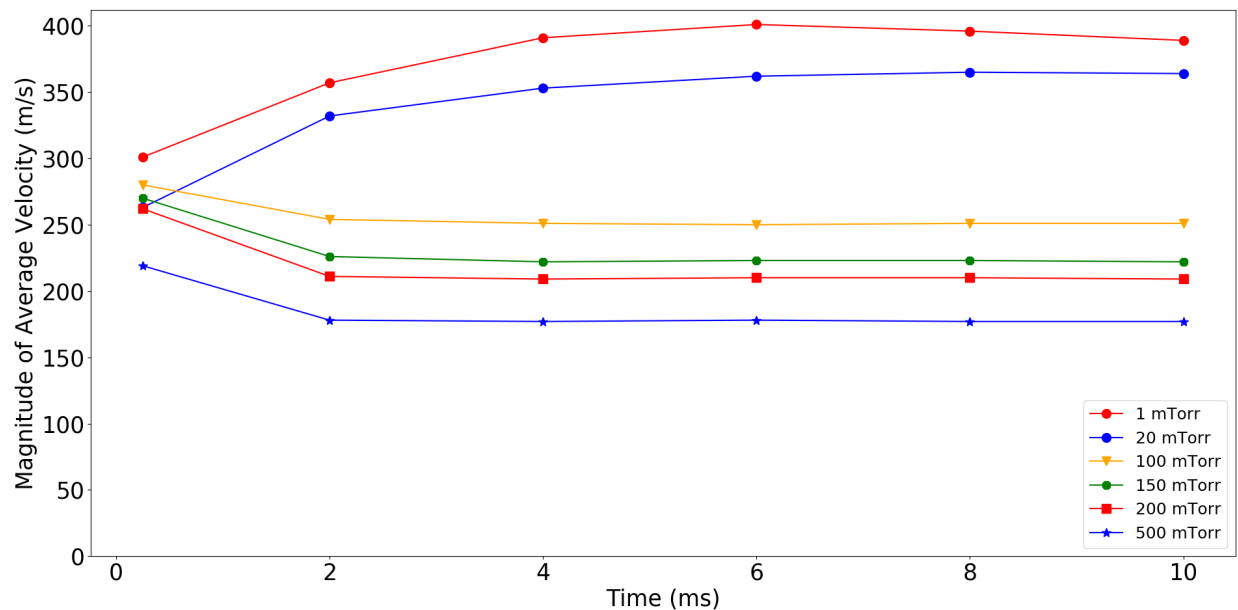


Figure 4.1: Magnitude of the mean velocity as a function of time in the ion trap and He buffer gas pressure. The lines are to guide the eyes. The He buffer gas serves to cool the beam and limits the velocity of the ions as they move through the RF field. Doppler broadening of the absorption linewidth is reduced as the ions slow.

pressures, the velocity of the ion bunch increases until it reaches an equilibrium point. At low pressures, there is not enough He in the RFQ ion trap to effectively cool the beam. The BECOLA RFQ ion trap is capable of operating at pressures lower than 20 mTorr, but the simulation suggests that the efficiency will suffer.

The mean velocity from the ion trap simulation was used to determine the FWHM of the absorption linewidth due to Doppler broadening. The results are shown in Figure 4.2. The He buffer gas plays a role by slowing the trapped ions as they move in the RF field. Collisions with the He buffer gas will limit and cool the trapped ions. The BECOLA RFQ ion trap is typically operated at 80 mTorr of He buffer gas, and the Doppler broadened absorption linewidth is comparable to the expected linewidth in air. The precision necessary to extract

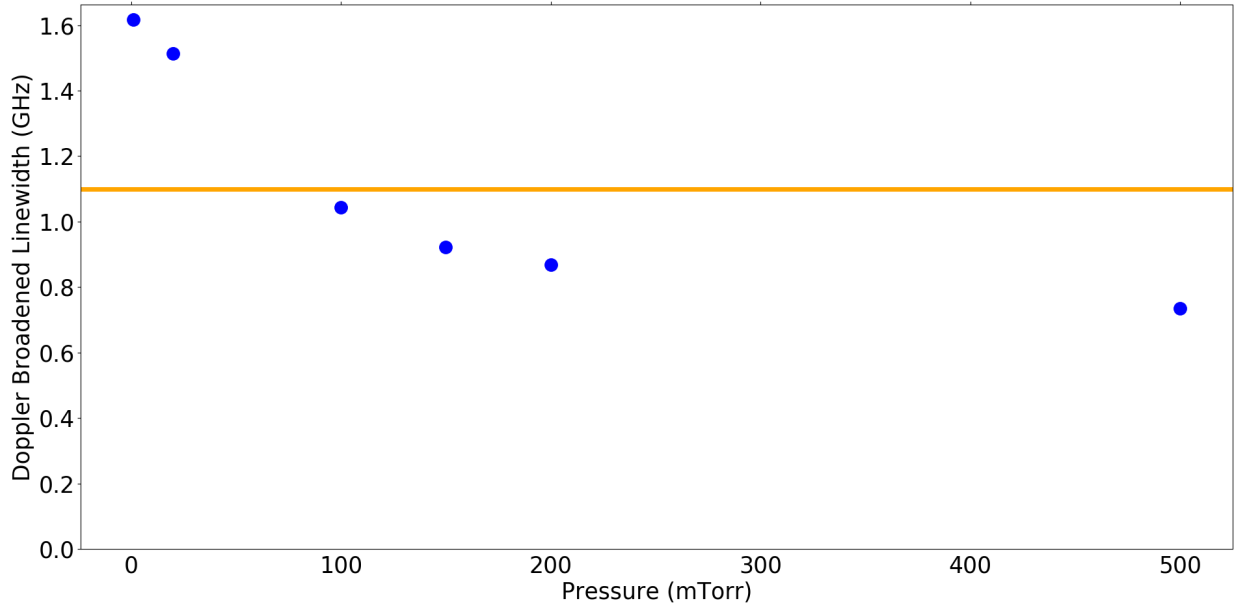


Figure 4.2: Doppler broadened absorption linewidth from RF motion as a function of He buffer gas pressure, calculated from the 3DCylPIC software [80]. The optical pumping process was performed in an RFQ ion trap and the motion of the ions from the RF field was used to determine the absorption linewidth. As the He buffer gas pressure increases, the neutral He atoms serve to limit the velocity of the trapped ions and the absorption linewidth reaches a plateau. The orange line indicates the expected Doppler broadened linewidth in air at 300 K. The BECOLA RFQ ion trap is operated at 80 mTorr of He buffer gas pressure and the Doppler broadened absorption linewidth from the RF motion is comparable to the expected linewidth in air.

the isotope shift and hyperfine coupling constants from the HFS is of the order of MHz, and precision measurements are not possible through spectroscopy of a Doppler broadened resonance.

The ion beam co-propagates with the laser light, and the Doppler shift of the resonance frequency can be determined through the velocity of the ion beam. The potential applied to the ions,  $V$ , is the sum of the high voltage of the system,  $V_0$ , and the scanning voltage applied at the photon detection region,  $V_{app}$ .

$$V = V_0 + V_{app} \quad (4.8)$$

An ion beam composed of ions of mass  $m$ , charge state  $q$ , and accelerated across a potential difference of  $V$ , the ion will have a kinetic energy of

$$E_{kin} = qV = \frac{1}{\sqrt{1 - \beta^2}} mc^2 - mc^2 \quad (4.9)$$

where  $\beta$  is the speed of the ion in units of  $c$ , the speed of light. By re-arranging the above equation and solving for  $\beta$ , we find the ion velocity as

$$\beta = \sqrt{1 - \frac{1}{1 + q^2(V/m)^2 + 2qV/m}} \quad (4.10)$$

As  $\beta$  represents the velocity of the ion, the Doppler shifted laser frequency,  $f_{obs}$ , can be expressed as

$$f_{obs} = f_0 \sqrt{\frac{1 - \beta}{1 + \beta}} \quad (4.11)$$

Antilinear laser spectroscopy is also possible, where the laser light propagates anti-linearly relative to the ion beam. The Doppler shifted laser frequency while performing antilinear laser spectroscopy would be defined as,

$$f_{obs,anti} = f_0 \sqrt{\frac{1 + \beta}{1 - \beta}} \quad (4.12)$$

The fluorescence is collected as a function of scanning voltage, which is readily converted to the rest-frame transition frequency according to Equation 4.11.

CLS mitigates Doppler broadening by measuring the resonance frequency of ions in flight as they travel through the beamline with kinetic energy on the scale of keV, through what is called kinematic compression [84]. As the kinetic energy is related to the velocity of the

ion by

$$E_{kin} = \frac{1}{2}mv^2 \quad (4.13)$$

The velocity spread of an trapped with a given energy spread is reduced at higher acceleration energies, reducing the spectral width of the absorption linewidth towards the natural linewidth and allowing for high precision measurements. As shown in Figure 4.3, for a given

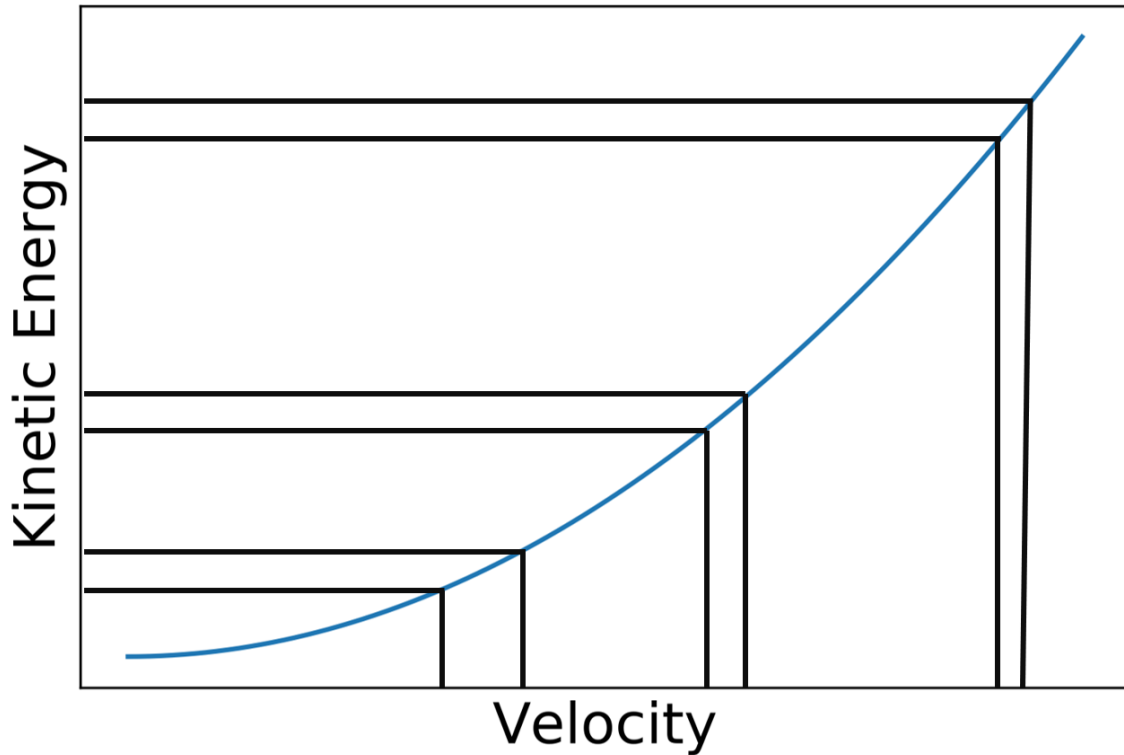


Figure 4.3: The relationship between kinetic energy and velocity. Three sets of ions with the same energy spread will have velocity spreads that become progressively narrower as the ion energy increases. CLS measurements take advantage of the kinetic compression of the linewidth to remove broadening effects and perform precise measurements of the transition frequency.

energy spread, the corresponding velocity spread of the ions will decrease as the acceleration potential is increased.

A 30 kV acceleration potential is used at BECOLA and the linewidth is dominated by fluctuations in the high voltage of 30 kV. The typical linewidth observed due to fluctuations

in the high voltage is approximately 60 MHz, as can be seen in the HFS spectrum of  $^{90}\text{Zr}$  shown in Figure 4.4.

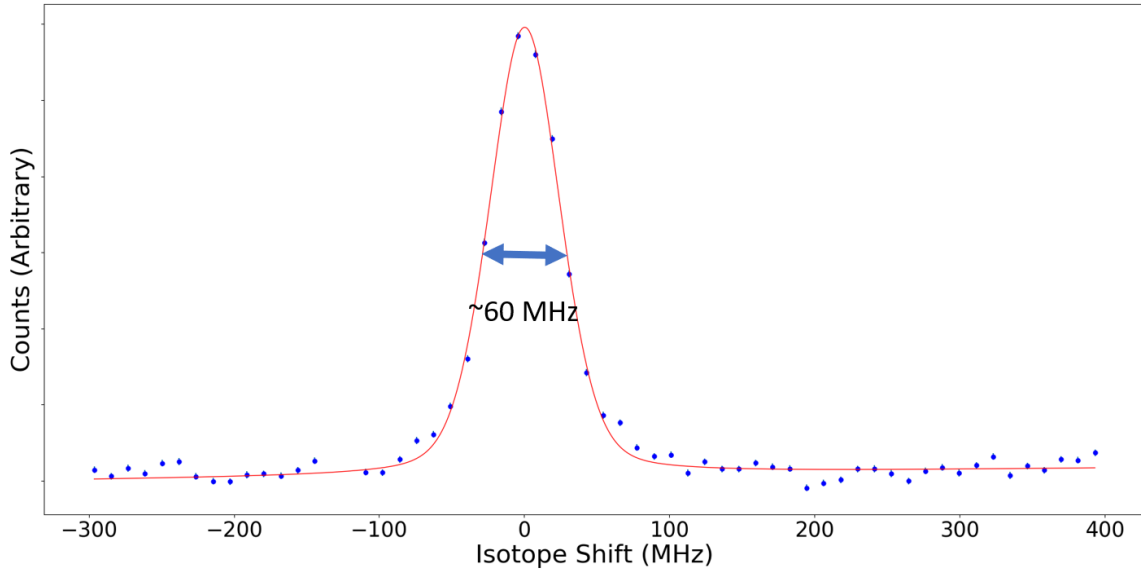


Figure 4.4: Hyperfine spectra of  $^{90}\text{Zr}$  measured using CLS. The width of the hyperfine spectra is approximately 60 MHz.

A consequence of the CLS technique is a limitation on the speed of transitions that can be used. Only electronic transitions that can be excited and decay before the ions pass the photon detection region can be used. Ions accelerated with a 30 keV potential pass the photon detection region, which has a length of less than 10 cm, in hundreds of ns. The lifetime of the excited state must be at most hundreds of ns long, corresponding to an Einstein coefficient  $A_{21}$  of  $10^7$ . On the timescale of a CLS measurement carried out using the existing photon detection system at BECOLA, any electronic state with a lifetime significantly longer than hundreds of ns can be considered a metastable state.

#### 4.1.1.2 Beam Bunching

A subset of CLS known as Bunched Beam CLS [27, 85, 2] is employed at the BECOLA facility. The most significant source of background during a CLS measurement is from

scattered laser light as the laser light passes the PMTs. The scattered light signal cannot be filtered from the fluorescence as the wavelengths of light are very similar. The stray light background prevents measurement of the HFS of radioactive ions with low production rates, as the signal to noise ratio (SNR) is too low and the peak cannot be adequately resolved.

The stray light background can be suppressed by concentrating the ions, trapping them in an RFQ cooler/buncher ion trap, and releasing them in short bunches. Typically the ion bunches reach the photon detection region with a temporal spread of approximately 1  $\mu$ s. The detected photons are only counted in the window of time as the ion bunch passes the photon detection region. The background outside of the time window can be neglected and assuming 100% efficiency in trapping the ions, the signal is concentrated into the ion bunch and the SNR is dramatically increased. If the ions are released once per second with a temporal width of 1  $\mu$ s, the background will be reduced by 6 orders of magnitude without reducing the observed signal. The bunched beam spectroscopy technique is critical for measurement of the HFS of radioactive beams.

## 4.2 BECOLA Facility

The optical pumping technique described in this thesis was developed at the BECOLA facility [1, 2], located at the NSCL. BECOLA is a dedicated end station for laser spectroscopy studies at the NSCL, and has been used to perform isotope shift measurements of rare isotopes [18, 12, 17], as well as having produced nuclear polarized beams for  $\beta$ -NMR studies and  $\beta$  asymmetry experiments. BECOLA can accept thermalized radioactive beams from the NSCL gas stopper [86] or stable ion beams produced by off-line ion sources [58]. A diagram of the BECOLA facility can be seen in Figure 4.5 and a description of the major

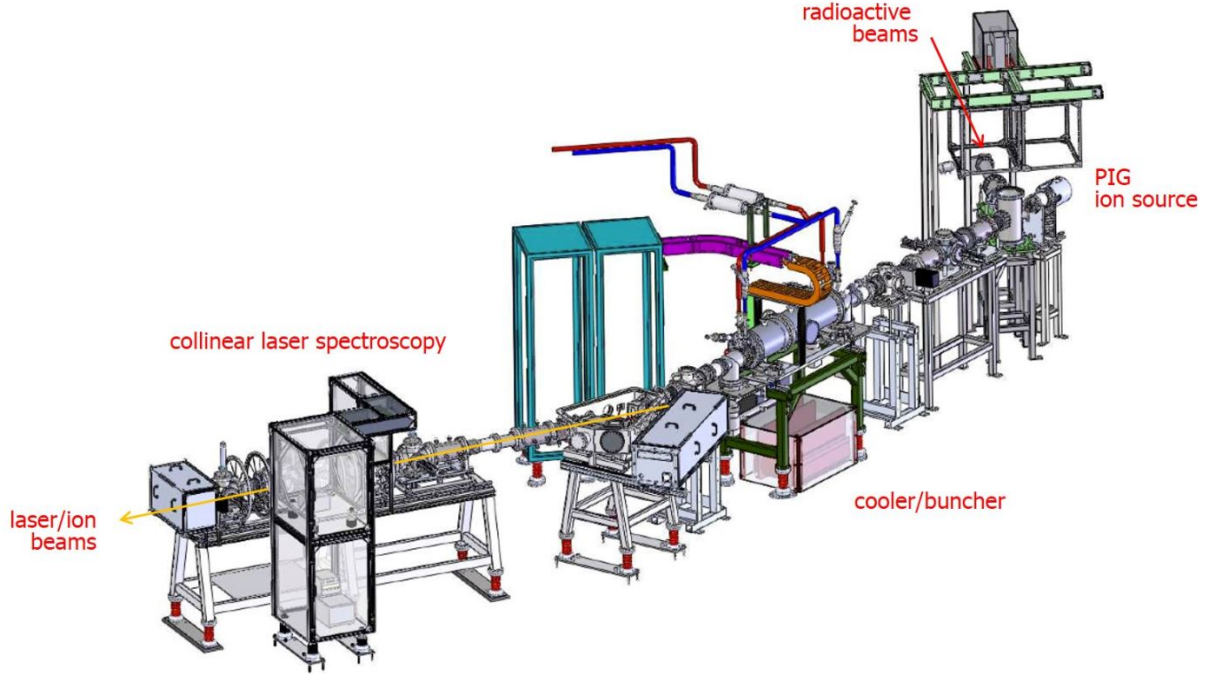


Figure 4.5: BECOLA Facility. Stable off-line beams or radioactive on-line beams are injected into the RFQ ion trap. The trapped beam is then transported to the collinear laser spectroscopy beamline for fluorescence measurements.

components of the facility follows.

### 4.2.1 Production of Ion Beams

The BECOLA facility can accept both radioactive ion beams produced by the coupled cyclotron facility and off-line stable beams from a variety of ion sources. The ions in the commissioning experiments were produced by a Penning Ionization Gauge (PIG) ion source [87]. The PIG ion source is a plasma discharge sputtering ion source, and is primarily used to produce ion beams of metallic elements and has been used at BECOLA to study Fe [12], Ca [17], Sc, Ni, and Pd isotopes. PIG ion sources work well to produce beams of metallic and gaseous elements, producing high ion currents.

A schematic of the BECOLA PIG ion source is shown in Figure 4.6, taken from [58] and

a photograph of the BECOLA PIG system is shown in Figure 4.7. The PIG ion source was

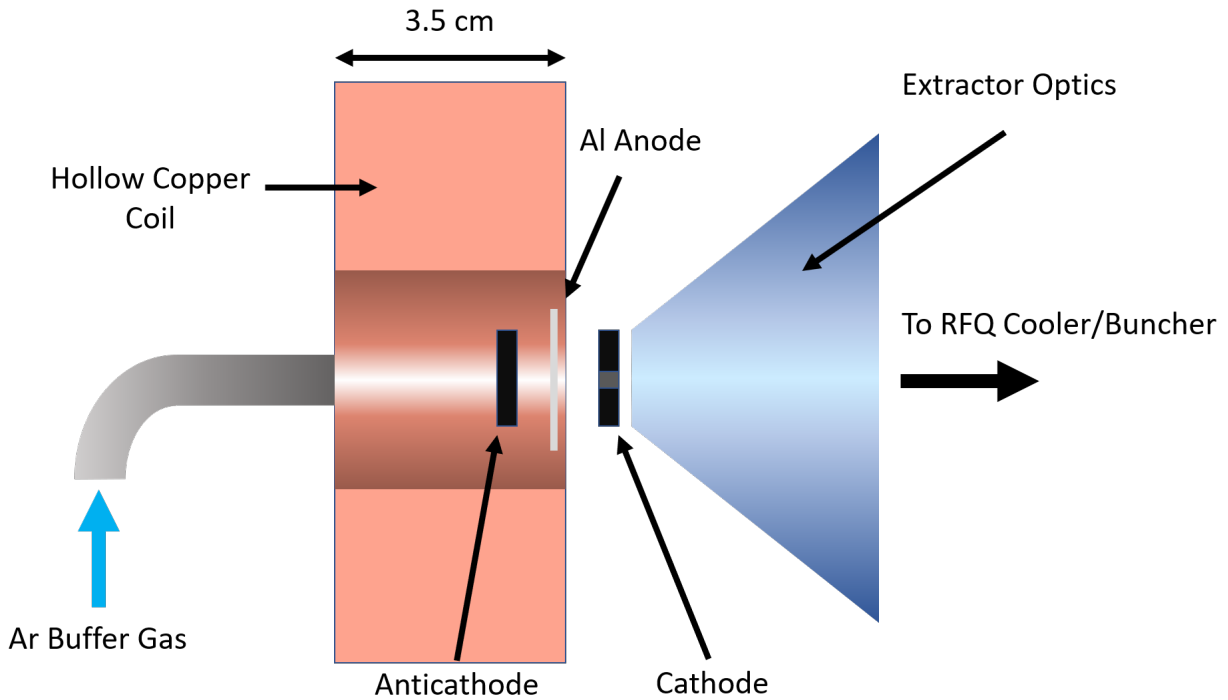


Figure 4.6: Cross section of the BECOLA PIG ion source. The PIG ion source can generate ion beams of many metallic elements via plasma sputtering, at rates up to 10s of nA.

used to produce  $Zr^+$  beams for the commissioning experiments. A potential difference of approximately 400 V was applied between a central aluminum anode held at +150V and a pair of small anticathode and cathode cylinders situated equidistant from the anode. The cathode and anticathode are approximately 11 mm in diameter and 3.4 mm thick and are made of the desired element for an ion beam. A buffer gas, typically an inert element, flows into the chamber and causes an electric discharge, producing a plasma. Buffer gas cations collide with the cathode and anticathode and produces sputtered ions of the element of interest, which are extracted from the chamber through a small hole of approximately 0.08 mm in the cathode by a conical extraction electrode, typically held at -3 kV. A magnetic coil surrounding the central chamber provides a magnetic field of approximately 500 G, applied

along the central axis of the anode and cathode, that confines the electrons and creates a self-sustaining plasma. A beam current of  $2.8 \mu\text{A}$  was measured with a Faraday cup immediately

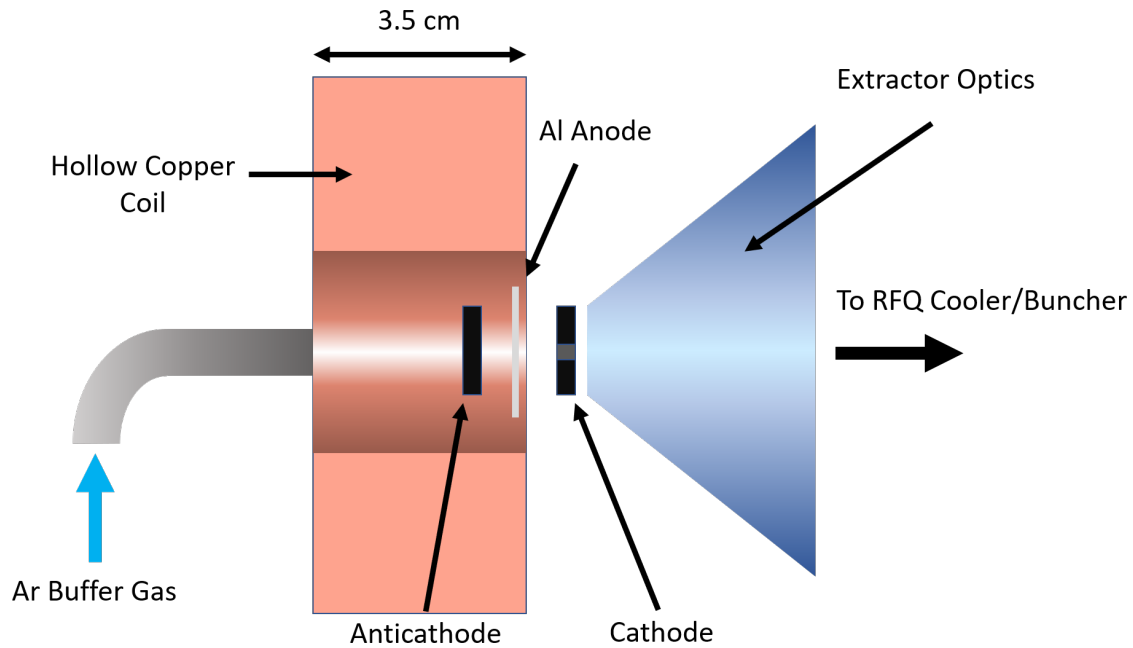


Figure 4.7: Photograph of the BECOLA PIG ion source. The PIG is attached to the BECOLA beamline with a 6 inch flange.

after the ion source, with a primary component of the  $\text{Ar}^+$  buffer gas. The beam current after the RFQ ion trap was measured with a Faraday cup at approximately 1.6 nA. The RFQ also serves as a mass filter and much of the  $\text{Ar}^+$  component of the beam is removed from the beam. The beam current after the photon detection region was measured with a Faraday cup at approximately 1.4 nA.

The PIG ion source was able to successfully produce beams of  $\text{Zr}^+$ , but the operation of the PIG was significantly different from the conditions observed with other elements. Sputtered ions can deposit inside the chamber during operation and short the cathodes and anode. When the short occurs, the PIG ion source must be removed and cleaned. The leakage current for producing Zr was an order of magnitude higher than what was observed

for producing Ni isotopes and the maintenance cycle was substantially reduced to 2-3 days. The reduced maintenance cycle did not impede these measurements, as it was an offline measurement that did not have a time limit. In addition, the Zr cathode and anticathode were substantially corroded through operation. Erosion of the Zr cathode increased the size of the hole used to extract ions from the central chamber, reducing the pressure of the plasma chamber and eventually rendering the PIG ion source inoperable. A comparison of



Figure 4.8: Cathode and Anticathode composed of Zr. The Zr cathodes quickly eroded over the course of the commissioning experiments. As the erosion progressed, the hole in the anticathode expanded and the cathode developed a large hole as well, which prevented operation of the PIG ion source.

a Zr cathode after extended period of operation and a new cathode is seen in Figure 4.8.

## 4.2.2 Radiofrequency Ion Trap

A helium-buffer-gas filled Radio Frequency Quadrupole (RFQ) ion trap is used to cool and bunch ionic beams at BECOLA. A more detailed description of the RFQ ion trap can be found in [78, 77] , but a brief description will follow. A schematic of the BECOLA RFQ ion

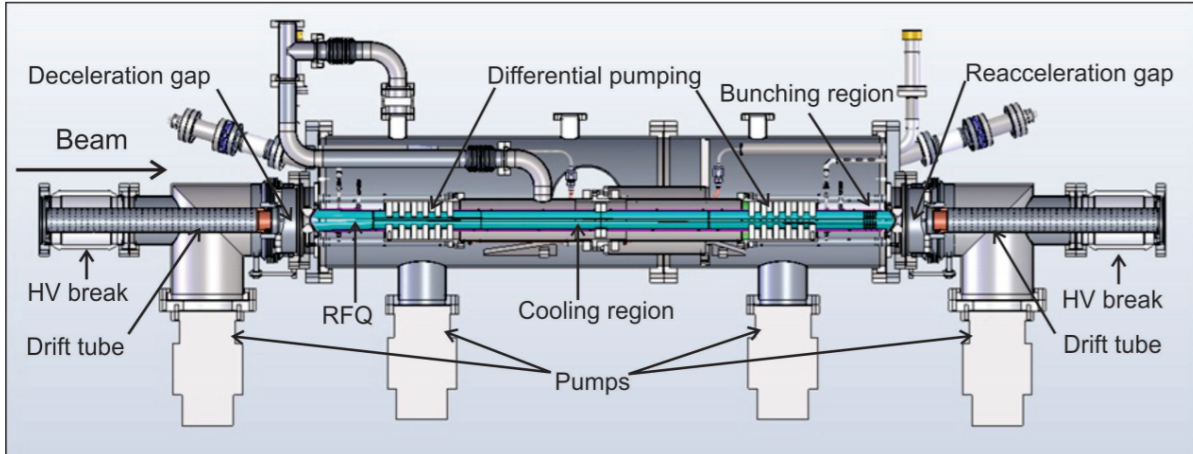


Figure 4.9: Schematic of the BECOLA RFQ ion trap, taken from [78]. The RFQ ion trap features three sections separated by differential pumping barriers. Ions are cooled through collisions with a He buffer gas in the cooling section, and are trapped in preparation for bunched beam CLS measurements in the trapping region.

trap is seen in Figure 4.9.

The RFQ ion trap is separated by differential pumping barriers between three sections, responsible for collection of ions, cooling via buffer gas collisions, and trapping. The incoming ion beam is captured and focused into the RFQ ion trap by injection optics consisting of a ring-shaped hyperboloid and a cone with a central aperture. Voltage applied to the hyperboloid decelerates and focuses the ion beam, while the cone prevents the RF field from penetrating into the deceleration field. Two DC drag field regions are used to move the ions through the RFQ ion trap, and an RF field provides transverse confinement. The first drag field is 0.8 V/cm, while the second drag field is gentler and is 0.4 V/cm. Instead of using segmented rods to produce the drag field, the BECOLA RFQ ion trap features a crosscut design that moves across the length of the electrode. A diagram of the crosscut geometry from [78] can be seen in Figure 4.10. The geometry of the crosscut allows for the production of a linear drag field with fewer components and power supplies.

After injection, the ions enter the cooling section of the ion trap. A He buffer gas was

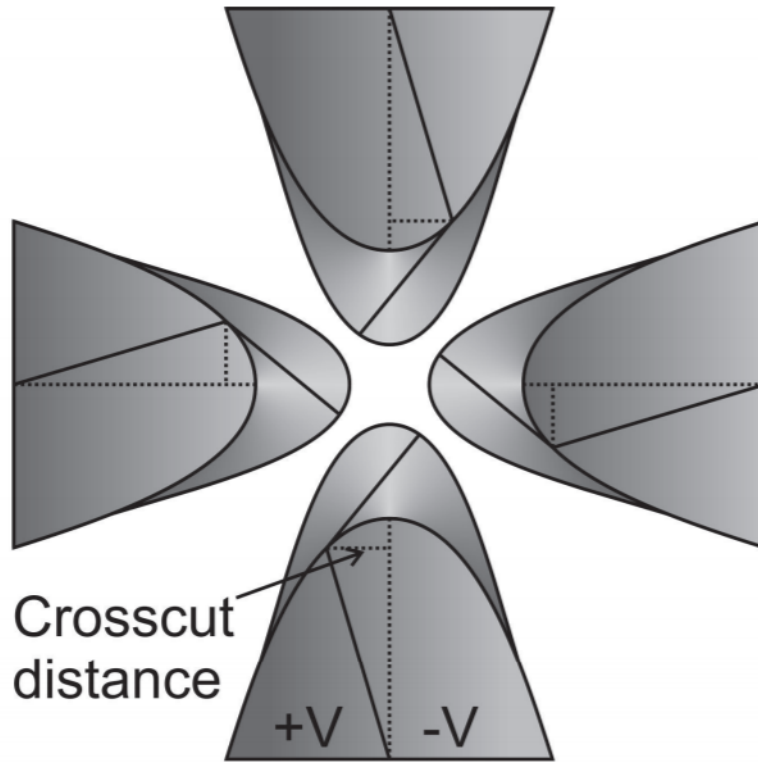


Figure 4.10: Diagram of the crosscut geometry of the BECOLA RFQ rods, taken from [78]. The view of the rods is longitudinal, with the beam direction coming out of the page. The crosscut design produces a linear drag field across the length of the RFQ ion trap with only two power supplies.

streamed into the cooling section. The pressure of the He buffer gas was measured at the gas inlet, and there are no pressure gauges within the RFQ ion trap itself. Typically the RFQ ion trap is operated at 80 mTorr of He buffer gas pressure at the gas inlet. The He buffer gas is held at room temperature and collisions between the ion beam and the buffer gas cool the ion beam to room temperature and reduces the emittance.

Another differential pumping barrier separates the cooling region from the trapping region, where the applied RF field and DC voltage at the segmented electrodes produces a trapping field. Simulations performed during the construction and installation of the BECOLA RFQ ion trap suggest that the He buffer gas pressure in the trapping region of

the ion trap are approximately 100 times smaller than the cooling section, or approximately  $800 \mu\text{Torr}$ . A detailed drawing of the segmented electrodes can be seen in Figure 4.11, taken from [78].

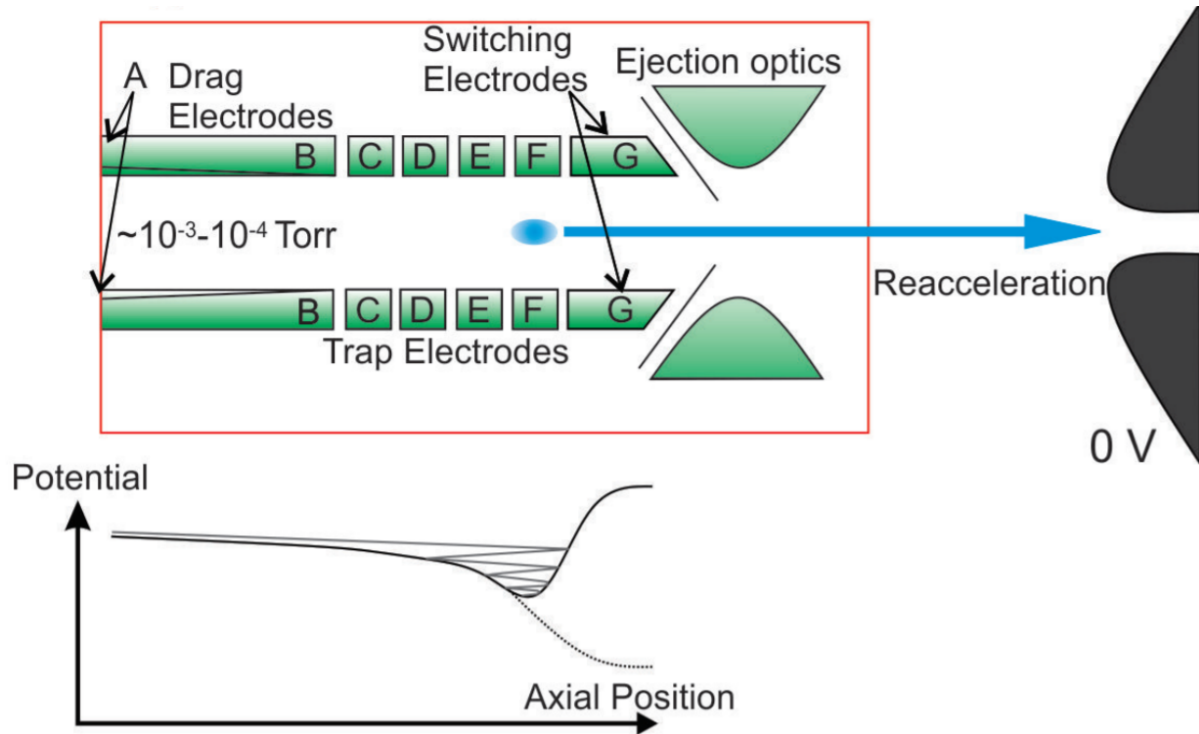


Figure 4.11: Diagram of the segmented electrodes of the BECOLA RFQ trapping region, taken from [78]. The diagram is a crosscut of the RFQ ion trap, with the beam traveling to the right. Voltages are applied to the segmented electrodes to produce a potential well to trap the ions and allow them to be released in bunches for laser spectroscopy measurements.

The first two segmented electrodes were grounded,  $-0.2$  V was applied to the third electrode,  $-4.2$  V was applied to the fourth electrode, and  $19.8$  V was applied to the final electrode to produce the potential well to trap the ions. The  $19.8$  V potential is flipped to  $-15$  V for ejection of the trapped ions. The flipping of the potential of the last segmented electrode takes approximately  $5 \mu\text{s}$ .

The stability of the ions in the trap can be calculated based on the amplitude and frequency of the RF field and mass of the ion, and is expressed as what is known as the

Mathieu stability parameter [88],  $q$ ,

$$q = \frac{4eV_{RF}}{mr_0^2\omega_{RF}^2} \quad (4.14)$$

where  $e$  is the charge of the ion,  $V_{RF}$  is the peak amplitude of the RF field,  $m$  is the mass of the ion,  $r_0$  is the radius of the trapping region defined by half the distance between the RFQ rods, and  $\omega_{RF}$  is the RF angular frequency. An ion is considered stable in the RF field if  $q$  is less than 0.908. During the commissioning experiments, the RF angular frequency was 7.5 MHz, with  $V_{RF}$  amplitude of 72.5 V. The mass of the  $Zr^+$  is 90 AMU. The radius of the trapping region is 3.5 mm or 0.0035 m. The Mathieu stability parameter was 0.44 under these operating conditions.

Ions that are not stable in the RF field will be removed from the beam, allowing the RFQ ion trap to serve as a mass filter as well. The mass resolution of the BECOLA system,  $m/\delta m$ , is roughly 2, meaning that conditions stable for an ion of mass 90 will be able to filter ions with masses more than 45 mass number away.

One limitation of the RFQ ion trap is that it is possible to overfill the trapping region. The energy spread of the trapped ions increases as the trapping region becomes overfilled and distorts the beam shape and beam energy, and subsequently the hyperfine spectrum, due to space charge effects. The temporal width of the ion bunch is significantly lengthened, serving as an indicator of the overfilling process. An example can be seen in Figure 4.12, where the time spectra of two filling conditions are compared. In the spectrum on the right the ion trap is overfilled and has approximately 10 times more ions than the spectrum on the left. The overfilling results in an almost 3 times increase in the FWHM.

The optics used to focus the beam into the RFQ ion trap can be detuned to decrease the

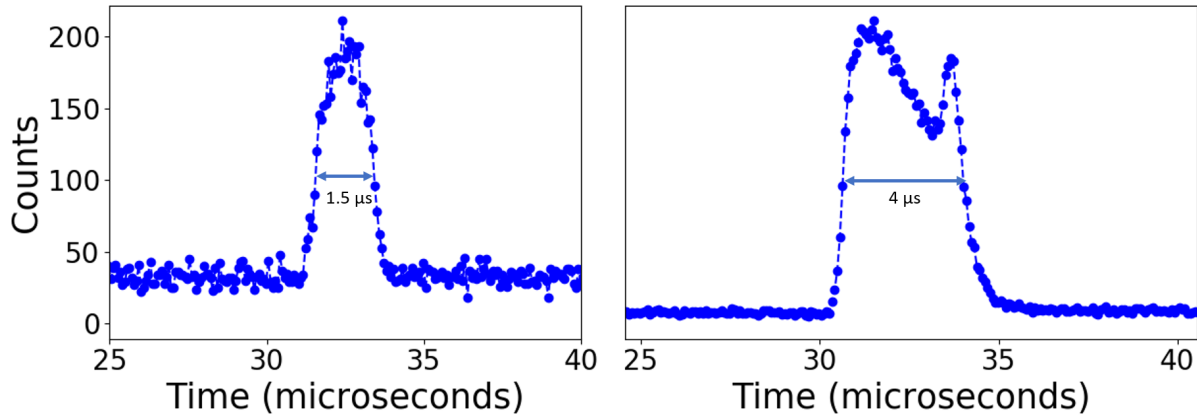


Figure 4.12: Measured time spectra of  $^{90}\text{Zr}$  with different numbers of ions trapped. The time spectrum on the left of the figure featured the fewest number of ions per bunch and had a FWHM of approximately  $1.5 \mu\text{s}$ . The time spectrum on the right contained approximately 10 times more ions per bunch, resulting in a significantly broader FWHM in time.

overall rate entering the trapping region and mitigate overfilling of the ion trap.

### 4.2.3 CLS Beamline

The  $\text{Zr}^+$  ions were transported through the CLS beamline after ejection from the BECOLA RFQ ion trap. Two kicking electrodes bent the beam 30 degrees in total, overlapping the ion beam with a continuous wave laser beam injected through a window port in the vacuum chamber of the bender.

The laser light in the CLS beamline was aligned to the ion beam through two adjustable apertures located in the beamline. Each aperture can be vertically adjusted to three different diameters, of 3, 5, and 7 mm respectively. The laser light was "walked" through the apertures, where the path of the laser beam is adjusted through the use of two mirrors, to minimize the stray light background. A telescope system of lenses was used to focus the CW laser light through the beamline. Typically, the best results for the minimization of the background were seen as the laser light was focused at the end of the beamline, with a beam

size of 1.4 mm, although the ion beam was assumed to be approximately 5 mm in diameter. 300  $\mu\text{W}$  of laser light power was used for the CLS measurement with a transmission through the beamline of 75%.

The ion beam and laser beam propagated collinearly through the beamline to the interaction region (photon detection region), where the laser light interacts with the ion beam to emit fluorescence. A scanning voltage was applied at the photon detection region, which Doppler shifts the ion beam in and out of resonance with the laser light, as described in Chapter 2. The laser-resonant photons were captured by three PMTs. One PMT was placed at the focal point of an ellipsoidal reflector, which is used to collect and focus light from the second focal point of the ellipsoid. Two other PMTs are part of a new system that was installed and used in a recent online experiment involving proton-rich isotopes of Ca [17, 89]. In the new system an elliptical reflector is used instead of an ellipsoidal reflector. The elliptical reflector also serves to focus the signal, but the focal region is a line instead of a point and photons can be collected from a longer path length. The fluorescence is focused to the second focal point of the elliptical reflector outside of the beamline through a vacuum window. An aperture is used to block stray light photons and the focused signal is sent to a compound parabolic concentrator. The parabolic concentrator rejects photons that enter at an angle of more than  $20^\circ$ , and concentrates the signal to the PMT. Stray light photons are more likely to enter at larger angles, and the background can be further reduced. Although the design of the reflectors for the PMTs are different, it is important to use both during experiments, as more collected photons reduces the statistical uncertainty of a measurement. A diagram of the photon detection region is shown in Figure 4.13.

After the photon detection region the CLS beamline terminates at an anti-reflection coated glass window. The glass window is used to prevent the laser light from reflecting

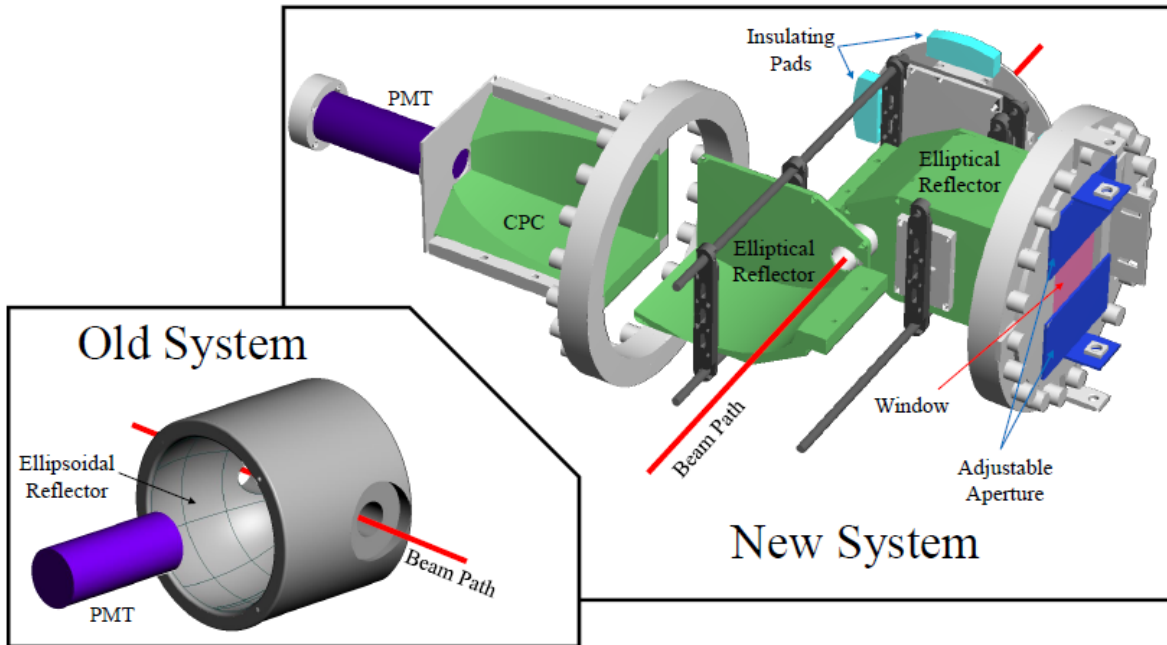


Figure 4.13: Diagram of the photon detection region in the BECOLA CLS beamline, taken from [89]. The photon detection region is located immediately after the charge exchange cell. The new design of the photon collection system is placed directly after the old design. The photon detection region serves to collect and focus fluorescence to photomultiplier tubes for CLS measurements.

back through the beamline and contributing to the scattered light background. After the glass window, a laser safety box is used to contain the laser light. A small optical breadboard is situated in the box, where the laser light that travels the length of the CLS beamline can be monitored with cameras or power meters during operation.

#### 4.2.4 Continuous Wave Laser System

A CW Sirah Matisse Titanium:Sapphire ring laser [90] was used to perform CLS for the commissioning experiments. The Matisse system was pumped by a Spectra Physics Millennia EV CW pump laser [91] at 532 nm with a maximum output power of 20 W and features a tunable range of 700-1000 nm, and is located in another room away from the BECOLA

experimental area.

Although the spectral bandwidth of the Ti:sapphire system is over 300 nm, the output of the Ti:Sapphire system is made up of over 370,000 modes, or resonances, separated by 160 MHz. The separation between these modes is called the Free Spectral Range(FSR). Frequency selective optics are used to separate these modes and deliver narrow linewidth laser beams on the order of 100 kHz.

The wavelength ranges of the CW laser systems can be extended through the use of a Sirah WaveTrain [92] frequency doubling system. As the CW laser light propagates through the nonlinear crystal, it causes the electron distribution to polarize. The polarization of the electron distribution in the crystal generates a second wave with twice the frequency of the fundamental light. Since this is a nonlinear process, the efficiency of the doubling process scales with the square of the laser power. CW laser systems have relatively low energy density, so the WaveTrain system uses a passive resonator ring cavity to produce constructive interference and increase the total efficiency of the conversion. The WaveTrain system allows BECOLA to extend the range of wavelengths available for CLS to 350 nm for the Ti:Sapphire laser system.

The light produced by the CW laser system was stabilized using a wavelength meter, model HighFinnese WSU-30 [93]. The frequency of the laser light is compared to 633 nm light produced by a frequency stabilized He-Ne laser [94] using a Fizeau interferometer to compare the frequencies. A feedback signal from the wavelength meter is used to adjust the piezo mirror of the Ti:Sapphire laser cavity and adjust the output frequency to match the desired frequency and controls long term drift of the laser frequency. Short term changes in the laser frequency are controlled by monitoring the laser light in a Fabry-Perot interferometer. An electronic signal from a photodiode in the interferometer is used to determine the frequency

of light in relation to the resonance frequency of the cavity and a feedback signal is sent to a PID controller to shift the internal optics of the Ti:Sapphire laser and control the output frequency.

Two methods of light transport were used for the CW laser system during the experiments described in this thesis. The first method was through fiber optic cable. The CW laser light was transported to the BECOLA experimental area using a polarization maintaining single-mode optical fiber. The relative location of the BECOLA CW laser system and the BECOLA experimental area is shown in Figure 4.14. The fiber led to a safety box containing optics

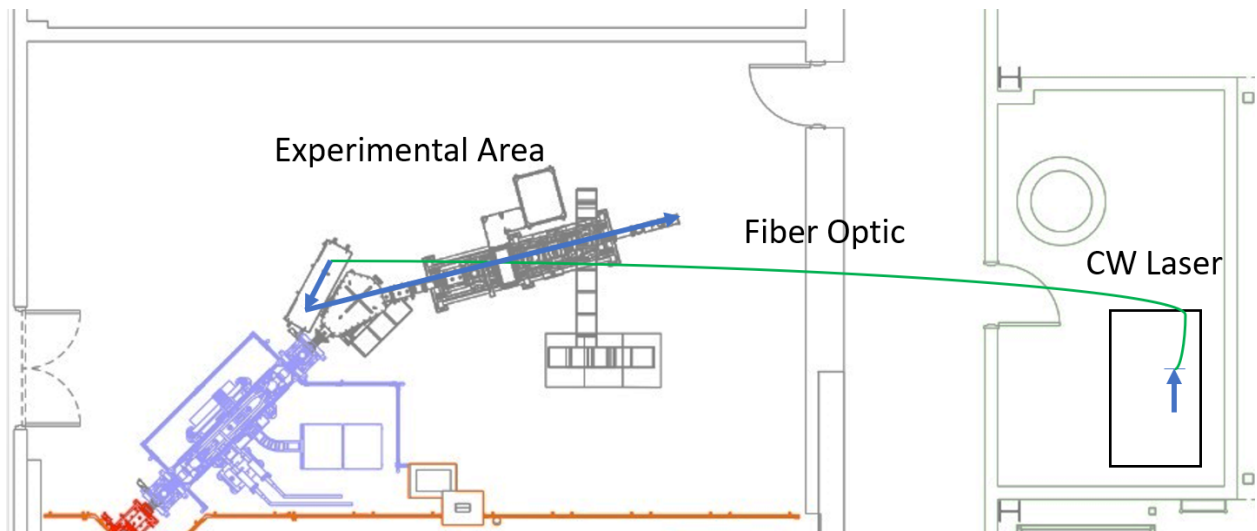


Figure 4.14: The BECOLA laser room is located approximately 15 m away from the BECOLA experimental area. The CW laser light is transported to the CLS beamline with the use of fiber optic cable. The output of the fiber optic cable is located in a laser safety box, where the laser light can be prepared for injection into the CLS beamline.

that prepared the CW laser light for injection into the CLS beamline. The safety box features pressure activated switches that are connected to the BECOLA safety system. Opening the box while laser light is passing through the system activates physical shutters that block the laser in two locations to prevent accidental exposure. One shutter is located immediately after the Ti:Sapphire output, and the other shutter is located after the fiber optic output in

the BECOLA experimental area.

The second light transport method was through a new free-space light transport system, which will be described in detail later in this Chapter. The CW laser light was translated upwards to an inverted optical breadboard where two mirrors were placed. The mirrors allow for alignment of the CW laser light through a 10-m long pipe connecting the BECOLA laser room and experimental areas. The 10-m long pipe terminates in a laser safety box in the BECOLA experimental area, where the light is translated down into the original laser safety box, and the light is prepared for injection into the CLS beamline as described for the fiber optic light transport system.

## **4.3 New Developments to BECOLA Facility**

A new pulsed laser system and method to transport the light from this laser to the BECOLA experimental area were required to perform the commissioning experiments and are described here.

### **4.3.1 Pulsed Laser System**

It is desirable to have access to a wide range of wavelengths for optical pumping. As mentioned in Chapter 1, some transition metals require deep UV laser light for the pumping process, which is difficult to produce with CW laser systems. A new pulsed laser system was procured and installed in the BECOLA laser infrastructure to better enable the optical pumping experiments. The pulsed laser system is composed of a Cobra-Stretch dye laser [95] produced by Sirah, pumped by a Quanta-Ray INDI Nd:YAG laser [96]. The Quanta-Ray INDI laser features a 10 Hz repetition rate and produces fundamental light at 1064 nm that

can be converted to 532 nm second harmonic light or 355 nm third harmonic light by a harmonic generator installed in the pump laser housing. The laser output was measured during installation. The INDI pulsed laser was able to produce 5 W of light at 1064 nm, 2 W of light at 532 nm, and 1.2 W of light at 355 nm. The pump laser light is split as it enters the Cobra-Stretch, to pump two dye cells which are used as a gain medium for lasing. The

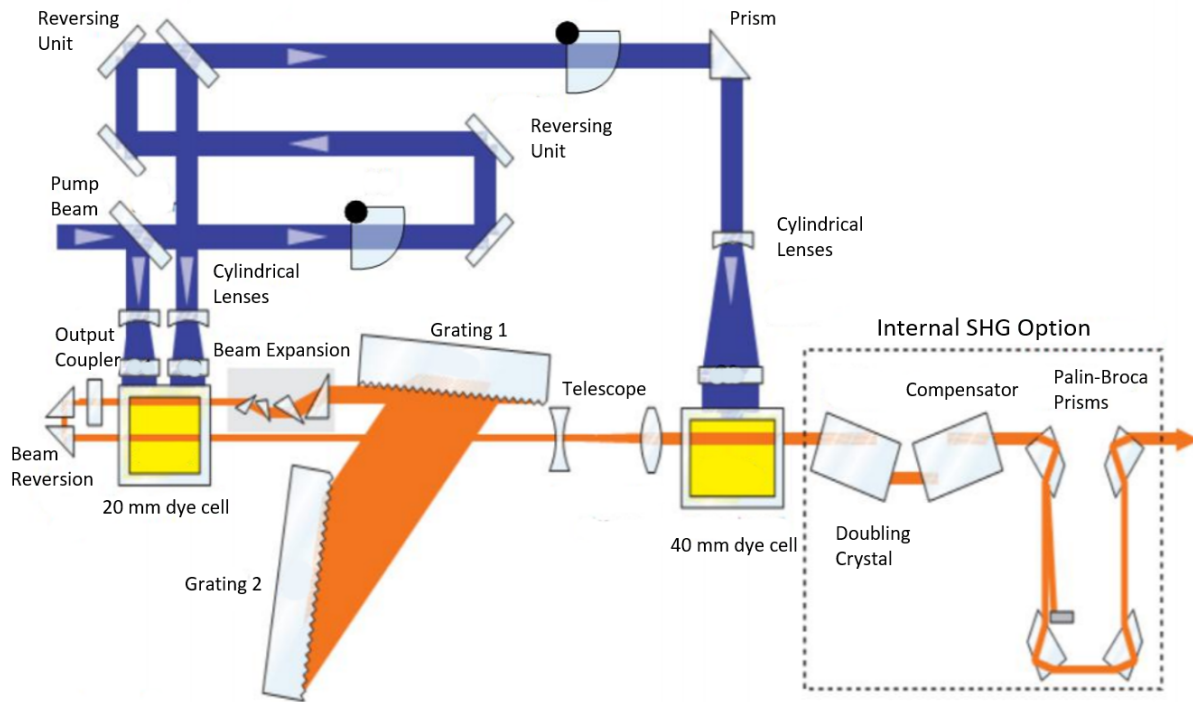


Figure 4.15: Laser path through the Cobra-Stretch dye laser system from [97]. Laser light from the INDI pump laser excites the lasing medium in the 20 mm oscillator cell and the 40 mm amplifier cell. The output wavelength is selected by the grating position, which is amplified in the amplifier cell, before entering the internal SHG unit where the frequency of light is doubled.

optical layout of the Cobra-Stretch system is shown in Figure 4.15. One cell is known as the oscillator cell and the other is the amplifier cell. The amplifier cell is shown in Figure 4.16. The pump laser excites the lasing medium in both cells. Lasing mediums in liquid solvents typically have very broad spectral ranges, and a system of gratings allows for a relatively

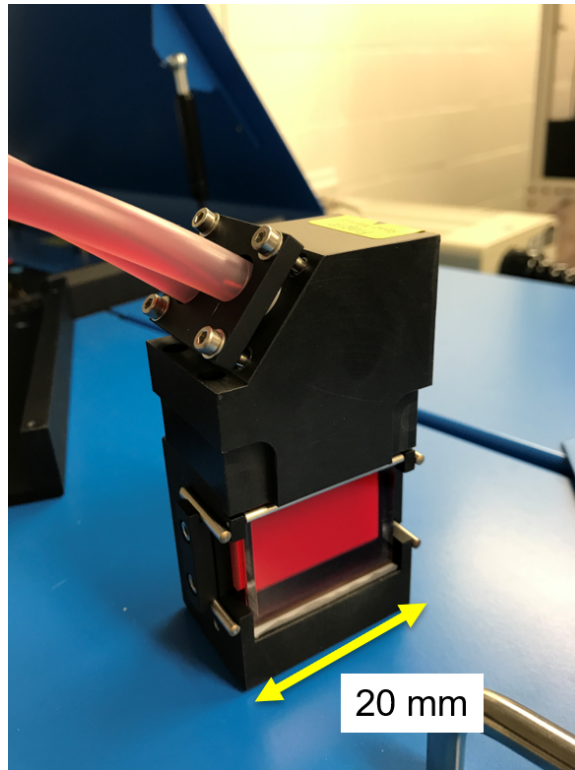


Figure 4.16: Amplifier dye cell of the Cobra-Stretch pulsed laser system. The dye acts as a lasing medium and is circulated through the cell to prevent laser-induced breakdown of the dye molecules and extend its lifetime. The amplifier cell is 20 mm in length.

narrow spectral range to be selected from the output of the oscillator cell. The laser light from the oscillator cell is sent through the amplifier cell where the total energy is greatly increased. Pumps circulate the dye through the cells to prevent laser-induced molecular breakdown and extend the lifetime of the dye.

The wavelength of light produced by the Cobra-Stretch system is determined by the dye, which for a specific dye can produce light within a range of 30-40 nm with the conversion efficiency of the fundamental light peaking at the center of the range. The wavelengths of light produced with different dyes is shown in Figures 4.17 and 4.18 for dyes pumped by 532 nm and 355 nm light, respectively. With a broad selection of dyes, the Cobra-Stretch system can produce light from 370-900 nm.

In addition to the INDI pump laser and the Cobra-Stretch system, a frequency doubling

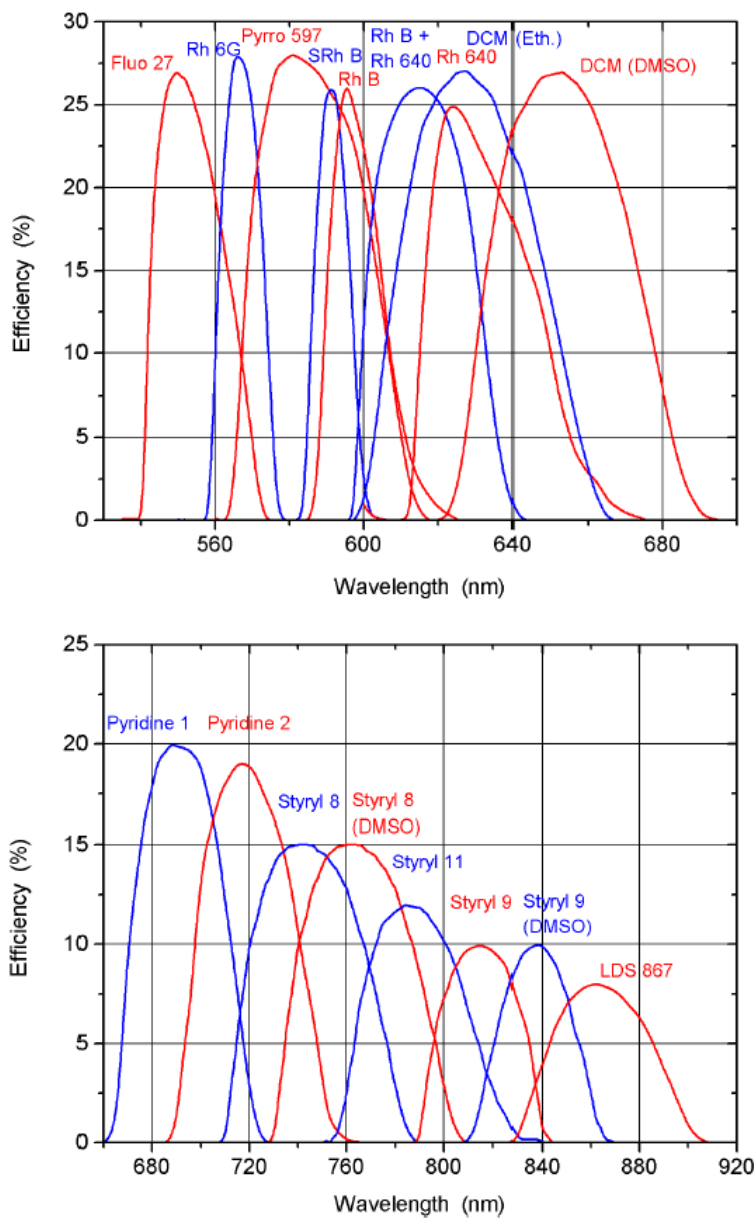


Figure 4.17: Conversion efficiency as a function of wavelength for different dyes across the range of 540-910 nm. Dyes in the range of 540-910 nm are pumped by second harmonic light at 532 nm produced by the INDI pulsed laser. Figure taken from Sirah Cobra-Stretch User's Manual [97].

unit was installed that generates second harmonic light using a nonlinear crystal in a manner similar to the WaveTrain system used for the CW laser systems. However, instead of a ring cavity, the pulsed laser frequency doubling unit uses only one pass of the pulsed laser to produce second harmonic light by taking advantage of the high energy density of the pulsed

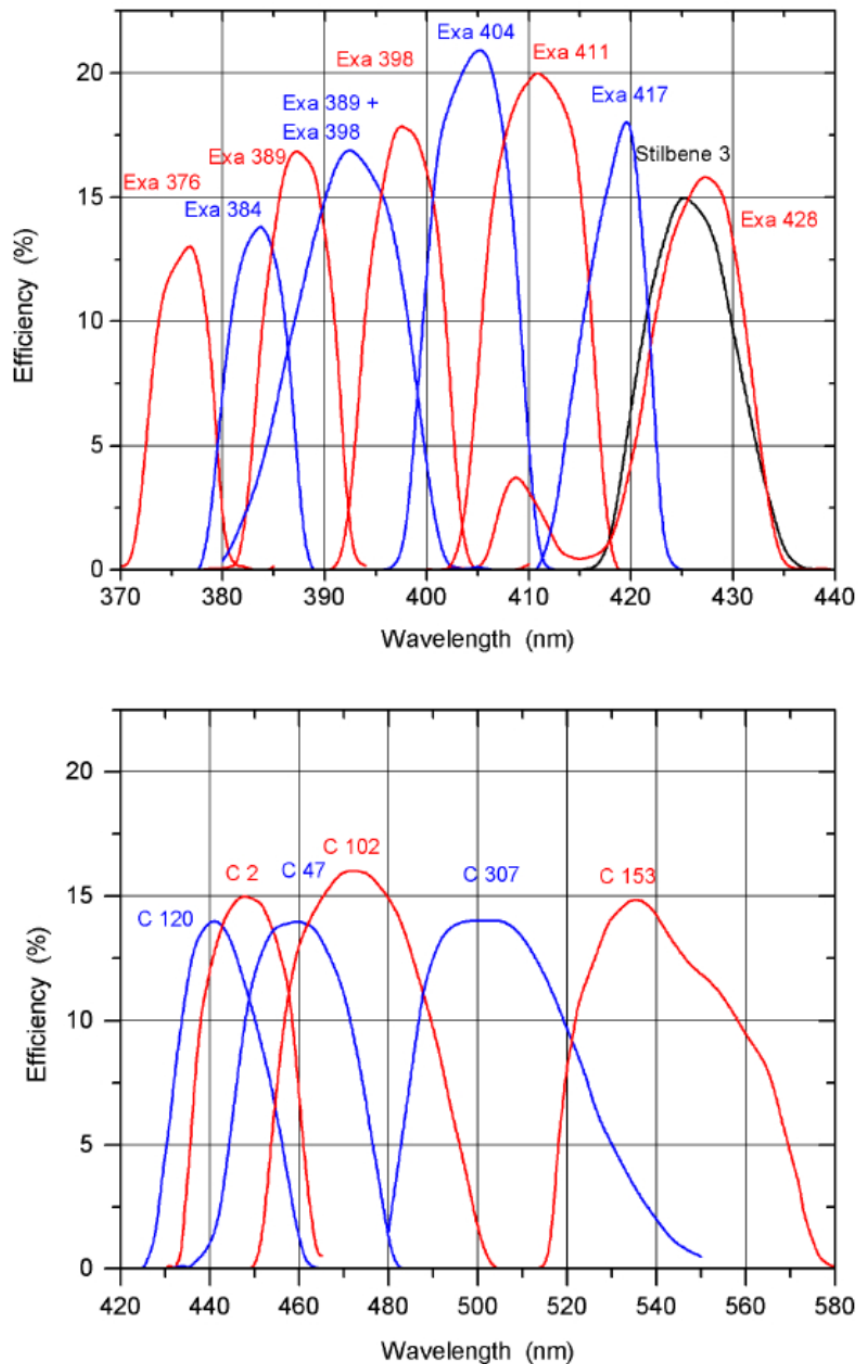


Figure 4.18: Conversion efficiency as a function of wavelength for different dyes across the range of 370-580 nm. Dyes in the range of 370-580 nm are pumped by third harmonic light at 355 nm produced by the INDI pulsed laser. Figure taken from Sirah Cobra-Stretch User's Manual [97].

laser light. A series of prisms after the doubling crystal are used to separate the fundamental Cobra-Stretch light from the frequency doubled light. The low end of the wavelength range

Table 4.1: Pulsed laser wavelengths and powers tested during installation of the Cobra-Stretch laser system at BECOLA.

Wavelength (nm)	Power (mW)
535	350
365	100
270	51
206	27
196	2

of the pulsed laser system is extended to 200 nm with the doubling unit.

A final unit was added to the pulsed laser system to reach 196 nm, which is not possible to generate with frequency tripling. This final unit consists of a Raman shifter filled with dimethyl sulfoxide (DMSO), which utilizes the anti-Stoke shift effect to shift the frequency of 663 nm light to 555 nm light. A portion of the fundamental light is doubled to 331.5 nm and mixed with the 555 nm light from Raman shifter to generate 196 nm light. Production of laser light through mixing is less efficient than doubling using a nonlinear crystal, and results in a sharp decrease in the laser power generated between 200 nm and 196 nm, but is sufficient for the use in optical pumping.

The production of a range of wavelengths was tested during installation of the laser system, with the results summarized in Table 4.1.

The INDI laser produces a laser pulse with a temporal width of 5-7 ns, which was measured by the manufacturer. The temporal width of the beam produced by the Cobra-Stretch was measured at the BECOLA facility using attenuated light on a photodiode. The temporal width of the beam at 360 nm was measured as approximately 6 ns and the oscilloscope capture is seen in Figure 4.19

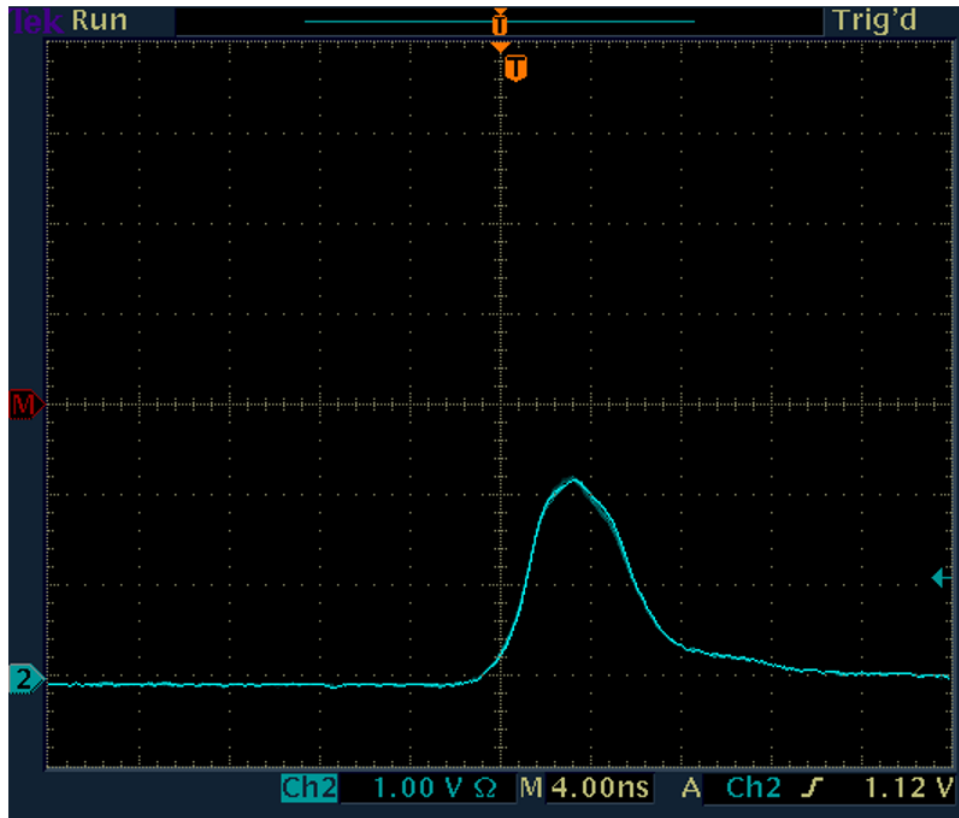


Figure 4.19: The width of the temporal pulse produced by the Cobra-Stretch laser system. The laser light was attenuated using a neutral density filter before being captured on a photodiode.

An additional property of interest is the spectral linewidth of the laser light. The natural linewidth of the optical pumping transition will be Doppler broadened to the order of GHz. The spectral width of the pulsed laser should match the Doppler broadened linewidth to ensure efficient excitation of the transition. The linewidth of the pulsed laser was measured by the manufacturer at 567 nm. The linewidth of the fundamental laser light after the Cobra-Stretch dye cells is approximately  $0.04 \text{ cm}^{-1}$ , which is doubled as the fundamental laser light passes through the doubling crystal. The end result is that the linewidth of the laser light is  $0.08 \text{ cm}^{-1}$  or 2.4 GHz, which matches the thermal broadened linewidth of a fast transition.

The frequency of the pulsed laser is monitored using a HighFinesse Angstrom WS6-600

wavelength meter [98], which features an absolute accuracy of 600 MHz. A portion of the discarded fundamental light is sampled and injected into a fiber optic cable, where it is sent to the wavelength meter. The wavelength meter was used to measure the pulse-to-pulse frequency stability. Over a period of approximately 1 hour the standard deviation of the frequency was found to be  $0.02 \text{ cm}^{-1}$ .

A final property of interest of the pulsed laser system is the quality of the laser beam. The laser beam profile from the INDI pump laser was examined using burn paper, which is a special kind of paper that is burnt by the laser light. The profile of the INDI laser light was circular and the power was evenly distributed. The burn paper results of both the INDI pump laser and the Cobra-Stretch dye laser are shown in Figure 4.20.

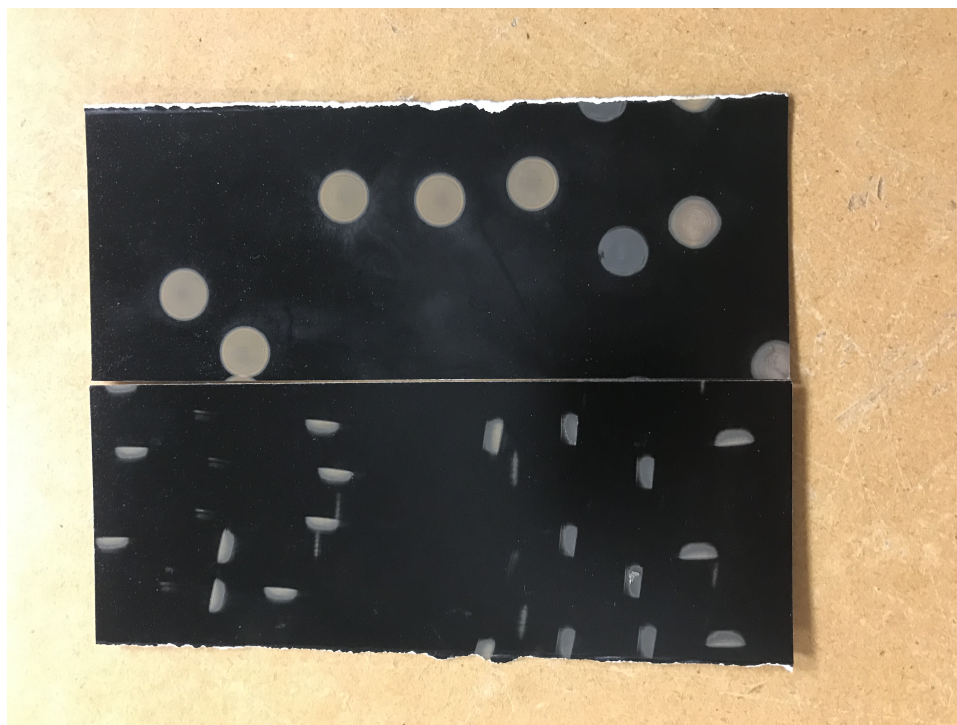


Figure 4.20: Laser beam profiles of the INDI pump laser(Top) and Cobra-Stretch dye laser(Bottom) as seen on burn paper. The laser profile of the INDI system is circular and the power is evenly distributed, while the laser beam profile of the Cobra-Stretch is elliptical and the power is not evenly distributed.

The laser light profile was also measured using a CCD camera, although the power output

from the INDI system was too high to safely image. The Cobra-Stretch system produces light that features more than one mode, resulting in a laser beam with three distinct local maxima of power. The pulsed laser light was attenuated and reflected to the camera to prevent damage, and the resulting screen capture is shown in Figure 4.21.

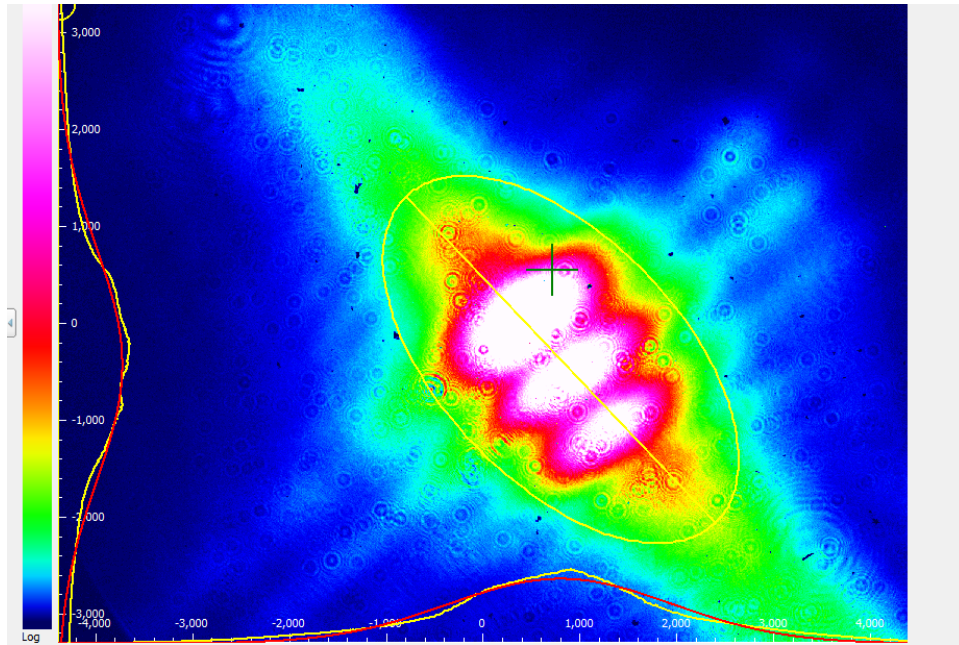


Figure 4.21: Power distribution of pulsed laser light produced by the Cobra-Strech system. Multiple modes of light are produced by the laser, resulting in a profile with three local maxima.

The optical pumping simulation assumes that the power is evenly distributed across the beam, a significant divergence from the experimental conditions and the implications will be discussed in Chapter 6.

### 4.3.2 Free-Space Light Transport System

The second major development necessary for the optical pumping system was a free-space light transport system. The BECOLA laser systems, including the new pulsed laser system described above, are housed in a climate-controlled room located approximately 15 meters

away from the BECOLA experimental area. The layout of the BECOLA laser room and experimental area can be seen in Figure 4.22.

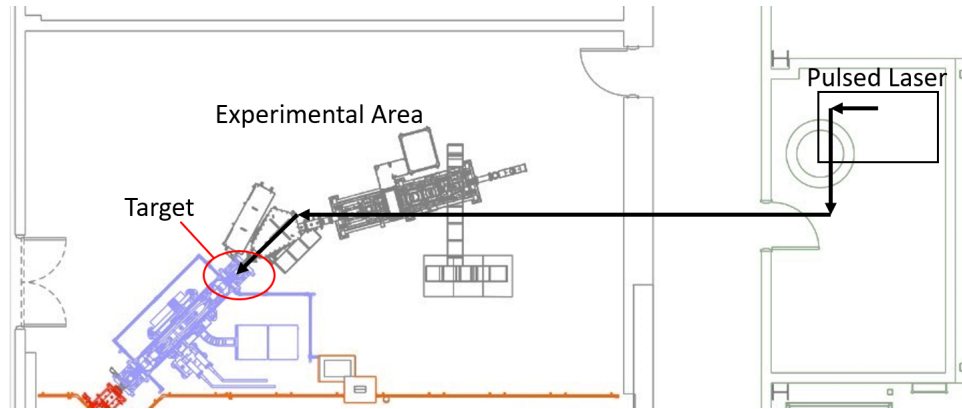


Figure 4.22: The BECOLA laser room is located approximately 15 meters away from the BECOLA experimental area. The free-space light transport system uses mirrors to deliver light to the experimental area with minimal loss of power.

#### 4.3.2.1 Pulsed Laser Fiber Optic Cable System

Although fiber optic cable is capable of transporting CW laser light of sufficient power for CLS measurements, high energy density pulsed laser light presents unique challenges that required a new system. The type of fiber optic cable used to transport the CW laser light was not suitable for pulsed laser light for multiple reasons. The specific fiber optic cable used at BECOLA has a damage threshold of  $250 \text{ kW/cm}^2$ . Efficient coupling of the laser light to the fiber optic cable requires the laser light to be focused to a size approximately 70-80% of the effective mode area of the fiber. The single-mode, polarization-maintaining fiber has a mode field diameter of  $2 \mu\text{m}$ , limiting the total output power of the CW laser system to 150 mW before risking damage to the fiber optic cable. Typical CLS measurements use less than 1 mW of laser light and the damage threshold is not considered, but the energy density of a pulsed laser is very high because the energy is distributed over a duration of nanoseconds. The single mode polarization maintaining fiber has a different damage threshold for pulsed

laser light. The provided damage threshold from the fiber manufacturer for a laser pulse with a temporal width of 10 ns is 5 GW/cm<sup>2</sup>. The Cobra-Stretch pulsed laser is capable of producing up to 12 mJ of laser energy per laser pulse at 360 nm, with a pulse duration of 6 ns. The mode field diameter is 2  $\mu\text{m}$ , giving an effective mode area of 25  $\mu\text{m}^2$  or  $2.5 \cdot 10^{-7}$  cm<sup>2</sup>. With 12 mJ of energy concentrated to  $2.5 \cdot 10^{-7}$  cm<sup>2</sup> over a duration of 6 ns, the peak energy density approaches 8000 GW/cm<sup>2</sup> and is very likely to damage the fiber optic cable.

Additionally, deep UV light causes wavelength and time-dependent damage to fiber optic cables in a process known as solarization. Solarization damage has been observed at BECOLA in time scales as low as days at less than 1 mW of laser power, and effectively lowers the transmission efficiency through the fiber optic cable, and results in a lower-quality laser beam. Solarization-resistant fibers exist, but allow for the propagation of multiple different modes of light, making it difficult to manipulate the light after ejection from the fiber.

Although these challenges were known, a fiber optic light transport system was explored due to its relative ease of use and enhanced safety in comparison with transporting the laser light through the air. A 2-m section of UV600-SR solarization-resistant optical fiber was purchased from Avantes Inc [99]. The solarization-resistant fiber was a multimode fiber optic cable with a core diameter of 600  $\mu\text{m}$ , compared to 2  $\mu\text{m}$  for the single mode fiber optic cable used for the CW laser light. The fiber was rated by the manufacturer to withstand the energy density of the pulsed laser light.

The laser light was successfully coupled to the fiber, but suffered from low transmission efficiency. In the testing of this fiber optic cable, the laser power after the Cobra-Stretch system was 110 mW, and the highest-achieved transmission efficiency through the fiber optic cable was 6%. Additionally, as the fiber optic cable was a multimode fiber, more than one

mode of light is able to travel through the fiber. After exiting the fiber, a lens telescoping system was employed to manipulate the laser light. In the BECOLA experimental area, the telescoping system would be used to prepare the light for injection into the beamline and is important for controlling the beam size and divergence. Due to the multimode nature of the output from the fiber optic cable, the beam waist of the laser light was very large. At a distance of 4.5 m, the smallest achievable beam size was approximately 7.5 cm in diameter, compared to the trapping region of the BECOLA RFQ ion trap, which has a diameter of 7 mm. Due to the low transmission and large beam size, the fiber transport system was determined to not be feasible.

#### **4.3.2.2 Free-Space Light Transport**

The alternative to fiber optic light transport for the pulsed laser light is a free-space light transport system, consisting of optics and infrastructure to safely transport the laser light in air to the BECOLA experimental area. The free-space light transport system was necessary to efficiently transport the pulsed laser light to the BECOLA experimental area and also opens the possibility of simultaneous transportation of CW laser light, delivering the laser beams to different physical locations in the BECOLA experimental area, where they are injected into the beamline. The ability to transport deep UV CW laser light will extend the range of elements that can be studied at BECOLA in the future.

Modifications to existing infrastructure were necessary to construct the light transport system. An optical breadboard was mounted to a steel support beam located approximately 2.5 m above the floor in the BECOLA laser room. A 10-m long steel pipe was installed connecting the BECOLA laser room to two new laser safety boxes that were constructed in the BECOLA experimental area, which are seen in Figure 4.23.



Figure 4.23: New laser safety boxes constructed in the BECOLA experimental area. Laser light from the BECOLA laser room is sent through a 10-m long steel pipe to the laser boxes. The upper box contains two breadboards to direct the light through steel pipes to the lower boxes for preparation before injection into the CLS beamline and RFQ ion trap.

The upper laser safety box contains two small breadboards mounted on the side of the box. Mirrors are attached to the breadboards to direct the laser light down to the lower safety boxes through shorter steel pipes. Holes in the safety boxes for pipes and cables are fitted with rubber seals to prevent any light from escaping. The laser safety boxes were mounted to heavy steel posts, which were aligned to the CLS beamline and bolted to the ground to improve the stability of the structure.

### 4.3.2.3 Optical Layout

The laser light must travel approximately 15 m from the pulsed laser system to the RFQ ion trap, and it is important to have good control of the laser beam along the light transport path. The optical elements to manipulate the laser light through the free-space light transport system were chosen through simulation using the FRED Optical Engineering software [100]. The optical layout is split into three sections, on the pulsed laser table, the upper section of the laser room, and the laser safety box in the BECOLA experimental area. The optical layout of the pulsed laser table is shown in Figure 4.24.

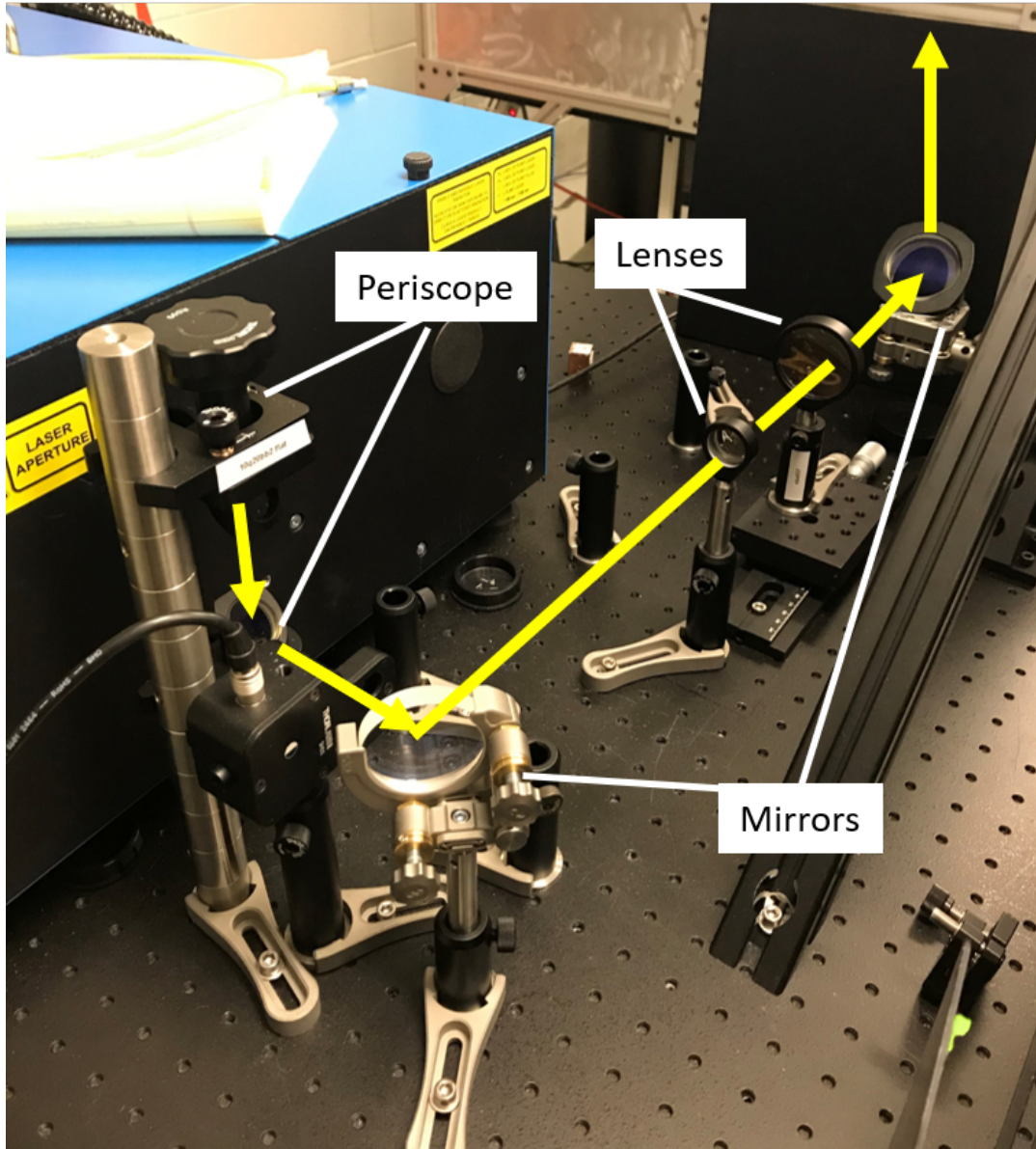


Figure 4.24: Optical layout on the pulsed laser table. The yellow light shows the path of the pulsed laser light. The light is translated from the output of the Cobra-Stretch system to a mirror using a pair of periscope mirrors. The light passes through two lenses, which are used as a telescoping system to slowly focus the light through the light transport system. The light is then reflected upward to an inverted breadboard.

The pulsed laser light exits the Cobra-Stretch system and is immediately translated downwards using a pair of mirrors that act as a periscope. The light is directed through a telescoping set of lenses that initially expand the laser beam and focus it over the free-space

light transport system, allowing for slow convergence to the BECOLA experimental area. A concave lens with a focal length of 7.7 cm is the first lens in the telescope and a 50 cm convex lens is the second lens. Initially, the first lens was a convex lens, but the pulsed laser light at the focal point of the lens was powerful enough to ionize the air, and was replaced for safety concerns. A second periscope system is used to translate the laser light up to an inverted breadboard that is attached to a structural beam. The upper breadboard features two mirrors that can be used to "walk" the laser light through the pipe and is critical for alignment. The optics of the upper area of the BECOLA laser room are shown in Figure 4.25.

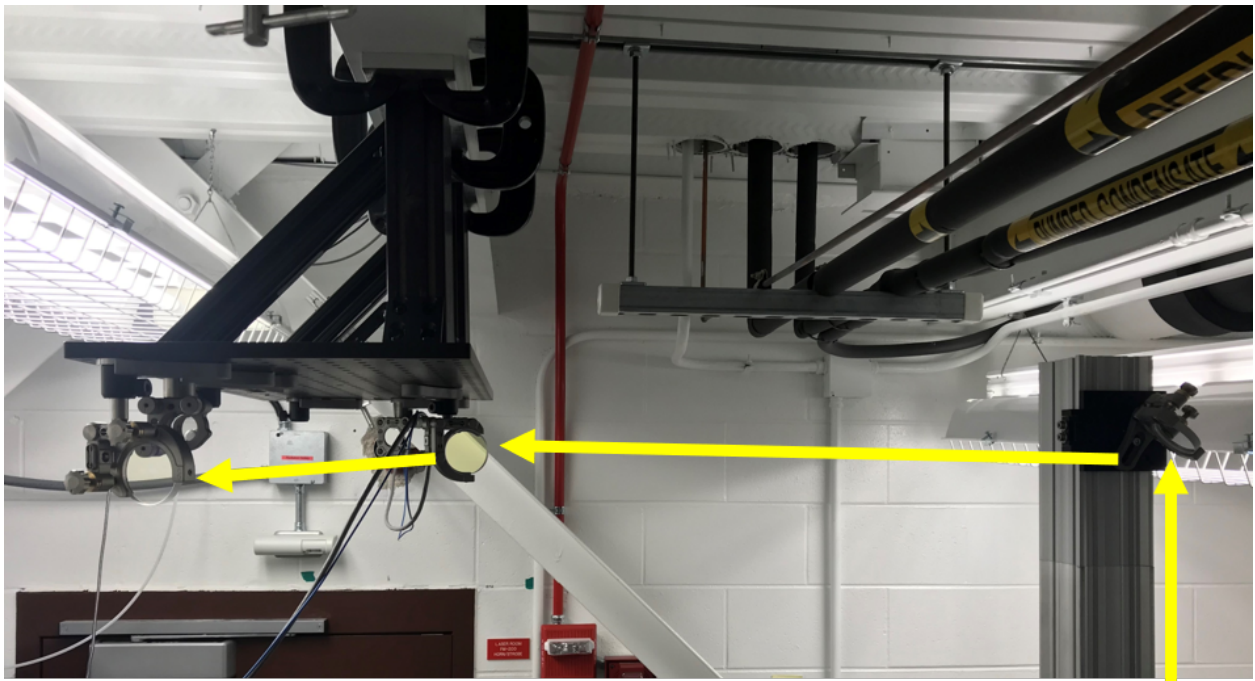


Figure 4.25: Optical layout of the inverted breadboard in the BECOLA laser area. The light is translated to the breadboard by a pair of mirrors used as a periscope. The light is reflected by two mirrors which can be used for alignment through a 10 m long pipe to the BECOLA experimental area.

In the BECOLA experimental area, the 10-m long pipe is attached to a pulsed laser safety box, which features one mirror to direct the laser light down into a second laser safety

box. In the lower pulsed laser safety box, the light is prepared for injection to the beamline and RFQ ion trap. The optical layout of the lower laser safety box is shown in Figure 4.26.

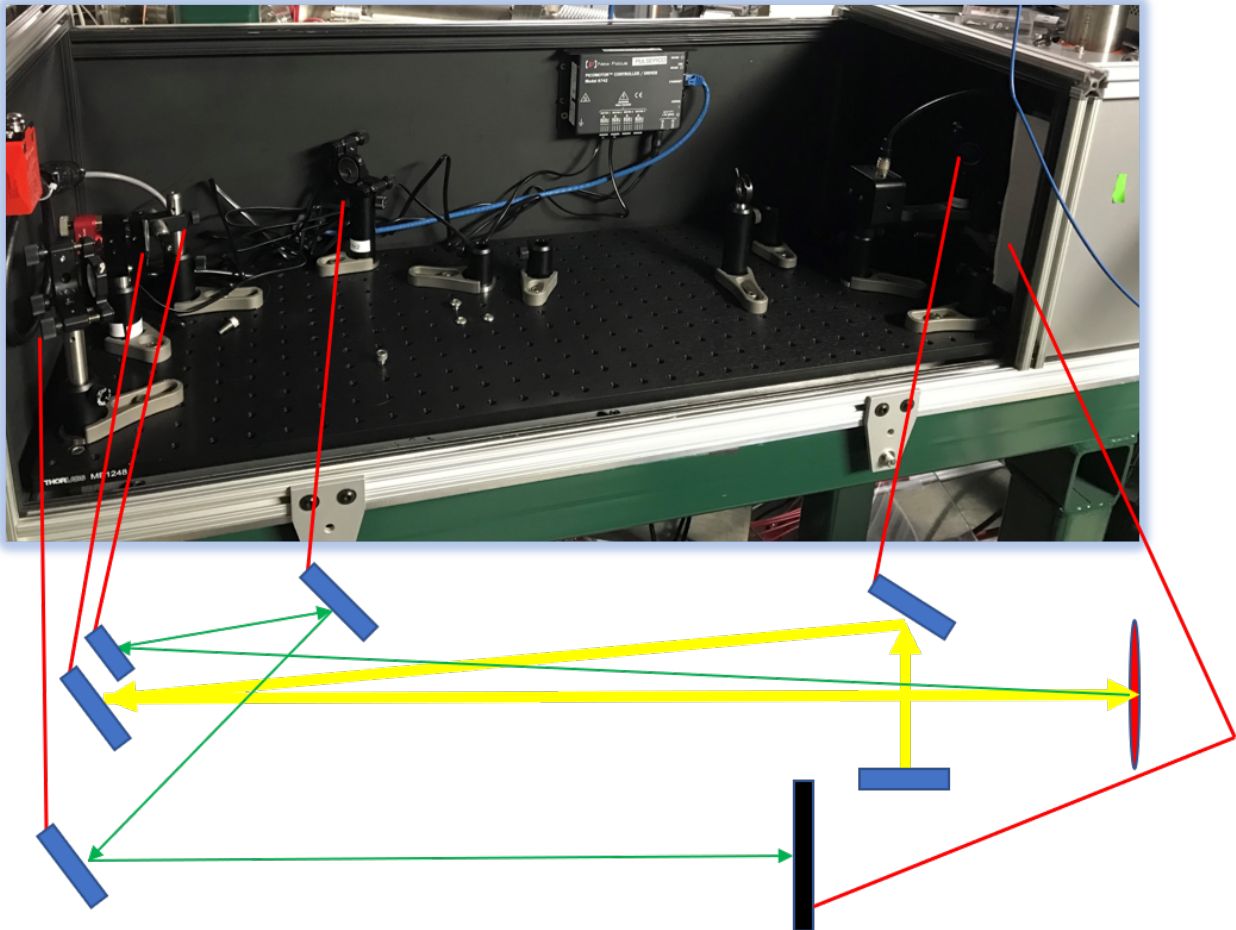


Figure 4.26: Optical layout of the pulsed laser safety box used to prepare the pulsed laser light for injection into the RFQ ion trap. The light is translated down to the safety box from the 10 m long pipe using a pair of mirrors used as a periscope. The light is reflected by two mirrors which can be used to align the laser light through the RFQ ion trap. The diagram below shows the laser light path in yellow and the reflected light path in green, mirrors are blue ovals, the backstop is black, and the wedged window is a red oval. The red lines indicate where the optical elements are located in the photograph.

There are three mirrors in the lower laser safety box, one is part of a periscope system to translate the laser light from the 10-m long pipe to the lower laser safety box, and two are used for alignment through the RFQ ion trap. The laser light is injected into the RFQ ion trap through a 2 degree wedged glass window, which reflects a small fraction of the beam.

A backstop was installed in the safety box, situated such that the back reflection from the wedged window could be picked off by a small 1/2" mirror and sent to the backstop. The beam path of the back reflection was 2.44 m, a distance equal to the RFQ trapping region from the wedged window. During operation, it is not possible to observe the beam spot at the trapping region or test the alignment through the RFQ ion trap. The back reflection serves as both an alignment tool and way to monitor the beam. During the initial alignment procedure, a flange with a glass window replaced the PIG ion source and the laser light was aligned through the full length of the RFQ ion trap. The beam spot on the backstop was used to mark the correct position for alignment, as well as two irises in the main beam path. During operation, the laser light path can be adjusted to pass through the irises and to the marked spot on the beam backstop, ensuring that the laser light is properly irradiating the trapping region.

#### **4.3.2.4 Stability**

Measurements of the stability of the free-space light transport system were performed to determine if active adjustment systems were necessary to ensure overlap between the pulsed laser light and the trapping region is maintained. The stability measurements were performed with laser light from the BECOLA CW laser system and assumes that the stability of the light transport system is independent of the qualities of the laser light. Movement of the laser light over a period of time was measured on a CCD camera at different locations in the free-space light transport system. The centroid of the laser beam was tracked over a period of 25 minutes, with the data shown in Figure 4.27

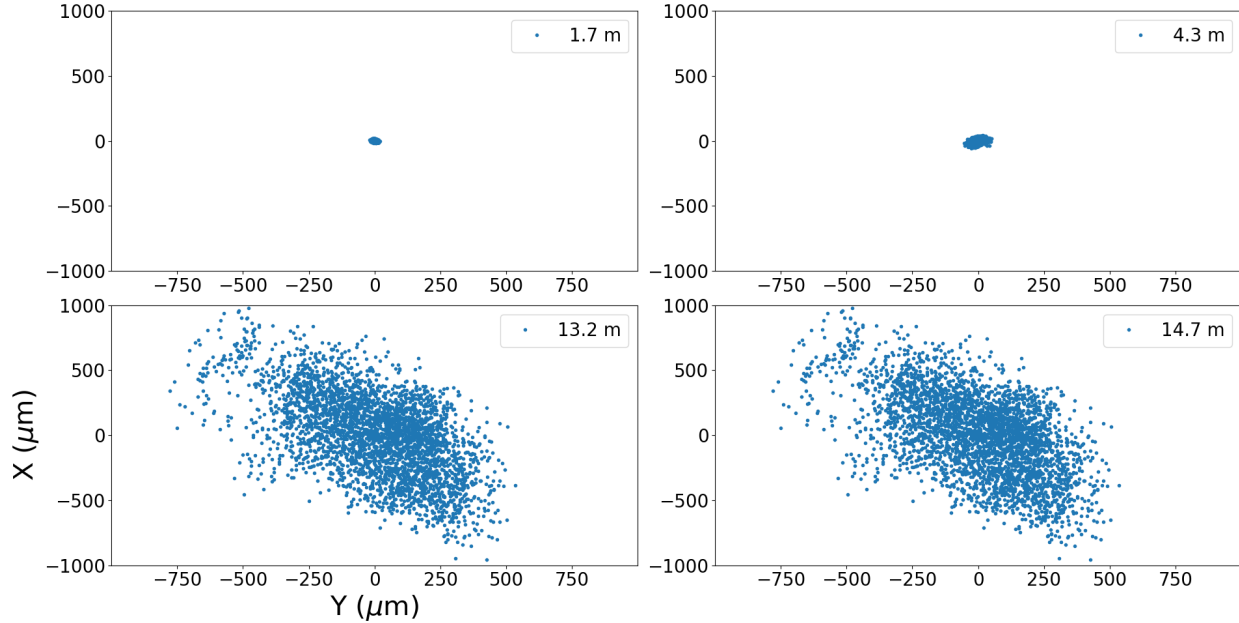


Figure 4.27: Center of laser beam tracked across 25 minutes at four different locations. Each set of data is relative to the average position of the laser light. The data was collected at four locations, on the laser table, at the entrance of the steel pipe connecting the BECOLA laser and experimental areas, at the exit of the steel pipe, and in the lower laser safety box before injection into the beamline. Although movement of the beam is small in the BECOLA laser room, the laser light moves on the order of millimeters by the end of the free-space light transport system.

The stability of the laser beam was measured at four locations, on the laser table (1.7 m from laser), at the entrance of the steel pipe connecting the BECOLA laser room and experimental area (4.3 m from laser), at the exit of the steel pipe (13.2 m from laser), and in the lower laser safety box before injection into the beamline (14.7 m from laser). The standard deviation of the laser light position is shown in Table 4.2. The results of the measurements show that the position of the laser light can fluctuate on the order of a few mm in the distance from the BECOLA laser room to the experimental area. The level of movement does not impact the overlap of the pulsed laser light and the trapped ions, but is concerning for the use of CW laser light transport. The stray light background is dependent on the position of the CW laser beam and the laser beam must pass through two apertures

Table 4.2: Standard deviation of the relative laser light position at four locations. The data was collected at four locations, on the laser table, at the entrance of the steel pipe connecting the BECOLA laser and experimental areas, at the exit of the steel pipe, and in the lower laser safety box before injection into the beamline.

Location	Distance (m)	Standard Deviation ( $\mu\text{m}$ )
Laser Table	1.7	6
Entrance of Aluminum Pipe	4.3	19
Exit of Aluminum Pipe	13.2	337
Lower Laser Safety Box	14.7	337

before the photon detection region. The apertures themselves can be as small as 3 mm and small movements of the laser beam position can result in the laser light clipping the alignment apertures and greatly increased the background.

#### 4.3.2.5 Safety System

Pulsed laser light has a high energy density and can be very dangerous. The BECOLA pulsed laser system is a Class IV laser system. The light from the pulsed laser is dangerous to the eyes under all conditions, can be dangerous to the skin, and can pose a fire hazard. It is important that the free-space light transport system features robust safety systems to prevent unexpected exposure to the pulsed laser light during operation. The new laser safety boxes were installed with two interlock systems. The weight of the lids of the boxes depresses a trigger, sending a signal to the safety system that the boxes are closed and laser light can be safely sent through the system. Screws are used to lock the lids in place, but if the lids are lifted while the light is being transported, the safety interlock activates and closes two physical shutters to block the laser light and prevent exposure. The shutters were placed immediately after the pulsed laser output and in the upper laser safety box of the BECOLA experimental area, where it can block the light immediately after exiting the steel pipe used

Table 4.3: Natural abundances of the stable isotopes of Zr.

Mass number	Natural Abundance (%)
90	51.45%
91	11.22%
92	17.15%
94	17.38%
96	2.8%

to contain the laser light between the BECOLA laser and experimental rooms.

The safety system features an override, where a key is used to unlock the system and allow the physical shutters to be opened while the safety box lids are off, and is used for alignment. New safety screens consisting of heavy canvas sheets were installed around the boxes to enclose the area and prevent light from leaving a prescribed area.

## 4.4 Experimental Method

The goal of the commissioning experiments was to demonstrate that the electronic populations of ions trapped in the BECOLA RFQ ion trap can be manipulated using optical pumping as predicted by the optical pumping simulation.

### 4.4.1 Choice of Zr Ion

Zr<sup>+</sup> ions were chosen as the element that would be used to demonstrate the optical pumping technique. As detailed in Chapter 1, studies of Zr are important from both a nuclear structure and stockpile stewardship perspective. Additionally, the transitions of interest for Zr are accessible to both the pulsed and CW laser systems. Zr cathodes were acquired from ACI Alloys [101] and were made of natural Zr. The natural abundances of the stable Zr isotopes are detailed in Table 4.3.

The PIG ion source was able to readily produce  $Zr^+$  beams as discussed in Chapter 4.2.1. A partial electronic level diagram of  $Zr^+$  is shown in Figure 4.28. Zr is a  $d$ -block element, and has a high electronic level density.

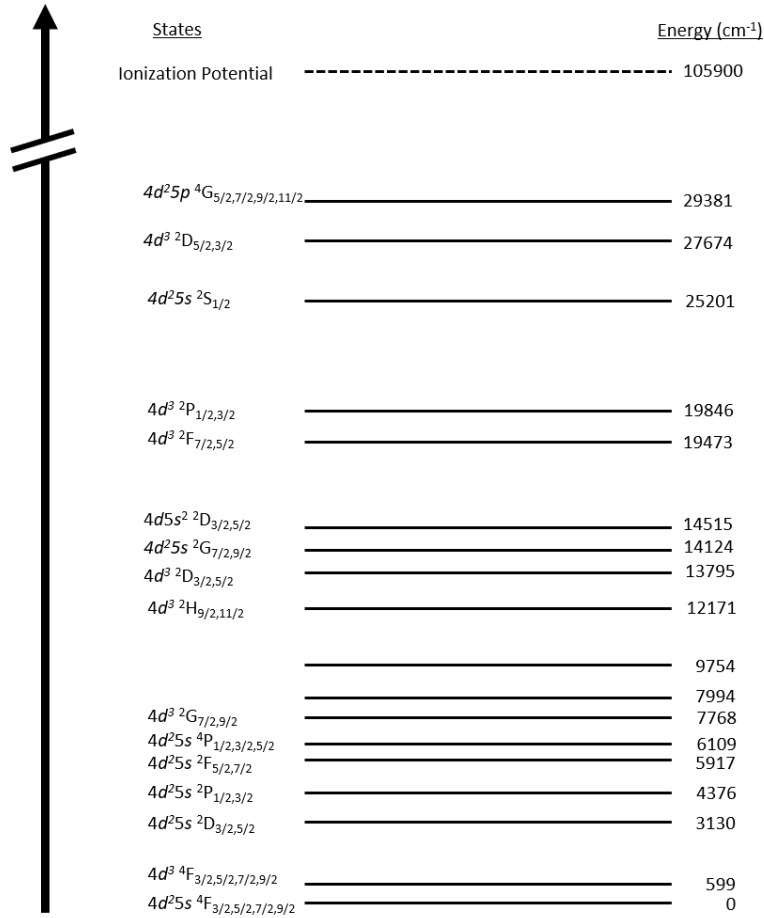


Figure 4.28: Partial electronic states of  $Zr^+$  [76]. The hyperfine levels of each electronic state are not shown, as the level density of  $Zr^+$  is very high.

At room temperature, only the first electronic level is appreciably populated, with the level split into four fine lines located at 0, 314,763, and 1322  $cm^{-1}$  respectively. Only the first three fine levels are appreciably populated, with approximately 72.3% in the ground state  $^4F_{3/2}$ , 23.9% in the first excited state  $^4F_{5/2}$ , and 3.7% in the second excited state  $^4F_{7/2}$ .

## 4.4.2 Transition Schemes

The optical pumping simulation discussed in Chapter 4 was used to determine the optical pumping schemes for  $\text{Zr}^+$ . Based on the simulation, two optical pumping schemes were chosen for the commissioning experiments. Both optical pumping schemes utilized the  $4d^25p\ ^4G_{5/2}$  state as the excited state. For the case of  $\text{Zr}^+$ , the branching ratios and transition probabilities of excited states in the Kurucz database were theoretically calculated. The calculations are based on calibrations of free-burning arc sources [102]. Additionally, experimental data for the decay of  $\text{Zr}^+$  was not available in the NIST database. In the literature, an experimental determination of the lifetime and branching ratios from the  $4d^25p\ ^4G_{5/2}$  was found from astrophysical observations [103]. The excited state has a lifetime of 7.1(3) ns, compared to the Kurucz prediction of 8.5 ns. The branching ratios to the low-energy metastable states were significantly different, and a comparison between the experimental data and Kurucz predictions are shown in Table 4.4.

The difference between the experimental and theoretical branching fractions to the low-energy metastable states has a significant impact on the expected optical pumping effect and is discussed later in this Chapter.

Table 4.4: Decay branches and transition probabilities from the  $4d^25p\ ^4G_{5/2}$  state of  $Zr^+$ , comparing theoretical calculations from the Kurucz database [75] with experimental results from [103]. The theoretical predictions included decays to three states that were not observed experimentally, and are marked as '-'.

Ground State ( $\text{cm}^{-1}$ )	Experimental Branching Ratio	Experimental Einstein Coefficient ( $\text{s}^{-1}$ )	Theoretical Branching Ratio	Theoretical Einstein Coefficient ( $\text{s}^{-1}$ )
0	0.668	$9.4 \times 10^7$	0.494	$5.8 \times 10^7$
314	0.16	$2.2 \times 10^7$	0.248	$2.92 \times 10^7$
763	0.004	$5.6 \times 10^5$	0.044	$5.2 \times 10^6$
2572	0.042	$5.9 \times 10^6$	0.042	$4.9 \times 10^6$
2895	-	-	0.015	$1.7 \times 10^6$
4248	0.041	$5.7 \times 10^6$	0.044	$5.2 \times 10^6$
4505	0.028	$3.9 \times 10^6$	0.039	$4.5 \times 10^6$
5752	0.051	$7.2 \times 10^6$	0.065	$7.6 \times 10^6$
7836	-	-	0.004	$4.51 \times 10^5$
14059	-	-	0.006	$6.8 \times 10^5$

#### 4.4.2.1 Depopulation of the Ground State

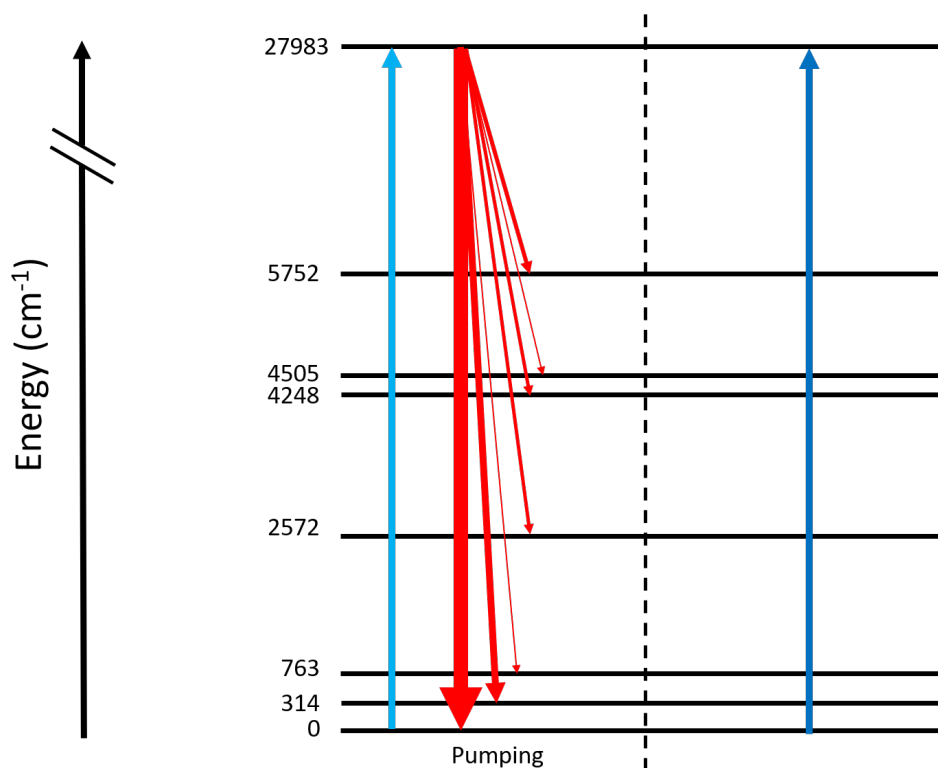


Figure 4.29: Optical pumping scheme for the depopulation of the ground state of  $Zr^+$ . Ions from the ground state are excited to the  $4d^25p\ ^4G_{5/2}$  state. Approximately 32% of ions decay to metastable states that are dark to subsequent CLS measurements, reducing the sensitivity.

The first optical pumping scheme was chosen to depopulate the ground state of  $Zr^+$  and can be seen in Figure 4.29. Ions in the ground state are excited to the  $4d^25p\ ^4G_{5/2}$  state. A significant proportion of the ions in the excited state will decay to low-energy dark metastable states and will be inaccessible to the subsequent CLS measurement that probes the ground state using the same  $4d^25s\ ^4F_{3/2}$  to  $4d^25p\ ^4G_{5/2}$  transition used for the optical pumping step. The predicted change in electronic population of the ground state is dependent on branching ratios from the excited state. Using the Kurucz theoretical calculation,  $(44.1 \pm 3)\%$  decrease in the electronic population is expected, while a  $(31.9^{+4}_{-3})\%$  decrease in the electronic population is expected if the experimental branching ratios are considered.

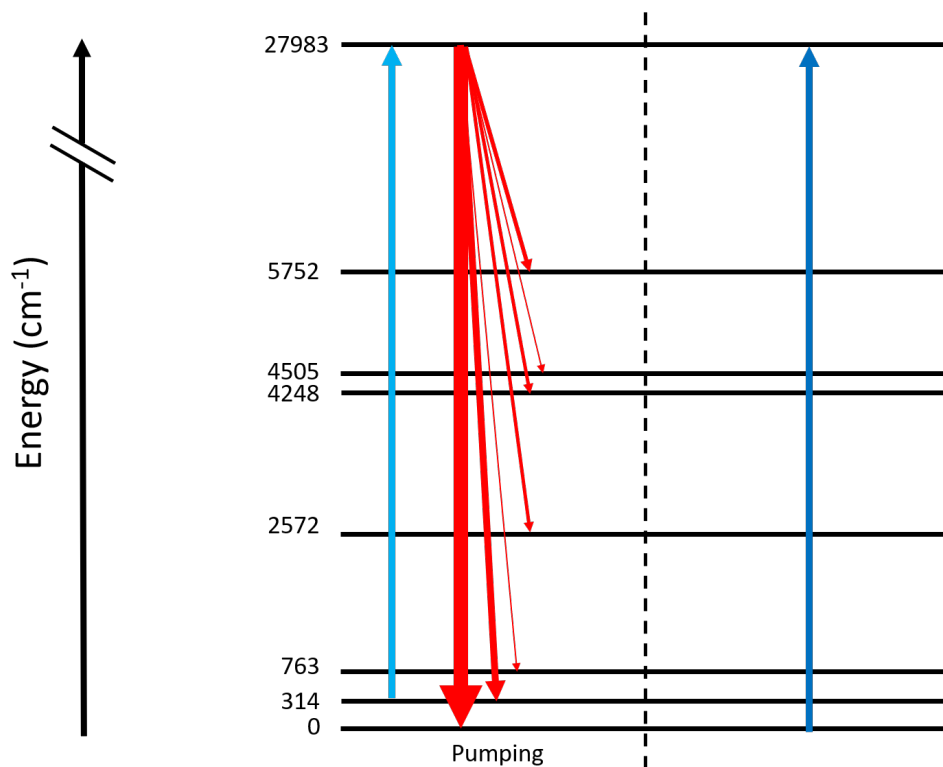


Figure 4.30: Optical pumping scheme for the augmentation of the ground state of  $\text{Zr}^+$ . Ions from the first excited state are excited to the  $4d^25p\ ^4G_{5/2}$  state. Approximately 66% of ions decay to the ground state, increasing the sensitivity of subsequent CLS measurements.

A second transition was used to verify the depopulation of the ground state, by probing the change in the electronic population of the first excited state of  $\text{Zr}^+$ . The pumping step of the optical pumping scheme remains the  $4d^25s\ ^4F_{3/2}$  to  $4d^25p\ ^4G_{5/2}$  transition, but the transition used to probe the electronic population manipulation excites ions from the first excited state at  $314\text{ cm}^{-1}$ , using the  $4d^25s\ ^4F_{5/2}$  to  $4d^25p\ ^4G_{5/2}$  transition. The optical pumping simulation estimates a  $(65\pm 6)\%$  increase in the population of the first excited state based on the theoretical branching ratios and a  $(48\pm 9)\%$  increase in the electronic population using the experimental branching ratios.

#### 4.4.2.2 Augmentation of the Ground State

The second optical pumping scheme was chosen to augment the population in the ground state, and can be seen in Figure 4.30. Ions in the first excited state  $4d^25s\ 4F_{5/2}$  at  $314\text{ cm}^{-1}$  are excited to the  $4d^25p\ 4G_{5/2}$  state. Although the majority of the ions will decay back to the ground state of  $\text{Zr}^+$ , the total population of the state being pumped is relatively small and only a modest increase in the electronic population of the ground state is expected. A  $(8.3\pm 1.5)\%$  increase in the electronic population of the ground state is expected using the theoretical branching values from the Kurucz database. A  $(14.8\pm 1)\%$  increase in the electronic population of the ground state is expected using the experimental branching ratios.

#### 4.4.3 Measurement Method

In a typical CLS measurement, the laser-resonant photon counts are measured as a function of the scanning voltage to determine the resonance frequency. The goal of the commissioning experiments was to determine the ability to manipulate the electronic populations using optical pumping, and a different strategy was used for efficient and reliable measurements.

##### 4.4.3.1 Timing Sequence

The commissioning experiments were not performed to measure the resonance frequency of the optical transition for  $\text{Zr}^+$ . Instead, interest was on the overall change in signal with and without optical pumping. The scanning voltage used to Doppler shift the ion beam was set to remain in resonance at all times. A physical shutter was used to block the pulsed laser beam for short increments of time, and the fluorescence signal was measured as a function of whether the pulsed laser was blocked or not. The measurements with and without the

pulsed laser light were performed in alternating, 1 second intervals. This method of data collection was aimed to control systematic fluctuations in the laser power and ion source intensity and mitigate any systematic uncertainties.



Figure 4.31: Optical pumping scheme for the augmentation of the ground state of  $\text{Zr}^+$ . Ions from the first excited state are excited to the  $4d^25p\ ^4G_{5/2}$  state. Approximately 66% of ions decay to the ground state, increasing the sensitivity of subsequent CLS measurements.

The physical shutter was controlled using a signal from the BECOLA Data Acquisition (DAQ) system [2]. A trigger signal from the flash lamp of the pulsed laser system was used to start the DAQ process. A one-second period of time was chosen to alternate between performing optical pumping and not performing optical pumping. The physical shutter can reliably open and close in one second increments. It is assumed that changes in the ion source and laser power intensity occur over many seconds or minutes and can be safely ignored in the data analysis. As the pulsed laser has a 10 Hz repetition rate with each laser pulse separated by 100 ms, each interval will consist of ten measurements of the fluorescence with the pulsed laser irradiating the trapped ions followed by ten measurements of the fluorescence with the pulsed laser blocked by the shutter. The 10 Hz trigger signal from the pulsed laser flash lamp was converted to an alternating 0.5 Hz signal to control the shutter. The process to convert the electronic signal is shown in Appendix B.

### 4.4.3.2 Determination of Optical Pumping Effect

Measurements were made of the number of photons as a function of both time and the shutter status. An example of the data for one run is seen in Figure 4.32.

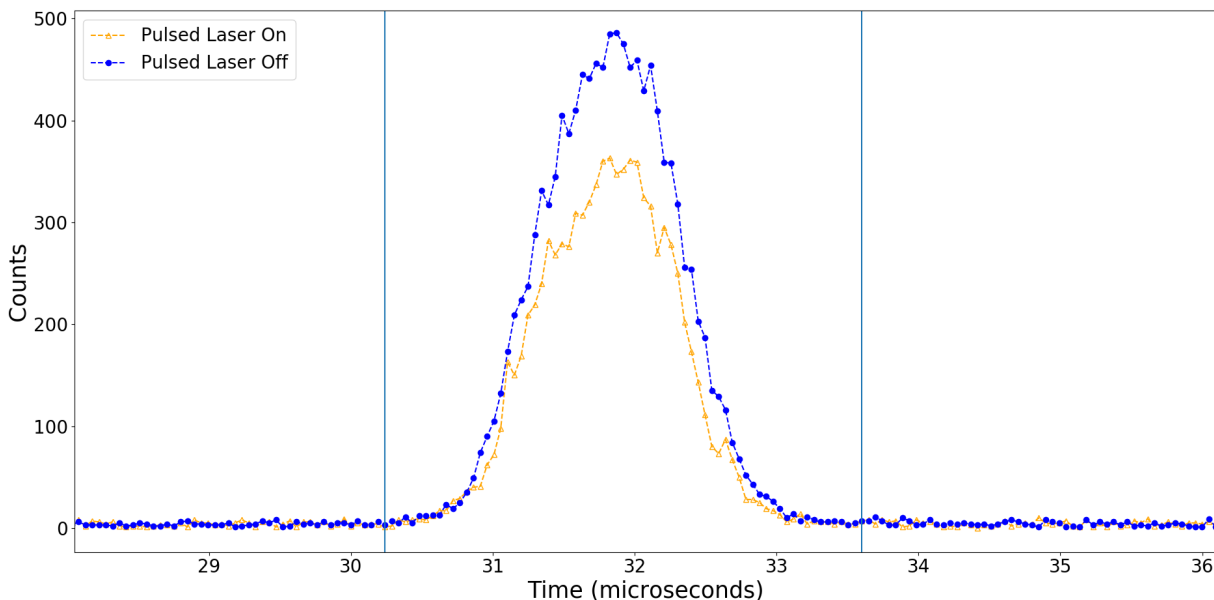


Figure 4.32: Example of optical pumping data, pumping ions from the ground state with the  ${}^4F_{3/2}$  to  ${}^4G_{5/2}$  transition of  $\text{Zr}^+$ . As the ion bunch passes the PMTs at approximately  $30 \mu\text{s}$ , the fluorescent photons are captured. The photon counts were measured as a function of time and shutter status. A time gate was applied to remove background. The time gate is shown as vertical lines around the peak.

The ions were released in approximately  $1 \mu\text{s}$  bunches in a repetition rate of 10 Hz. The time-of-flight of the ion bunch to the interaction region was approximately  $32 \mu\text{s}$  and a time gate was applied to the data to exclude photon counts outside of the arrival of the ion bunch. Photon counts within the time gate were integrated to obtain the total signal as the ion bunch passed the interaction region. A background subtraction was performed by taking an average of the signal in each time bin outside of the time gate.

The results of the optical pumping measurement will be reported henceforth as the optical pumping effect. The optical pumping effect is the percent change in fluorescent signal of the

ion bunches that are irradiated with pulsed laser light relative to the fluorescent signal of ion bunches of the same measurement that are not irradiated by pulsed laser light. The optical pumping effect,  $P$  is determined by,

$$P = \left( \frac{S_{OP}}{S_{NoOP}} - 1 \right) 100 \quad (4.15)$$

where  $S_{OP}$  is the fluorescent signal with optical pumping and  $S_{NoOP}$  is the fluorescent signal without optical pumping, both with the background signal subtracted. The fluorescent signal is directly related to the electronic population of the state being probed, and it is assumed that the proportional change in signal is the same as the proportional change in the electronic state being probed by CLS.

# Chapter 5

## Results

The commissioning experiments of the optical pumping technique were performed at the BECOLA facility. A stable beam of  $\text{Zr}^+$  ions was produced by the BECOLA PIG ion source. Ions trapped in the BECOLA RFQ ion trap were irradiated with pulsed laser light and the resulting re-distribution of the electronic population was measured with a subsequent CLS measurement. Two different optical pumping schemes were explored. The results of the commissioning experiments are described in this chapter.

### 5.1 Properties of Optical Pumping in the RFQ Ion Trap

The optical pumping technique was applied to  $\text{Zr}^+$  ions captured in the BECOLA RFQ ion trap. Initial measurements were performed to identify ideal conditions for pumping experiments, including laser beam size, laser power, and the overlap of the laser and the spectral absorption linewidths.

#### 5.1.1 Laser Beam Size

Initial tests were performed with the pulsed laser focused to the trapping region, with a laser beam of 1 mm diameter. The laser light was scanned across the trapping region of the RFQ

ion trap by adjusting the angle of the final mirror in the pulsed laser optics system, using piezo electronics driven linear actuators produced by Newport [104]. The actuators will be henceforth referred to as picomotors. Adjustment of the laser position with the picomotors was performed to ensure good overlap between the trapped ions and laser beam. The mirror mount with the picomotors has an angular resolution of  $0.7 \mu\text{rad}$ , and as the mirror is located 3.7 m away from the trapping region, the resolution of each step of the picomotors was  $2.5 \mu\text{m}$  in comparison with the expected diameter of the trapped ions of 2.8 mm (See Section 3.2.1).

An attempt was made to measure the size of the trapped ion distribution by scanning the laser across the trapping region. Hysteresis of the picomotor was observed, where the number of motor steps to move the laser beam to a position was different from the number of steps required to return the laser beam to its original position. The laser beam was scanned in one direction across the trapped ions to try and mitigate the hysteresis effect, and to approximate the size of the trapped ions by observing the optical pumping effect at each location. The measurement was performed with the pulsed laser power set to 6 mW. Results are shown in Figure 5.1.

The optical pumping effect as a function of the pulsed laser light position was fitted to a Gaussian lineshape and the standard deviation was  $(1.4 \pm 0.1)$  mm, with 95% of the distribution within a  $(2.8 \pm 0.2)$  mm radius. Assuming that the trapped ion distribution is spherical in shape and that the laser beam profile is circular, the optical pumping effect will reach zero when the distance between the center of the laser beam and the center of the trapped ion distribution is equal to the sum of the radii of the laser beam and trapped ion distribution. Since the radius of the laser beam is known, the size of the trapped ion distribution can be determined. The radius of the laser beam was 0.5 mm, leading to an

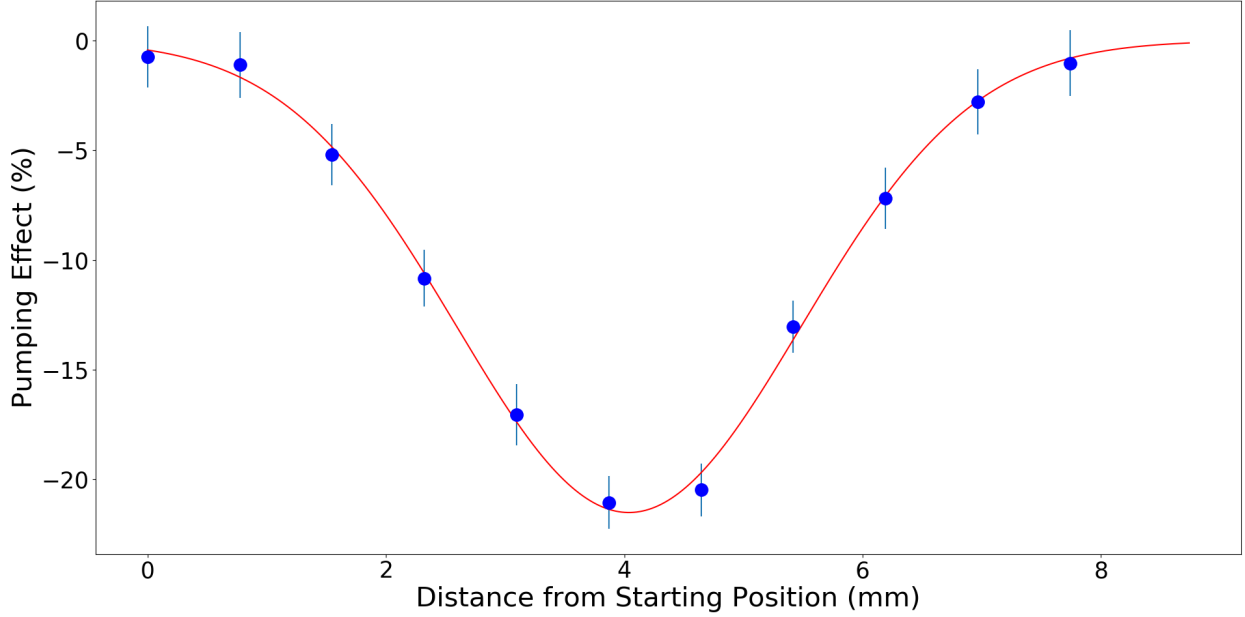


Figure 5.1: Optical pumping effect as a function of pulsed laser beam position. The pulsed laser light was moved off of the trapped ions and scanned in one direction across the trapped ions to approximate its size.

trapped ion distribution radius of  $(2.3 \pm 0.2)$  mm. A simulation of the trapped ion conditions in the BECOLA RFQ ion trap was performed using the 3DCylPIC software [80] and discussed in Chapter 3. The results of the simulation provided an estimate that 95% of the trapped ions could be found within a 1.4 mm radius of the center of the trapping region.

An unexpectedly large optical pumping effect of up to -79% was observed while the laser beam was focused to a small diameter and at high powers, as shown in Figure 5.2. Even if 100% of the ions were excited by the pulsed laser light, based on either the branching ratios of the excited state from Ljung *et al.* or the theoretical values from the Kurucz database, the optical pumping effect should not rise above 51%. It is believed that the high energy density of the pulsed laser light disrupted the ion trap. Other explanations for this behavior are that the laser light could have been focused onto one of the RFQ rods and disrupted the RF field, or it is also possible that the laser light forced ions to be expelled from the

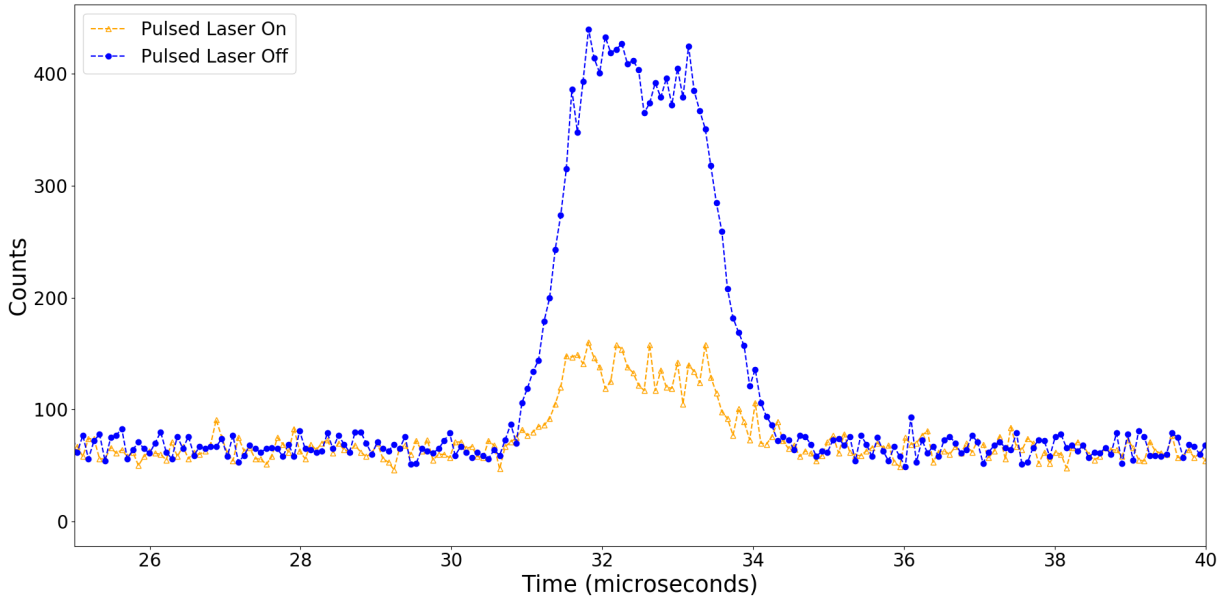


Figure 5.2: Spectra of fluorescent photon counts as a function of time, with and without optical pumping. The measurement was performed with a tightly focused laser beam and high laser power and the optical pumping effect is much larger than expected.

bunch. The measurement of the optical pumping effect is dependent on the assumption that the number of ions in the RFQ ion trap does not change due to the laser, and cannot discriminate between a change in the electronic population and a change in the number of ions in the ion trap.

The focus of the pulsed laser light was adjusted to increase the size of the laser beam at the trapping region after measurements of the trapped ion distribution were complete. The beam spot at the trapping region was elliptical in shape and approximately 7 mm in diameter along the major axis and 5 mm in diameter along the minor axis. The optical pumping effect was insensitive to scanning of the picomotor after increasing the laser beam size, indicating that the trapping region was fully illuminated. The unexpectedly large attenuation of the fluorescence signal was not observed at the maximum laser power of 120 mW with the larger laser beam. All subsequent measurements were performed with the larger laser beam

diameter.

### 5.1.2 Laser Power

Saturation of the transition for optical pumping is important to provide the largest possible improvement in sensitivity for CLS measurements. The Cobra-Stretch laser system is capable of producing light down to 196 nm with the energy per pulse decreasing with the wavelength. At 357 nm, the laser system is capable of producing approximately 12 mJ per pulse, or 120 mW as the pulsed laser has a repetition rate of 10 Hz. The optical pumping effect was measured as a function of the laser power to determine if the optical transition can be fully saturated by the pulsed laser light.

The saturation curve was measured with laser beams of two diameters, a smaller laser beam of 1 mm in diameter, and a larger elliptical beam with a major axis diameter of 7 mm and a minor axis diameter of 5 mm (See Section 4.2.2 for more detail). The laser power was measured immediately after the pulsed laser system. The transmission through the free-space light transport system was approximately 65%. The saturation curve was fit using the function,

$$I = A \frac{P}{P + P_{sat}} \quad (5.1)$$

Where  $I$  is the pumping effect,  $A$  is a constant,  $P$  is the laser power, and  $P_{sat}$  is the saturation power.

The saturation curve measured using the smaller 1 mm diameter laser beam is shown in Figure 5.3. The optical pumping effect shows a departure from the expected behavior at high laser powers, where a second plateau is observed above 40 mW of laser power.

The appearance of a second curve and plateau in the optical pumping effect as a function

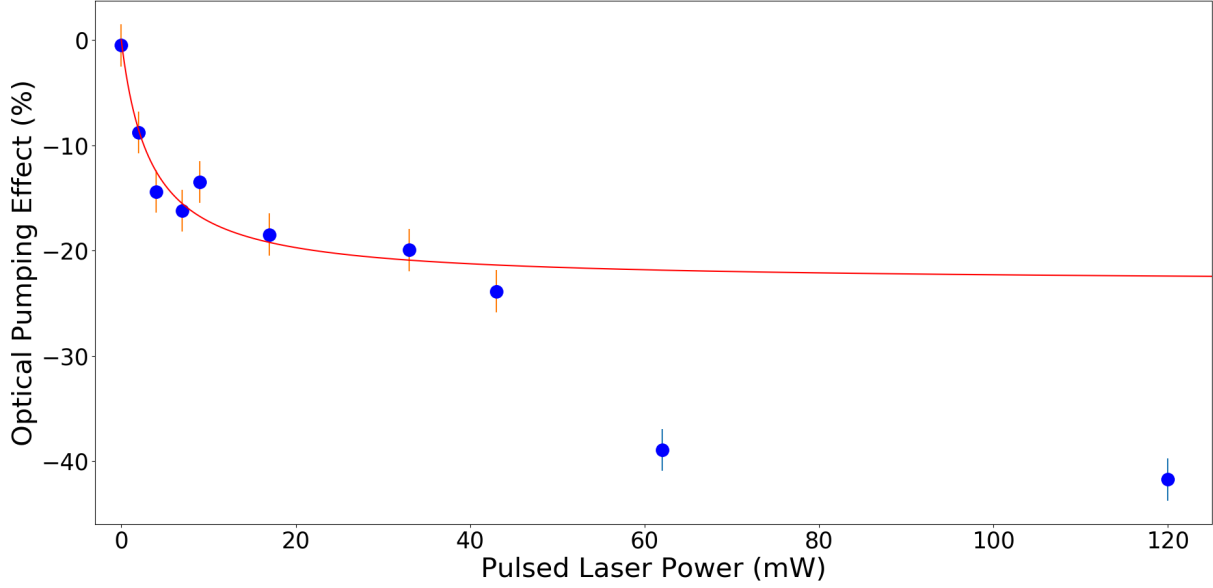


Figure 5.3: Optical pumping effect as a function of the laser power for the  ${}^4F_{3/2}$  to  ${}^4G_{5/2}$  transition in  $Zr^+$ . The transition quickly saturates, but experiences a second sharp increase in the optical pumping effect above 40 mW.

of laser power above 40 mW was unexpected in addition to observation of optical pumping effects as large as 79%, it is believed that the pulsed laser light disrupted the RFQ ion trap at very high energy densities.

The size of the laser beam was increased to try and mitigate this issue. The laser beam size was increased by adjusting the position of one of the lens of the telescope used to focus the light to the trapping region. The resulting laser beam was elliptical in shape and had a major axis diameter of 7 mm and a minor axis diameter of 5 mm. The saturation curve was measured with this larger beam size and is shown in Figure 5.4. The saturation data were fitted and the saturation power was found to be  $(3.2 \pm 0.3)$  mW. The beam area is  $110 \text{ mm}^2$ , or  $1.1 \text{ cm}^2$ , and the saturation power density was  $(2.9 \pm 0.3) \text{ mW/cm}^2$ . The pulsed laser has a temporal width of 6 ns, and with the fitted saturation power density, the peak power density is approximately  $48 \text{ MW/cm}^2$

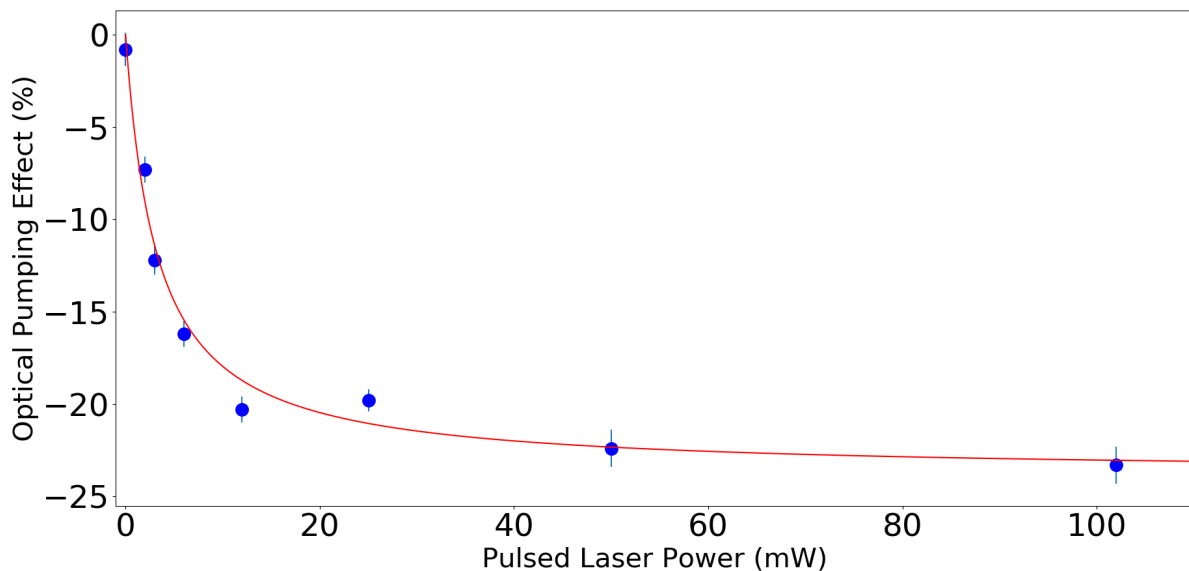


Figure 5.4: Optical pumping effect as a function of the laser power for the  ${}^4F_{3/2}$  to  ${}^4G_{5/2}$  transition in  $\text{Zr}^+$ . A fast transition, the optical pumping effect quickly saturates.

The theoretical saturation power density calculated from the Einstein coefficient of the optical transition is approximately  $8 \text{ mW}/\text{cm}^2$  (See Section 3.2.2). The experimental results show that the BECOLA pulsed laser system can readily saturate the transition.

### 5.1.3 Linewidth

As previously discussed, a major strength of CLS measurements is the ability to reduce the absorption linewidth of the optical transition to approach the natural linewidth, on the order of 10s of MHz. In the RFQ ion trap, the thermal movement of the ions results in a Doppler broadened linewidth, which is typically of the order GHz. The  ${}^4F_{3/2}$  to  ${}^4G_{5/2}$  transition of  $\text{Zr}^+$  has a natural linewidth of 22 MHz, which is broadened at room temperature to 1.1 GHz. Efficient excitation of the pumping transition requires good overlap between the absorption and pulsed laser spectral linewidths.

The absorption linewidth of the pumping transition was measured by shifting the fre-

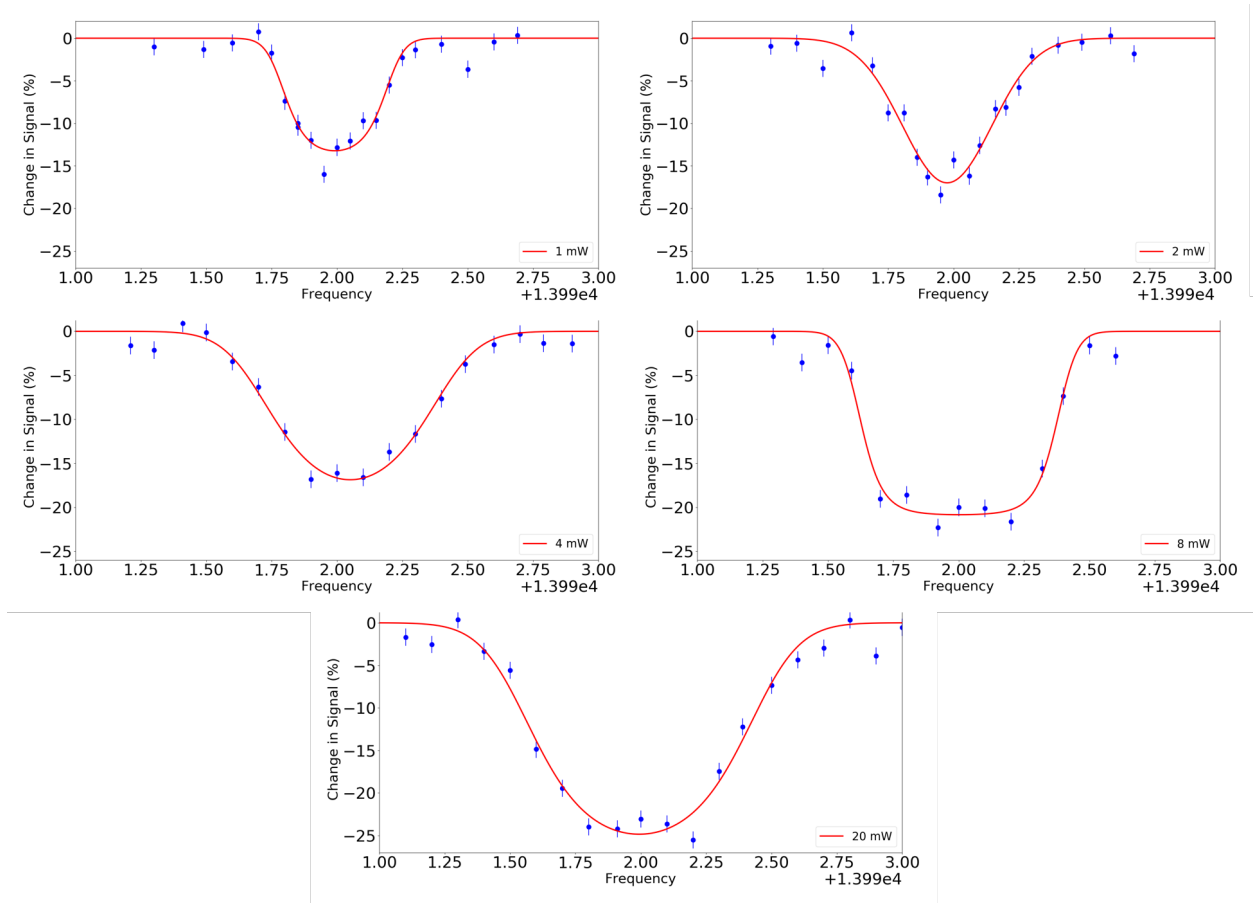


Figure 5.5: Effective absorption linewidth of the  ${}^4F_{3/2}$  to  ${}^4G_{5/2}$  transition in  $Zr^+$  at different laser powers. As the laser power increases, the transition remains saturated even as the laser moves off resonance, resulting in a flat-top spectrum.

quency of the pulsed laser light off resonance measuring the optical pumping effect via CLS. The measurement was repeated at different laser powers to observe power broadening effects, and the results are shown in Figure 5.5. The flat top feature of the spectra measured above 4 mW indicates that the transition is fully saturated even as the frequency of the pulsed laser is moved far from the resonance frequency.

A saturated Gaussian function was determined to be better suited to the data, as significant power broadening was observed. A saturated Gaussian function is often used to fit power broadened spectral profiles [105, 106, 107]. The saturated gaussian function is

Table 5.1: Effective absorption linewidth of the  ${}^4F_{3/2}$  to  ${}^4G_{5/2}$  transition in  $Zr^+$  at different pulsed laser powers.

Laser Power (mW)	Absorption Linewidth ( $cm^{-1}$ )
1	$0.44 \pm 0.02$
2	$0.49 \pm 0.02$
4	$0.68 \pm 0.02$
8	$0.69 \pm 0.02$
20	$0.68 \pm 0.02$

expressed as,

$$P = A \frac{S * e^{-\frac{(\nu-\nu_0)^2}{2w^2}}}{S * e^{-\frac{(\nu-\nu_0)^2}{2w^2}} + 1} \quad (5.2)$$

where  $A$  is an amplitude parameter,  $\nu$  is the frequency of the pulsed laser light,  $\nu_0$  is the resonance frequency,  $w$  is the FWHM of the spectral profile, and  $S$  is a saturation parameter. Significant power broadening was observed at only 4 mW of laser power. The overall magnitude of the optical pumping effect and the linewidth of the spectral profile increased with the laser power. The linewidths obtained from the fit are detailed in Table 5.1.

## 5.2 Depopulation of the $Zr^+$ Ground State

Using the measurement method outlined in Chapter 4, commissioning experiments were performed to demonstrate the ability to manipulate the electronic state population of  $Zr^+$  in the BECOLA RFQ ion trap.

Measurements were first performed to depopulate the ground state of  $Zr^+$  using the  ${}^4F_{3/2}$  to  ${}^4G_{5/2}$  transition. A  $(-31.9^{+4}_{-3})\%$  reduction in signal was expected from the optical pumping simulation based on experimental branching ratios and a  $(-44.1 \pm 3)\%$  based on the theoretical values from the Kurucz database. The depopulation of the ground state was observed

through the fluorescence signal. An example of the collected spectra is shown in Figure 5.6. The observed reduction in signal for the depopulating transition was  $(-24.6 \pm 1.6)\%$ .

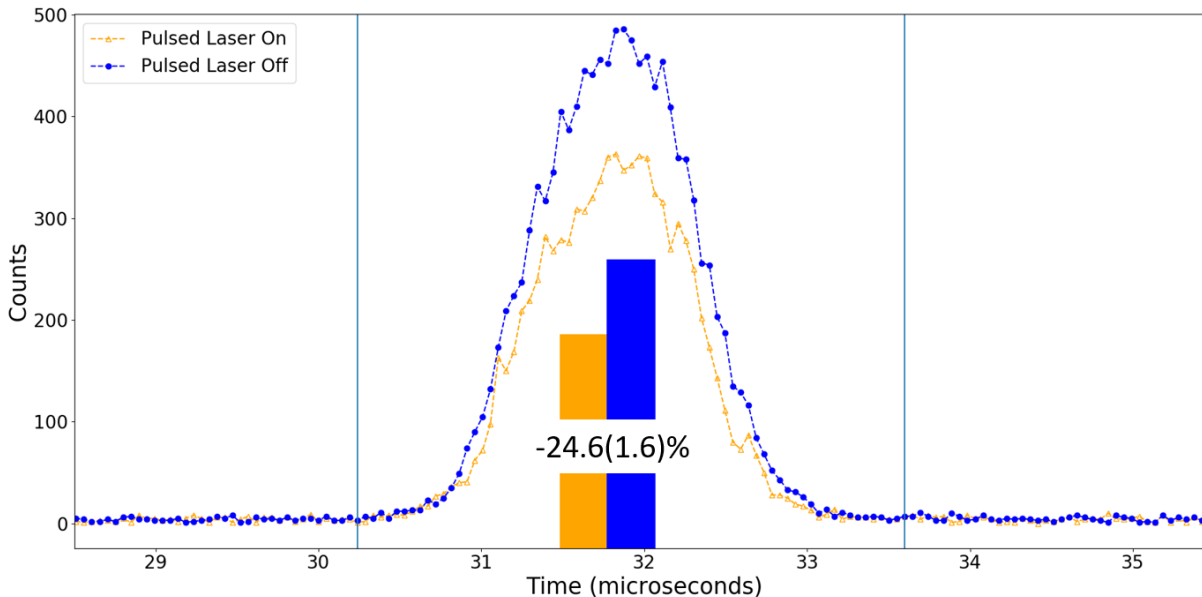


Figure 5.6: Depopulation of the ground state of  $\text{Zr}^+$  via optical pumping. The fluorescent photons are measured using CLS as a function of time. The ion beam is kept in resonance with the probe laser and alternating measurements were made with and without the pump laser.

The uncertainty is dominated by systematic error. The ion beam remains in resonance with the CW laser light during the CLS measurement, allowing for fast accumulation of photons and reducing the statistical error. The overall statistical error is not totally captured by a single measurement. The internal consistency of the measurements was used to estimate the overall statistical error by comparing the optical pumping effect observed by measurements taken under similar conditions, namely with the He buffer gas pressure set to 80 mTorr, with the laser power set to its maximum of 120 mW, and with a large laser beam. The measurement was repeated 26 times under these conditions. The overall statistical error from the counting statistics from these measurements was 0.07%. The standard deviation of the 26 measurements was used to estimate the contribution of the internal consistency to

the statistical error, and was evaluated as 1.6%.

A set of measurements was also performed that depopulated the ground state of  $\text{Zr}^+$ , but probing the change in population of the 1st excited state of  $\text{Zr}^+$  located at  $314 \text{ cm}^{-1}$ . An example of the collected spectra is shown in Figure 5.7 The 1st excited state has a room

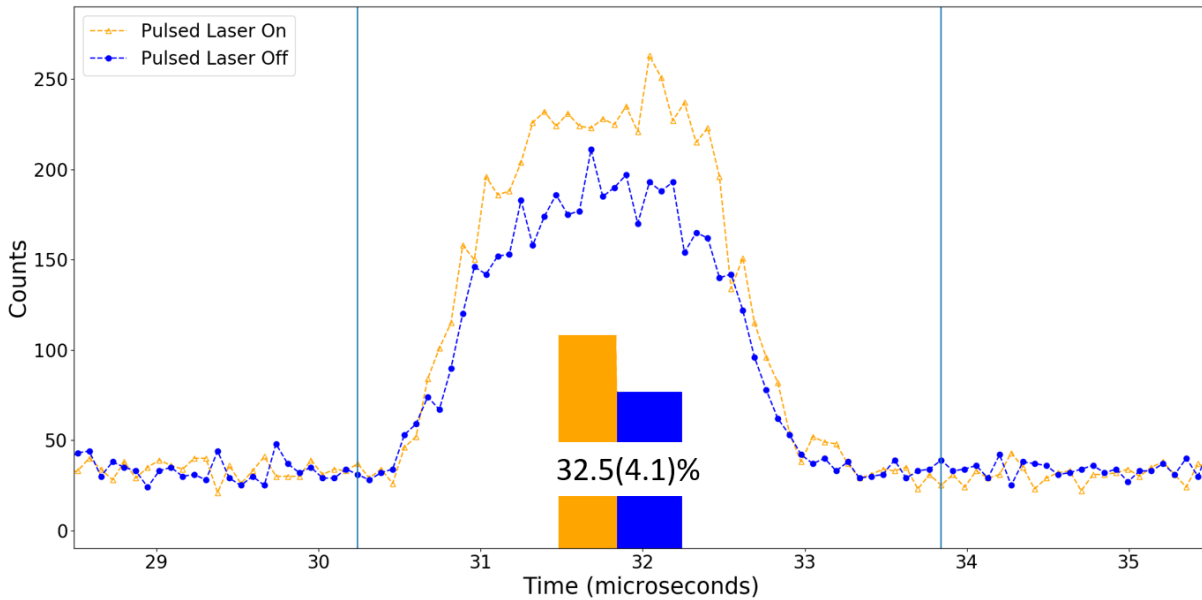


Figure 5.7: Depopulation of the ground state of  $\text{Zr}^+$  via optical pumping and probing the increased electronic population of the first excited state.

temperature population of 23.9%. Based on the experimental results of probing the ground state, it is expected that the 1st excited state population would grow by  $(36 \pm 2)\%$ . The measurement probing the 1st excited state resulted in an observed increase in the electronic state population of  $(32.5 \pm 4.1)\%$ , agreeing well with the expected value. A summary of the optical pumping effects from this section is shown in Table 5.2.

Table 5.2: Results of the depopulation of the ground state of  $\text{Zr}^+$  using the  $^4\text{F}_{3/2}$  to  $^4\text{G}_{5/2}$ . Results reported as the optical pumping effect.

Probing State ( $\text{cm}^{-1}$ )	Experiment	Expected from $^4\text{F}_{3/2}$ Results	Simulation, Ljung	Simulation, Kurucz
0	$-24.6 \pm 1.6$	-	$-31.9^{+4}_{-3}$	$-44.1 \pm 3$
314	$36 \pm 2$	$32.5 \pm 4.1$	$47.7 \pm 6$	$65.6 \pm 6$

### 5.3 Augmentation of the $\text{Zr}^+$ Ground State

The second optical pumping scheme that was studied involved exciting ions in the first excited state,  $^4\text{F}_{5/2}$  located at  $314 \text{ cm}^{-1}$ , which were optically pumped to the ground state. The overall magnitude of the optical pumping effect is smaller than the depopulating optical pumping scheme because the first excited state is populated by only 23.9% of the total electronic population. The optical pumping simulation predicts a  $(8.3 \pm 1.5)\%$  increase in the population of the ground state using the theoretical values of the branching ratios from the Kurucz database, and a  $(14.8 \pm 1)\%$  increase in the ground state population if the experimental values of the branching ratios from the excited state are used. An example of the spectra captured for the populating optical pumping scheme is shown in Figure 5.8. The observed increase in signal for the populating transition was  $12.6(2.7)\%$ . The overall statistical error of the measurement was evaluated in a similar manner, by comparing the observed optical pumping effect for many measurements performed under the same conditions. 32 measurements were compared where the He buffer gas pressure was set to 80 mTorr, with a pulsed laser power of 120 mW, and a large laser beam, and the standard deviation of the optical pumping effect was used to determine the magnitude of the error.

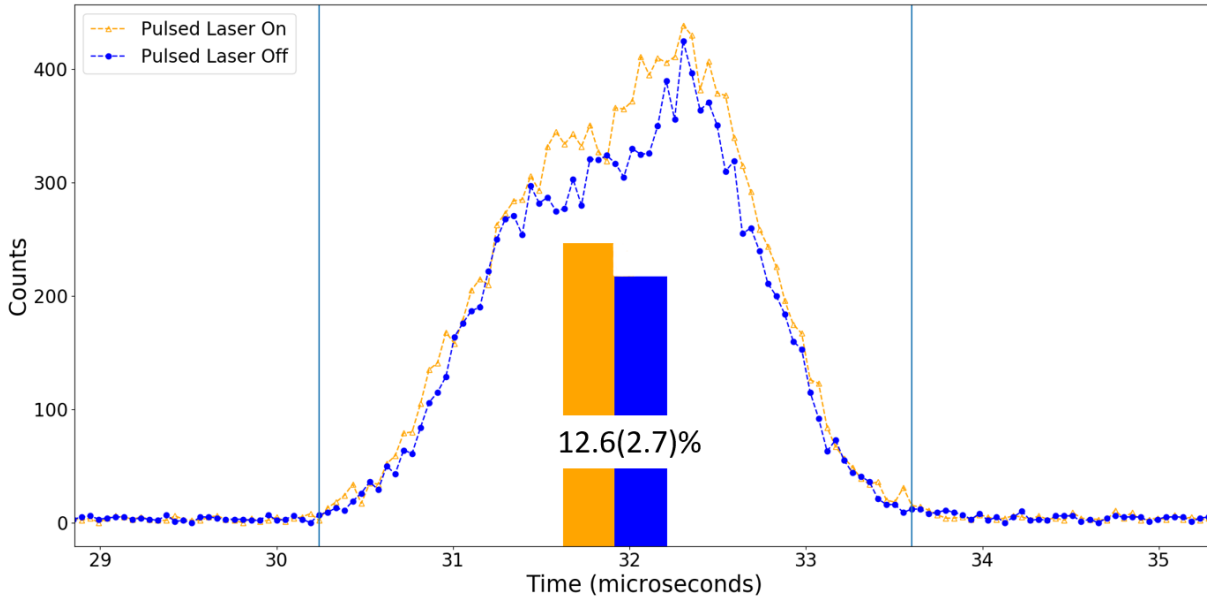


Figure 5.8: Augmented population of the ground state of  $\text{Zr}^+$  via optical pumping. The fluorescent photons are measured using CLS as a function of time. The ion beam is kept in resonance with the probe laser and alternating measurements were made with and without the pump laser.

## 5.4 Quenching of Optical Pumping

The BECOLA RFQ ion trap is capable of holding ions for up to one second with minimal loss of efficiency. The BECOLA optical pumping simulation was used to estimate the optical pumping effect after irradiating the trapped ions with multiple laser pulses. A measurement of the optical pumping effect after irradiation of the trapped ions by multiple pulsed laser pulses was attempted, but results indicated that the optical pumping effect was not enhanced by multiple laser pulses. A comparison of the simulated optical pumping effect and the experimental results is shown in Figure 5.9. Instead, it was observed that holding the trapped ions after irradiation by the pulsed laser resulted in quenching of the optically pumped electronic populations due to collisional decay with the He buffer gas in the RFQ ion trap. The quenching continued until the electronic state populations returned to thermal

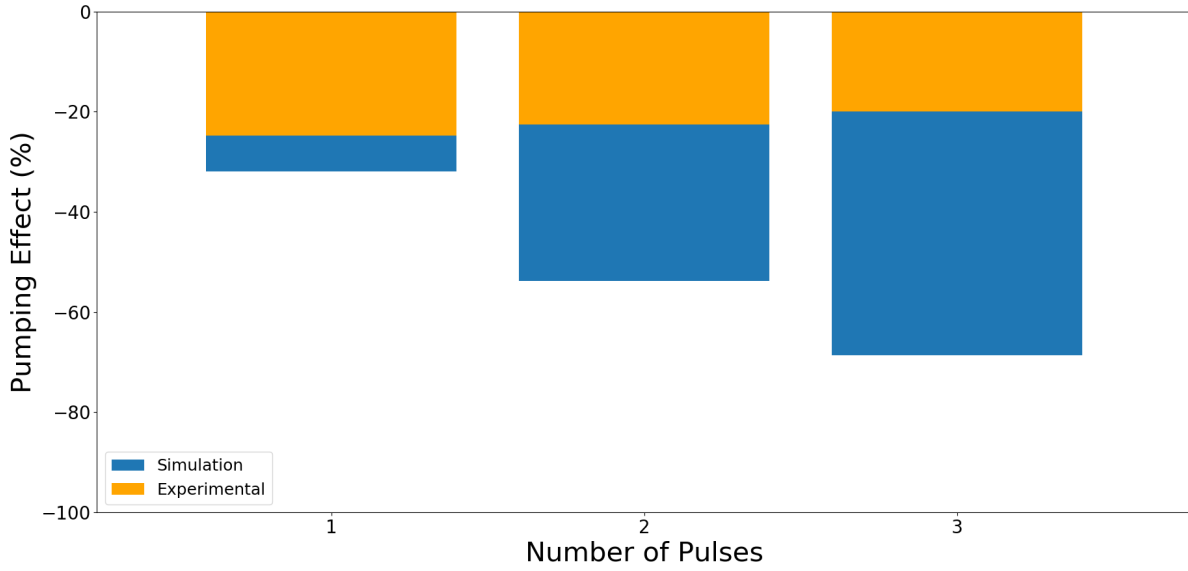


Figure 5.9: Optical pumping effect of  $\text{Zr}^+$  as a function of number of laser pulses used to irradiate the trapped ions. The blue bars show the expected optical pumping effect based on the optical pumping simulation, with the orange bars showing the experimental results. The experimental results show no enhancement of the optical pumping effect, providing evidence that collisions with the He buffer gas re-thermalize the trapped ions to a room temperature distribution.

equilibrium with the He buffer gas.

The optical pumping effect as a function of the delay time for the release of the trapped ions is shown in Figures 5.10 and Figure 5.11, for the populating and depopulating optical pumping schemes respectively.

The quenching of the optical pumping effect was fitted to an exponentially decaying function,

$$P = P_0 e^{-t/\tau} \quad (5.3)$$

where  $P_0$  is the maximum pumping effect observed at time 0 and  $\tau$  is the time constant of the decay. At 80 mTorr, the time constant of the quenching of the depopulating optical pumping scheme was found to be  $(2.25 \pm 0.1)$  ms and the time constant of the quenching of

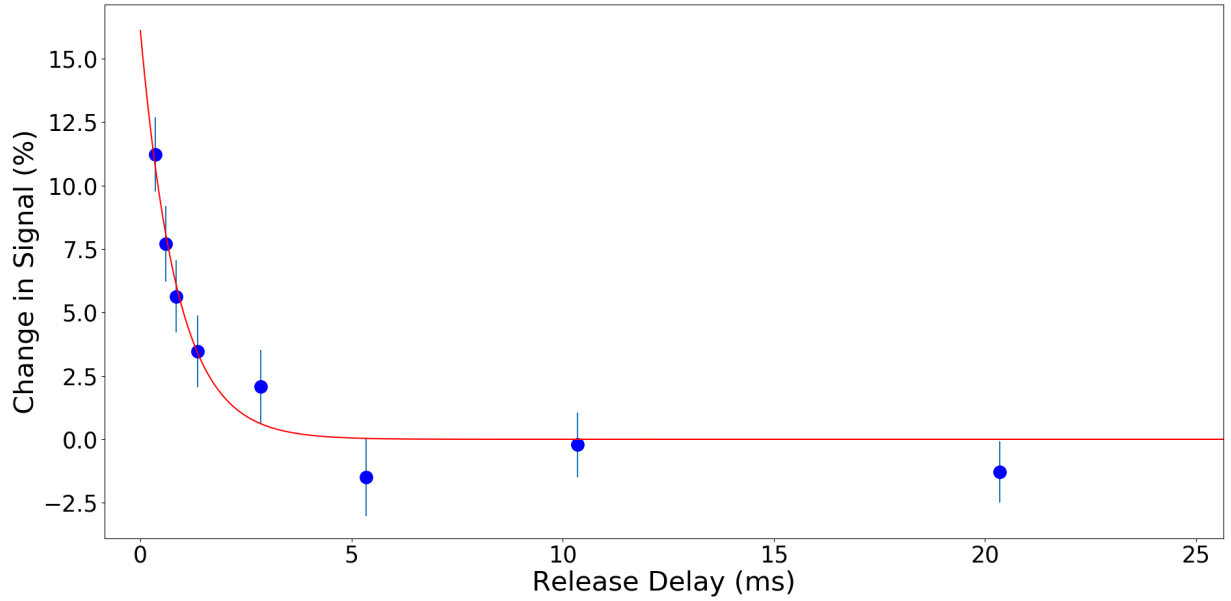


Figure 5.10: Quenching of the optically pumped electronic populations in  $\text{Zr}^+$ . The ions held in the RFQ ion trap were excited with a pulsed laser and held for increasing lengths of time. Interactions with the He buffer gas used in the RFQ ion trap leads to cooling of the trapped ions back to a room temperature Boltzmann distribution.

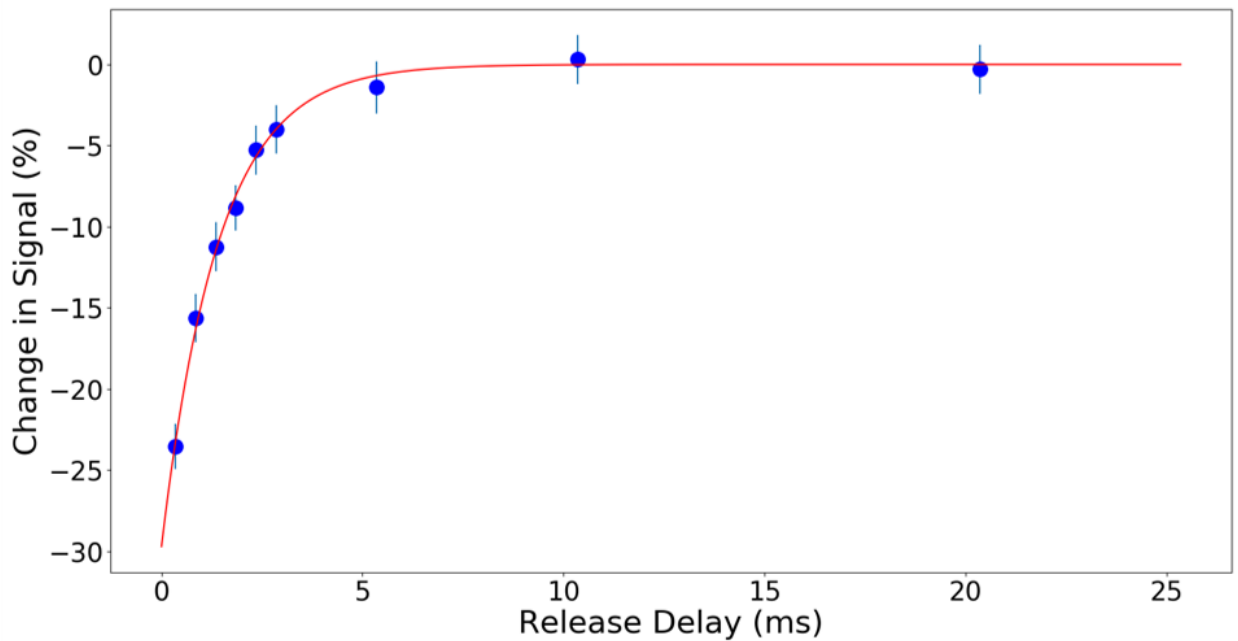


Figure 5.11: Quenching of the optically pumped electronic populations in the depopulating pumping scheme of  $\text{Zr}^+$ .

Table 5.3: Time constant of the quenching of the optically pumped electronic populations by collisional decay with the He buffer gas, across a range of pressures. The time constants of both the depopulating optical pumping scheme and populating optical pumping scheme are shown. If the time constant was not measured at a specific pressure, '-' is shown.

Pressure (mTorr)	Depopulating Scheme Time Constant (ms)	Populating Scheme Time Constant (ms)
10	-	7.3±1.2
20	8.6±0.5	4.4±0.6
30	5.1±0.5	-
40	4.6±0.4	-
50	-	1.3±0.2
60	2.7±0.3	-
80	2.2±0.2	1.0±0.3
100	1.9±0.2	-
120	2.4±0.3	0.5±0.2
140	1.0±0.2	-

the populating optical pumping scheme was determined to be (0.76±0.1) ms.

The quenching process involves collisions with the He buffer gas, and is thus sensitive to the pressure. A measurement was performed where the quenching process was observed across a range of pressures, and the results were compared. The optical pumping effect as a function of the release delay is shown for the different pressures that were tested in Figures 5.12 and 5.13 for the depopulating and populating optical pumping schemes respectively. More detailed information about the time constant of the relaxation process across the pressures is shown in Table 5.3. The minimum He buffer gas pressure that was tested was 10 mTorr at the He gas inlet. The trapping efficiency of the RFQ ion trap is drastically affected at lower pressures. The upper limit of the He buffer gas pressure that could be used was 140 mTorr. High buffer gas pressures can cause more frequent high voltage sparks, which disrupt measurements and can damage equipment. A correction factor was applied to the measured data based on the observation of ions entering into the ion trap after irradiation

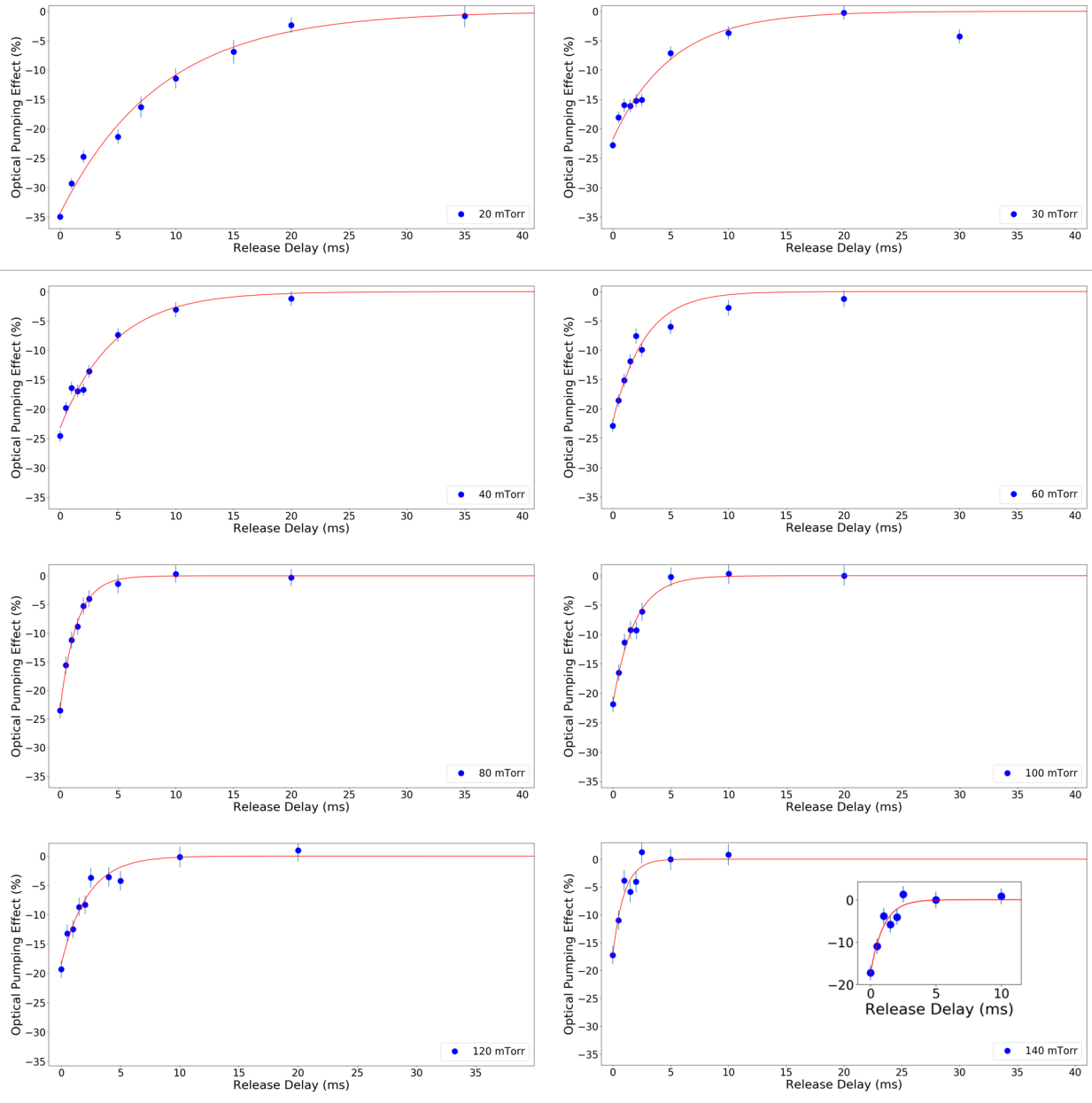


Figure 5.12: Optical pumping effect as a function of the release time of the trapped ions after irradiation by the pulsed laser light across a range of pressures. The quenching of the optically pumped electronic populations takes a longer time at lower pressures.

of the pulsed laser. The ion rate from the PIG ion source was high enough to overflow the trap. The ion beam was deflected by the application of 1 kV to a quadrupole immediately after the PIG ion source. The deflecting voltage was applied for 98 ms, then turned off for 2 ms to allow the ion trap to be filled. It was discovered that the deflecting voltage was not

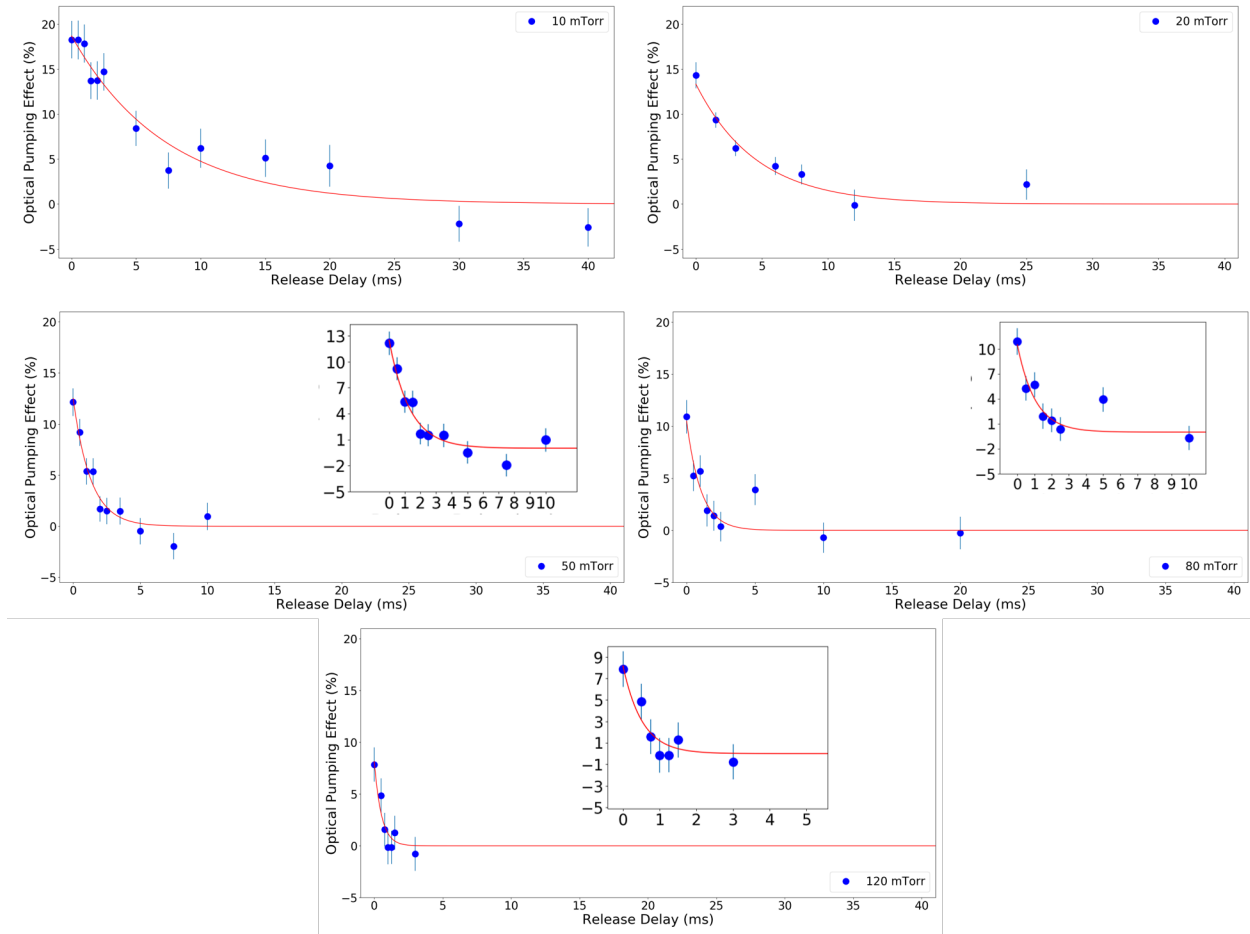


Figure 5.13: Optical pumping effect as a function of the release time of the trapped ions after irradiation by the pulsed laser light across a range of pressures. The quenching of the optically pumped electronic populations takes a longer time at lower pressures. The curves of 50 mTorr, 80 mTorr, and 120 mTorr feature a zoom in of the data.

applied for the measurement of the relaxation time across the range of pressures, and the ion beam was continuously entering the ion trap. As ions enter the trap after irradiation by the pulsed laser light the total fluorescent signal will increase and dilute the observed optical pumping effect.

The correction factor was applied assuming that the ion rate was continuous. The signal increase from the added ions should be the same between the ions that are optically pumped and not optically pumped, and will be proportional to the additional time spent in the ion trap. The ions are held for at least 100 ms, so ions that are held for 10 additional ms will

gain 10% more signal from the added ions. The correction factor subtracted photon counts that are assumed to have been caused by the additional beam, and the optical pumping effect was calculated based on the corrected counts. The change in the optical pumping was small, and the corrected data points are compared to uncorrected data in Figure 5.14.

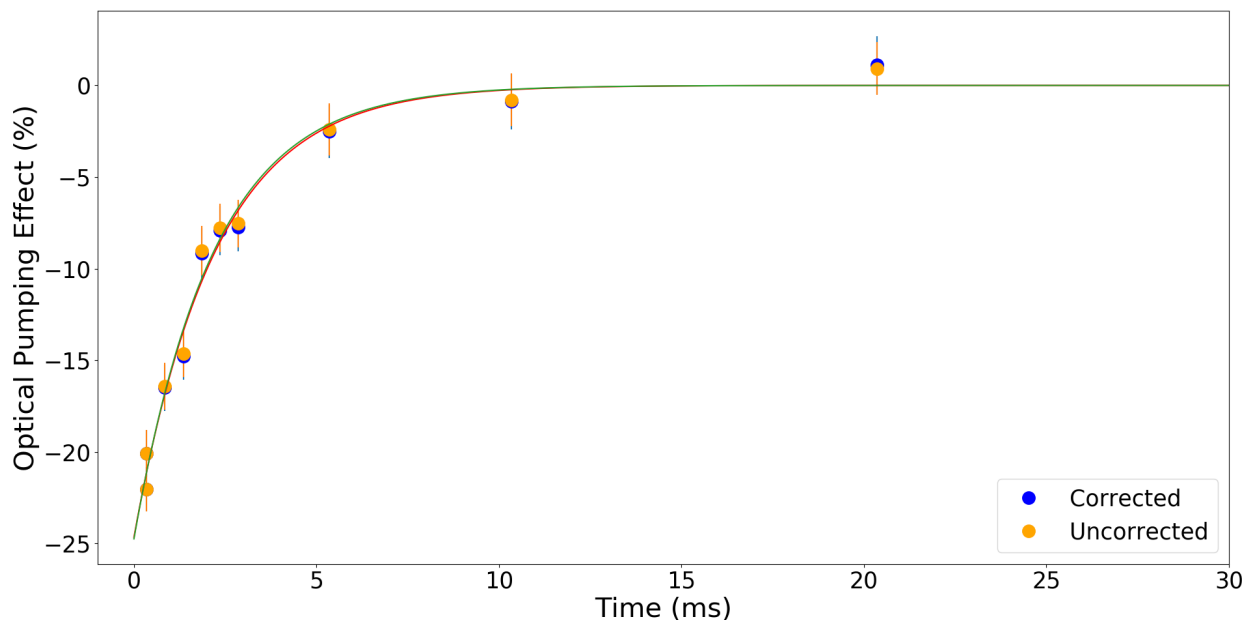


Figure 5.14: Optical pumping effect as a function of release delay of the ions after they are irradiated by pulsed laser light, comparing corrected and uncorrected data points for additional ions that enter the trap after the laser pulse. The overall correction is small.

The decay rate due to collisional decay can be determined from the time constant, simply as the inverse of the time constant. The decay rates of the populating and depopulating optical pumping schemes as a function of pressure is shown in Figure 5.15. The decay rate follows a linear relationship with the He buffer gas pressure. The slope of the fit gives the dependence of the pressure on the collisional quenching rate, and was found to be  $(5.4 \pm 0.2)$  Hz/mTorr and  $(12.6 \pm 0.9)$  Hz/mTorr for the depopulating and populating optical pumping schemes respectively.

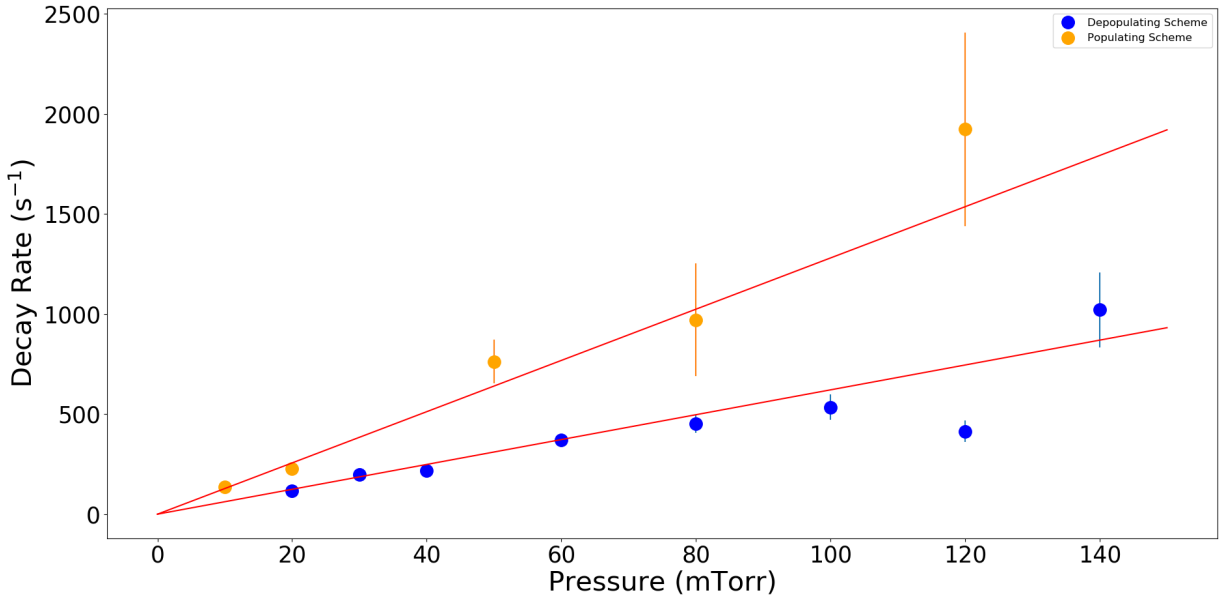


Figure 5.15: Collisional decay rate between He and the optically pumped electronic populations of  $\text{Zr}^+$ . The decay rate follows a linear relationship with the pressure of the He buffer gas.

### 5.4.1 Extrapolation of the Optical Pumping Effect

The BECOLA DAQ system features a delay of  $350 \mu\text{s}$ , meaning that even at the fastest release times there is a delay between irradiation and the release. The  $350 \mu\text{s}$  delay provides an opportunity for the He buffer gas to significantly cool the trapped ions. The optical pumping effect immediately after irradiation by the pulsed laser light can be extrapolated from the relaxation times. It is expected that the extrapolated optical pumping effect would converge across pressures.

The extrapolation was performed for both optical pumping schemes. The extrapolated values of the depopulation of the ground state are shown in Figure 5.16, compared to the experimentally observed values. The experimentally-observed data generally trend towards zero as the pressure increases. The error bars of the extrapolated data are larger based on uncertainty in the time constant of the quenching process and the statistical uncertainty of

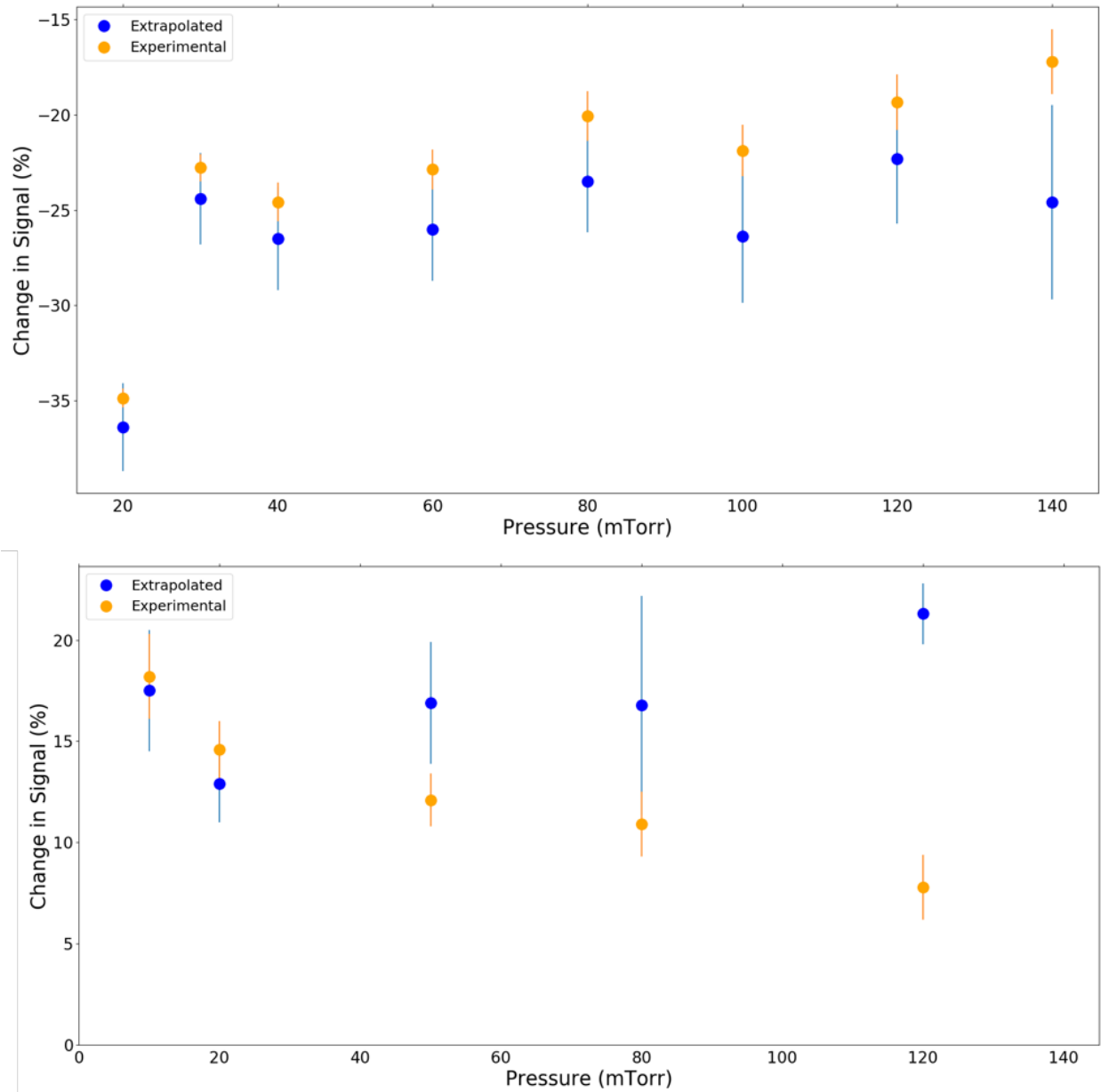


Figure 5.16: Comparison of the extrapolated optical pumping effect with the experimentally observed optical pumping effect. The results of the depopulating optical pumping are shown on top and the results of the populating optical pumping scheme are shown on bottom. The extrapolated data is based on the time constant of the quenching of the optically pumped electronic populations.

the experimental data. Collisions between the He buffer gas and the trapped ions are more likely, and the quenching process occurs faster. The difference between the extrapolated values and the experimental data is relatively small in the depopulating optical pumping

scheme, but becomes significant in the populating optical pumping scheme because the rate of the re-thermalization process is faster.

The extrapolated values were also compared to the results of the optical pumping simulation. The extrapolated values of the depopulation of the ground state are shown in Figure 5.17, compared to the simulated values. In general, the extrapolated values converge across

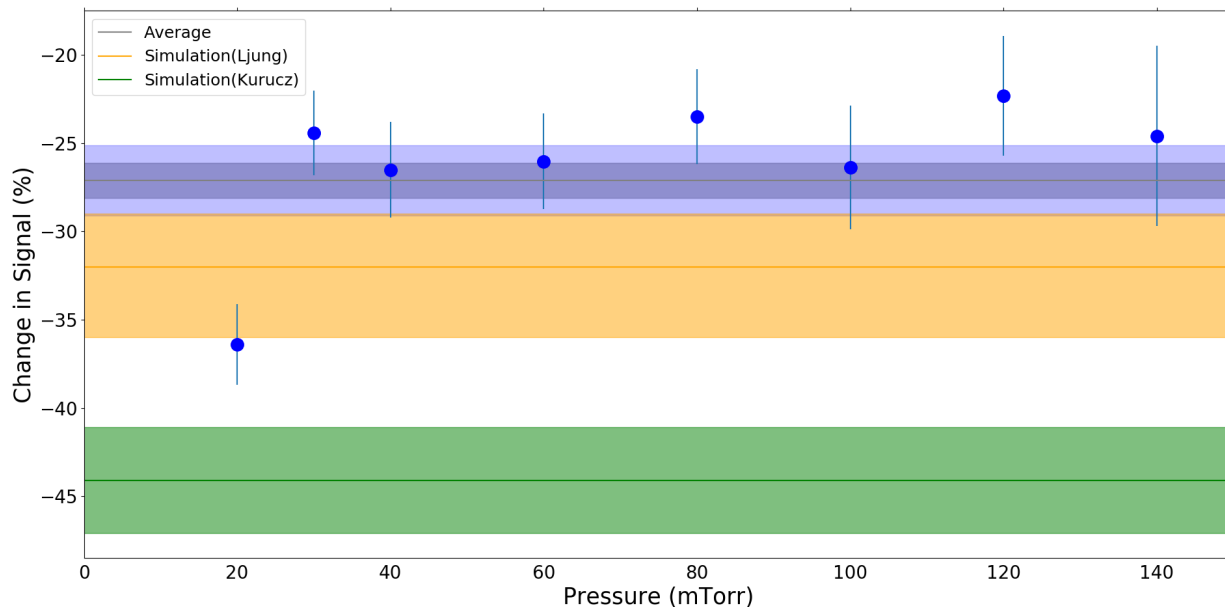


Figure 5.17: Extrapolated optical pumping effect of the trapped ions immediately after irradiation by the pulsed laser, as a function of pressure. The simulated values are shown as orange and blue bands respectively. The experimental data agrees with the simulated value of the optical pumping effect using experimental branching ratios from Ljung *et al.* [103]

pressures, with the exception of an outlier at 20 mTorr. The weighted average of the optical pumping effect is  $(-27.1 \pm 3)\%$ . The experimental data agree with the simulated optical pumping effect using the experimental branching ratios from Ljung *et al.* [103].

The extrapolation of the optical pumping effect was repeated for the optical pumping scheme that increased the population of the ground state, and results are shown in Figure 5.18. The extrapolated values of the optical pumping effect converge across the measured pressures. The weighted average of the extrapolated optical pumping effect is  $(16.8 \pm 2.9)\%$ .

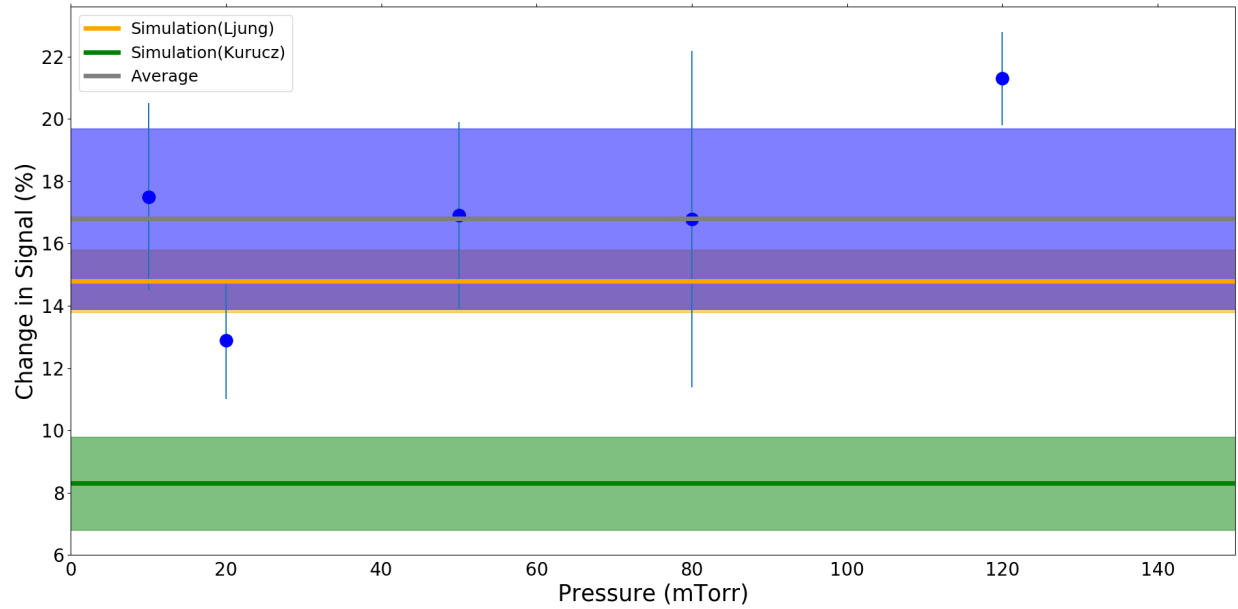


Figure 5.18: Extrapolated optical pumping effect of the trapped ions immediately after irradiation by the pulsed laser, as a function of pressure. The simulated optical pumping effect using the Kurucz and Ljung branching ratios are shown as green and orange bands respectively. The experimental results agree well with the simulated value based on the Ljung simulation value.

The weighted average value agrees well with the simulated value derived from the experimental branching ratios of Ljung *et al.* [103].

# Chapter 6

## Discussion

### 6.1 Improvements to the BECOLA Facility

The infrastructure improvements to the BECOLA facility to enable the optical pumping technique, the pulsed laser system and the free-space light transport system, were new to BECOLA and resulted in different lessons that were learned that will assist in guiding future improvements.

#### 6.1.1 Free-Space Light Transport System

The free-space light transport system was constructed to deliver laser light to the BECOLA experimental area for both optical pumping and CLS experiments. As the longest arm of the system is over 10 m, the system was designed to minimize vibrations that would translate into large movements of the pulsed laser beam position at the target region.

The new free-space light transport system was able to successfully deliver pulsed laser light to the RFQ ion trap. Movement of the laser light due to vibrations did not have a measurable effect on the experiments performed for this thesis, even when the beam was tightened to a small radius.

On the other hand, the performance of the light transport system for the CLS measurement was significantly worse. The CW laser light was kept at approximately 300  $\mu\text{W}$ . The

background due to stray light in the CLS beamline was over 300 kHz, as opposed to the less than 50 kHz background that is possible with fiber optic light transport, where light from the BECOLA laser room is coupled to a fiber optic cable and delivered to the experimental area. The increase in the stray light background is thought to have three main contributions.

The first contribution is due to the size of the laser light through the CLS beamline. The focus of the laser light was controlled via a telescope system in the BECOLA laser room, which slowly focuses the light to the CLS interaction region. The beam waist was larger with the free-space light transport system. The measured beam waist was 2 mm in diameter, whereas with the fiber optic transport system a beam waist of 1.3 mm is possible. The larger laser beam can be clipped by the aperture system inside the CLS beamline, and stray light scattered from the aperture will increase the background.

The second contribution is the propagation of higher-order modes of light through the light transport system, which reflect through the beamline as stray light. Although the Ti:Sapphire produces a Gaussian TEM<sub>00</sub> beam, the WaveTrain system produces light that interferes with itself as it propagates, producing halos around the main laser beam, as seen in Figure 6.1. These halos are typically blocked during injection into the fiber optic system, but can propagate freely with the main laser beam through the free-space light transport system. The higher-order modes of light will focus at different distances after passing through a lens. The free-space light transport system relies on a lens telescope system to collimate the laser beam, and any slight change in the focal length for each mode of light results in spatial broadening of the higher-order modes of light. As the higher-order modes of light diverge through the free-space light transport system, they can clip on components such as the metal pipe used to safely contain the laser light between rooms. Some proportion of the reflections from the light clipping on a surface are able to transverse the entire free-space

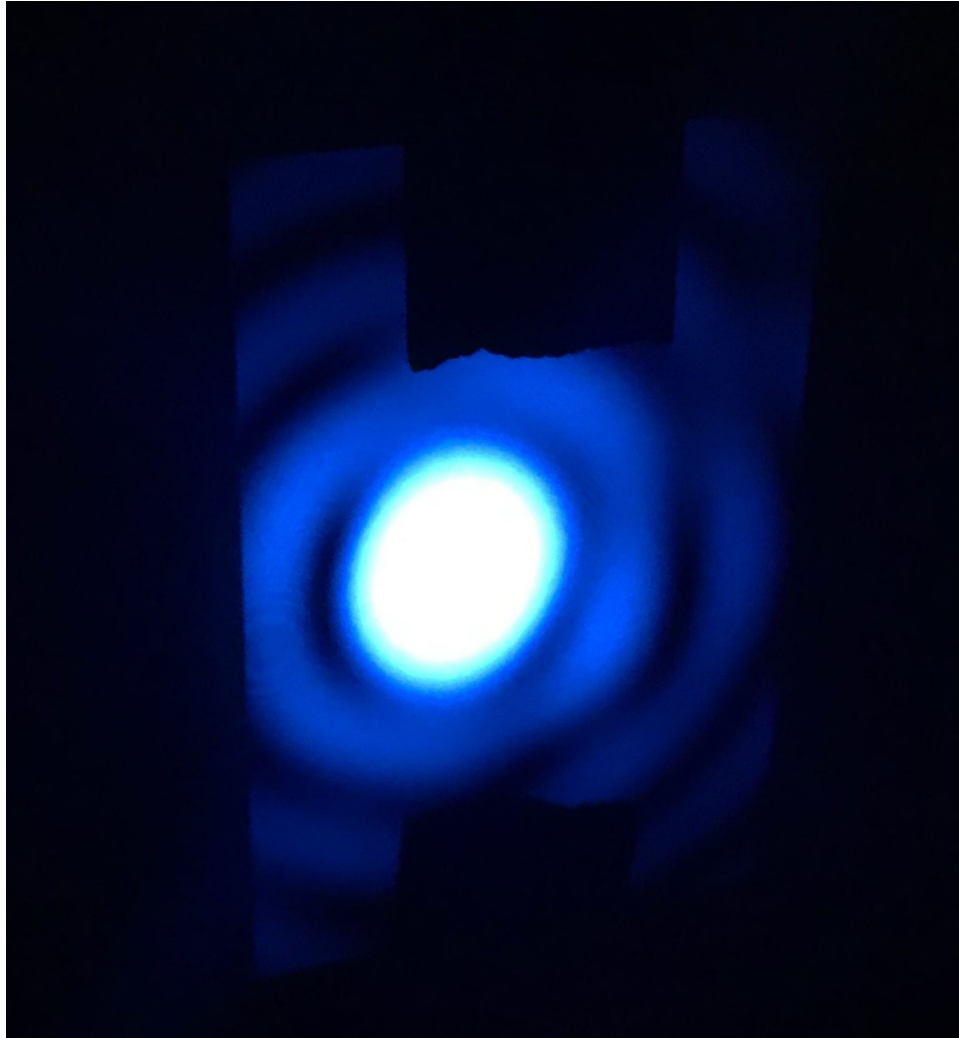


Figure 6.1: Frequency doubled CW laser light produced by a Sirah WaveTrain system. The frequency doubled light was measured approximately 2 m from the WaveTrain system. No lenses were used to focus or collimate the light. The doubled laser light features higher order modes of light seen as halo structures. The higher order light can propagate through the free-space light transport system and induce high stray light background.

light transport system and are injected into the CLS beamline, where they contribute to a higher background. The background produced by the higher-order modes of light can be partially mitigated by using a iris to block the halos while leaving the center untouched, but reflections of the higher-order modes from the iris is possible and contributes to the background. Another possible future solution is to coat the inside of the 10-m long pipe with anti-reflection paint that can reduce the scattered light.

The third contribution is movement of the laser beam due to vibrations. Although not an issue for the pulsed laser light injected into the RFQ ion trap, the CW laser light is carefully aligned through an aperture system that blocks stray light. The laser light is reflected from two mirrors on a breadboard that is secured to a building support beam in the BECOLA laser room, and these optics are responsible for the most significant sources of vibration in the free-space light transport system. If the air conditioning unit is turned on, or the door to the laser room opens, or heavy foot traffic passes through the hallway separating the BECOLA laser and experimental rooms, these optics will vibrate. Although the standard deviation of the movement is  $337 \mu\text{m}$ , spikes in the movement can cause the laser beam to clip the apertures and induce spikes in the background.

The background rates observed with the free-space light transport system do not inhibit the study of isotopes produced by off-line ion sources since the fluorescence signal is large, but would severely limit the range of radioactive isotopes that can be studied. There are possible ways to mitigate the vibration and reduce the background. Active stabilization systems can be installed to monitor the position of the laser light through the free-space light transport system and counteract movements of the laser beam due to vibrations or any other source. An active stabilization technique has been employed at GSI to transport laser light over 80 m [108].

In combination with the active stabilization system, a mode filter could be used in the BECOLA experimental area to remove higher order modes of light from the beam. The mode filter works by focusing the laser light through a small hole on the order of  $\mu\text{m}$ . The higher order modes of light will not focus to a tight spot, and the lowest order Gaussian mode can be selected and cleaned. The mode filter technique was attempted for the commissioning experiments of the optical pumping system, but the transmission of the laser light through the mode filter was very sensitive to the movement of the laser light and the power could not be stabilized for spectroscopy measurements.

### 6.1.2 Characteristics of the Pulsed Laser System

The Cobra-Stretch pulsed laser system was able to successfully excite and saturate the optical pumping transition in the RFQ ion trap and many additional findings were observed that will benefit future studies at BECOLA. Initial assumptions made during development of the optical pumping simulation led us to underestimate the sensitivity of the temporal width of the pulsed laser on the optical pumping effect.

The Cobra-Stretch pulsed laser delivers pulses with a temporal width of approximately 6 ns. The optical pumping effect becomes very sensitive to the width of the temporal laser pulse as the lifetime of the excited state approaches the temporal laser width. At these time scales, the ions can be excited multiple times by the pulsed laser, magnifying the pumping effect. The  ${}^4\text{G}_{5/2}$  state of  $\text{Zr}^+$  has a lifetime of  $(7.1 \pm 0.3)$  ns and the optical pumping effect as a function of the temporal width of the laser pulse is shown in 6.2. It was assumed that the optical transition remained saturated. The magnitude of the optical pumping effect grows very quickly and the ground state is almost completely depopulated with a laser pulse of 100 ns.

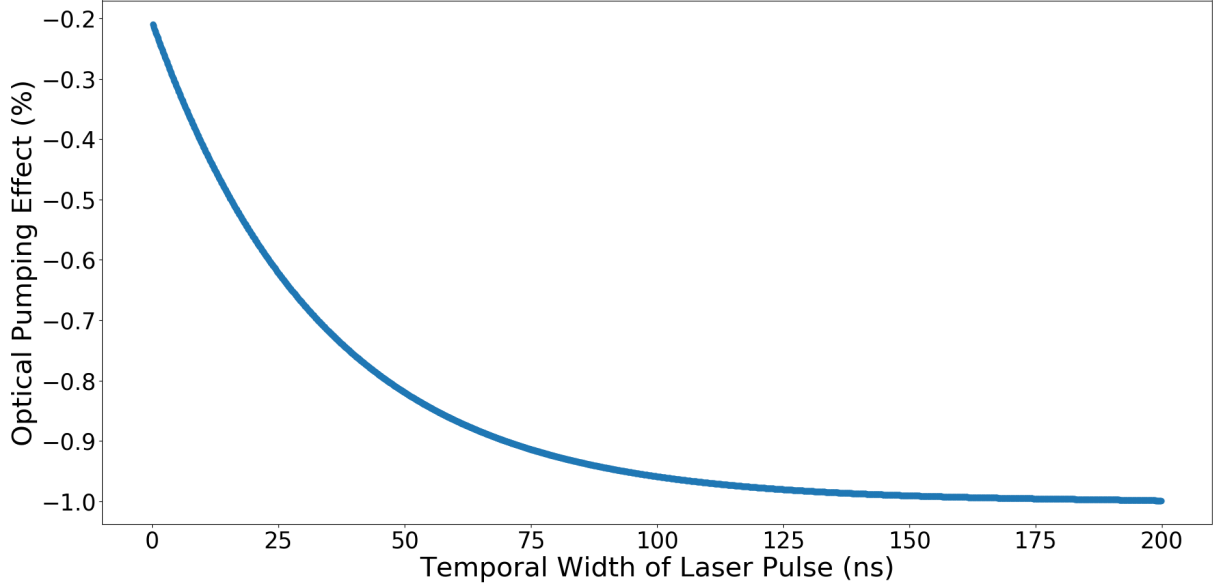


Figure 6.2: Simulated optical pumping effect as a function of the temporal width of the laser pulse. Assuming that the transition remains saturated, the ground state of  $\text{Zr}^+$  can be almost completely depopulated with a laser pulse of approximately 100 ns in width.

A 10 Hz pulsed laser was used for the commissioning experiments, but the use of higher repetition rate lasers or CW laser would provide the largest change in the electronic population. A limitation of the use of CW lasers is the energy density of the light that is used to perform optical pumping. The low energy density will limit the wavelength range of the CW laser system, and subsequently the optical pumping schemes that can be explored. The current BECOLA CW laser system has a lower limit of 350 nm and of the first- and second-row transition metals, the optical pumping schemes of all elements except Sc, Ti, and Zr require laser light below 350 nm.

There are currently efforts towards the development of 4<sup>th</sup> harmonic CW laser light at BECOLA, but currently only a few hundred  $\mu\text{W}$  of laser power has been produced at 230 nm, and is not enough power for efficient optical pumping. Additionally, if 4<sup>th</sup> harmonic CW laser was produced at BECOLA, it would likely be experimentally simpler to use that laser system

and transition for CLS measurements, as the CW laser light could access the populated low-lying states and would not rely on favorable decays which could reduce the sensitivity. Further development will open opportunities for laser spectroscopy measurements, and with the optical pumping system, will provide access to multiple techniques, allowing the choice of one that is best-suited for a given element or experiment.

## 6.2 Optical Pumping in the RFQ Ion Trap

The results obtained from measurements of the effective linewidth and saturation curve indicate that the pulsed laser light efficiently performed optical pumping.

### 6.2.1 Ion Bunch Size

It was assumed that the spatial distribution of the ion bunch in the RFQ ion trap had a radius of approximately 1.4 mm, based on results from simulations performed with the 3DCyIPIC software [80]. A rough measurement of the spatial distribution of the trapped ions in the X-Y plane of the RFQ ion trap was performed and the 95% inclusion radius was determined to be  $(2.3 \pm 0.2)$  mm (See Section 5.1.1).

The results confirm that the ion bunch is small, although the measurement was hampered by hysteresis of the picomotors used to scan the pulsed laser beam across the ion bunch. The size of the laser beam was increased to roughly the same size of the trapping region defined by the RFQ rods, with a diameter of 7 mm. The large size of the laser beam ensures that the entire ion bunch is irradiated by the laser light and mitigates small movement of the laser light due to vibrations in the free-space light transport system.

The trapped ion distribution in the simulation was not sensitive to the He buffer gas

temperature parameter. The BECOLA RFQ ion trap is designed to operate at liquid N<sub>2</sub> temperatures, and further work should be done to determine if the trapped ion distribution will change at low temperature.

### 6.2.2 Laser Power

The optical pumping effect as a function of the pulsed laser power was performed (See Section 5.1.2) The results demonstrated that the BECOLA pulsed laser system was capable of saturating the optical transition, with a saturation power of  $(2.9 \pm 0.3)$  mW/cm<sup>+</sup>. The theoretical saturation power of  $(8 \pm 0.2)$  mW/cm<sup>2</sup> was much lower than the total available power from the Cobra-Stretch laser system, and can be used to estimate the limits of optical pumping schemes that can be explored at BECOLA.

The saturation power is inversely proportional to the lifetime of the excited state [81], such that

$$I_{sat} = \frac{\pi \hbar c}{3\lambda^3 \tau} \quad (6.1)$$

The Cobra-Stretch laser system is capable of producing 120 mW of laser light at 360 nm for a power density of approximately 109 mW/cm<sup>2</sup>, 37 times greater than the saturation power density. The lifetime of the excited state in the commissioning experiments was  $(7.1 \pm 0.3)$  ns and saturation can be achieved with transitions that are 37 times slower, or with lifetime on the order 265 ns. A lifetime of 265 ns corresponds to an Einstein coefficient  $A$  of  $3.6 \cdot 10^6$ , while a lifetime of 7.1 ns corresponds to  $1.4 \cdot 10^7$ . In Table 6.1 are presented the minimum Einstein coefficients for future optical pumping experiments using similar conditions as the commissioning experiments described here and based on the available laser powers at different wavelengths. Light at higher wavelengths does not need to undergo the doubling process

Table 6.1: Einstein coefficient  $A$  limits based on saturation of the transition using similar conditions as the commissioning experiments, namely a laser beam size of  $0.27 \text{ cm}^2$ . The wavelength ranges are those that were tested during installation of the pulsed laser system.

Wavelength (nm)	Laser Power Density (mW/cm <sup>2</sup> )	Minimum Einstein Coefficient $A$ (s <sup>-1</sup> )
196	7	$2.2 \cdot 10^8$
202-212	98	$1.6 \cdot 10^7$
230-270	185	$8.7 \cdot 10^6$
360-365	435	$3.7 \cdot 10^6$
535	1270	$1.3 \cdot 10^6$

after being produced in the Cobra-Stretch dye laser, and will thus have much higher energy per pulse and allow access to slower transitions.

### 6.2.3 Linewidth

Good spectral overlap between the absorption linewidth of the electronic transition and the linewidth of the pulsed laser light is necessary for efficient optical pumping. If the linewidth of the pulsed laser is smaller than the absorption linewidth, a proportion of the ions will not be excited. If the linewidth of the pulsed laser is too large, a proportion of the laser power will be distributed off-resonance with the absorption linewidth and is effectively wasted. In Chapter 4, it was shown that at room temperature the absorption linewidth of an electronic transition is dominated by Doppler broadening effects, and results in an absorption linewidth of approximately 1.1 GHz, or approximately  $0.04 \text{ cm}^{-1}$ . The linewidth of the fundamental light of the pulsed laser system is also  $0.04 \text{ cm}^{-1}$ , but is doubled to  $0.08 \text{ cm}^{-1}$  when 2<sup>nd</sup> harmonic light is produced, significantly larger than the expected absorption linewidth. The effective absorption linewidth was determined by measuring the optical pumping effect as a function of the pulsed laser frequency. The measurement was repeated at different pulsed

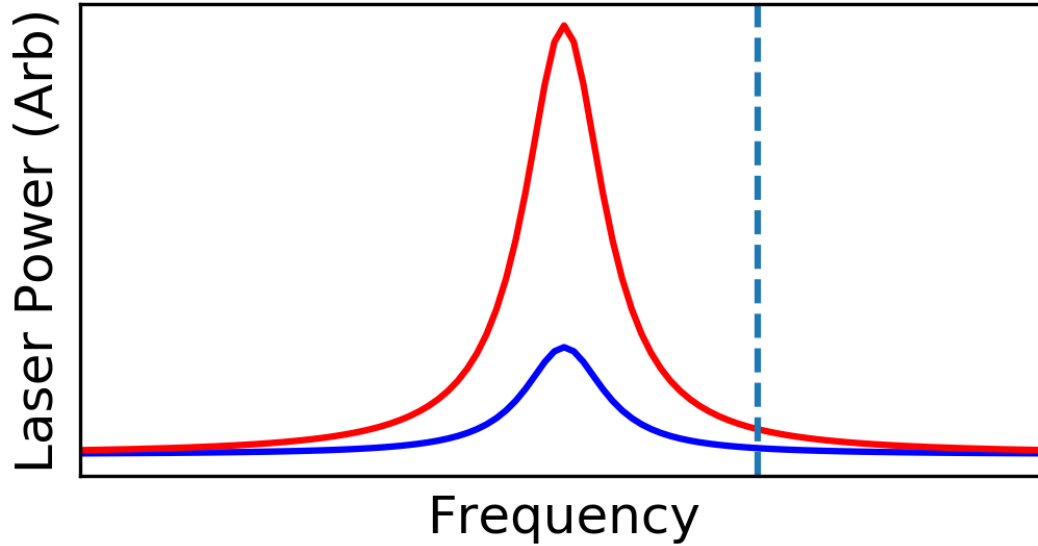


Figure 6.3: Power broadening of spectral lines. As the laser power increases, the wings of the spectral profile raise and can excite transitions far from the center of the center frequency.

laser powers and the resonance linewidth was extracted. The absorption linewidth was observed to significantly grow at laser powers as low as 4 mW. At higher laser powers a flat top profile was observed as the electronic transition was saturated by laser light even though the pulsed laser frequency was centered off resonance. The increase in the effective absorption linewidth is due to what is known as power broadening. The power broadening phenomenon is illustrated in Figure 6.3. If we assume that the spectral line profile of the pulsed laser follows a Lorentzian distribution, as the laser power is increased the wings of the profile will raise and can excite a transition even if the peak of the spectral profile is off resonance. The observed power broadening and flat-top behavior confirmed that the pulsed laser is capable of completely exciting the electronic transition for all ions in the RFQ ion trap.

## 6.3 Manipulation of Electronic Populations

The primary goal of the commissioning experiments was to demonstrate that the pulsed laser system is capable of manipulating the electronic populations of ions in the BECOLA RFQ ion trap. The population manipulation was performed in the RFQ ion trap and probed via measurement of the fluorescence signal with CLS. The results of the commissioning experiments clearly demonstrated that the population manipulation was successful. A statistically-significant change was observed in the fluorescence signal, and subsequently in the electronic population of the electronic state being probed. The observed optical pumping effects of  $(-24.6 \pm 1.6)\%$  for the depopulation optical pumping scheme and  $(12.6 \pm 2.7)\%$  were in better agreement with the results of the optical pumping simulation based on the experimental branching ratios provided by Ljung *et al.*[103].

The branching ratios from the Kurucz database are based on calculations from emission spectra from free-burning arc sources [102]. It was assumed that the oscillator strengths can be described by a linear relationship between the wavelength of the transition, the energy of the excited state, and the intensity of the measured peak. The difference between the experimental results and the Kurucz calculations may be due to both experimental error in the measurement of the emission spectra, and a non-linear dependence between the oscillator strength and the parameters used to calculate the oscillator strength. The experimental branching ratios from Ljung *et al.* are based on direct measurement of  $\text{Zr}^+$  emission spectra and should be more reliable.

The difference between the results of the simulation and the experimental observations can be explained by the occurrence of collisional excitation and decay that redistributed the electronic populations of ions in the RFQ trap back to thermal equilibrium.

### 6.3.1 Quenching of Optically Pumped Populations

The observed optical pumping effect for both the depopulating and populating transitions were smaller than expected based on the developed optical pumping simulation, for both the simulated values using the Kurucz theoretical branching ratios [75] and the Ljung experimental branching ratios [103]. The discrepancy between the observed optical pumping effect and the simulated value can be explained by the observation of collisional decay inside the RFQ ion trap. The He buffer gas quenched the optically pumped electronic populations and re-thermalized the ion bunch back to a room temperature Boltzmann distribution. Although the BECOLA DAQ system was set to release the ion bunch immediately after irradiation by the pulsed laser light, there is a 350  $\mu\text{s}$  delay between the laser pulse and the release of the ion bunch. In the 350  $\mu\text{s}$  time frame, the He buffer gas began to quench the optical pumping effect. Measurement of the time constant of the decay provided a method to extrapolate the optical pumping effect immediately after irradiation by the pulsed laser.

The extrapolated optical pumping effect of the depopulation of the ground state of  $\text{Zr}^+$  was  $(-27.1 \pm 3)\%$ . The optical pumping simulation predicted a value of  $(-31.9_{-3}^{+4})\%$  based on the experimental branching ratios found in Ljung *et al.*, and  $(44.1 \pm 3)\%$  using the theoretical branching ratios from the Kurucz database. The extrapolated optical pumping effect of the population of the ground state of  $\text{Zr}^+$  was  $(12.6 \pm 2.7)\%$ , while the simulated values were  $(14.8 \pm 1)\%$  and  $(8.3 \pm 1.5)\%$  using the experimental and theoretical branching ratios respectively. The extrapolated data of both optical pumping schemes agree well with the simulated optical pumping effect using the experimental branching ratios from Ljung *et al.*. The theoretical branching ratios from the Kurucz database significantly overestimate the fraction of excited state ions that decay to the metastable dark states.

The effect of collisional excitation and decay on the optical pumping effect was measured across a range of He buffer gas pressures, from 10-140 mTorr measured at the gas inlet. The rethermalization time decreased with the He buffer gas pressure, as the probability of a collision between a Zr ion and a He atom became smaller, and a difference in the rethermalization time was observed between the depopulating and populating optical pumping schemes. The rates were fitted to a linear regression line, with slopes of  $(5.4 \pm 0.2)$  Hz/mTorr and  $(12.6 \pm 0.9)$  Hz/mTorr for the depopulating and populating optical pumping schemes, respectively. The difference in the slopes between the two optical pumping schemes can be explained by the difference in probability between a collisional excitation and a collisional decay. In Chapter 3, it was shown that the thermal populations of the electronic states can be described by a Boltzmann distribution. The ions in a system populate the low-energy states through collisional excitation and decay, which will eventually reach equilibrium, such that the relative population  $N_i$  is

$$N_i = \frac{2J + 1}{Q} e^{-E_i/kT}. \quad (6.2)$$

In a two-level system at equilibrium with levels  $i$  and  $j$ , the rate of change in the population of state  $i$  can be given by the rate equation,

$$\delta N_i = N_j K_{ji} - N_i K_{ij} = 0 \quad (6.3)$$

where  $K_{ij}$  is the collisional excitation or decay rate from state  $i$  to state  $j$ . By substituting

Eq. 6.2 into Eq. 6.3, it can be shown that,

$$\frac{2J_i + 1}{Q} e^{-E_i/kT} K_{ij} = \frac{2J_j + 1}{Q} e^{-E_j/kT} \quad (6.4)$$

The degeneracy of the states,  $g$ , is given by the  $2J + 1$  term, and by simplifying the equation we find,

$$g_i e^{-E_i/kT} K_{ij} = g_j e^{-E_j/kT} K_{ji} \quad (6.5)$$

Finally, Equation 6.5 can be further simplified to show that the rates of collisional excitation and decay are related by

$$K_{ij} = \frac{g_j}{g_i} e^{-(E_j - E_i)/kT} K_{ji} \quad (6.6)$$

The two optical pumping schemes involved optically pumping ions from the ground or first excited states of  $\text{Zr}^+$ . Assuming that the ground and first excited states are responsible for most of the collisional decay and excitation during the rethermalization process, it can be shown that the rate of the rethermalization process should differ by a factor of 2.7 with a  $g_i$  of 1.5 and  $g_j$  of 2.5. The slopes of the rethermalization process for the populating and depopulating transition differ by a factor of  $(2.3 \pm 0.2)$ , agreeing well with the expected value and demonstrates why the difference occurs.

The fit of the collisional rate was also used as an input to the optical pumping simulation to incorporate the collisional rethermalization and check the experimental results. The simulated optical pumping effect is shown as a function of He buffer gas pressure in Figure 6.4, compared with the experimental data. The simulated optical pumping effect is based on the experimentally-determined branching ratios from Ljung *et al.*. The uncertainty of the simulated values results from the experimental error of the branching ratios from the

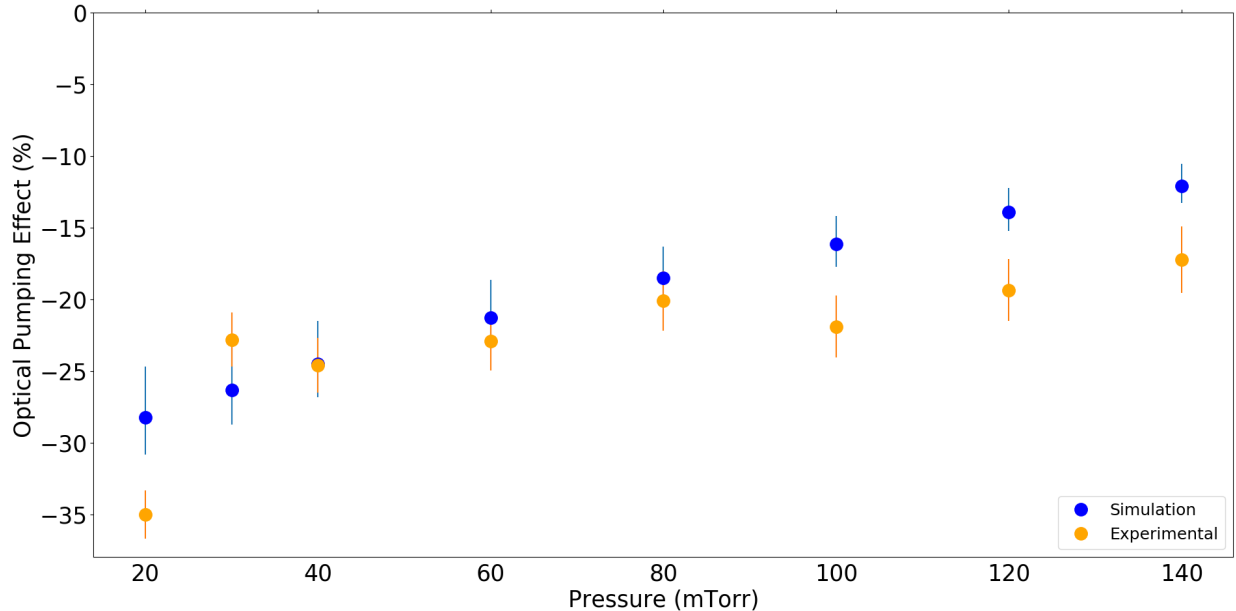


Figure 6.4: Comparison of the experimental optical pumping effect as a function of pressure with the simulated optical pumping effect with collisional rethermalization added. The simulation shows good agreement with the experimental results and demonstrates that the rethermalization process can be accounted for in simulation.

excited state as well as the uncertainty of the fit of the collisional rethermalization rate. The simulated values agree well with the experimental data, demonstrating that the collisional rethermalization can be accounted for in future experiments through simulation. Future preparatory experiments should test the collisional rethermalization as a function of time to improve the simulation, as it is unclear if the collisional rate will be element-dependent.

## 6.4 Outlook

The results of the optical pumping simulation for the first- and second-row transition metals shows promise for future studies of many elements. During the FRIB era, BECOLA will be in a unique position to gain access to rare isotopes of the transition metals at very high rates, but future experiments will need to verify optical pumping schemes during preparatory

experiments.

### 6.4.1 Optical Pumping Simulation Accuracy

The discrepancy between experimental results and the predictions based on the Kurucz database present an issue for future experiments using the optical pumping system. As a tool for planning future experiments, it is important that the estimates of the increase in electronic population given by the optical pumping simulation be accurate. The results shown in Chapter 3 for the first- and second-row transition metals are based on the NIST and Kurucz databases. Currently, the optical pumping schemes of V, Nb, Mo, and Ru are at least partially based on theoretical values of the transition scheme. The NIST line database does not include the Einstein coefficients of these elements, and preparatory experiments should test multiple optical pumping schemes to determine the most efficient scheme. Future use of the simulation for planning experiments should investigate the most promising optical pumping schemes to verify the predictions from the optical pumping simulation. The preparation can be performed with stable ion beams and off-line ion sources, and multiple schemes can be tested to find the most suitable. Literature searches can also be performed to find the most up-to-date data behind the transitions that would be used.

### 6.4.2 FRIB Reach

Based on the statistics of a previous experiment performed at BECOLA to study the isotope shifts of  $^{52,53}\text{Fe}$  [12], an estimate of BECOLA's reach in the FRIB was performed. The estimate was based on the statistical precision and length of measurement time of the neutron-deficient Fe isotopes. The measurement of  $^{52}\text{Fe}$  required 13 hours of collection time

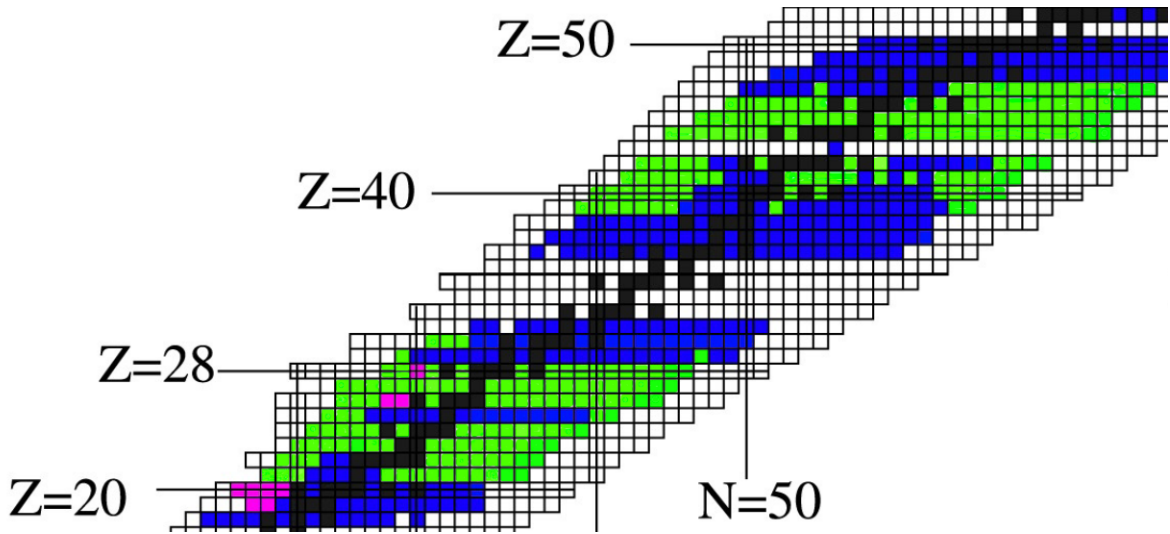


Figure 6.5: Chart of the nuclides zoomed in on the first- and second-row transition metals. Isotopes in black are stable, isotopes in blue are radioactive and have previously been studied using laser spectroscopy, isotopes in green will be accessible for studies at BECOLA, and isotopes in pink have previously been studied at BECOLA.

for a statistical error of 3 MHz, or approximately 0.2% of the overall isotope shift of 1.836 GHz. At the 3 MHz level of statistical error, the systematic error becomes a limiting factor for precision. The average rate of the  $^{52}\text{Fe}$  beam over the 13 hour collection time was  $4.4 \cdot 10^5$  particles/s, for a total of  $2.06 \cdot 10^{10}$  particles for the 13 hour collection time. The BECOLA charge exchange cell was used to neutralize the beam at an efficiency of 50%, and only 5% of the neutralized beam populated the electronic state used for the CLS measurement, leading to an estimate of  $5.2 \cdot 10^8$  total ions required for a 3 MHz uncertainty.

Using estimates of the final beam rates for the first- and second-row transition metals provided by FRIB and based on the LISE++ software [50], the experimental time necessary to achieve a 3 MHz uncertainty was calculated for each isotope. A cutoff of 5 days was applied, as that is the typical length of an online experiment. The results of the estimate are shown in Figure 6.5 with more detail in Table 6.2. During the FRIB era, BECOLA will be able to study essentially every element in the transition metal region far from stability. One

Table 6.2: Experimental reach of the first- and second-row transition metals at BECOLA during the FRIB era. BECOLA will be in a unique position to study wide chains of virtually every element in the region.

<b>Element</b>	<b>Mass Number</b>
Sc	39-56
Ti	40-58
V	43-60
Cr	44-63
Mn	46-66
Fe	48-70
Co	50-72
Ni	53-74
Cu	56-77
Zn	58-78
Y	77-104
Zr	79-107
Nb	82-109
Mo	85-112
Tc	N/A
Ru	88-118
Rh	91-119
Pd	94-122
Ag	96-124
Cd	98-128

exception is the case of Tc, where studies are limited by sparse knowledge of the electronic structure and not by beam rate or technological limitations at BECOLA. Due to the high beam rates, even elements that require charge exchange reactions for CLS measurements will be accessible.

### 6.4.3 Future Laser Systems

Future optical pumping experiments will be able to take advantage of three new pulsed laser systems that will be installed at BECOLA. The pulsed laser systems are 10 kHz repetition rate Ti:Sapphire lasers that were previously used at the Holifield Radioactive Beam Facility

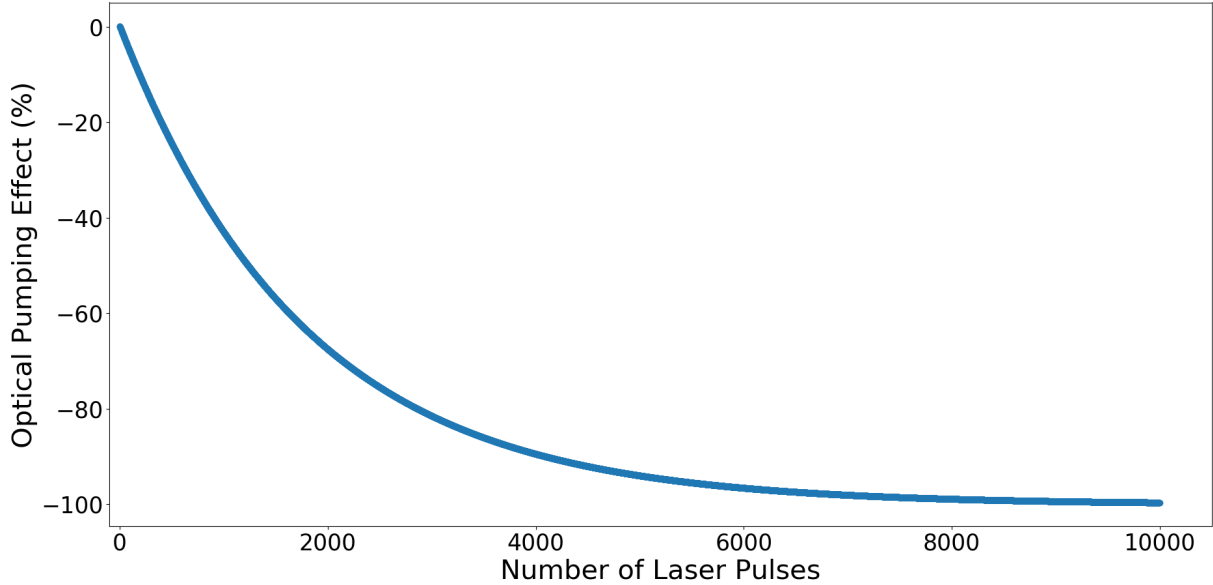


Figure 6.6: Simulated optical pumping effect of the depopulating optical pumping scheme in  $\text{Zr}^+$ . The 10 kHz laser system is able to deliver more laser pulses to the ion bunch, but more laser pulses are required to depopulate the ground state due to the lower energy density of the laser light.

[109] located at Oak Ridge National Lab prior to being decommissioned. The pulsed lasers were used as part of a Resonant Ionization Laser Ion Source (RILIS) system and were described in Liu *et. al* [110]. Two of the three laser systems are equipped with units to generate 2<sup>nd</sup>, 3<sup>rd</sup>, and 4<sup>th</sup> harmonic light and have a wavelength range of 217-960 nm. The systems can produce up to 30 mW of laser light at 217 nm, 120 mW of light at 270 nm, 800 mW at 410 nm, and 2.5 W at 820 nm, which are the peak powers for the fundamental and harmonic light respectively. Although the overall power of the system is comparable to the Cobra-Stretch laser system, the laser power is distributed over 1000 times more laser pulses. Assuming that the overall laser power and temporal width of the two systems are the same and that the difference that the energy per pulse of the 10 kHz laser system is a factor of 1000 lower, the optical pumping effect was simulated and is shown in Figure 6.6. Although the 10 kHz laser system would be able to irradiate the ion bunch many times,

the low energy density of the laser light prevents saturation of the transition. The optical pumping effect after 100 ms is -42.9%, which is a significant improvement over the simulated and experimentally observed optical pumping effect using the 10 Hz Cobra-Stretch laser system.

Another benefit of using the 10 kHz laser system is an increase in flexibility regarding the amount of time that ion bunches can be held in the RFQ ion trap. Currently, the 10 Hz laser system requires that the ions be held for at least 100 ms to irradiate each ion bunch. A 10 kHz pulsed laser system would allow for ions to be held for shorter periods of time, and periods of time that are not multiples of 100 ms.

Finally, the 10 kHz pulsed laser system could potentially mitigate the effect of collisional decay on the observed optical pumping effect. Each laser pulse is separated by approximately 100  $\mu$ s, compared to the 100 ms separation time between laser pulses with the Cobra-Stretch pulsed laser system. The collisional rethermalization process was observed to occur over the time span of a few ms, and the 10 kHz laser system will be able to continuously excite the laser transition and prevent the ion bunch from returning to thermal equilibrium.

# Chapter 7

## Conclusion

Laser spectroscopy studies of the first- and second-row transition elements can provide important information for nuclear structure and stockpile stewardship. However, radioactive isotopes of the transition metals have remained difficult to study. An optical pumping system was commissioned at the BECOLA facility to enable the study of rare transition metal isotopes. Through optical pumping, the electronic populations of ions held in an RFQ ion trap were manipulated and improved the sensitivity of subsequent collinear laser spectroscopy measurements.

An optical pumping simulation was developed to guide the experiments performed in this thesis, as well as future experiments. The simulation solves the rate equations of the electronic states to determine the most efficient laser transitions for optical pumping studies. The results of the simulation indicate that most transition metals will see an improvement in measurement sensitivity through optical pumping.

A new pulsed laser system and a free-space light transport system were installed at the BECOLA facility to deliver high-power pulsed laser light to the BECOLA RFQ ion trap and perform the optical pumping. Commissioning experiments involving a stable  $Zr^+$  indicate that the electronic populations of ions held in the RFQ ion trap can be successfully manipulated. The observed optical pumping effect was in good agreement with the simulation, bolstering confidence that the simulation can be used for future experiments.

An unexpected contribution of collisional decay was observed, quenching the optical

pumping effect as collisions between the optically pumped  $\text{Zr}^+$  ions and the He buffer gas rethermalized the electronic populations back to room temperature. The rethermalization process was measured over a range of pressures and the results were used to both extrapolate the experimental results to determine the initial optical pumping effect, and to add the collisional process to the optical pumping simulation. The extrapolated data converged across the tested range of pressures and was in good agreement with the optical pumping simulation. The experimental data also agreed well with the results of the optical pumping simulation with the collisional process added. Through the commissioning experiments, the collisional decay effect is well understood and can be accounted for in future experiments.

In the FRIB era, BECOLA is well situated to study essentially all elements in the transition metal region, and with the addition of three new pulsed laser systems, there is potential for further development of the optical pumping program.

## APPENDICES

# APPENDIX A

## Optical Pumping Schemes of First and Second-Row Transition Metals

This appendix contains the potential optical pumping schemes for the first- and second-row transition metals, as calculated using the optical pumping simulation discussed in Chapter 4. Each table is split into sections with a potential pumping step, featuring the ground and excited states and properties of the corresponding transition, and different possible CLS transitions that can be used. The optical pumping schemes are in order of decreasing electronic population of the state being probed for the CLS measurement, and within each scheme the possible transitions for CLS are sorted in order of the speed of the transition. It was assumed that no collisional decay will occur for the calculation of the change in the electronic population, and should be seen as the maximum possible optical pumping effect.

### A.1 Scandium

Promising optical pumping schemes of Sc are shown in Figure A.2. The first three states of Sc are populated, with the relative populations shown in Table A.1.

Table A.1: Low-energy populated states of  $\text{Sc}^+$

State ( $\text{cm}^{-1}$ )	Population
0	0.312
67.72	0.376
177	0.311

The first three states of  $\text{Sc}^+$  are almost evenly populated, but the first excited state at  $67 \text{ cm}^{-1}$  is the most populated and the most promising optical pumping schemes move the electronic population to that state.

Table A.2: Optical Pumping Schemes of  $\text{Sc}^+$

Pumping Ground State ( $\text{cm}^{-1}$ )	Pumping Excited State ( $\text{cm}^{-1}$ )	$A$ ( $\text{s}^{-1}$ )	$\lambda$ (nm)	CLS Ground State ( $\text{cm}^{-1}$ )	Population in State	CLS Excited State ( $\text{cm}^{-1}$ )	$A$ ( $\text{s}^{-1}$ )
177	27602	1.43E7	362.3	67.72	0.605	29742	1.58E8
				67.72	0.605	28021	1.41E8
				67.72	0.605	29742	1E8
				67.72	0.605	27917	5.09E7
				0	0.505	27443	1.52E8
				0	0.505	27917	1.48E8
0	39115	7.11E7	255.6	67.72	0.581	30815	3.33E6
				67.72	0.581	27602	1.58E8
				67.72	0.581	28021	1.41E8
				67.72	0.581	29742	1E8
				67.72	0.581	27917	5.09E7
				177	0.312	27841	1.88E8
				177	0.312	28161	1.83E8
0	29742	3.19E7	336.2	67.72	0.53	27602	1.58E8
				67.72	0.53	28021	1.41E8
				67.72	0.53	29742	1E8
				67.72	0.53	27917	5.09E7
				67.72	0.53	29823	2.01E7
				177	0.312	27841	1.88E8
				177	0.312	28161	1.83E8
67.72	27443	2.51E7	365.4	0	0.505	27443	1.52E8
				0	0.505	27917	1.48E8
				0	0.505	29736	1.38E8
				177	0.312	27841	1.88E8
				177	0.312	28161	1.83E8

## A.2 Titanium

The promising optical pumping schemes of  $\text{Ti}^+$  are shown in Table A.4, with the distribution of the electronic population shown in Table A.3.

Table A.3: Low-energy populated states of  $\text{Ti}^+$

State ( $\text{cm}^{-1}$ )	Population
0	0.312
94	0.376
225	0.311
393	0.223
908	0.004
983	0.004

Although  $\text{Ti}^+$  features 6 states below  $1000 \text{ cm}^{-1}$ , only four are appreciably populated. The study of Ti isotopes with CLS does not require charge exchange, but optical pumping can provide a 52% improvement in the sensitivity of laser spectroscopy measurements.

Table A.4: Optical Pumping Schemes of  $\text{Ti}^+$

Pumping Ground State ( $\text{cm}^{-1}$ )	Pumping Excited State ( $\text{cm}^{-1}$ )	$A$ ( $\text{s}^{-1}$ )	$\lambda$ (nm)	CLS Ground State ( $\text{cm}^{-1}$ )	Population in State	CLS Excited State ( $\text{cm}^{-1}$ )	$A$ ( $\text{s}^{-1}$ )
94.1	29544	2.48E7	339.5	0	0.503	32532	1.54E8
				0	0.503	30836	1.16E8
				0	0.503	29544	1.09E8
				0	0.503	32602	3.3E7
225.7	29544	2.48E7	341.1	0	0.488	32532	1.54E8
				0	0.488	30836	1.16E8
				0	0.488	29544	1.09E8
				0	0.488	30958	2.87E7
0	32602	3.3E7	306.7	94.1	0.472	32602	1.12E8
				94.1	0.472	29734	1.11e8
				94.1	0.472	30958	3.38E7
				94.1	0.472	31113	2.66E7
				94.1	0.472	32025	8.21E6
94.1	30836	3.38E7	325.3	0	0.471	32532	1.54E8
				0	0.471	30836	1.16E8
				0	0.471	29544	1.09E8
				0	0.471	32602	3.3E7
225.73	29734	2.18E7	338.9	94.1	0.434	32602	1.12E8
				94.1	0.434	29734	1.11e8
				94.1	0.434	30958	3.38E7
				94.1	0.434	31113	2.66E7
				94.1	0.434	32025	8.21E6

### A.3 Vanadium

The promising optical pumping schemes of  $\text{V}^+$  are shown in Table A.6 and the low-energy populated states are shown in Table A.5.

Table A.5: Low-energy populated states of  $V^+$

State ( $\text{cm}^{-1}$ )	Population
0	0.092
36	0.233
106	0.276
208	0.237
339	0.163

There are many low-energy states of  $V^+$  and the electronic population is already highly fragmented at room temperature. Additionally, the study of  $V$  typically requires charge exchange reactions, which result in only 4% of the total ion beam populating the state used for CLS. Considering a charge exchange efficiency of 50%, only 2% of the total ion beam is available for study. For each optical pumping step, there are relatively few transitions that can be used for CLS measurements.

Table A.6: Optical Pumping Schemes of  $V^+$

Pumping Ground State ( $\text{cm}^{-1}$ )	Pumping Excited State ( $\text{cm}^{-1}$ )	$A$ ( $\text{s}^{-1}$ )	$\lambda$ (nm)	CLS Ground State ( $\text{cm}^{-1}$ )	Population in State	CLS Excited State ( $\text{cm}^{-1}$ )	$A$ ( $\text{s}^{-1}$ )
106.6	46754	6.47E7	214.3	36.1	0.335	36489	3.47E6
106.6	37369	1.98E7	268.3	36.1	0.292	36489	3.47E6
339	47181	1.24E7	213.5	13594	0.154	37369	1E6
106	46690	1.08E7	214.7	13511	0.124	37259	1.45E6
106	46740	1.08E7	214.4	13594	0.115	37520	1E6

## A.4 Chromium

The promising optical pumping schemes of  $\text{Cr}^+$  are shown in Table A.7. All ions are found in the ground state at room temperature, requiring that all optical pumping schemes start from that state. Traditional CLS measurements of Cr require atomic charge exchange reactions to neutralize the beam, with 12% of the total population in the electronic state that is probed. A large gain in sensitivity is expected through optical pumping of Cr.

Table A.7: Optical Pumping Schemes of  $\text{Cr}^+$

Pumping Ground State ( $\text{cm}^{-1}$ )	Pumping Excited State ( $\text{cm}^{-1}$ )	$A$ ( $\text{s}^{-1}$ )	$\lambda$ (nm)	CLS Ground State ( $\text{cm}^{-1}$ )	Population in State	CLS Excited State ( $\text{cm}^{-1}$ )	$A$ ( $\text{s}^{-1}$ )
0	48632	2.09E8	205.6	12496	0.586	48632	2.22E8
				12496	0.586	47751	1.99E8
				12147	0.293	47040	1.19E8
0	48491	1.63E8	206.2	12303	0.405	1.63E8	
				12303	0.405	47227	6.27E7
				12147	0.218	47040	1.19E8
				12147	0.218	48398	9.81E7
0	49005	1.06E7	204.1	19797	0.329	49005	1.39E8
				19797	0.329	49564	1.1E8
				19797	0.329	49351	4.5E7
0	49351	7.65E6	202.6	20024	0.282	1.38E8	
				20024	0.282	49838	1.98E6
				19797	0.134	49005	1.39E8
				19797	0.134	49544	1.1E8

## A.5 Manganese

Promising optical pumping schemes for  $\text{Mn}^+$  are shown in Table A.8. The entire electronic population is found in the ground state of  $\text{Mn}^+$ . Typically atomic charge exchange reactions are required for CLS measurements, with 12% of the total ion population in the state being probed. There are relatively few possible optical pumping schemes, with only transition is

suitable for the pumping step of the scheme.

Table A.8: Optical Pumping Schemes of  $\text{Mn}^+$

Pumping Ground State ( $\text{cm}^{-1}$ )	Pumping Excited State ( $\text{cm}^{-1}$ )	$A$ ( $\text{s}^{-1}$ )	$\lambda$ (nm)	CLS Ground State ( $\text{cm}^{-1}$ )	Population in State	CLS Excited State ( $\text{cm}^{-1}$ )	$A$ ( $\text{s}^{-1}$ )
0	43370	1.55E6	230.5	9472	0.584	43557	1.96E8
				9472	0.584	43484	1.86E8
				9472	0.584	43370	1.86E8
				14325	0.136	43370	4.32E7

## A.6 Iron

The promising optical pumping schemes of  $\text{Fe}^+$  are shown in Table A.10, with the electronic population of the low-energy states shown in Table A.9.

Table A.9: Low-energy populated states of  $\text{Fe}^+$

State ( $\text{cm}^{-1}$ )	Population
0	0.863
384	0.109
667	0.021
862	0.006
977	0.002

The vast majority of the electronic population is in the ground state of  $\text{Fe}^+$ . Typical CLS measurements require atomic charge exchange reactions, where only 5% of the total ion beam is in the electronic state being probed. There are only two transitions from the low-energy states that can be used for optical pumping. Both transitions pump ions into the electronic state located at  $7955 \text{ cm}^+$ , from which there are only a handful of transitions

suitable for laser spectroscopy measurements. A very large gain in sensitivity is expected with optical pumping.

Table A.10: Optical Pumping Schemes of Fe<sup>+</sup>

Pumping Ground State (cm <sup>-1</sup> )	Pumping Excited State (cm <sup>-1</sup> )	A (s <sup>-1</sup> )	λ (nm)	CLS Ground State (cm <sup>-1</sup> )	Population in State	CLS Excited State (cm <sup>-1</sup> )	A (s <sup>-1</sup> )
0	44232	4.85E6	226.1	7955	0.564	44232	2.11E8
				7955	0.564	44446	1.13E8
0	44446	4.14E6	224.9	7955	0.444	44232	2.11E8
				7955	0.444	44446	1.13E8

## A.7 Cobalt

The promising optical pumping schemes of Co<sup>+</sup> are shown in Table A.12, with the populated low-energy electronic states shown in Table A.11.

Table A.11: Low-energy populated states of Co<sup>+</sup>

State (cm <sup>-1</sup> )	Population
0	0.998
950	0.002

Essentially all of the electronic population is found in the ground state. CLS measurements typically require atomic charge exchange reactions, resulting in only 5% of the atoms in the state being probed. Many optical pumping schemes of Co<sup>+</sup> require very deep UV light but it remains a very promising case for the optical pumping system, as the gain in sensitivity is very large in the schemes that are accessible to the BECOLA pulsed laser system.

Table A.12: Optical Pumping Schemes of  $\text{Co}^+$

Pumping Ground State ( $\text{cm}^{-1}$ )	Pumping Excited State ( $\text{cm}^{-1}$ )	$A$ ( $\text{s}^{-1}$ )	$\lambda$ (nm)	CLS Ground State ( $\text{cm}^{-1}$ )	Population in State	CLS Excited State ( $\text{cm}^{-1}$ )	$A$ ( $\text{s}^{-1}$ )
0	48556	1.67E7	205.9	9812	0.692	45197	1.7E6
				9812	0.692	45378	1.39E6
0	49697	7.68E7	201.2	10708	0.644	45972	1.01E6
0	49348	9.83E7	202.6	9812	0.589	45197	1.7E6
				9812	0.589	45378	1.39E6

## A.8 Nickel, Copper, and Zinc

No suitable optical pumping schemes were identified for Ni, Cu, and Zn. The most suitable ground state transitions of Ni and Cu require 150 nm light, and will not be experimentally possible at BECOLA for the foreseeable future. There is a ground state transition of  $\text{Zn}^+$ , exciting the  $3d^{10}4s^2S_{1/2}$  to  $3d^{10}4p^2P_{3/2}^o$  transition and requiring 202.5 nm, but it is a cyclical transition and does not feature branches from the excited state to metastable states accessible to the BECOLA CW laser system.

## A.9 Yttrium

The promising optical pumping schemes of  $\text{Y}^+$  are shown in Table A.14 with the room temperature electronic population distribution shown in Table A.13.

Table A.13: Low-energy populated states of  $\text{Y}^+$

State ( $\text{cm}^{-1}$ )	Population
0	0.949
840	0.051

Almost all of the electronic population is found in the ground state of  $Y^+$ . There are multiple transitions suitable for CLS from the ground state, and atomic charge exchange reactions are not necessary. Optical pumping can benefit the study of  $Y^+$  because the ground state has electronic angular momentum  $J = 0$  and the HFS does not feature splitting. The nuclear moments cannot be deduced without the hyperfine splitting, but by pumping the electronic population to another state, the hyperfine splitting can be observed.

Table A.14: Optical Pumping Schemes of  $Y^+$

Pumping Ground State ( $\text{cm}^{-1}$ )	Pumping Excited State ( $\text{cm}^{-1}$ )	$A$ ( $\text{s}^{-1}$ )	$\lambda$ (nm)	CLS Ground State ( $\text{cm}^{-1}$ )	Population in State	CLS Excited State ( $\text{cm}^{-1}$ )	$A$ ( $\text{s}^{-1}$ )
0	28595	3.46E7	349.7	840	0.697	32048	2.77E8
				840	0.697	28595	1.13E8
				8003	0.224	28595	3.93E7
				8003	0.224	27227	1.33E7
0	32124	1.32E6	311.3	1045	0.498	32124	2.05E8
				1045	0.498	28730	1.32E8
				1045	0.498	27532	1.08E8
				840	0.252	32048	2.77E8
				840	0.252	28595	1.13E8
0	44568	1.22E8	224.3	3296	0.438	33336	1.16E8
				3296	0.438	26147	1.01E8
				14098	0.375	44568	2.32E8
				14098	0.375	32283	1.16E7

## A.10 Zirconium

The promising optical pumping schemes of  $Zr^+$  are shown in Table tab:Zr and the electronic population distribution is shown in Table A.15. In contrast to the other elements in this work, data about the transitions is not based on the Kurucz database. The experimental branching ratios from Ljung *et al.* [103] were used instead, as the experimental data was found to better describe the results of the commissioning experiments.

Table A.15: Low-energy populated states of  $\text{Zr}^+$ 

State ( $\text{cm}^{-1}$ )	Population
0	0.723
314	0.239
767	0.037

There are suitable ground state transitions in  $\text{Zr}^+$  without optical pumping, but a modest gain in sensitivity can be gained through optical pumping. All optical pumping schemes involve pumping ions from the first excited state located at  $314 \text{ cm}^{-1}$  to the ground state, from which CLS measurements can be performed.

Table A.16: Optical Pumping Schemes of  $\text{Zr}^+$ 

Pumping Ground State ( $\text{cm}^{-1}$ )	Pumping Excited State ( $\text{cm}^{-1}$ )	$A$ ( $\text{s}^{-1}$ )	$\lambda$ (nm)	CLS Ground State ( $\text{cm}^{-1}$ )	Population in State	CLS Excited State ( $\text{cm}^{-1}$ )	$A$ ( $\text{s}^{-1}$ )
314	27983	2.92E7	361.4	0	0.830	27983	1.34E8
				0	0.830	36451	1.8E8
314	30435	7.67E6	331.9	0	0.801	27983	1.34E8
				0	0.801	36451	1.8E8
314	29505	4.38E6	342.6	0	0.771	27983	1.34E8
				0	0.771	36451	1.8E8

## A.11 Niobium

The promising optical pumping schemes of  $\text{Nb}^+$  are shown in Table A.18 and the electronic population distribution is shown in Table A.17.

Table A.17: Low-energy populated states of Nb<sup>+</sup>

State (cm <sup>-1</sup> )	Population
0	0.316
158	0.443
438	0.193
801	0.047

The electronic population is spread among four low-energy states, from which there are limited options for optical transitions. Available transitions have weak oscillator strengths, leading to low detection efficiency. Through optical pumping the electronic population can be moved to a state from which a strong transition can be probed. The first demonstration of optical pumping for electronic population manipulation for CLS measurements was used to study rare Nb isotopes [28] and the optical pumping simulation identifies the optical pumping scheme used in that experiment as the most promising. Although the low-energy states feature weak oscillator strengths, two optical pumping schemes are included that probe the first excited state of Nb<sup>+</sup>, as a consideration due to its relatively high electronic population.

Table A.18: Optical Pumping Schemes of Nb<sup>+</sup>

Pumping Ground State (cm <sup>-1</sup> )	Pumping Excited State (cm <sup>-1</sup> )	A (s <sup>-1</sup> )	λ (nm)	CLS Ground State (cm <sup>-1</sup> )	Population in State	CLS Excited State (cm <sup>-1</sup> )	A (s <sup>-1</sup> )
438	37797	3.09E7	267.6	158	0.467	35520	2.52E7
				158	0.467	34886	1.09E7
0	36731	9.49E6	272.2	158	0.465	35520	2.52E7
				158	0.465	34886	1.09E7
158	37298	1.27E8	269.2	2356	0.275	36731	1.2E8
				2356	0.275	37298	2.05E8
				2356	0.275	33351	1.2E8
158	38985	1.17E7	257.5	12805	0.182	38985	4.73E7
				12805	0.182	44638	3.51E7

## A.12 Molybdenum

The promising optical pumping schemes of Mo<sup>+</sup> are shown in Table A.19. There are no low-energy states, and all of the ions can be found in the ground state at room temperature. Typical CLS measurements of Mo<sup>+</sup> requires atomic charge exchange reactions, where only 4% of the atomic population is in the state being probed. Mo is a very promising case for the optical pumping system, as the optical pumping simulation predicts electronic populations of up to 70% for CLS measurements.

Table A.19: Optical Pumping Schemes of Mo<sup>+</sup>

Pumping Ground State (cm <sup>-1</sup> )	Pumping Excited State (cm <sup>-1</sup> )	A (s <sup>-1</sup> )	λ (nm)	CLS Ground State (cm <sup>-1</sup> )	Population in State	CLS Excited State (cm <sup>-1</sup> )	A (s <sup>-1</sup> )
0	49481	2.57E7	202.1	13460	0.702	48959	2.27E8
				13960	0.702	47999	5.63E7
0	48860	1.84E7	204.6	12900	0.544	47232	8.76E7
				12900	0.544	47999	1.6E8
0	49608	1.57E7	201.5	12034	0.34	46148	1.28E8
				12034	0.34	46614	8.39E7

## A.13 Technetium

Technetium was not considered for this study due to a dearth of knowledge about its electronic structure (See Section 3.4.2).

## A.14 Ruthenium

The promising optical pumping schemes of  $\text{Ru}^+$  are shown in Table A.20. All of the electronic population is found in the ground state of  $\text{Ru}^+$ . Typical CLS measurements of  $\text{Ru}^+$  require atomic charge exchange reactions, and only 7% of the atoms will populate the state being probed. There is only one optical pumping step that is available for use at BECOLA, exciting ions in the ground state to an excited state located at  $50845 \text{ cm}^{-1}$  and requiring 196 nm light. This is the edge of the wavelength range of the BECOLA pulsed laser system. The excited state strongly decays to a metastable state at  $10150 \text{ cm}^{-1}$ , from which CLS measurements can be performed.

Table A.20: Optical Pumping Schemes of  $\text{Ru}^+$

Pumping Ground State ( $\text{cm}^{-1}$ )	Pumping Excited State ( $\text{cm}^{-1}$ )	$A$ ( $\text{s}^{-1}$ )	$\lambda$ (nm)	CLS Ground State ( $\text{cm}^{-1}$ )	Population in State	CLS Excited State ( $\text{cm}^{-1}$ )	$A$ ( $\text{s}^{-1}$ )
0	50845	1.72E8	196.6	10150	0.746	46711	9.27E8
				10150	0.746	46420	1.67E8
				19378	0.153	55694	7.87E8
				19378	0.153	50845	4.21E8

## A.15 Rhodium, Palladium, Silver, and Cadmium

There are no suitable optical schemes for the cases of Rh (160 nm), Pd (137 nm), Ag (120 nm), and Cd (226 nm). Rh, Pd, and Ag require vacuum UV laser light, down to 120 nm

in the case of Ag, and will not be possible in the foreseeable future at BECOLA. Cd does feature a transition at 226 nm, exciting the  $4d^{10}5s^2S_{1/2}$  to  $4d^{10}5p^2P_{1/2}^o$  transition, but it is almost completely cyclical and cannot be used for optical pumping. The next available transition requires 105 nm and will not be possible.

# APPENDIX B

## Logic of Shutter Control System

A physical shutter was used to block and unblock the pulsed laser light during the commissioning experiments. The shutter allowed measurements of the fluorescence signal with and without the pulsed laser light in quick succession and mitigated any systematic changes in the ion source intensity or laser power. The shutter was controlled by the BECOLA DAQ system. A schematic diagram of the electronics modules can be seen in Figure B.1. A trigger signal from the pulsed laser is used to start the DAQ system, and the physical shutter is opened and closed in one second intervals to control for systematic fluctuations. Approximately  $350 \mu\text{s}$  after the trigger signal arrives from the pulsed laser, the trapped ions are released from the trap and a signal is sent to a level adapter to convert the TTL signal to NIM. The NIM signal is sent to a fan-in/fan-out(FIFO) electronic module. From the FIFO module, a signal is sent to a Gate Generator module to delay and broaden the signal. From the gate generator, the signal is split and sent to two separate scale down modules(SDM). In one module, after 10 ion bunch releases, a signal is sent to one input of a coincidence module and to the second SDM. In a second SDM, the signal from the first SDM is scaled down to one pulse per two pulses, and two signals are created and used. One signal from the second SDM is sent to the same coincidence unit as the first SDM. When the signals from the SDM coincide, a signal is sent to a gate generator with start/stop operation. The gate generator provides a 5 V signal that opens the shutter. The second output from the second SDM is sent to the gate generator with start/stop operation, and is used to stop the 5 V signal that

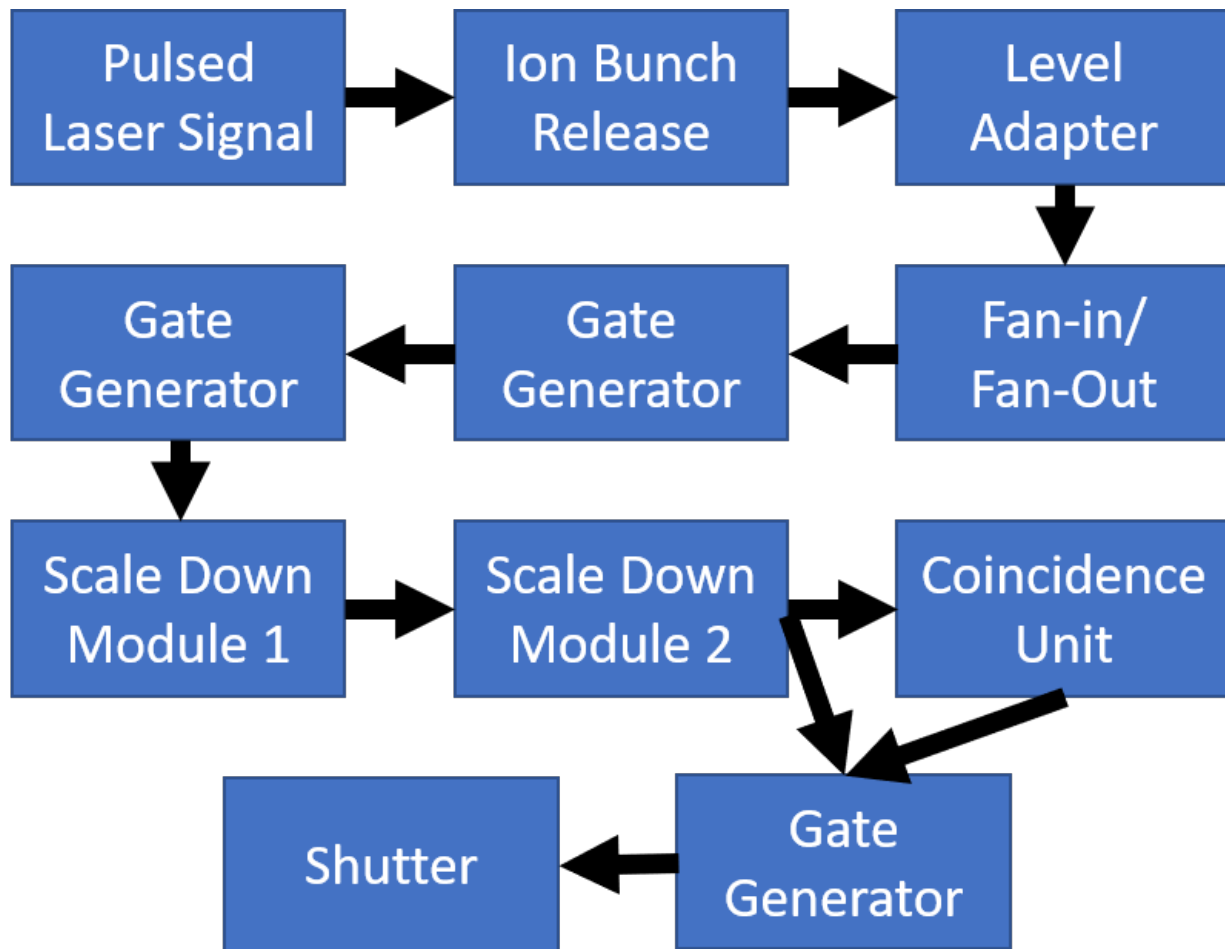


Figure B.1: Schematic diagram of the connectivity of the electronic modules used to control the physical shutter for measurement of the optical pumping effect.

it generates. The result is that for every 10 ion bunches, a signal is generated to either open or close the shutter.

## REFERENCES

## REFERENCES

- [1] K. Minamisono, P.F. Mantica, A. Klose, S. Vinnikova, A. Schneider, B. Johnson, and B.R. Barquest. Commissioning of the collinear laser spectroscopy system in the BECOLA facility at NSCL. *Nucl. Instrum. Methods Phys. Res. A*, **709**:85–94, 2013.
- [2] D.M. Rossi, K. Minamisono, B.R. Barquest, G. Bollen, K. Cooper, M. Davis, K. Hamerton, M. Hughes, P.F. Mantica, D.J. Morrissey, R. Ringle, J.A. Rodriguez, C.A. Ryder, S. Schwarz, R. Strum, C. Sumithrarachi, D. Tarazona, and S. Zhao. A field programmable gate array-based time-resolved scaler for collinear laser spectroscopy with bunched radioactive potassium beams. *Rev. Sci. Instrum.*, **85**:093503, 2014.
- [3] B. Cheal and K.T. Flanagan. Progress in laser spectroscopy at radioactive ion beam facilities. *J. Phys. G Nucl. Part. Phys.*, **37**:113101, 2010.
- [4] P. Campbell, I.D. Moore, and M.R. Pearson. Laser spectroscopy for nuclear structure physics. *Prog. Part. Nucl. Phys.*, **86**:127–180, 2016.
- [5] E.W. Otten. *Nuclear radii and moments of unstable isotopes*. Springer US, Boston, MA, 1989.
- [6] H.-Jürgen Kluge and W. Nörtershäuser. Lasers for nuclear physics. *Spectrochim. Acta A*, **58**:1031–1045, 2003.
- [7] K. Blaum, J. Dilling, and W. Nörtershäuser. Precision atomic physics techniques for nuclear physics with radioactive beams. *Phys. Scr.*, **T152**:014017, 2013.
- [8] I. Angeli and K.P. Marinova. Table of experimental nuclear ground state charge radii: An update. *At. Data Nucl. Data Tables*, **99**:69–95, 2013.
- [9] M. Avgoulea, Yu. P. Gangrsky, K.P. Marinova, S.G. Zemlyanoi, S. Fritzsche, D. Iablonskyi, C. Barbieri, E.C. Simpson, P.D. Stevenson, J. Billowes, P. Campbell, B. Cheal, B. Tordoff, M.L. Bissell, D.H. Forest, M.D. Gardner, G. Tungate, J. Huikari, A. Nieminen, H. Penttilä, and J. Äystö. Nuclear charge radii and electromagnetic moments of radioactive scandium isotopes and isomers. *J. Phys. G Nucl. Part. Phys.*, **38**:025104, 2011.

- [10] Yu. P. Gangrsky, K.P. Marinova, S.G. Zemlyanoi, I.D. Moore, J. Billowes, P. Campbell, K.T. Flanagan, D.H. Forest, J.A.R. Griffith, J. Huikari, R. Moore, A. Nieminen, H. Thayer, G. Tungate, and J. Äystö. Nuclear charge radii of neutron deficient titanium isotopes  $^{44}\text{Ti}$  and  $^{45}\text{Ti}$ . *J. Phys. G Nucl. Part. Phys.*, **30**:1089–1098, 2004.
- [11] H. Heylen, C. Babcock, R. Beerwerth, J. Billowes, M.L. Bissell, K. Blaum, J. Bonnard, P. Campbell, B. Cheal, T. Day Goodacre, D. Fedorov, S. Fritzsche, R.F. Garcia Ruiz, W. Geithner, Ch. Geppert, W. Gins, L. K. Grob, M. Kowalska, K. Kreim, S.M. Lenzi, I.D. Moore, B. Maass, S. Malbrunot-Ettenauer, B. Marsh, R. Neugart, G. Neyens, W. Nörtershäuer, T. Otsuka, J. Papuga, R. Rossel, S. Rothe, R. Sánchez, Y. Tsunoda, C. Wraith, L. Xie, X.F. Yang, and D.T. Yordanov. Changes in nuclear structure along the Mn isotopic chain studied via charge radii. *Phys. Rev. C*, **94**:054321, 2016.
- [12] K. Minamisono, D.M. Rossi, R. Beerwerth, S. Fritzsche, D. Garand, A. Klose, Y. Liu, B. Maaß, P.F. Mantica, A.J. Miller, P. Müller, W. Nazarewicz, W. Nörtershäuser, E. Olsen, M.R. Pearson, P.-G. Reinhard, E.E. Saperstein, C. Sumithrarachchi, and S.V. Tolokonnikov. Charge radii of neutron deficient  $^{52,53}\text{Fe}$  produced by projectile fragmentation. *Phys. Rev. Lett.*, **117**:252501, 2016.
- [13] S. Kaufmann, J. Simonis, S. Bacca, J. Billowes, M.L. Bissell, K. Blaum, B. Cheal, R.F. Garcia Ruiz, W. Gins, C. Gorges, G. Hagen, H. Heylen, A. Kanellakopoulos, S. Malbrunot-Ettenauer, M. Miorelli, R. Neugart, G. Neyens, W. Nörtershäuer, R. Sánchez, S. Sailer, A. Schwenk, T. Ratajczyk, L.V. Rodríguez, L. Wehner, C. Wraith, L. Xie, Z.Y. Xu, X.F. Yang, and D.T. Yordanov. Charge radius of the short-lived  $^{68}\text{Ni}$  and correlation with the dipole polarizability. *Phys. Rev. Lett.*, **124**:132502, 2020.
- [14] M.L. Bissell, T. Carette, K.T. Flanagan, P. Vingerhoets, J. Billowes, K. Blaum, B. Cheal, S. Fritzsche, M. Godefroid, M. Kowalska, J. Krämer, R. Neugart, G. Neyens, W. Nörtershäuser, and D.T. Yordanov. Cu charge radii reveal a weak sub-shell effect at  $N = 40$ . *Phys. Rev. C*, **93**:064318, 2016.
- [15] R.P. de Groote, J. Billowes, C.L. Binnersley, M.L. Bissell, T.E. Cocolios, T. Day Goodacre, G.J. Farooq-Smith, D.V. Fedorov, K.T. Flanagan, S. Franchoo, R.F. Garcia Ruiz, W. Gins, J.D. Holt, A. Koszorús, K.M. Lynch, T. Miyagi, W. Nazarewicz, G. Neyens, P.-G. Reinhard, S. Rothe, H.H. Stroke, A.R. Vernon, K.D.A. Wendt, S.G. Wilkins, Z.Y. Xu, and X.F. Yang. Measurement and microscopic description of odd-even staggering of charge radii of exotic copper isotopes. *Nat. Phys.*, **16**:620–624, 2020.
- [16] L. Xie, X.F. Yang, C. Wraith, C. Babcock, J. Bieroń, J. Billowes, M.L. Bissell, K. Blaum, B. Cheal, L. Filippin, K.T. Flanagan, R.F. Garcia Ruiz, W. Gins,

- G. Gaigalas, M. Godefroid, C. Gorges, L.K. Grob, H. Heylen, P. Jönsson, S. Kaufmann, M. Kowalska, J. Krämer, S. Malbrunot-Ettenauer, R. Neugart, G. Neyens, W. Nörtershäuser, T. Otsuka, J. Papuga, R. Sánchez, Y. Tsunoda, and D.T. Yordanov. Nuclear charge radii of  $^{62-80}\text{Zn}$  and their dependence on cross-shell proton excitations. *Phys. Lett. B*, **797**:134805, 2019.
- [17] A.J. Miller, K. Minamisono, A.Klose, D.Garand, C.Kujawa, J.D. Lantis, Y. Liu, B. Maaß, P.F. Mantica, W. Nazarewicz, W.Nörtershäuser, S.V. Pineda, P.-G. Reinhard, D.M. Rossi, F. Sommer, C. Sumithrarachchi, A. Teigelhöfer, and J. Watkins. Proton superfluidity and charge radii in proton-rich calcium isotopes. *Nat. Phys.*, **15**:432–436, 2019.
- [18] D.M. Rossi, K. Minamisono, H.B. Asberry, G. Bollen, B.A. Brown, K. Cooper, B. Isherwood, P.F. Mantica, A. Miller, D.J. Morrissey, R. Ringle, J.A. Rodriguez, C. A. Ryder, A. Smith, R. Strum, and C. Sumithrarachchi. Charge radii of neutron-deficient  $^{36}\text{K}$  and  $^{37}\text{K}$ . *Phys. Rev. C*, **92**:014305, 2015.
- [19] F. Touchard, P. Guimbal, S. Buttgenbach, R. Klapisch, M. De Saint Simon, J.M. Serre, and C. Thibault. Isotope shifts and hyperfine structure of  $^{38-47}\text{K}$  by laser spectroscopy. *Phys. Lett.*, **108B**:169–171, 1982.
- [20] A.Klein, B.A. Brown, U. Georg, M. Keim, P. Lievens, R. Neugart, M. Neuroth, R.E. Silverans, L. Vermeeren, and ISOLDE Collaboration. Moments and mean square charge radii of short-lived argon isotopes. *Nuc. Phys. A*, **607**:1–22, 1996.
- [21] R. Broda, B. Fornal, W. Królas, T. Pawlat, D. Bazzacco, S. Lunardi, C. Rossi-Alvarez, R. Menegazzo, G. de Angelis, P. Bednarczyk, J. Rico, D. De Acuña, P.J. Daly, R.H. Mayer, M. Sferrazza, H. Grawe, K.H. Maier, and R. Schubart.  $N = 40$  neutron subshell closure in the  $^{68}\text{Ni}$  nucleus. *Phys. Rev. Lett.*, **74**:868–871, 1995.
- [22] W. Rother, A. Dewald, H. Iwasaki, S.M. Lenzi, K. Starosta, D. Bazin, T. Baugher, B.A. Brown, H.L. Crawford, C. Fransen, A. Gade, T.N. Ginter, T. Glasmacher, G.F. Grinyer, M. Hackstein, G. Illie, J. Jolie, S. McDaniel, D. Miller, P. Petkov, Th. Pissulla, A. Ratkiewicz, C.A. Ur, P. Voss, K.A. Walsh, D. Weisshaar, and K.-O Zell. Enhanced quadrupole collectivity at  $N = 40$ : The case of neutron-rich Fe isotopes. *Phys. Rev. Lett.*, **106**:022502, 2011.
- [23] A. Gade, R.V.F. Janssens, T. Baugher, D. Bazin, B.A. Brown, M.P. Carpenter, C.J. Chiara, A.N. Deacon, S.J. Freeman, G.F. Grinyer, C.R. Hoffman, B.P. Kay, F.G. Kondev, T. lauritsen, S. Mcdaniel, K. Meierbachtol, A. Katkiewicz, S.R. Stroberg, K.A. Walsh, D. Weisshaar, R. Winkler, and S. Zhu. Collectivity at  $N = 40$  in neutron-rich  $^{64}\text{Cr}$ . *Phys. Rev. C*, **81**:051304, 2010.

- [24] B. Pritychenko, M. Birch, B. Singh, and M. Horoi. Tables of the e2 transition probabilities from the first  $2^+$  states in even-even nuclei. *At. Data Nucl. Data Tables*, **107**:1, 2016.
- [25] B. Cheal, M.D. Gardner, M. Avgoulea, J. Billowes, M.L. Bissell, P. Campbell, T. Eronen, K.T. Flanagan, D.H. Forest, J. Huikari, A. Jokinen, B.A. Marsh, I.D. Moore, A. Nieminen, H. Penttilä, S. Rinta-Antila, B. Tordoff, G. Tungate, and J. Äystö. The shape transition in the neutron-rich yttrium isotopes and isomers. *Phys. Lett. B*, **645**:133–137, 2007.
- [26] D.H. Forest, J. Billowes, P. Campbell, P. Dendooven, K.T. Flanagan, J.A.R. Griffith, J. Huikari, A. Jokinen, R. Moore, A. Nieminen, H.L. Thayer, G. Tungate, S. Zemlyanoi, and J. Äystö. Laser spectroscopy of neutron deficient zirconium isotopes. *J. Phys. G Nucl. Part. Phys.*, **28**:L63–L68, 2002.
- [27] P. Campbell, H.L. Thayer, J. Billowes, P. Dendooven, K.T. Flanagan, D.H. Forest, J.A.R. Griffith, J. Huikari, A. Jokinen, R. Moore, A. Nieminen, G. Tungate, S. Zemlyanoi, and J. Äystö. Laser spectroscopy of cooled zirconium fission fragments. *Phys. Rev. Lett.*, **89**:082501, 2002.
- [28] B. Cheal, K. Baczyńska, J. Billowes, P. Campbell, F.C. Charlwood, T. Eronen, D.H. Forest, A. Jokinen, T. Kessler, I.D. Moore, M. Reponen, S. Rothe, M. Ruffer, A. Saastamoinen, G. Tungate, and J. Äystö. Laser spectroscopy of niobium fission fragments: First use of optical pumping in an ion beam cooler buncher. *Phys. Rev. Lett.*, **102**:222501, 2009.
- [29] F.C. Charlwood, K. Baczyńska, J. Billowes, P. Campbell, B. Cheal, T. Eronen, D.H. Forest, A. Jokinen, T. Kessler, I.D. Moore, H. Penttilä, R. Powis, M. Ruffer, A. Saastamoinen, G. Tungate, and J. Äystö. Nuclear charge radii of molybdenum fission fragments. *Phys. Lett. B*, **674**:23–27, 2009.
- [30] R. Ferrer, N. Bree, T.E. Cocolios, I.G. Darby, H. De Witte, W. Dexters, J. Diriken, J. Elseviers, S. Franchoo, M. Huyse, N. Kesteloot, Yu. Kudryavtsev, D. Pauwels, D. Radulov, T. Roger, H. Savajols, P. Van Duppen, and M. Venahrt. In-gas-cell laser ionization spectroscopy in the vicinity of  $^{100}\text{Sn}$ : Magnetic moments and mean-square charge radii of  $N = 50$ -54 Ag. *Phys. Lett. B*, **728**:191–197, 2014.
- [31] U. Dinger, J. Eberz, G. Huber, and R. Menges. Nuclear moments and change in the charge radii of neutron-deficient silver isotopes. *Nucl. Phys.*, **A503**:331–348, 1989.
- [32] M. Hammen, W. Nörtershäuser, D.L. Balabanski, M.L. Bissell, K. Blaum, I. Budinčević, B. Cheal, K.T. Flanagan, N. Frömmgen, G. Georgiev, Ch. Geppert,

- M. Kowalska, K. Kreim, A. Krieger, W. Nazarewicz, R. Neugart, G. Neyens, J. Papuga, P.-G. Reinhard, M.M. Rajabali, S. Schmidt, and D.T. Yordanov. From calcium to cadmium: testing the pairing functional through charge radii measurements of  $^{100-130}\text{Cd}$ . *Phys. Rev. Lett.*, **121**:102501, 2018.
- [33] H. Schatz, A. Aprahamian, J. Görres, M. Wiescher, T. Rauscher, J.F. Rembges, F.-K. Thielemann, B. Pfeiffer, P. Möller, K.L. Kratz, H. Herndl, B.A. Brown, and H. Rebel. rp-process nucleosynthesis at extreme temperature and density conditions. *Phys. Rep.*, **294**:167–263, 1998.
- [34] S. J. Zheng, F. R. Xu, S.F. Shen, H.L. Liu, R. Wyss, and Y.P. Yan. Shape coexistence and triaxiality in nuclei near  $^{80}\text{Zr}$ . *Phys. Rev. C*, **90**:064309, 2014.
- [35] M. Akbari and A. Kardan. Shape evolution and coexistence in neutron-deficient Kr, Rb, Sr, and Zr nuclei. *Nucl. Phys. A*, **990**:109–117, 2019.
- [36] F.N. Mortensen, J.M. Scott, and Stirling A. Colgate. How archival test data contribute to certification. *Los Alamos Science*, **28**:38–46, 2003.
- [37] L. Ahle, M. Hausmann, R. Relfarth, K. Roberts, M. Roeben, B. Rusnak, and D. Vieira. Realizing the opportunities of neutron cross-section measurements at RIA. *AIP Conf. Proc.*, **769**:796–799, 2005.
- [38] M.N. Kreisler. National nuclear security and other applications of rare isotopes. In *Proceedings of Particle Accelerator Conference (PAC07)*, pages 124–126. Institute of Electrical and Electronics Engineers, 2007.
- [39] E. Hartouni. Role of radioactive beams in stockpile stewardship science, 2010. presentation.
- [40] R. Jeanloz. Science-based stockpile stewardship. *Physics Today*, **53**:44–50, 2000.
- [41] J.E. Escher, J.T. Burke, F.S. Dietrich, N.D. Scielzo, I.J. Thompson, and W. Younes. Compound-nuclear reaction cross sections from surrogate measurements. *Rev. Mod. Phys.*, **84**:353–397, 2012.
- [42] A. Spyrou, S.N. Liddick, A.C. Larsen, M. Guttormsen, K. Cooper, A.C. Dombos, D.J. Morrissey, F. Naqvi, G. Perdikakis, S.J. Quinn, T. Renstrøm, J.A. Rodriguez, A. Simon, C.S. Sumithrarachchi, and R.G.T. Zegers. Novel technique for constraining r-process ( $n, \gamma$ ) reaction rates. *Phys. Rev. Lett.*, **113**:232502, 2014.

- [43] J.A. Paisner. Atomic vapor laser isotope separation. *Appl. Phys. B*, **46**:253–260, 1988.
- [44] C.R. Locke, T. Kobayashi, T. Fujiwara, and K. Midorikawa. Selective photoionization of palladium isotopes using a two-step excitation scheme. *Appl. Phys. B*, **123**:240, 2017.
- [45] T. Kobayashi T. Fujiwara and K. Midorikawa. Selective resonance photoionization of odd mass zirconium isotopes towards efficient separation of radioactive waste”. *Sci. Rep.*, **9**:1754, 2019.
- [46] W.S. Yang, Y. Kim, R.N. Hill, T.A. Taiwo, and H.S. Khalil. Long-lived fission product transmutation studies. *Nucl. Sci. Eng.*, **146**:291–318, 2004.
- [47] S. Chiba, T. Wakabayashi, Y. Tachi, N. Takaki, A. Terashima, S. Okumura, and T. Yoshida. Method to reduce long-lived fission products by nuclear transmutations with fast spectrum reactors. *Sci. Rep.*, **7**:13961, 2017.
- [48] T.H. Maiman. Stimulated optical radiation in ruby. *Nature*, **187**:493–494, 1960.
- [49] K.-R. Anton, S.L. Kaufman, W. Klempt, G. Moruzzi, R. Neugart, E.-W Otten, and B. Schinzler. Collinear laser spectroscopy on fast atomic beams. *Phys. Rev. Lett.*, **40**:642–645, 1978.
- [50] O.B. Tarasov and D. Bazin. Lise++: Radioactive beam production with in-flight separators. *Nucl. Instrum. Methods Phys. Res. B*, **266**:4657–4664, 2008.
- [51] M.J.G. Borge and Björn Jonson. ISOLDE past, present and future. *J. Phys. G Nucl. Part. Phys.*, **44**:044011, 2017.
- [52] A. Voss, T.J. Procter, O. Shelbaya, P. Amaudruz, F. Buchinger, J.E. Crawford, S. Daviel, E. Mané, M.R. Pearson, and W. Al Tamimi. The collinear fast beam laser spectroscopy( $C_{FBS}$ ) experiment at TRIUMF. *Nucl. Instrum. Meth. Phys. Res. A*, **811**:57–69, 2016.
- [53] U. Köster, P. Carbonez, A. Dorsival, J. Dvorak, R. Eichler, S. Fernandes, H. Frånberg, J. Neuhausen, Z. Novackova, R. Wilfinger, and A. Yakushev. (im-)possible ISOL beams. *Eur. Phys. J Spec. Top.*, **150**:285–291, 2007.
- [54] D.J. Morrissey, B.M. Sherrill, M. Steiner, A. Stolz, and I. Wiedenhoever. Commissioning the A1900 projectile fragment separator. *Nucl. Instrum. Methods Phys. Res. B*, **204**:90–96, 2003.

- [55] R.W. Boyd. *Nonlinear Optics*. Academic Press, Orlando, Florida, 2008.
- [56] N. Bendali, H.T. Duong, P. Juncar, J.M. Saint Jalm, and J.L. Vialle. Na<sup>+</sup>-Na charge exchange processes studied by collinear laser spectroscopy. *J. Phys. B At. Mol. Phys.*, **19**:233–238, 1986.
- [57] A. Klose, K. Minamisono, Ch. Geppert, N. Frömmgen, M. Hammen, J. Krämer, A. Krieger, C.D.P. Levy, P.F. Mantica, W. Nörtershäuser, and S. Vinnikova. Tests of atomic charge-exchange cells for collinear laser spectroscopy. *Nucl. Instrum. Methods Phys. Res. A*, **678**:114–121, 2012.
- [58] C.A. Ryder, K. Minamisono, H.B. Asberry, B. Isherwood, P.F. Mantica, A. Miller, D.M. Rossi, and R. Strum. Population distribution subsequent to charge exchange of 29.85 keV Ni<sup>+</sup> on sodium vapor. *Spectrochim. Acta. B*, **113**:16–21, 2015.
- [59] M. Keim, U. Georg, A. Klein, R. Neugart, M. Neuroth, S. Wilbert, P. Lievens, L. Vermeeren, B.A. Brown, and the ISOLDE Collaboration. Measurement of the electric quadrupole moments of <sup>26-29</sup>Na. *Eur. Phys. J. A*, **8**:31–40, 2000.
- [60] B. Fenker, J.A. Behr, D. Melconian, R.M.A. Anderson, M. Anholm, D. Ashery, R.S. Behling, I. Cohen, I. Craiciu, J.M. Donohue, C. Farfan, D. Friesen, A. Gorelov, J. McNeil, M. Mehlman, H. Norton, K. Olchanski, S. Smale, O. Theriault, A.N. Vantghem, and C.L. Warner. Precision measurement of the nuclear polarization in laser-cooled optically pumped <sup>37</sup>K. *New J. Phys.*, **18**:073028, 2016.
- [61] K. Baczynska, J. Billowes, P. Campbell, F.C. Charlwood, B. Cheal, T. Eronen, D.H. Forest, A. Jokinen, T. Kessler, I.D. Moore, M. Ruffer, G. Tungate, and J. Äystö. Nuclear spin determination of <sup>100m</sup>Y by collinear laser spectroscopy of optically pumped ions. *J. Phys. G: Nucl. Part. Phys.*, **37**:105103, 2010.
- [62] F.C. Charlwood, J. Billowes, P. Campbell, B. Cheal, T. Eronen, D.H. Forest, S. Fritzsche, M. Honma, A. Jokinen, I.D. Moore, H. Penttilä, R. Powis, A. Saastamoinen, G. Tungate, and J. Äystö. Ground state properties of manganese isotopes across the N=28 shell closure. *Phys. Lett. B*, **690**:346–351, 2010.
- [63] H. de Vries, C.W. de Jager, and C. de Vries. Nuclear charge-density-distribution parameters from elastic electron scattering. *At. Data Nucl. Data Tables*, **36**:495–536, 1987.
- [64] A. Estradé, R. Kanungo, W. Horiuchi, F. Ameil, J. Atkinson, Y. Ayyad, D. Cortina-Gil, I. Dillmann, A. Evdokimov, F. Farinon, H. Geissel, G. Guastalla, R. Janik, M. Kimura, R. Knöbel, J. Kurcewicz, Yu. A. Litvinov, M. Marta, M. Mostazo,

- I. Mukha, C. Nociforo, H.J. Ong, S. Pietri, A. Prochazka, C. Scheidenberger, B. Sitar, P. Strmen, Y. Suzuki, M. Takechi, J. Tanaka, I. Tanihata, S. Terashima, J. Vargas, H. Weick, and J.S. Winfield. Proton radii of  $^{12-17}\text{B}$  define a thick neutron surface in  $^{17}\text{B}$ . *Phys. Rev. Lett.*, **113**:132501, 2014.
- [65] F. Boehm and P.L. Lee. Changes of mean-square nuclear charge radii from isotope shifts of electronic  $K_\alpha$  x-rays. *At. Data Nucl. Data Tables*, **14**:605–611, 1974.
- [66] R. Engfer, H. Schneuwly, J.L. Vuilleumier, H.K. Walter, and A. Zehnder. Charge-distribution parameters, isotope shifts, isomer shifts, and magnetic hyperfine constants from muonic atoms. *At. Data Nucl. Data Tables*, **14**:509–597, 1974.
- [67] H. Schuler and J.E. Keyston. Über einen isotopenverschiebungseffekt der hyperfeinstrukturermene von thallium. *Z. Phys.*, **70**:1–9, 1931.
- [68] H. Schuler and Th. Schmidt. Über abweichungen des atomkerns von der kugelsymmetrie. *Z. Phys.*, **94**:457–468, 1935.
- [69] B. Maaß, T. Huther, K. König, Jörg Kramer, J. Krause, A. Lovato, P. Müller, Krzysztof Pachucki, M. Puchalski, R. Roth, R. Sánchez, F. Sommer, R.B. Wiringa, and W. Nörtershäuser. Nuclear charge radii of  $^{10,11}\text{B}$ . *Phys. Rev. Lett.*, **122**:182501, 2019.
- [70] W.H. King. *Isotope Shifts in Atomic Spectra*. Springer Science and Business Media, New York, 1984.
- [71] G. Fricke and K. Heilig. *Nuclear Charge Radii*. Springer-Verlag Berlin, Heidelberg, 2004.
- [72] D. York, N.M. Evensen, M. López Martínez, and J. De Basabe Delgado. Unified equations for the slope, intercept, and standard errors of the best straight line. *Am. J. Phys.*, **72**:367–375, 2004.
- [73] S. Kaufmann. *Laser spectroscopy of nickel isotopes with a new data acquisition system at ISOLDE*. PhD thesis, Technische Universität Darmstadt, 2019.
- [74] G. Zizak, J.D. Bradshaw, and J.D. Winefordner. Rate equation solution for the temporal behavior of a three-level system. *Appl. Opt.*, **19**:3631–3639, 1980.
- [75] R.L. Kurucz. The Kurucz Smithsonian Atomic and Molecular Database. In *Astrophysical Applications of Powerful New Databases*, pages 205–210. International Astronomical Union, 1995.

- [76] A. Kramida, Yu. Ralchenko, J. Reader, and NIST ASD Team. *NIST Atomic Spectra Database (Version 5.7.1)*. [Online] <https://www.nist.gov/pml/atomic-spectra-database>, 2019.
- [77] B.R. Barquest, G. Bollen, P.F. Mantica, K. Minamisono, R. Ringle, S. Schwarz, and C.S. Sumithrarachchi. RFQ beam cooler and buncher for collinear laser spectroscopy of rare isotopes. *Nucl. Instrum. Methods Phys. Res. A*, **866**:18–28, 2017.
- [78] B. Barquest. *An advanced ion guide for beam cooling and bunching for collinear laser spectroscopy of rare isotopes*. PhD thesis, Michigan State University, 2014.
- [79] A.V. Tolmachev, A.N. Vilkov, B. Bogdanov, L. Pasa-Tolic, C.D. Masselon, and R.D. Smith. Collisional activation of ions in RF ion traps and ion guides: The effective ion temperature treatment. *J. Am. Soc. Mass Spectrom.*, **15**:1616–1628, 2004.
- [80] R. Ringle. 3dCylPIC-a 3D particle-in-cell code in cylindrical coordinates for space charge simulations of ion trap and ion transport devices. *Int. J. Mass Spectrom.*, **303**:42–50, 2011.
- [81] P.W. Milonni and J.H. Eberly. *Laser Physics*. John Wiley and Sons, 2010.
- [82] T. Kron, R. Beerwerth, S. Raeder, S. Fritzsche, R. Heinke, P. Schönberg, M. Trümper, and K. Wendt. Hyperfine structure study of  $^{97,98,99}\text{Tc}$  in a new laser ion source for high-resolution laser spectroscopy. *Phys. Rev. C*, **102**:034307, 2020.
- [83] S. Raeder, T. Kron, R. Heinke, J.L. Henares, N. Lecesne, P. Schönberg, M. Trümper, and K. Wendt. High resolution spectroscopy of the hyperfine structure splitting in  $^{97,99}\text{Tc}$ . *Hyperfine Interact.*, **238**:15, 2017.
- [84] S.L. Kaufman. High-resolution laser spectroscopy in fast beams. *Opt. Commun.*, **17**:309–312, 1976.
- [85] A. Nieminen, P. Campbell, J. Billowes, D.H. Forest, J.A.R. Griffith, J. Huikari, A. Jokinen, I.D. Moore, R. Moore, G. Tungate, and J. Äystö. Cooling and bunching of ion beams for collinear laser spectroscopy. *Nucl. Instrum. Meth. Phys. Res. B*, **204**:563–569, 2003.
- [86] C.S. Sumithrarachchi and D.J. Morrissey, S. Schwarz, K. Lund, G. Bollen, R. Ringle, G. Savard, and A.C.C. Villari. Beam thermalization in a large gas catcher. *Nucl. Instrum. Methods Phys. Res.*, **463**:305–309, 2020.

- [87] Z. Nouri, R. Li, R.A. Holt, and S.D. Rosner. A penning sputter ion source with very low energy spread. *Nucl. Instrum. Methods Phys. Res. A*, **614**:174–178, 2010.
- [88] W. Paul. Electromagnetic traps for charged and neutral particles (Nobel Lecture). *Angew. Chem. Int. Ed. Engl.*, **29**:739–748, 1990.
- [89] A.J. Miller. *Measurements of Charge Radii of Neutron-Deficient Calcium Using Collinear Laser Spectroscopy at BECOLA*. PhD thesis, Michigan State University, 2019.
- [90] Matisse 2 TS. <http://www.sirah.com/laser/cw-ring-lasers/matisse-ts>.
- [91] Spectra-Physics Millennia eV. <https://www.spectra-physics.com/products/cw-lasers/millennia-ev>.
- [92] Spectra-Physics WaveTrain. <https://www.spectra-physics.com/products/tunable-lasers/wavetrain>.
- [93] Highfinesse WSU-30 Wavemeter. <https://www.highfinesse.com/en/wavelengthmeter>.
- [94] R-32734 stabilized HeNe laser. <http://www.newport.com/p/R-32734>.
- [95] Cobra-Stretch Pulsed Laser. <http://www.sirah.com/laser/pulsed-lasers/cobra-stretch>.
- [96] Quanta-Ray INDI Pulsed Nd:YAG Laser User’s Manual. <http://www.Spectra-Physics.com>.
- [97] Pulsed Dye Laser’s Manual version 2.0.4. <http://www.Spectra-Physics.com>.
- [98] Highfinesse Angstrom WS6-600 wavelength meter. <https://www.highfinesse.com/en/wavelengthmeter>.
- [99] Avantes Inc. <http://www.avantes.com>.
- [100] Fred version 19.40.2. <http://www.photonengr.com>.
- [101] Acl Alloys Inc. <http://www.aclalloys.com>.
- [102] C.R. Cowley and C.H. Corliss. Moderately accurate oscillator strengths from nbs intensities. *Mon. Not. R. astr. Soc.*, **203**:651–659, 1983.

- [103] G. Ljung, H. Nilsson, M. Asplund, and S. Johansson. New and improved experimental oscillator strengths in Zr II and the solar abundance of zirconium. *Astron. Astrophys.*, **456**:1181–1185, 2006.
- [104] Picomotor piezo linear actuators. <https://www.newport.com/f/picomotor-piezo-linear-actuators>.
- [105] T. Kessler, K. Brück, C. Baktash, J.R. Beene, Ch. Geppert, C.C. Havener, H.F. Krause, Y. Liu, D.R. Schultz, D.W. Stracener, C.R. Vane, and K. Wendt. Three-step resonant photoionization spectroscopy of Ni and Ge: ionization potential and odd-parity Rydberg levels. *J. Phys. B Mol. Opt. Phys.*, **40**:4413–4432, 2007.
- [106] S. Raeder, V. Sonnenschein, T. Gottwald, I.D. Moore, M. Reponen, S. Rothe, N. Trautmann, and K. Wendt. Resonance ionization spectroscopy of thorium isotopes-towards a laser spectroscopic identification of the low-lying 7.6 eV isomer of  $^{229}\text{Th}$ . *J. Phys. B At. Mol. Opt. Phys.*, **44**:165005, 2011.
- [107] Y. Liu, T. Gottwald, C. Mattolat, and K. Wendt. Three-photon resonance ionization of atomic Mn in a hot-cavity laser ion source using Ti:Sapphire lasers. *J. Phys. B Mol. Opt. Phys.*, **48**:115006, 2015.
- [108] S. Schmidt, Ch. Geppert, and Z. Andelkovic. Laser spectroscopy methods for probing highly charged ions at GSI. *Hyperfine Interact.*, **227**:29–43, 2014.
- [109] J. Beene, D.W. Bardayan, A. Galindo Urbarri, C.J. Gross, K.L. Jones, J.F. Liang, W. Nazarewicz, D.W. Stracener, B.A. Tatum, and R.L. Varner. ISOL science at the Holifield Radioactive Ion Beam facility. *J. Phys. G Nucl. Part. Phys.*, **38**:024002, 2011.
- [110] Y. Liu, C.U. Jost, A.J. Mendez II, D.W. Stracener, C.L. Williams, C.J. Gross, R.K. Grzywacz, M. Madurga, K. Miernik, D. Miller, S. Padgett, S.V. Paulauskas, K.P. Rykaczewski, and M. Wolinska-Cichocka. On-line commissioning of the HRIBF resonant ionization laser ion source. *Nucl. Instrum. Meth. Phys. Res. B*, **298**:5–12, 2013.